UNPRECEDENTED WAVE CONTROL WITH ACTIVE ELASTIC METAMATERIALS

A Dissertation

presented to

the Faculty of the Graduate School

at the University of Missouri-Columbia

In Partial Fulfillment

of the Requirements for the Degree

Doctor of Philosophy

---

by

QIAN WU

Dr. Guoliang Huang, Dissertation Supervisor

JULY 2022

The undersigned, appointed by the dean of the Graduate School, have examined the dissertation entitled

UNPRECEDENTED WAVE CONTROL WITH ACTIVE ELASTIC METAMATERIALS

presented by Qian Wu,
a candidate for the degree of Doctor of Philosophy in Mechanical Engineering,
and hereby certify that, in their opinion, it is worthy of acceptance.

Professor Guoliang Huang

Professor Hussein Nassar

Professor Zheng Yan

Professor Sarah Orton

Professor Frank Feng

DEDICATION

I am grateful for my parents, aunt and uncle who have been continuously loving, supporting and guiding me through all my hardships in my life.

ACKNOWLEDGEMENTS

I would like to start by thanking my supervisor, Prof. Guoliang Huang, for his help during my entire Ph.D. career. His patience, guidance and support allow me to have a fulfilling research experience in the past five years. As one of the most important mentors in my life, he trained me how to collaborate with people, how to prepare the academic career, and most importantly how to deliver research for maximum impact. His active attitudes towards the academic research and dedication have been consistently influencing me and impacting upon my ways of conducting research.

I would like to thank Professors Zaichun "Frank" Feng, Hussein Nassar, Zheng Yan and Sarah Orton for patiently responding to my emails and taking time to be my thesis committee.

I am also grateful for all the discussions that ever happened with all the current and former members from the research group. I would like to appreciate the discussions and guidance from Prof. Hussein Nassar and Prof. Yangyang Chen on some of the research topics covered in this dissertation. I also highly appreciate the help provided by Dr. P Shivashankar, Dr. Xiaodong Zhang and Dr. Xianchen Xu for all the sample fabrications and experimental testing in the last three sections (Sections 4-6) of the dissertation.

In addition, I would like to thank Dr. Huy Nguyen, Dr. Hui Chen, Dr. Rongyu Xia, Dr. Xiaopeng Li, Dr. Miles V. Barnhart, Dr. Yanzheng Wang, Chen Zhang, Shaoyun Wang, Yukai Yu, Jiaji Chen, Honghua Qian, and Xuanbo Miao for their help in research and life. Besides, I would like to thank Ms. Marilyn Nevels for her support during the past five years of my Ph.D. study.

The financial support from the Air Force Office of Scientific Research for the research on active metmaterials and the related topics is greatly acknowledged as well.

Lastly, I would like to thank all the friends and colleagues who have not been mentioned above for having supported me during this journey.

TABLE OF CONTENTS

LIST OF TABLES

LIST OF ILLUSTRATIONS

UNPRECEDENTED WAVE CONTROL WITH ACTIVE ELASTIC METAMATERIALS

Qian Wu

ABSTRACT

The research of elastic metamaterials has received tremendous attention from both academic and industrial communities over the past decade or so. Elastic metamaterials are a type of structured artificial composites whose macroscopic properties are determined by their periodic subwavelength building blocks. Due to their extreme obtainable material parameters, elastic metamaterials have been used to illustrate numerous exotic physical phenomena such as negative refraction and superlensing. Their potential applications include vibration and wave mitigations, waveguiding, energy harvesting, cloaking and so forth. In recent years, passive elastic metamaterials cannot meet the needs from modern wave functional devices, because their material parameters cannot be altered once they are fabricated. This drawback has eventually led to the development of active elastic metamaterials, which involves reprogrammable components and provides real time reconfigurability. Among the existing active control strategies, shunted piezoelectric materials have received considerable attention as they provide reprogrammable interactions between mechanical and electrical parts with large degree of freedom. They have been utilized to enhance the performance of conventional wave manipulation strategies such as broadband wave and/or vibration mitigations and reconfigurable wave beam steering. In this dissertation, some prototypes of active elastic metamaterials and metasurfaces are proposed for unconventional wave manipulation, by leveraging the circuit control concept of shunted piezoelectric materials. Theoretical and experimental approaches are utilized for illustrating design principles, characterizing system properties, and validating theoretical predictions. Specifically, various types of reprogrammable reciprocal/nonreciprocal interactions are employed to break certain symmetries in order to observe some nonreciprocal and asymmetric wave propagation behaviors. First, a type of non-Hermitian parity-time symmetric metabeam enable by balanced positive and negative resistance is introduced, which features unidirectional reflectionlessness at phase transition points. Then, a space-time modulated surface of a semi-infinite medium is investigated to support nonreciprocal frequency and mode conversions for Rayleigh waves. In addition, by leveraging the nonreciprocal coupling between piezoelectric sensors and actuators, a nonlocal metabeam and an active solid with odd mass density are proposed to realize nonreciprocal wave amplification/attenuation for flexural waves in dimension one and in-plane waves in dimension two, respectively. Last, in combination of time-dependent transfer functions and piezoelectric sensing-actuating system, a linear active metasurface capable of independently converting a flexural incidence into arbitrary frequency

components with phases and amplitudes on demand is presented with theoretical characterizations and experimental validations. It is emphasized that the dissertation focuses primarily on discovering and characterizing the fundamentals of some unconventional wave manipulation strategies in sold structures. The examples involved provide conceptual designs which could be readily transformed to the micro/nano scales. It is also hoped that the content covered by the dissertation could pave the ways for the development of next-generation wave control devices, in the areas of structural health monitoring, one-way mechanical devices as well as ultrasensitive sensing.

Chapter 1

INTRODUCTION

1.1 Acoustic and elastic metmaterials

Metamaterials are periodic artificial structures enabled by microscopic constituent units that determines the macroscopic physical manifestations of the bulk which may not be available in nature. Their working principle is based on the local resonances of the building blocks. It requires the lattice size to to be much smaller than the operating wavelengths. As a result, the metamaterials, the assembly of these building blocks, are similar to continuous materials, and exhibit effective constitutive parameters that may be flexibly tailored by structural and/or material modifications. In other words, one can design complex microscopic building blocks so that the bulk can respond to the external stimuli in unusual ways. The beginning of the exploration of the electromagnetic metamaterials dates back over two decades, featuring various emergent phenomena not readily observed in nature, such as negative refraction, hyperbolic dispersion and so forth. Unlike the metamaterials, photonic and phononic crystals are also periodic artificial structures, but rely on Bragg scattering mechanism requiring lattice constants on the comparable orders of operating wavelengths [1–6]. They feature relatively broad bandgaps which have led to practical applications, such as photonic/phononic waveguides, lasing, wave mitigation and so forth.

The first realization of acoustic metamaterials was based on a multi-phase design involving rubber-coated lead spheres embedded within an epoxy matrix to generate strong local resonance at extremely subwavelength scales [7]; see Fig. 1.1(a). This class of acoustic metamaterials possess frequency-dependent effective mass density and exhibit exotic acoustic properties such as negative mass density [8–11]. Inspired by this concept, frequency-dependent effective bulk modulus and even doubly negative materials have been proposed to enrich the research of acoustic metamaterials [12, 13]. Acoustic metamaterials are very useful in manipulating acoustic waves governed by Newton's law of

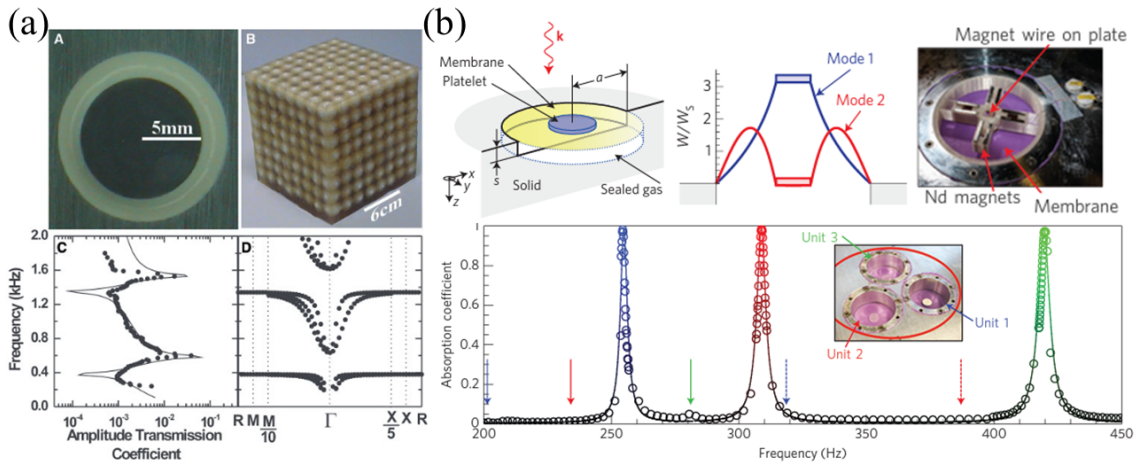

Figure 1.1: Acoustic metamaterials. (a) Acoustic metamaterial enabled by rubber-coated lead spheres embedded within an epoxy matrix to support strong local resonance at subwavelength scales [7]. (b) Membrane-type acoustic metamaterial used to achieve multi-band acoustic absorption and acoustic-electrical power conversion [16].

motion. For instance, membrane-type acoustic metamaterials can exhibit excellent sound absorption and attenuation performance together with broadband operability to go beyond the mass density law of sound attenuation [11, 14–16]; see Fig. 1.1(b). In addition, acoustic metamaterials are also a perfect candidate for achieving omnidirectional acoustic cloaking [17]. In recent years, acoustic metamaterials have also influenced the emergent research of elastic metamaterials (Fig. 1.2). The mechanical local resonance that results in tunable subwavelength properties has made the elastic metamaterial a promising candidate for many practical applications such as low-frequency vibration mitigation, earthquake mitigation, elastic cloaking, sensing, novel elastic waveguides and so forth [18–23]. elastic metamaterials have also been constructed to demonstrate several exotic physical phenomena such as hyperlensing by hyperbolic dispersion, negative constitutive parameters, and negative refraction of elastic waves [23–27].

However, the functionality of passive acoustic/elastic metamaterials supported by local resonances is very limited, simply due to the narrowband responses and lack of reconfigurability and adaptability. For instance, the mechanical wave mitigation and suppression with passive elastic metamaterials are prominent only within the vicinity of the resonance frequencies. The performance dies down quite fast as the operating frequencies deviate from the resonance frequencies. In order to tackle this issue, mechanically reconfigurable metamaterials, responsive to various external excitation, were used for broadband operability [28, 29]. However, the involved mechanisms usually require invasively structural designs of host media and complicated external conditions, which is not favorable for practical applications.

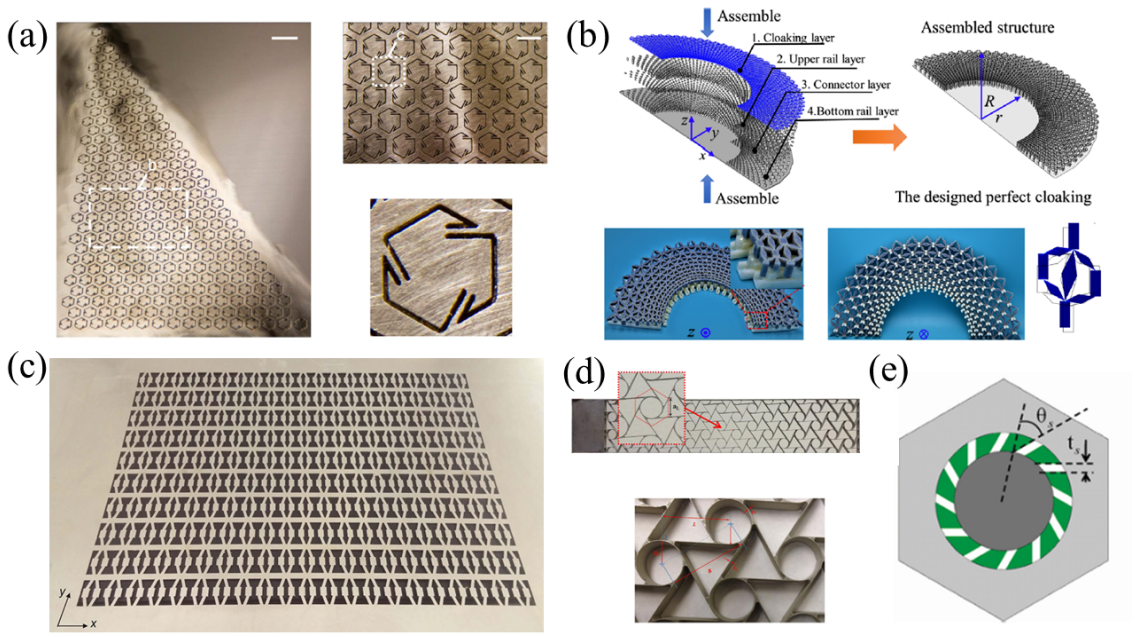

Figure 1.2: Passive elastic metamaterials. (a) Single-phase elastic metamaterial for realizing negative refraction of elastic waves [26]. (b) Physical realization of an elastic cloak with a polar metamaterial [18]. (c) Elastic metamaterials for subwavelength imaging [23]. (d) A chiral elastic metamaterial beam for broadband vibration suppression [20]. (e) An elastic metamaterial with simultaneously negative mass density and bulk modulus [27].

1.2 Active control with shunted piezoelectric materials

To address the aforementioned issue, integrating external adaptive materials or structures into passive elastic metamaterials has been considered as an effective non-invasive approach for accommodating the requirements of reconfigurability and adaptability. These "smart" inclusions constitute the so-called active elastic metamaterials whose dynamic constitutive parameters can be tuned with large degrees of freedom in a real-time fashion.

Various approaches of using adaptive materials and structures for achieving active elastic metamaterials have been reported. Among them, shunted piezoelectric materials have been widely explored simply due to their strong electromechanical responses (interplay between mechanical and electrical energy) and straightforward electronic tunability (external shunting circuits). Besides, as opposed to those reconfigurable metamaterials with invasive designs, the use of shunted piezoelectric materials does not necessarily requires the modification of host structures, thereby maintaining structural integrity. As for the real-time tunability, external shunting circuits with reprogrammable electric components, i.e., resistors, inductors and positive/negative capacitors, are adopted to modulate the electromechanical responses of shunted piezoelectric materials. In this way, the dynamic constitutive

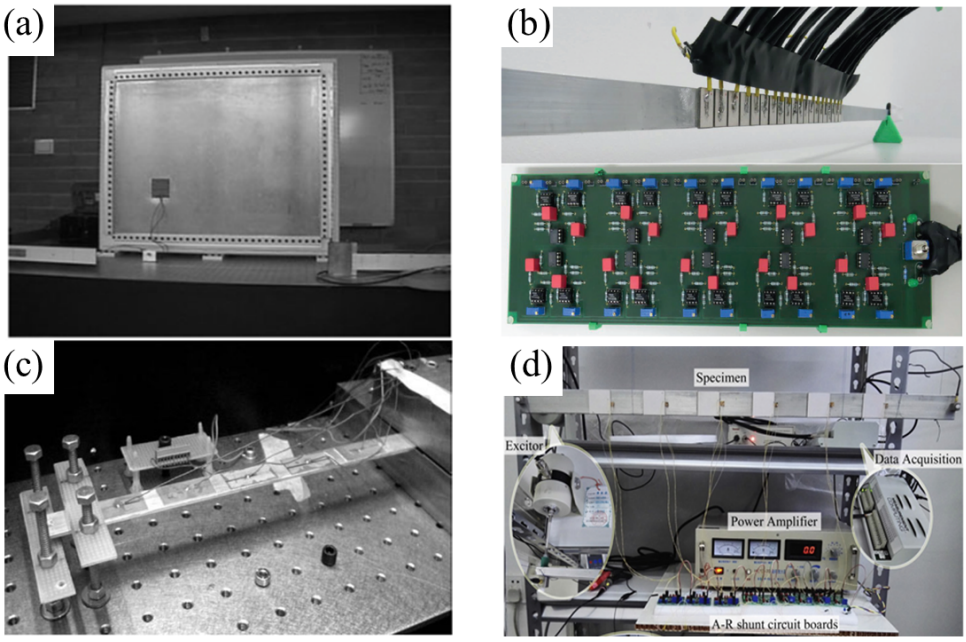

Figure 1.3: Piezoelectric-based vibration and wave control strategies. (a) A broadband active approach for controlling vibration in piezoelectric laminated structures [35]. (b) Hybrid electromechanical phononic crystal for elastic transmission modulation [36]. (c) Passive damping of beam vibrations with distributed piezoelectric-based electric networks [38]. (d) A periodic array of piezoelectric patches powered by enhanced resonant shunting circuits for broadband vibration attenuation [42].

parameters of active acoustic/elastic metamaterials, namely effective moduli and mass density, can be tuned electronically in a fairly straightforward way. The piezoelectric shunting technique was first introduced by Forward in 1979 for dampening mechanical vibrations in optical structures [30]. Later, Hagood and von Flotow were the first to formulate theoretically for the damping of structural vibrations with piezoelectric materials and passive electrical networks [31]. Inspired by these pioneering works, various control approaches involving piezoelectric materials modulated with programmable external shunts were used to realize vibration control, wave mitigation and spatial wave control functionalities [32–47]; see Fig. 1.3. Aside from the conventional approaches, enormous efforts have also been devoted in developing other modern wave control strategies using piezoelectric shunts, which appears to be more compact yet more efficient. To be specific, elastic metasurfaces equipped with reprogrammable piezoelectric shunts can shape the transmitted and/or reflected wavefronts upon certain incidences with electronically tunable degree of freedom [48, 49]. Thanks to the shunted piezoelectric inclusions, a single elastic metasurface can be programmed to perform multiple tasks, including beam steering, airy beam, focusing, and even skin cloaking, in a real-time fashion [50]; see Fig. 1.4(a). Shaping elastic wave mode conversion has also been proved possible with a piezoelectric-based programmable meta-boundary [51]; see Fig. 1.4(b). Moreover, a recent

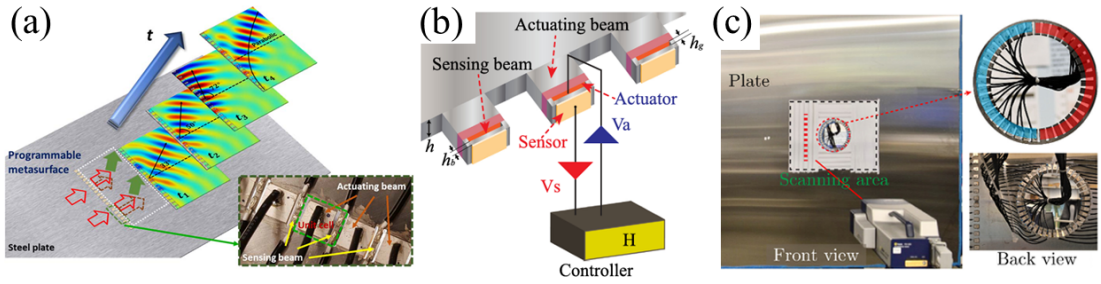

.

Figure 1.4: Active elastic metasurfaces enabled by reprogrammable piezoelectric shunts. (a) A reprogrammable metasurface capable of conducting real-time control of broadband elastic rays [50]. (b) A piezoelectric-based programmable meta-boundary that shapes elastic wave mode conversion [51]. (c) Optimal flexural wave absorption and cloaking with an active meta-layer [52].

work demonstrated optimal flexural wave absorption and cloaking with an active meta-layer powered by programmable piezoelectric shunts [52]; see Fig. 1.4(c).

1.3 Motivations and outline

Taking advantage of the current state of art of programmable elastic metamaterial building blocks used in conventional wave control problems, this dissertation will explore some unconventional wave manipulation schemes in which asymmetry and nonreciprocity of elastic wave propagation will be realized. The exotic elastic wave behaviors to be discussed will be characterized and demonstrated using analytical, numerical and experimental approaches.

This dissertation is structured as follows. In Chapter 2, a non-Hermitian parity-time ($\mathcal{PT}$) symmetric metamaterial beam system is analytically and numerically demonstrated to support unidirectional reflectionlessness of one-dimensional (1D) flexural wave propagation. The physical realization of the metamaterial beam is based on piezoelectric patches with shunted circuits that include balanced positive and negative resistances. This way, a balanced gain-loss pairs for flexural motions are formed, and a parity-time phase transition through exceptional points (EPs) can be observed to interpret the unidirectional reflectionlessness. In Chapter 3, a space-time modulated metamaterial consisting of discrete spring-mass oscillators is analytically and numerically reported to achieve one-way nonreciprocal Rayleigh wave conversion on the surface of a semi-infinite medium. The time-reversal symmetry is effectively broken by the space-time modulation of the spring constants in a wave-like fashion. As a result, reciprocity is broken for Rayleigh wave propagation, and the harmonic and mode conversions are therefore asymmetric. In Chapter 4, a new class of active metamaterial beams with nonlocal piezoelectric interactions is reported to realize nonreciprocal wave

amplification and attenuation and nonreciprocal roton-like behavior for flexural waves. It is shown numerically that by properly modifying the transfer functions and order of nonlocality, the complex dispersion relation of the metamaterial beam can be engineered with great flexibility. This in turn leads to the emergence of one-way flexural amplification and attenuation, which is experimentally validated. The asymmetric roton-like dispersion, realized by multiple nonlocal feed-forward control loops, leads to multiple wave components propagating at one frequency along both directions, but experiencing various degrees of amplification and attenuation. In Chapter 5, a new class of active solid is introduced possessing odd/asymmetric dynamic mass density tensor owing to a non-conservative force relation in two dimensions (2D). This concept is first physically explained by the consideration of kinetic energy cycle of an odd-mass-density unit cell. Then, it is validated experimentally by demonstrating a 1D nonreciprocal wave coupling between transverse and longitudinal modes in a piezo-based sensing-actuating beam system. Additionally, the active metamaterial can perform energy phase transition between energy-unbroken and energy-broken phases separated by EPs, which exhibits similarities with the non-Hermitian $\mathcal{PT}$ symmetric systems with balanced gain and loss (Chapter 2). This intriguing phenomenon features directional in-plane wave amplification and attenuation and lays the foundation for 2D unprecedented elastic wave manipulation. In Chapter 6, a linear active meta-layer capable of independently converting a flexural incidence of one frequency into arbitrary frequency components with demanded output phases and amplitudes is both theoretically and experimentally proposed. The meta-layer is driven by a time-dependent transfer function through bonded piezoelectric actuators and sensors to perform independent parallel operations over waves at different frequencies. The design breaks energy conservation by pumping in electrical energy to cancel incidence and freely emit any demanded transmitted waves. Then, the proposed meta-layers with programmable phase and frequency gradients are adopted to realize frequency-converted beam deflection and dynamic beam steering functions, respectively, for 2D flexural waves.

Chapter 2

ASYMMETRIC SCATTERING OF FLEXURAL WAVES IN A PARITY-TIME SYMMETRIC METAMATERIAL BEAM

2.1 Introduction

Non-Hermitian $\mathcal{PT}$ symmetric systems that possess real spectra have attracted a great deal of attention and been intensively investigated in quantum mechanics during the past two decades [53, 54]. EP points behaving as thresholds of phase transitions are of particular interest. For example, below the EP, the spectrum of the system is real, corresponding to the exact $\mathcal{PT}$ symmetric phase. On the contrary, beyond the EP, the system enters the $\mathcal{PT}$ broken phase where the spectrum becomes complex [53]. Owing to the similarity between Schördinger and Helmholtz equations, $\mathcal{PT}$ symmetric systems have been recently extensively studied in electromagnetic and acoustic devices [55–81], and paved the way to some fascinating and unconventional applications, such as sensors with extremely high sensitivity [76, 78, 79], unidirectional cloaks [59, 72, 77] and robust wireless power transfer [80]. The key in designing acoustic and optical $\mathcal{PT}$ symmetric devices is to introduce balanced loss and gain components. In other words, the imaginary part of the refractive index is required to be an odd function in space, while the real part is even [53–57, 59, 60, 64, 66]. Based on this strategy, many interesting and unconventional wave phenomena have been demonstrated numerically and/or experimentally in optics and acoustics, such as asymmetric scattering [55–57, 59, 61, 63, 64, 66, 68], negative refraction [70, 71] and coherent perfect absorber and laser [73–75].

Metamaterials provide an appealing solution to achieving loss and gain mediums for $\mathcal{PT}$ symmetric devices [45, 82, 83]. In order to realize optical loss and gain components, active materials such as Fe-doped $LiNbO_3$ and InGaAsP have been utilized [56, 67]. In acoustics, leaky waveguides with multiple slits and active microphone arrays have been designed to access loss and gain [66]. In

practice, gain components usually require active approaches, resulting in complex control systems. To circumvent this complexity, quasi-$\mathcal{PT}$ symmetric devices containing only passive loss components have been proposed. Even though those systems are not strictly $\mathcal{PT}$ symmetric, similar acoustic and optical asymmetric scattering phenomena can still be observed [56, 57, 61, 68].

Nevertheless, the study on non-Hermitian $\mathcal{PT}$ symmetry for elastic waves in solid media is still in the early stage. Shunted piezoelectric materials have been regarded as one of the best candidates to achieve the elastic gain and loss because the energy conversion between mechanical and electrical domains can be controlled by electrical circuits in real-time [21, 39, 43–45, 84–86]. Piezotronics effect in piezoelectric semiconductors was first utilized to amplify and attenuate pressure waves in the $\mathcal{PT}$ symmetric elastic system, where the asymmetric scattering (or unidirectional reflectionlessness) has been proposed theoretically [69]. On the other hand, electrical-circuit-shunted piezoelectric ceramic materials have been extensively applied in vibration and wave attenuation applications for decades, where elastic energy can be transferred and absorbed by the shunted resistance [21, 39, 43, 84–86]. In addition, a tunable $\mathcal{PT}$ symmetric elastic system with shunted piezoelectric materials has been investigated analytically for pressure waves [84]. With the help of the negative and positive shunting resistances together with inductance, balanced gain and loss can be built.

In this Chapter, the $\mathcal{PT}$ symmetry in an elastic beam for flexural waves is explored based on shunted piezoelectric patches. It is first presented that the $\mathcal{PT}$ symmetry condition for flexural waves, based on Euler's beam assumptions, also requires the balanced gain and loss. They are then realized with shunted negative and positive resistances, respectively, together with a negative capacitance for the sake of functionality amplification and storage modulus tuning. In particular, two analytical approaches, effective medium theory and transfer matrix method, are employed to determine effective material parameters and asymmetric scattering properties of the $\mathcal{PT}$ symmetric metamaterial beam. Numerical simulations are carried out to validate analytical predictions and demonstrate the unidirectional reflectionlessness phenomena. It is shown that the unidirectional reflectionlessness originates from the $\mathcal{PT}$ phase transitions or EPs. Furthermore, tunability of EPs is examined through selecting different spacing between piezoelectric patches and shunting circuit parameters. The design expands material parameters governing the propagation of flexural waves to the complex domain, and explores the asymmetric flexural wave scattering originating from the $\mathcal{PT}$ symmetry. This could open new pathways to applications such as asymmetric control, enhanced sensing, amplification and localization of flexural waves.

2.2 Characterizations of the parity-time symmetric beam

$\mathcal{PT}$ symmetry condition for flexural waves and design principles

To examine the exact $\mathcal{PT}$ symmetry condition for flexural waves propagating in the x-direction along a 1D thin beam, we consider Euler's beam assumptions and the governing equation is written as

$$\frac{\partial^2}{\partial x^2}\left(D_{eff}(x)\frac{\partial^2 w(x)}{\partial x^2}\right)+\rho_{eff}(x)h_b\frac{\partial^2 w(x)}{\partial t^2}=0, \tag{2.1}$$

where $w(x), D_{eff}(x), \rho_{eff}(x)$ and h_b denote the displacement field of the flexural wave, effective bending stiffness, effective mass density and thickness of the thin beam. The $\mathcal{PT}$ symmetry of Eq. (2.1) implies

$$\begin{aligned}\hat{\mathcal{P}}\hat{\mathcal{T}}\left\{\frac{\partial^2}{\partial x^2}\left(D_{eff}(x)\frac{\partial^2 w(x)}{\partial x^2}\right)+\rho_{eff}(x)h_b\frac{\partial^2 w(x)}{\partial t^2}\right\}\\ =\frac{\partial^2}{\partial x^2}\left(D^*_{eff}(-x)\frac{\partial^2\hat{\mathcal{P}}\hat{\mathcal{T}}\{w(x)\}}{\partial x^2}\right)\\ +\rho^*_{eff}(-x)h_b\frac{\partial^2\hat{\mathcal{P}}\hat{\mathcal{T}}\{w(x)\}}{\partial t^2},\end{aligned} \tag{2.2}$$

where $\hat{\mathcal{P}}$ and $\hat{\mathcal{T}}$ are the parity and time reversal operators, respectively. Performing $\mathcal{PT}$ transformations in Eq. (2.2), the $\mathcal{PT}$ symmetry condition can be simply derived as

$$D_{eff}(x)=D^*_{eff}(-x),\quad \rho_{eff}(x)=\rho^*_{eff}(-x), \tag{2.3}$$

indicating that loss and gain of flexural waves should be balanced in space. Based on the condition illustrated in Eq. (2.3), Fig. 2.1(a) shows the schematic of a $\mathcal{PT}$ symmetric beam for asymmetric scattering of flexural waves, where discrete loss and gain components are distributed along the beam in a manner that follows an odd function respect to a point. Without loss of generality, ρ_{eff} is assumed as real values in the study. We focus on the physical realization of the complex effective bending stiffness to induce the loss and gain of flexural waves. For this purpose, two piezoelectric patches are bonded onto a host beam and each patch is shunted with a negative or positive resistors (R_{sh} or $-R_{sh}$) and a negative capacitor C_{sh} connected in parallel [Fig. 2.1(b)]. In particular, the negative resistance, $-R_{sh}$, aims to constitute the gain component, whereas the positive resistance, R_{sh}, aims to constitute the loss component. The negative capacitance is mainly responsible for amplifying the gain and loss effects and, at the same time, tuning the storage modulus. In general, both negative resistance and negative capacitance can be physically attained by negative impedance

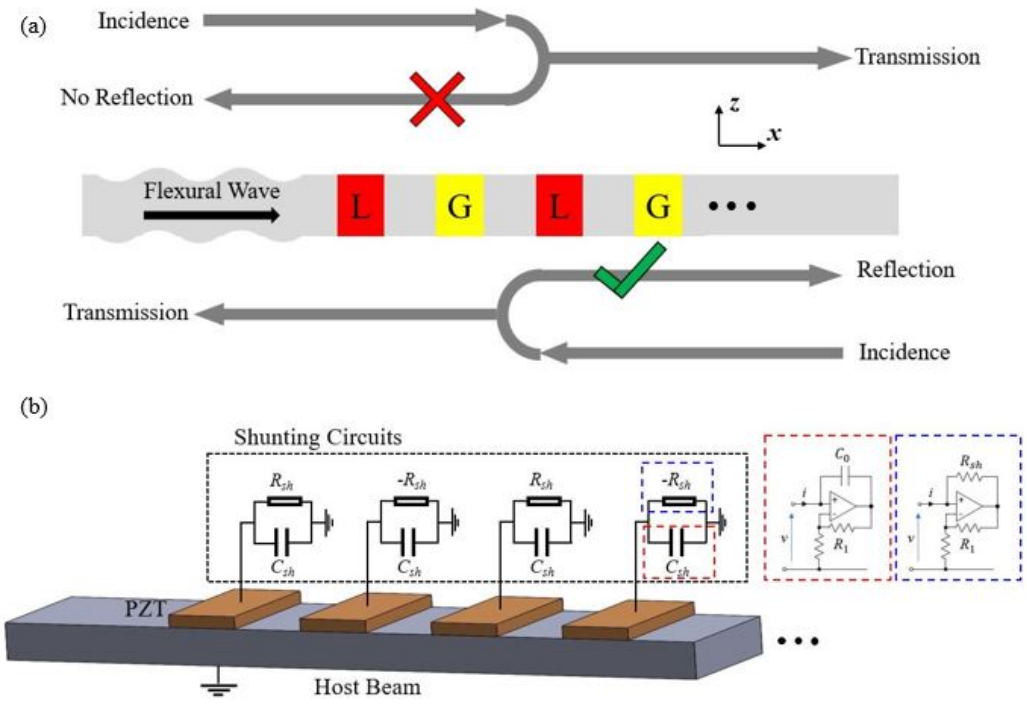

Figure 2.1: (a) Schematic of the non-Hermitian $\mathcal{PT}$ symmetric beam for asymmetric flexural wave scattering. Unidirectional reflectionlessness is illustrated in the figure. (b) Physical realization of the $\mathcal{PT}$ symmetric beam with piezoelectric patches shunted with negative and positive resistances together with a negative capacitance connected in parallel. The insets highlighted in red and blue illustrate the physical realization of the electrical shunting components. Reproduced from The Journal of the Acoustical Society of America 146, 850 (2019), with the permission of AIP Publishing.

converters (non-Foster circuits) [insets of Fig. 2.1(b)]. The resulted effective negative impedance can be analytically determined

$$Z_{eff} = -Z \tag{2.4}$$

where Z denotes a positive electric impedance element. In the design, Z is a positive resistance R_{sh} or a positive capacitance C_0 for the realization of a negative resistance $-R_{sh}$ or a negative capacitance $C_{sh} = -C_0$, as illustrated by the insets of Fig. 2.1(b).

Note that the negative capacitance is technically not equivalent to the inductance [84]. Adding inductance to the shunting circuit will produce electrical resonance, which makes the resulted effective parameters and its related wave behavior highly frequency-dependent. On the other hand, using negative capacitance can prevent the frequency-dependency and achieve exceptional points at multiple frequencies in the $\mathcal{PT}$ symmetric beam. Since gain and loss components are purely controlled by shunting circuit parameters, the system designed possesses a huge potential for real-time and remote tuning of asymmetric scattering of flexural waves.

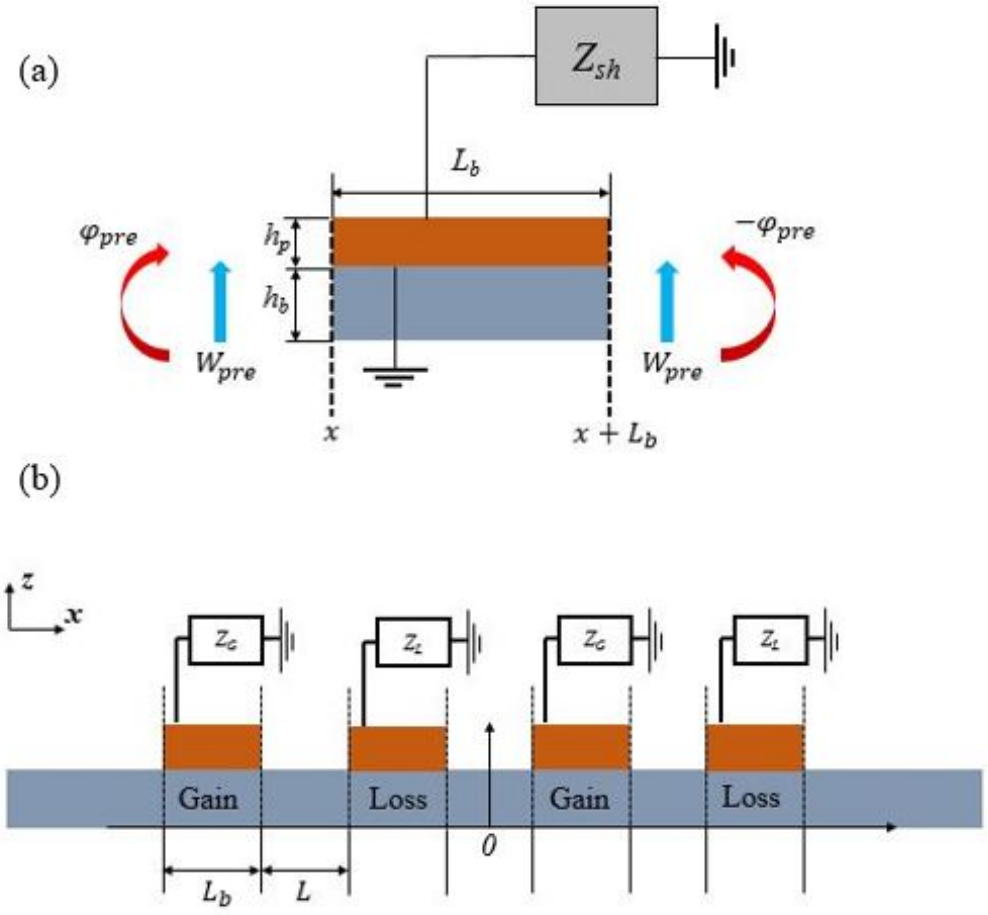

.

Figure 2.2: (a) Loss or gain unit cell used in effective medium theory and transfer matrix method. (b) Schematic of the $\mathcal{PT}$ symmetric metamaterial beam used in transfer matrix method. Reproduced from The Journal of the Acoustical Society of America 146, 850 (2019), with the permission of AIP Publishing.

Analytical characterizations

To characterize the asymmetric scattering of flexural waves within the $\mathcal{PT}$ symmetric metamaterial beam with shunted piezoelectric patches, the scattering matrix of a finite $\mathcal{PT}$ symmetric metamaterial beam is derived first based on the transfer matrix method (TMM) and its effective material parameters is then retrieved using the effective medium theory (EMT). Plane stress assumptions are considered in the study.

For the unit cell structure shown in Fig. 2.2(a), thicknesses and lengths of the host beam and piezoelectric patches are denoted as h_b, h_p and L_b, respectively. The shunting impedance is represented by Z_{sh}. Considering traction-free boundary conditions on top and bottom surfaces of

the metamaterial beam, linear constitutive relations of piezoelectric patches can be simplified and written as

$$\begin{aligned} S_1 &= s_{11}^E T_1 + d_{31} E_3, \\ D_3 &= d_{31} T_1 + \varepsilon_{33}^T E_3, \end{aligned} \tag{2.5}$$

where S_1 and T_1 represent the normal strain and stress along the x-direction, respectively, and D_3, and E_3 represent the electric displacement and electric field along the z-direction, respectively. s_{11}^E, $d_3 1$; and $e_3^T 3$ are the compliance coefficient under constant electric field, dielectric constant under constant stress and piezoelectric coefficient, respectively. For the unit cell shown in Fig. 2.2(a), the displacement field along the x-direction, u, can be assumed as the combination of the displacements at the mid-plane of the host beam in the form of

$$u(x,z) = u_0(x) - z\frac{\partial w}{\partial x}, \tag{2.6}$$

where u_0 represents the displacement along the x-direction. A linear electric field distribution and its corresponding electric potential are assumed as

$$\begin{aligned} E_3(x,z) &= z \cdot a(x) + b(x), \\ V(x,z) &= -\left[\frac{a(x)}{2} z^2 + b(x) z + c(x)\right] \end{aligned} \tag{2.7}$$

where a, b, and c are the distribution functions which can be obtained through piezoelectric governing equations and electric boundary conditions. By combining Eqs. (2.5)-(2.7) and considering the electrical governing equation $\partial D_3/\partial_z = 0$, the distribution functions a, b, and c, and the electric potential on the upper electrode Vupper can be determined, respectively, as

$$\begin{aligned} a &= \frac{d_{31}}{s_{11}^E \varepsilon_{33}^T - d_{31}^2} \frac{\partial^2 w}{\partial x^2}, \\ b &= -\frac{V_{upper}}{h_p} - \frac{a}{2}\left(h_b + h_p\right), \\ c &= -\frac{h_b^2}{8} a - \frac{h_b}{2} b, \\ V_{upper} &= \frac{i\omega \frac{d_{31}}{s_{11}^E} Z_{sh} \int_0^{L_b} \left(\frac{\partial u_0}{\partial x} - \frac{h_p + h_b}{2} \frac{\partial^2 w}{\partial x^2}\right) dx}{1 + i\omega C_p^T \left(1 - k_{31}^2\right) Z_{sh}} \end{aligned} \tag{2.8}$$

where $k_{31}^2 = d_{31}^2 / s_{11}^E \varepsilon_{33}^T$ is the electromechanical coupling coefficient and the capacitance of the piezoelectric patch, $C_p^T = \varepsilon_{33}^T L_b / h_p$

Integrating stress components over the thickness of the beam with respect to the mid-plane in

the host beam, the bending moment, normal and shear forces in the unit cell can be obtained as

$$\begin{aligned} M &= I\frac{\partial^2 w}{\partial x^2} - J\frac{\partial u_0}{\partial x} - FV_{\text{upper}}\ , \\ N &= K\frac{\partial u_0}{\partial x} - J\frac{\partial^2 w}{\partial x^2} + GV_{upper}, \\ T &= I\frac{\partial^3 w}{\partial x^3} - J\frac{\partial^2 u_0}{\partial x^2} \end{aligned} \tag{2.9}$$

where

$$\begin{aligned} I &= \frac{Eh_b^3}{12} + \frac{6h_b h_p^2 + 3h_b^2 h_p + 4h_p^3}{12s_{11}^E} + \frac{h_p^3 d_{31}^2}{12s_{11}^E\left(s_{11}^E\varepsilon_{33}^T - d_{31}^2\right)}, \\ J &= \frac{h_p^2 + h_b h_p}{2s_{11}^E}, \quad K = Eh_b + \frac{h_p}{s_{11}^E}, \quad F = \frac{(h_b + h_p)\, d_{31}}{2s_{11}^E}, \\ G &= \frac{d_{31}}{s_{11}^E}, \end{aligned}$$

and E denotes the Young's modulus of the host beam. Based on Eq. (2.9), equations of motion for coupled flexural and longitudinal waves are derived as

$$\begin{aligned} I\frac{\partial^4 w}{\partial x^4} - J\frac{\partial^3 u_0}{\partial x^3} + \bar{\rho}\frac{\partial^2 w}{\partial t^2} &= 0 \\ K\frac{\partial^2 u_0}{\partial x^2} - J\frac{\partial^3 w}{\partial x^3} - \bar{\rho}\frac{\partial^2 u_0}{\partial t^2} &= 0 \end{aligned} \tag{2.10}$$

in which $\bar{\rho} = \rho_b h_b + \rho_p h_p$. Here ρ_b and ρ_p are the mass density of the support beam and the piezoelectric material, which are given in Table I. General solutions to Eq. (2.10) can be found as

$$\begin{aligned} u_0 &= \sum_{n=1}^{6} \bar{A}_n \beta_n e^{\gamma_n x}, \\ w &= \sum_{n=1}^{6} \bar{A}_n e^{\gamma_n x} \end{aligned} \tag{2.11}$$

where $\bar{A}_n$ are arbitrary constants, γ_n are the roots of the characteristic equations given by Eq. (2.10) and $\beta_n = (I\gamma_n^4 - \omega^2\bar{\rho}/(J\gamma_n^3)$. Substituting Eq. (2.11) into Eq. (2.8), the electric potential on the upper electrode of the piezoelectric patch can be rewritten as

$$V_{upper} = \sum_{n=1}^{6} \frac{i\omega\frac{d_{31}}{s_{11}^E} Z_{sh}\left(\beta_n - \frac{h_b+h_p}{2}\gamma_n\right)\left(e^{\gamma_n L_b} - 1\right)}{1 + i\omega C_p^T\left(1 - k_{31}^2\right) Z_{sh}}. \tag{2.12}$$

Similarly, for host beam sections without piezoelectric patches, longitudinal and flexural wave

components are decoupled and can be simply written as

$$\begin{aligned} u_0^{(b)} &= \sum_{n=5}^{6} \bar{A}_n^{(b)} e^{\gamma_n^{(b)} x} \\ w^{(b)} &= \sum_{n=1}^{4} \bar{A}_n^{(b)} e^{\gamma_n^{(b)} x} \end{aligned} \tag{2.13}$$

in which $\bar{A}_n^{(b)}$ are arbitrary constants, and

$$\gamma_{1,2}^{(b)} = \pm i \sqrt[4]{\frac{12\rho_b\omega^2}{Eh_b^2}}, \quad \gamma_{3,4}^{(\mathrm{b})} = \pm \sqrt[4]{\frac{12\rho_\mathrm{b}\omega^2}{\mathrm{Eh}_\mathrm{b}^2}}, \text{ and}$$
$$\gamma_{5,6}^{(b)} = \pm i \sqrt{\frac{\rho_b\omega^2}{E}}$$

To construct transfer matrices, a vector $Y_i = [w, \partial w/\partial x, M, T, u_0, N]^T$ is then defined where $i = b$ or p representing host beam sections or shunted piezoelectric beam sections, respectively. With the help of Eqs. (2.11-2.13), Eq. (2.9) can be rewritten in the form of

$$\begin{aligned} Y_p &= \boldsymbol{B}_p A_p \\ Y_b &= \boldsymbol{B}_b A_b \end{aligned} \tag{2.14}$$

where the characteristic matrix $\boldsymbol{B}_i$ and the vector A_i representing the complex wave amplitudes are shown as

$$\boldsymbol{B}_p(x) = \begin{bmatrix} a_{11} & a_{12} & a_{13} & a_{14} & a_{15} & a_{16} \\ a_{21} & a_{22} & a_{23} & a_{24} & a_{25} & a_{26} \\ a_{31} & a_{32} & a_{33} & a_{34} & a_{35} & a_{36} \\ a_{41} & a_{42} & a_{43} & a_{44} & a_{45} & a_{46} \\ a_{51} & a_{52} & a_{53} & a_{54} & a_{55} & a_{56} \\ a_{61} & a_{62} & a_{63} & a_{64} & a_{65} & a_{66} \end{bmatrix}$$

and

$$\boldsymbol{B}_b = \begin{bmatrix} 1 & 1 & 1 & 1 & 0 & 0 \\ \gamma_1^b & \gamma_2^b & \gamma_3^b & \gamma_4^b & 0 & 0 \\ Eh_b^3\left(\gamma_1^b\right)^2/12 & Eh_b^3\left(\gamma_2^b\right)^2/12 & Eh_b^3\left(\gamma_3^b\right)^2/12 & Eh_b^3\left(\gamma_4^b\right)^2/12 & 0 & 0 \\ Eh_b^3\left(\gamma_1^b\right)^3/12 & Eh_b^3\left(\gamma_2^b\right)^3/12 & Eh_b^3\left(\gamma_3^b\right)^3/12 & Eh_b^3\left(\gamma_4^b\right)^3/12 & 0 & 0 \\ 0 & 0 & 0 & 0 & 1 & 1 \\ 0 & 0 & 0 & 0 & Eh_b\gamma_5^b & Eh_b\gamma_6^b \end{bmatrix}$$

where

$$a_{1n} = 1$$

$$a_{2n} = \gamma_n$$

$$a_{3n} = I\gamma_n^2 - J\beta_n\gamma_n - FV_{upper}e^{-\gamma_n x}$$

$$a_{4n} = I\gamma_n^3 - J\beta_n\gamma_n^2$$

$$a_{5n} = \beta_n$$

$$a_{6n} = K\beta_n\gamma_n - J\gamma_n^2 + GV_{upper}e^{-\gamma_n x}$$

Based on Eq. (2.14) and applying continuity boundary conditions, the transfer matrix $\boldsymbol{M}_i$ of the unit cell, where $i = G$ or L, is derived as

$$A_b\left(x + L_b\right) = \boldsymbol{B}_b^{-1}\boldsymbol{B}_p\left(x + L_b\right)\boldsymbol{P}_p\boldsymbol{B}_p^{-1}(x)\boldsymbol{B}_b A_b(x) = \boldsymbol{M}_i A_b(x) \tag{2.15}$$

where $\boldsymbol{P}_p$ is the propagation matrix of the shunted piezoelectric beam section and reads

$$\boldsymbol{P}_p = \mathrm{diag}(e^{\gamma_1 L_b}, e^{\gamma_2 L_b}, e^{\gamma_3 L_b}, e^{\gamma_4 L_b}, e^{\gamma_5 L_b}, e^{\gamma_6 L_b})$$

Then the global transfer matrix for an array of m unit cells illustrated in Fig. 2.2(b) then reads

$$\boldsymbol{M}^{TMM} = \left(\boldsymbol{M}_G\boldsymbol{P}_b^{-1}\boldsymbol{M}_L\boldsymbol{P}_b^{-1}\right)^m \tag{2.16}$$

in which $\boldsymbol{P}_b$ is the propagation matrix of the host beam sandwiched by the gain and loss sections, and is given by

$$\boldsymbol{P}_p = \mathrm{diag}(e^{\gamma_1^b L}, e^{\gamma_2^b L}, e^{\gamma_3^b L}, e^{\gamma_4^b L}, e^{\gamma_5^b L}, e^{\gamma_6^b L})$$

To obtain the scattering matrix, an incident flexural wave with unitary displacement amplitude is prescribed on the left or right background beams as

$$\begin{bmatrix} t_{l(r)} \\ 0 \\ t^e_{l(r)} \\ 0 \\ t^p_{l(r)} \\ 0 \end{bmatrix} = M^{TMM}_{l(r)} \begin{bmatrix} 1 \\ r_{l(r)} \\ 0 \\ r^e_{l(r)} \\ 0 \\ r^p_{l(r)} \end{bmatrix} \tag{2.17}$$

where the subscripts denote the incident direction, and the superscripts "e" and "p" represent the evanescent flexural and the propagating longitudinal waves, respectively. Here, $\boldsymbol{M}_l^{TMM} = (\boldsymbol{M}_G\boldsymbol{P}_b\boldsymbol{M}_L\boldsymbol{P}_b)^m$ for the transmission from the left side, while $\boldsymbol{M}_r^{TMM} = (\boldsymbol{M}_L\boldsymbol{P}_b\boldsymbol{M}_G\boldsymbol{P}_b)^m$ for the opposite. Solving the first, second, fourth, and sixth equations involved in Eq. (2.16) gives the scattering matrix

$$\boldsymbol{S}^{TMM} = \begin{bmatrix} t_l & r_r \\ r_l & t_r \end{bmatrix} \tag{2.18}$$

for flexural waves.

Next, we determine the effective mass density ρ_{eff} and effective bending stiffness D_{eff} for the beam section with a shunted piezoelectric patch.37 Note that the size of the unit cell should be sufficiently small compared to the wavelength in order for effective medium theory to work properly. For the unit cell structure shown in Fig. 2.2(a), the physical quantities on the right edge ($x = L_b$) are related to that on the left edge ($x = 0$) as

$$Y_b\left(L_b\right) = \boldsymbol{T}_{bb}Y_b(0) \tag{2.19}$$

in which the value of x in the schematic of the unit cell is set to be 0, and the transfer matrix reads

$$\boldsymbol{T}_{bb} = \boldsymbol{B}_p\left(L_b\right)\boldsymbol{P}_p\boldsymbol{B}_p^{-1}(0) \tag{2.20}$$

To determine the effective mass density, the transverse harmonic displacement field at the left ($x = 0$) and right ($x = L_b$) boundaries of the metamaterial unit cell is prescribed by W_{pre}, where the rotational angle and longitudinal displacement is set to zero at these two boundaries. A commercial finite element software COMSOL Multiphysics is then used to solve the harmonic problem, and the reaction forces are calculated at boundaries. The effective mass density can be determined according to the following expression:

$$\rho_{eff} = \frac{2T^l(0)}{\omega^2 W_{pre}L_b h_b}, \tag{2.21}$$

where T^l denotes the calculated reaction force at the left edge of the unit cell.

To determine the effective bending stiffness, the harmonic rotational angles at the left ($x = 0$) and right ($x = L_b$) boundaries of the metamaterial unit cell are assumed as φ_{pre} and $-\varphi_{pre}$, respectively. The transverse displacements are fixed at zero for both the boundaries. We release the longitudinal displacement at the boundaries on either one side or two sides (the longitudinal force is set to be zero) such that the global reaction bending moments on the boundaries can be naturally obtained

Parameters	Values	Parameters	Values
L_b	20 mm	c_{11}^E	126 GPa
E_b	70 GPa	c_{12}^E	79.5 GPa
h_b	1.6 mm	c_{13}^E	84.1 GPa
h_p	0.5 mm	c_{33}^E	117 GPa
ρ_b	2700 kg/m^3	c_{44}^E	23 GPa
ρ_p	7600 kg/m^3	c_{66}^E	23.25 GPa
e_{15}	17 C/m^2	d_{31}	-2.74 $\times 10^{-12}$
e_{31}	-6.55 C/m^2	ε_{11}^S	1700 ε_0
e_{33}	23.3 C/m^2	ε_{33}^S	1470 ε_0
L	200 mm	ε_{33}^T	3443 ε_0

Table 2.1: Unit cell geometrical and material parameters.

with respect to the rotational center, where effects of the longitudinal displacement are decoupled. Specifically, the longitudinal displacement on the left boundary ($x = 0$) of the unit cell is fixed and the longitudinal force on the right boundary ($x = L_b$) is set to be zero, where the obtained reaction bending moment with respect to the rotational center can be used for the effective bending stiffness calculation. After solving the harmonic problem numerically, the effective bending stiffness can be determined according to the following equation:

$$D_{eff} = \frac{M^{(r)}\left(L_b\right)}{2\varphi_{pre}} \tag{2.22}$$

where $M^{(r)}$ represents the reaction bending moment.

The explicit expressions of the effective parameters calculated from matrix operations are too complicated and impractical to be given here. In fact, solving matrix numerically for reaction force T^l and the reaction bending moment $M^{(r)}$ at boundaries of the unit cell is much easier. Note that, in the linear region, those reaction force and reaction bending moment are proportional to W_{pre} and φ_{pre}, respectively. In light of this, effective properties are independent on the prescribed displacement/rotation, which is consistent with the effective medium theory. In the next subsection, the effective material parameters obtained with the EMT will be compared with the numerically calculated ones for model validations. The results will demonstrate how the shunting circuits can realize desired loss and gain components for flexural waves. After that, the TMM will be used to characterize the scattering properties of the shunted piezoelectric metamaterial beam.

Effective material parameters

In the study, the $\mathcal{PT}$ symmetric beam contains piezoelectric patches bonded on an aluminum beam. Half of them are shunted with negative capacitance and negative resistance connected in parallel

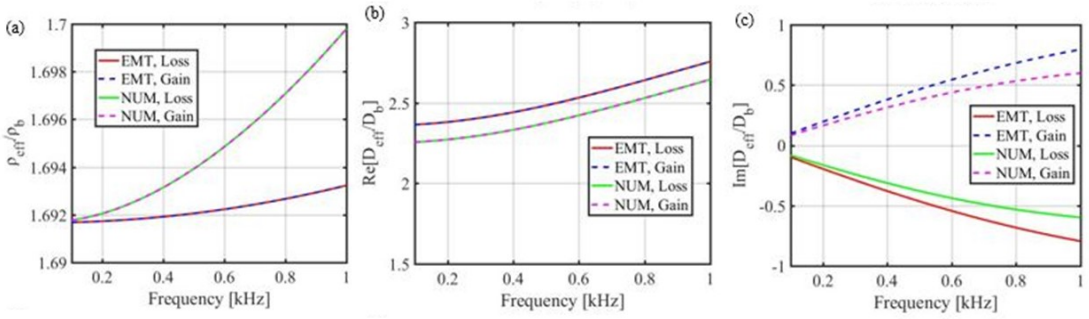

.

Figure 2.3: Analytically calculated and numerically simulated effective material parameters: (a) normalized effective mass density $\rho_{eff} = \rho_b$; (b) Real and (c) imaginary parts of the normalized effective bending stiffness $D_{eff} = D_b$. The solid curves correspond to the loss while the dashed to the gain. Reproduced from The Journal of the Acoustical Society of America 146, 850 (2019), with the permission of AIP Publishing.

with the shunting impedance $Z_{sh} = -R_{sh}/\left(-R_{sh}i\omega C_{sh} + 1\right)$ to amplify waves, whereas the rest are shunted with negative capacitance and positive resistance connected in parallel with the shunting impedance $Z_{sh} = R_{sh}/\left(R_{sh}i\omega C_{sh} + 1\right)$ to attenuate waves. We define $\alpha_N = C_{sh}/C_T^p$ to represent the shunted negative capacitance. The unit cells are arranged in the fashion that satisfies $\mathcal{PT}$ symmetry condition indicated in Fig. 2.1.

To quantitatively characterize the $\mathcal{PT}$ symmetric beam, effective mass density and effective bending stiffness of the shunted piezoelectric beam section are calculated analytically based on Eqs. (2.21) and (2.22) and compared with numerical simulations in Fig. 2.3. Material and geometric parameters used in the study are given in TABLE 2.1. The negative capacitance ratio α_N, and the magnitudes of the positive/negative resistances are chosen to be -0.8 and 1000 Ω, respectively. Numerical simulations are conducted with COMSOL Multiphysics, where plane stress assumptions are applied. In the study, we employ a weak formulation on the upper boundary of the piezoelectric patch, where the electrical impedance is shunted. Implementing an external impedance to the electrode on the surface of the piezoelectric patch poses a constrain on the potential and free charge relation

$$\int_{\partial\Omega} \dot{\mathbf{Q}} \cdot \mathbf{n} dA = \frac{V_A}{Z_{sh}} \tag{2.23}$$

where $\mathbf{Q}$ and V_A denote the free charge density and the applied potential on the electrode. Therefore, the weak formulation on this boundary reads

$$\int_{\partial\Omega} \delta V_A \mathbf{Q} \cdot \mathbf{n} dA = \frac{\delta V_A V_A}{i\omega Z_{sh}} \tag{2.24}$$

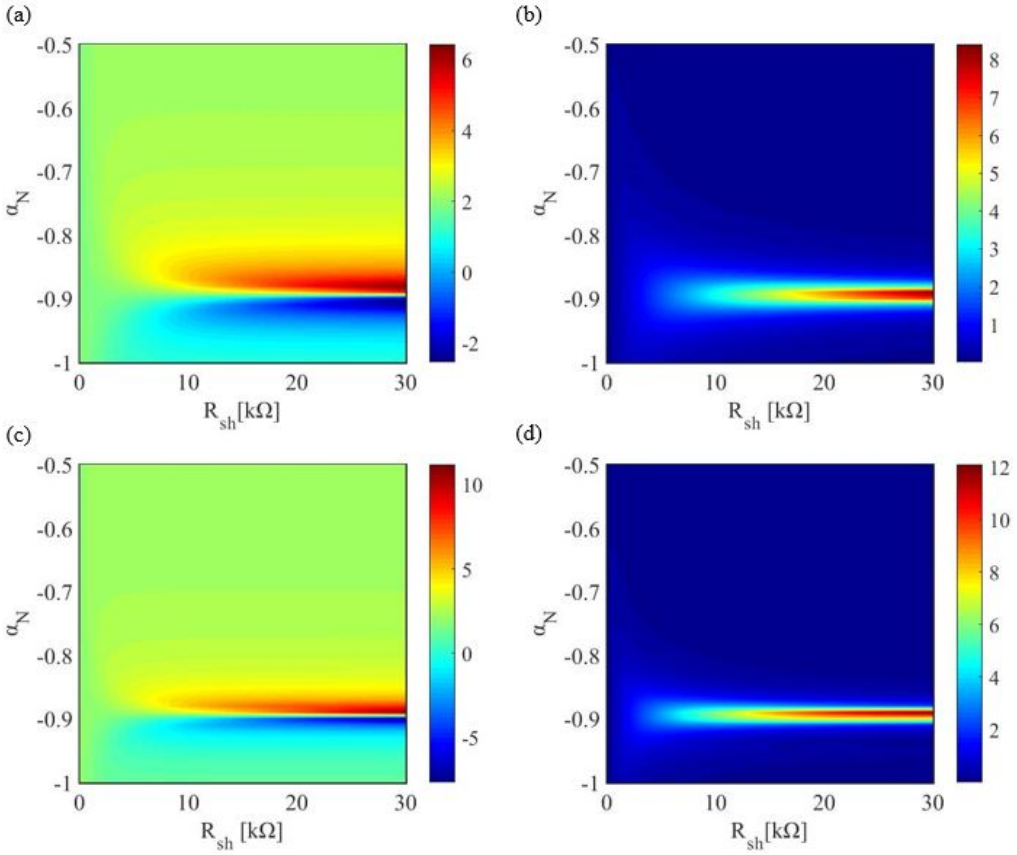

.

Figure 2.4: (a) Real and (b) imaginary parts of the effective bending stiffness with continuously changed R_{sh} at 0.5 kHz. (c) Real and (d) imaginary parts of the effective bending stiffness with continuously changed R_{sh} at 1 kHz. Reproduced from The Journal of the Acoustical Society of America 146, 850 (2019), with the permission of AIP Publishing.

As shown in Fig. 2.3(a), the effective mass densities of the metamaterial beam, ρ_{eff} , with both positive (denoted by "Loss" in the legend) and negative resistances (denoted by "Gain") are the same and nearly constant over the frequencies from 0.1 to 1kHz. Note that imaginary parts of effective mass densities, ρ_{eff}, are small enough to be negligible. In Figs. 2.3(b) and 2.3(c), the normalized effective bending stiffness of the metamaterial beam, D_{eff}/D_b, is shown, where $D_b = E_b h_b^3/12$ is the bending stiffness of the beam section without piezoelectric patch. D_{eff} with positive and negative resistances are conjugate pairs, indicating that the storage stiffnesses are the same, while the loss stiffnesses are opposite, being able to compose balanced loss and gain units required by the flexural wave $\mathcal{PT}$ symmetry condition in Eq. (2.3). It should be noted that the effective bending stiffness is frequency dependent thanks to the presence of the resistance in the shunting circuits. This can be easily checked with Eq. (2.12). When only the capacitance appears in Z_{sh}, ω is cancelled. Whereas, in the presence of resistance, ω cannot be cancelled anymore. In particular, the normalized storage stiffnesses are around 2.5 for the frequencies from 0.1 to 1kHz, and the magnitudes of loss and gain stiffness gradually increase as the frequency increases from 0.1 to 1kHz. Overall, good agreement between analytical and numerical results is clearly seen, validating the proposed EMT model. Note that small discrepancies of the effective mass density and effective bending stiffness can be attributed to the assumptions used in the analytical model such as linearized displacement and electric fields along the thickness direction.

To further characterize the effective bending stiffness of the metamaterial beam controlled by the shunting circuit, Figs. 2.4(a) and 2.4(b) show analytically calculated real and imaginary parts of the normalized effective bending stiffness by continuously changing the negative capacitance and the resistance. In the calculations, the frequency is selected as 0.5kHz, and other parameters are left unchanged as those in Fig. 2.3. Only positive resistance is used for loss characterizations. As illustrated in Figs. 2.4(a) and 2.4(b), when R_{sh} is sufficiently small, the shunting circuit is nearly shorted, producing nearly constant bending stiffness with zero loss, no matter what kinds of negative capacitances are used. By gradually increasing R_{sh}, the effects of the negative capacitance become more prominent, i.e., the real part of the bending stiffness can be changed from positive to negative values near $\alpha_N = -0.89$, and the loss is strong, which results in a large material mismatch with respect to the background medium. However, extremely large resistance will suppress the loss properties (not shown in the figure), as an infinitely large impedance will make the circuit open, and only the negative capacitance is left. By changing the frequency to 1 kHz [Figs. 2.4(c) and 2.4(d)], both the real and imaginary bending stiffnesses are in the same patterns as those in Figs. 2.4(a) and 2.4(b), and only the gradients with respect to the circuit parameters become a little bit larger.

As can be found from Figs. 2.3 and 2.3, the requirements on material parameters of the $\mathcal{PT}$ symmetric beam can be fully satisfied by the metamaterial with different shunting circuits, namely positive and negative resistances. In addition, the material parameters, including both the real and imaginary parts, can be flexibly tuned to extremely large regions through the circuit control.

2.3 Unidirectional reflectionlessness and parity-time phase transition

Scattering matrix

To characterize wave transmission and reflection properties of the $\mathcal{PT}$ symmetric metamaterial beam, one pair of loss and gain components is first considered and illustrated in Fig. 2.5(a). The design contains two piezoelectric patches. Each of them is connected with a negative capacitance and a positive/negative resistance in parallel. The transmission and reflection coefficients are calculated analytically and numerically and shown in Figs. 2.5(b)-2.5(d). In analytical calculations, the TMM is applied. In numerical simulations, two perfectly matched layers (PMLs) are attached to the two ends of the host beam to suppress boundary reflections, and other boundaries are left free, as shown in the top panel of Fig. 2.6. To generate propagated flexural waves, a point load is applied on the host beam on the left or right side of the sample. In the study, $L_b = 45$ mm, and the distance between the two patches, L, is selected as 200 mm. Other geometric and material parameters used in the calculations are the same as those used in Fig. 2.3. The negative capacitance ratio α_N and the magnitudes of the positive/negative resistances are chosen to be -0.855 and 1900Ω, respectively. As shown in Figs. 2.5(b)-2.5(d), good agreement can be found between the TMM and numerical simulations. Figure 2.5(b) shows the amplitude of transmission coefficient $|t|$ for the incidences from the left and right sides of the $\mathcal{PT}$ symmetric beam.

Since the $\mathcal{PT}$ symmetric beam does not break reciprocity, the transmission coefficients $|t|$ are identical for the two incidences. For the case studied in Fig. 2.5(a), transmission amplitudes fluctuate around 1 from 0.1 to 1kHz. It is interesting to note that the reflection coefficients $|r_r|$ and $|r_l|$ for the incidences from the left and right sides of the $\mathcal{PT}$ symmetric beam are asymmetric, i.e., their amplitudes shown in Figs. 2.5(c) and 2.5(d) are not equal. In particular, several zero reflection points (dips) are clearly seen in the figures when the flexural wave is incident from one direction, whereas the reflection is non-zero when incident from the other direction, indicating unidirectional reflectionlessness (reflection is zero for the incidence from one side, while the reflection is nonzero

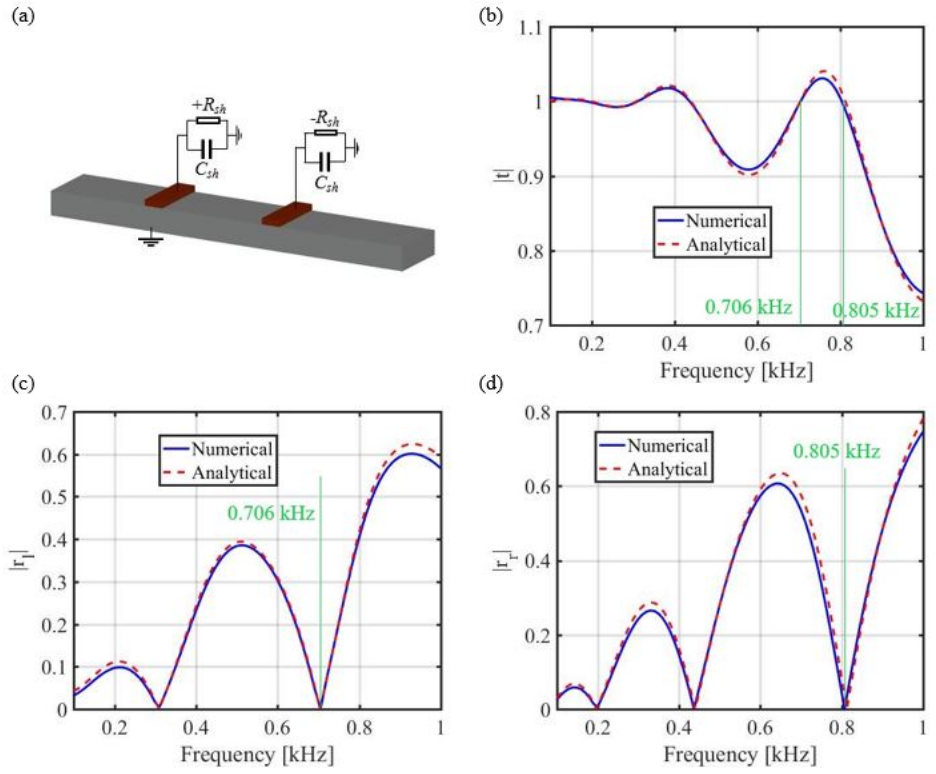

Figure 2.5: (a) Schematic of the $\mathcal{PT}$ symmetric metamaterial beam with one pair of loss and gain components. (b-d) Analytically calculated and numerically simulated amplitudes of (b) transmission, (c) left reflection and (d) right reflection coefficients. Two of the unidirectional reflectionlessness points (0.706 and 0.805 kHz) are denoted by green lines. Reproduced from The Journal of the Acoustical Society of America 146, 850 (2019), with the permission of AIP Publishing.

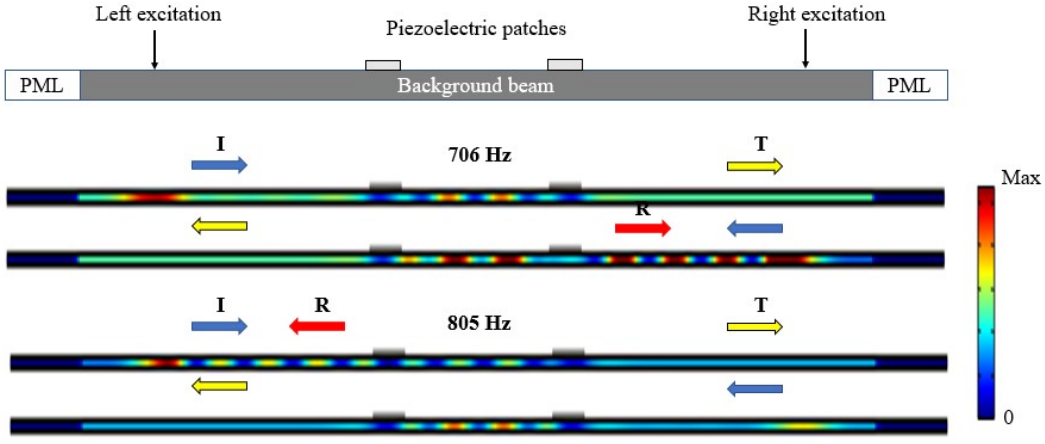

Figure 2.6: Top: Schematic of the $\mathcal{PT}$ symmetric metamaterial beam in numerical simulations. Bottom: Simulated flexural wave field $|w|$ at two unidirectional reflectionlessness points. The arrows indicate the propagation directions of different wave components. The blue (I), yellow (T), and red (R) arrows correspond to the incidence, transmission, and reflection, respectively. Reproduced from The Journal of the Acoustical Society of America 146, 850 (2019), with the permission of AIP Publishing.

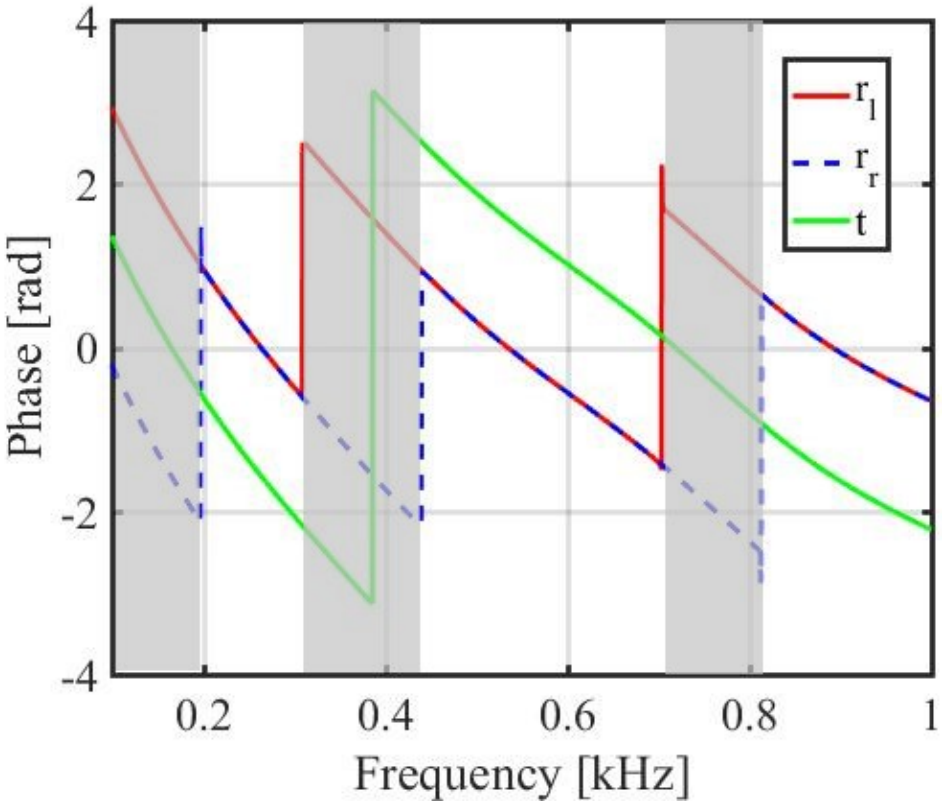

Figure 2.7: Analytically calculated phase angles of transmission, left reflection and right reflection coefficients. Reproduced from The Journal of the Acoustical Society of America 146, 850 (2019), with the permission of AIP Publishing.

when incident from the other side, which is different from the unidirectional transmission). To see the unidirectional reflectionlessness, flexural wave field, $|w|$, from numerical simulations at two of those unidirectional reflectionlessness points (706 and 805 Hz) are presented in Fig. 2.6. The figures are stretched vertically to help see the field distributions more clearly. As shown in the figures, when the incident frequency is selected at 805 Hz, no reflection is found for the flexural wave incident from the right, whereas the reflection is clearly seen for the flexural wave incident from the left, where interference patterns are produced. However, when the incident frequency is selected at 706 Hz, no reflection is found for the incidence from the left, whereas the reflection is clearly seen for the incidence from the right. Similar wave phenomena can also be found at 202, 310, and 435 Hz, which are not shown in the figure. In addition, it can be found from Fig. 2.6 that the transmission is unitary at those unidirectional reflectionlessness points (green dashed lines at 706 and 805 Hz), making the $\mathcal{PT}$ symmetric beam perfectly transparent. This property can be applied in designing one-way cloaks of flexural waves [59, 72, 77].

In addition to the unique features in amplitudes of transmission and reflection coefficients, their phase angles also present interesting properties that are shown in Fig. 2.7. It can be found from the figure that the phase differences between transmission and reflection coefficients are always $\pi/2$, and the two reflection coefficients are either in phase or out of phase. The transition points are exactly at the unidirectional reflectionlessness points in Fig. 2.5. When the two reflections are in-phase, $|t|$ is less than 1. Whereas, when they are outof-phase (shaded areas), $|t|$ is greater than 1. To gain more insights into the transmission and reflection coefficients, the generalized conservation law of the $\mathcal{PT}$ symmetric beam is derived. Thanks to the $\mathcal{PT}$ symmetry, the transfer matrix must satisfy [74, 81]

$$\boldsymbol{M}^{-1} = \boldsymbol{M}^{*}. \tag{2.25}$$

From Eq. (2.25), the generalized conservation law can then be derived [81],

$$|T - 1| = \sqrt{R_L R_R}, \tag{2.26}$$

in which $T = |t|^2, R_L = |r_i|^2$ and $R_R = |r_r|^2$ denote transmittance, left and right reflectance, respectively. According to Eq. (2.26), when $T < 1, T + \sqrt{R_R R_L} = 1$, the net dissipation or amplification in the $\mathcal{PT}$ symmetric beam is zero, considering the same two incidences from the right and left sides of the $\mathcal{PT}$ symmetric beam. On the other hand, when $T > 1$, the transmitted power is always greater than the input power, and $T - \sqrt{R_R R_L} = 1$. Furthermore, at the unidirectional reflectionlessness points, the transmittance must be equal to 1 [Eq. (2.26)], which coincides with the findings in Fig. 2.5 There also exist several points where $R_L = R_R$ accidentally occurs. We notice in Fig. 2.5 that those points with $R_L = R_R$ can be in regions where $T < 1$(0.233 and 0.51kHz) and regions where $T > 1$(0.375 and 0.766kHz).

To characterize the properties of the $\mathcal{PT}$ symmetric beam, eigenvalues $s_{1,2}$ and corresponding eigenvectors $\bar{S}_{1,2}$ of the scattering matrix are calculated analytically and shown in Fig. 8. Figures 2.8(a) and 2.8(b) present amplitudes and phases of the two eigenvalues, respectively. Compare with Fig. 2.5, when $T < 1$, the amplitudes of the two eigenvalues are unitary [$|s_{1,2}| = 1$ in Fig. 2.8(a)]. Whereas, when $T > 1$, the amplitude of one of the eigenvalue is less than 1, while the amplitude of the other one is greater than 1 (shaded area). It is important to notice that the two eigenvalues coalesce (both the amplitudes and the phases are equal) at the unidirectional reflectionlessness points. In Figs. 2.8(c)-2.8(f), the real and imaginary parts of the first and second components of the two eigenvectors are shown. At the unidirectional reflectionlessness points, the two eigenvectors

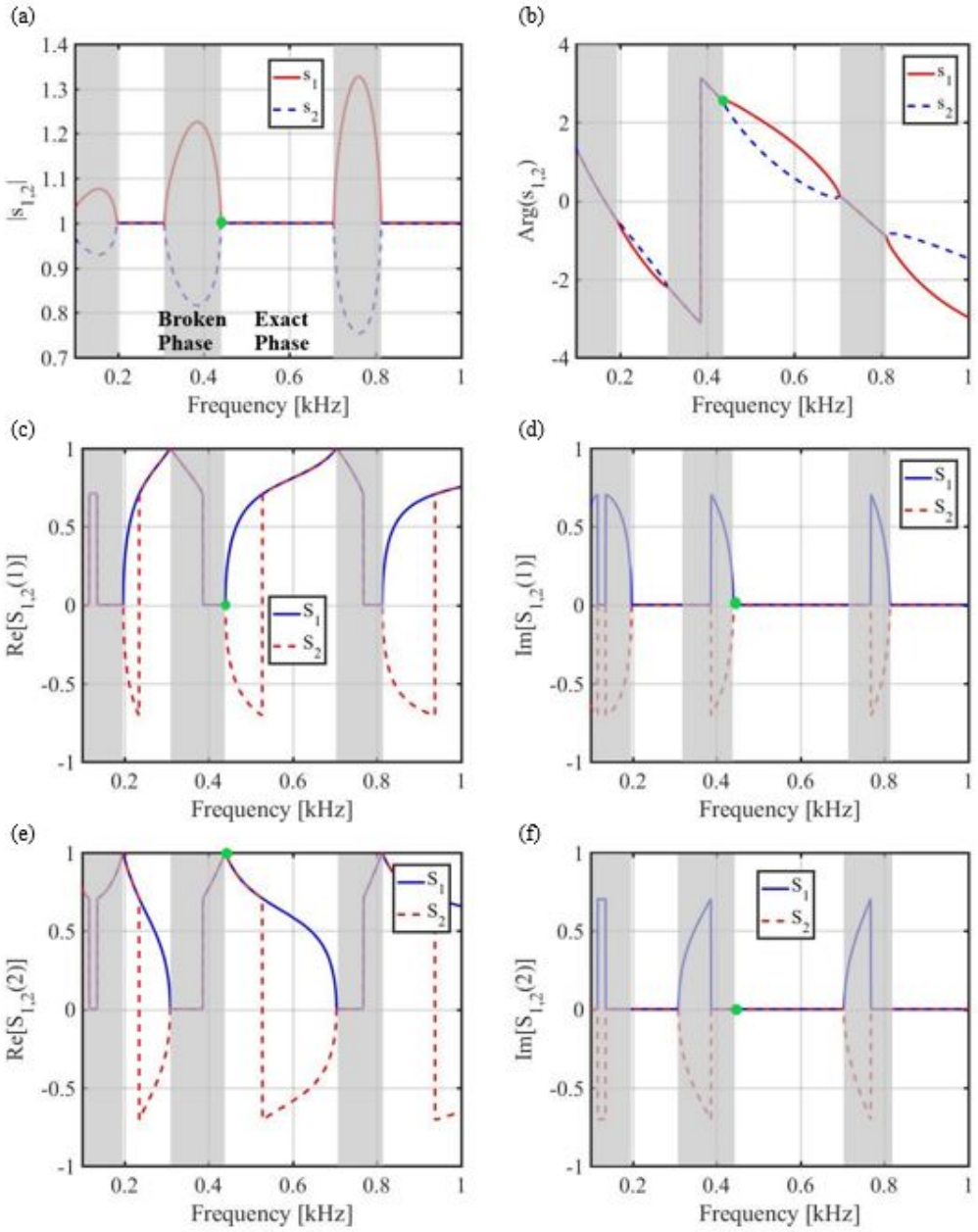

.

Figure 2.8: Analytically calculated (a) amplitude and (b) phase of the two eigenvalues. Analytically calculated (c) real and (d) imaginary parts of the first components of the two eigenvectors. Analytically calculated (e) real and (f) imaginary parts of the second components of the two eigenvectors. Reproduced from The Journal of the Acoustical Society of America 146, 850 (2019), with the permission of AIP Publishing.

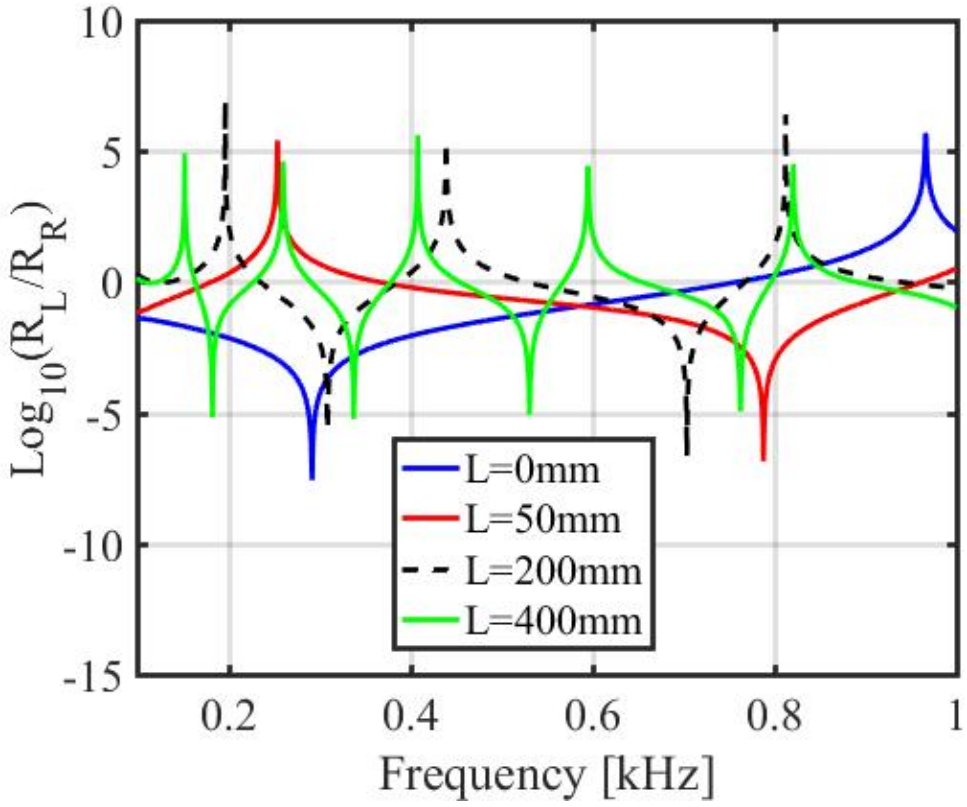

.

Figure 2.9: Analytically calculated $\log_{10}(R_L/R_R)$ with different distances separating two piezoelectric patches. Reproduced from The Journal of the Acoustical Society of America 146, 850 (2019), with the permission of AIP Publishing.

coalesce again, indicating that the unidirectional reflectionlessness points of the non-Hermitian $\mathcal{PT}$ symmetric beam are exceptional points (EPs), where only one possible state exists. In addition, when the amplitudes of two eigenvalues are unitary, the two eigenvectors satisfy $\hat{\mathcal{P}}\hat{\mathcal{T}}\bar{S}_{1,2} = \pm\bar{S}_{1,2}$, which corresponds to the $\mathcal{PT}$ exact phase. On the other hand, when the amplitudes of two eigenvalues are not unitary, $\hat{\mathcal{P}}\hat{\mathcal{T}}\bar{S}_{1,2} = \pm\bar{S}_{2,1}$, corresponding to the $\mathcal{PT}$ broken phase. The phase transition points are exactly the EPs or the unidirectional reflectionlessness points. Furthermore, the unidirectional reflectionlessness observed in Fig. 2.5 can also be explained by the eigenvectors. For instance, considering the EP at 0.435kHz [green dots in Figs. 2.8(c)-2.8(f)], the first components of the two eigenvectors are zero, indicating that the reflection for the right incidence is zero, which agrees with the reflection coefficients in Fig. 2.5(d).

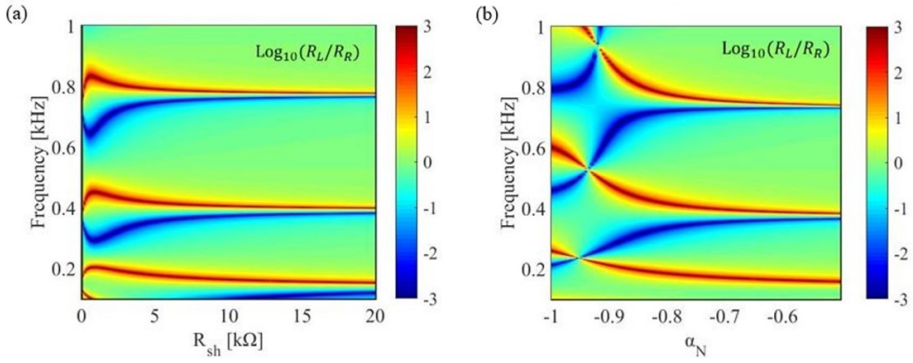

Figure 2.10: Analytically calculated $\log_{10}(R_L/R_R)$ by continuously changing (a) R_{sh} and (b) α_N. Reproduced from The Journal of the Acoustical Society of America 146, 850 (2019), with the permission of AIP Publishing.

Tunability of the PT symmetric metamaterial beam

In this section, the tunability of EPs is shown by changing the spacing between the two piezoelectric patches (Fig. 2.9) and implementing different circuit parameters, i.e., resistance and capacitance (Fig. 2.10). In the figures, the quantity $\log_{10}(R_L/R_R)$ characterizing the asymmetric reflection is calculated. As a result, small or large values will represent the unidirectional reflectionlessness points or the EPs.

The two reflection coefficients with different distances between the two piezoelectric patches, L, are calculated analytically and shown in Fig. 2.9. It can be seen that when $L = 0$, only two EPs (one dip and one peak in the blue curve) are observed at the frequencies between 0.1 and 1kHz. Increasing L, the frequencies of EPs as well as the frequency difference between EPs are decreased such that the EPs are tuned to different frequencies. Here, the EPs can be regarded as anisotropic transmission resonances with unitary transmission and asymmetric reflection [81]. Increasing the length therefore reduces the resonance frequencies. In particular, when $L = 400$ mm, nine EPs are found at the frequencies between 0.1 and 1kHz.

In Fig. 2.10, the frequency tunability of the EP is demonstrated by continuously changing the negative capacitance and the negative and positive resistance. Figure 2.10(a) shows the ratio $\log_{10}(R_L/R_R)$ by continuous increasing R_{sh}, where $\alpha_N = -0.855$. Six EPs are clearly seen, when R_{sh} is less than 7kΩ. By increasing R_{sh}, the frequencies of the two EPs near 400 and 800 Hz diverge and then become gradually closer. A new EP emerges between the other two EPs near 200 Hz, when R_{sh} is greater than 7 kΩ. The frequency tunability become negligible for R_{sh} greater than 7 kΩ. In Fig. 2.10(b), R_{sh} is selected as 10 kΩ, and α_N is modulated from -1 to -0.5. As shown in the figure, when α_N is less than -0.8, the EPs can be tuned across nearly the entire frequency range of

interest. Whereas, with α_N greater than -0.8, they become convergent and lack tunability, which is due to the small variation of the modulus within this range. Note that the two kinds of EPs cross around $\alpha_N = -0.92$, where the modulus has a pole with changes to the negative capacitance. Based on the results demonstrated in Fig. 2.10, both the frequency and reflection bias ratio of EPs can be flexibly tailored by properly selecting the shunting circuit parameters.

2.4 Summary

In conclusion, the non-Hermitian $\mathcal{PT}$ symmetric beam based on shunted piezoelectric patches has been proposed. The realization of gain and loss components relies on the introduction of negative and positive resistances and the negative capacitance into external shunting circuits. Asymmetric flexural wave scattering is investigated analytically and numerically with the focus on the unidirectional reflectionlessness. The scattering matrix and its eigenvalues and eigenvectors are studied in detail for the analyses of exact and broken $\mathcal{PT}$ phases. EPs are then identified at the unidirectional reflectionlessness points. Last, the tunable EPs are demonstrated through varying the spacing between the piezoelectric patches and the shunting circuit parameters. This design could be promising in various applications, such as asymmetric wave control, enhanced sensing, amplification, and localization of flexural waves.

The content of this section is reproduced from *The Journal of the Acoustical Society of America* **146**, 850 (2019), with the permission of AIP Publishing.

Chapter 3

NON-RECIPROCAL RAYLEIGH WAVE PROPAGATION IN SPACE–TIME MODULATED SURFACE

3.1 Introduction

Rayleigh waves, discovered in 1885 by Lord Rayleigh, are a type of surface acoustic waves (SAWs) that propagate over relatively long distances at the free surfaces of solids with amplitudes exponentially decaying perpendicular to the surfaces. Research on effectively controlling and manipulating Rayleigh waves has been gathering great attention from both scientific and engineering communities for decades. Several well-studied strategies have been proposed across multiple research fields involving designs of distributions of simple artificial micro- and macro-structures such as pillars, grooves, resonators, etc, on the surface of the host medium [87–96]. Advantages of doing so are twofold. First, the existence of these external inclusions does not require any modification on the geometrical or material properties of the continuum, keeping the host media intact. Second, tunable features can be easily realized in experimental implementations. As an outstanding example, the use of phononic crystals and mechanical metamaterials provides extra degree of freedom in tailoring the propagating behaviors of Rayleigh waves, such as scattering performance, polarization control and so on. Further, existing developments in novel SAW devices enable a wide range of applications in sensing [97–102], rf filters [103], duplexers [104] and seismic wave mitigation [92, 105, 106].

Despite decades of research on the manipulation of Rayleigh waves, most studies are by far focused on reciprocal systems with time-reversal symmetry, where scattering does not necessarily rely on propagation sense. To break time-reversal symmetry, a novel class of materials, called dynamic or spatio-temporal materials [107], in the fields of acoustics and elasticity have been vastly investigated in both discrete and continuous systems. This type of materials features properties which not only

change in space but also in time in a wave-like fashion referred to as a "pump wave". Some studies have theoretically and numerically unveiled unprecedented wave-transmission behavior in dynamic materials [108–113]. Examples of applications include directional mode converters [114, 115], selective acoustic circulators [116], directional wave reflectors [117, 118] and directional wave accelerators [110]. However, very little theoretical work has been conducted on realizing non-reciprocal propagation of Rayleigh waves with space-time modulations.

In this Chapter, an extensive study of Rayleigh wave propagation in a 2D semi-infinite medium bound by an array of space-time modulated spring-mass oscillators is performed. Note that as suggested by Casadei et al. [119] and Chen et al. [43, 120], modulating the stiffness of oscillators is technologically feasible using programmable piezoelectric components. To characterize the propagation of Rayleigh waves in the medium involving both continuous and discrete interfaces, an analytical model is developed with the aid of asymptotic method and coupled mode theory to obtain modified dispersion relations of the Rayleigh wave due to the wave-like modulation. Theoretical findings for non-reciprocal wave transmission are validated by transient numerical simulations. Specifically, one-way wave mode conversion is quantitatively characterized. Various relevant physical quantities, such as gap widths and interaction lengths, are estimated so as to guide future experimental implementations. This study can lead to further advance of Rayleigh wave-based devices to enable asymmetric propagation of energy, topological insulators and one-way waveguiding.

3.2 Theoretical modeling: asymptotic approach

Rayleigh wave dispersion in space-time modulated media

Let us start with a brief review of Rayleigh wave solution in a 2D isotropic semi-infinite medium. In that context, the governing Navier's equations are expressed as

$$[(2\mu+\lambda)\,\partial_x^2+\mu\partial_z^2]u+(\mu+\lambda)\,\partial_x\partial_z w=\rho\partial_t^2 u, \tag{3.1}$$

$$(\mu+\lambda)\,\partial_x\partial_z u+[(2\mu+\lambda)\,\partial_z^2+\mu\partial_x^2]w=\rho\partial_t^2 w, \tag{3.2}$$

where μ and λ denote Lamé constants of the medium and u and w represent the displacement fields along the $x-$ and $z-$directions, respectively. Operator ∂_i with i denoting x, z or t is a partial derivative operator with respect to i, and will be used throughout the paper. By introducing the potentials $u=\partial_x\Phi+\partial_z\Psi$ and $w=\partial_z\Phi-\partial_x\Psi$, the Navier's equations (3.1) and (3.2) are reformulated

as

$$\nabla^2\Phi - \frac{1}{c_L^2}\partial_t^2\Phi = 0, \tag{3.3}$$

$$\nabla^2\Psi - \frac{1}{c_T^2}\partial_t^2\Psi = 0, \tag{3.4}$$

where $c_L = \sqrt{\lambda + 2\mu/\rho}$ and $c_T = \sqrt{\mu/\rho}$ are the phase velocities for longitudinal (L) and transverse (T) waves. By solving Eqs. (3.3) and (3.4) and applying stress conditions at the free boundary: $\sigma_{zz} = \sigma_{xz} = 0$, the non-dispersive Rayleigh wave solution at the free surface can be obtained as

$$\Phi = D_1(z)\exp\left[i\left(q_0 x - \omega_0 t\right)\right], \tag{3.5}$$

$$\Psi = D_2(z)\exp\left[i\left(q_0 x - \omega_0 t\right)\right], \tag{3.6}$$

where q_0 is the wave number along x-axis and ω_0 is angular frequency. In this Chapter, instead of using k, we use q to represent the wave number for the sake of clarity since K will be designated to represent the spring stiffness constant.

In the study that follows, instead of the above free surface, we will consider Rayleigh wave propagation at a space-time modulated surface by introducing an array of linear oscillators connected at the surface to the semi-infinite medium, as shown in Fig. 3.1. Each linear oscillator is composed of a mass m and spring constant K and the spacing between oscillators is set to be l_s. Now a wave-like modulation on the spring constant is assumed as $K_m = K + \delta K\cos\left(q_m x - \omega_m t\right) = K + \delta K\left(\xi\right)$, with δK, q_m and ω_m being the modulation amplitude, modulation wave number and modulation frequency, respectively. The modulation wavelength can be subsequently defined as $\lambda_m = 2\pi/q_m$. The modulation amplitude δK is assumed to be small compared with K but great enough to break reciprocity.

The perturbative approach based on the amplitude of the modulation then is utilized to investigate how an incident Rayleigh wave is transformed by the modulation [108–110]. In the presence of perturbation, the governing equations given in Eqs. (3.1) and (3.2) are modified accordingly as

$$\left[\left(2\mu + \lambda\right)\partial_x^2 + \mu\partial_z^2\right]\widetilde{u} + \left(\mu + \lambda\right)\partial_x\partial_z\widetilde{w} = \rho\partial_t^2\widetilde{u}, \tag{3.7}$$

$$\left(\mu + \lambda\right)\partial_x\partial_z\widetilde{u} + \left[\left(2\mu + \lambda\right)\partial_z^2 + \mu\partial_x^2\right]\widetilde{w} = \rho\partial_t^2\widetilde{w}, \tag{3.8}$$

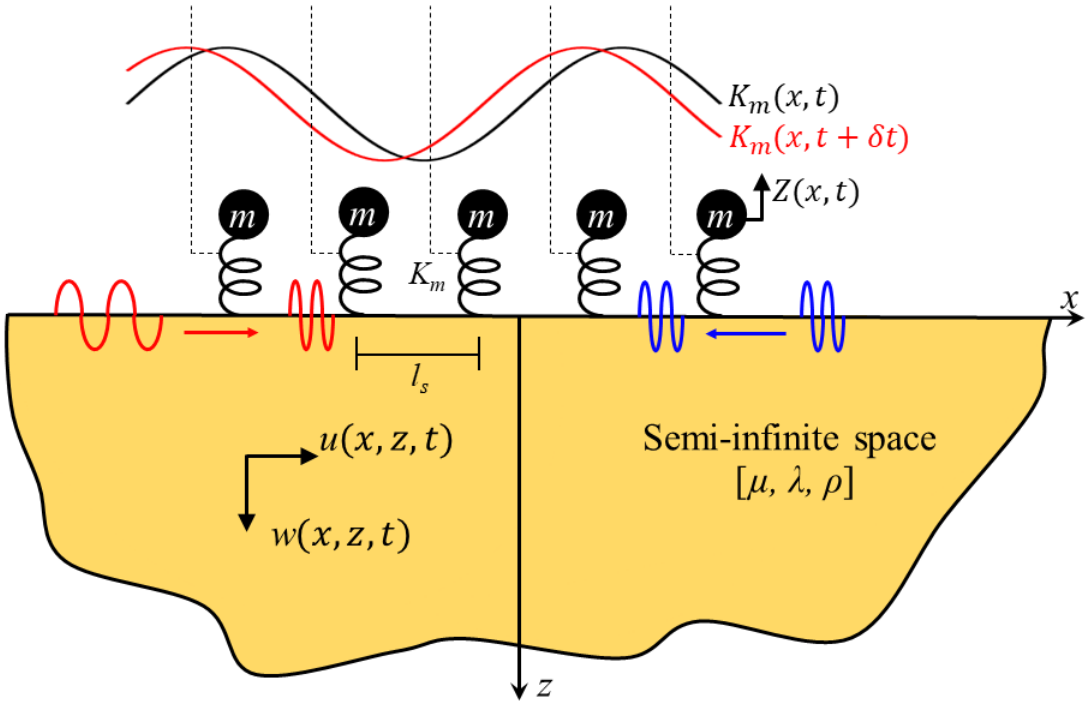

Figure 3.1: Schematic of non-reciprocal propagation of Rayleigh waves at the space-time modulated surface of a semi-infinite medium. An array of oscillators, including masses m and modulated spring constants $K_m(x,t) = K + \delta K \cos(q_m x - \omega_m t)$ with K being unperturbed spring constant, are attached to the surface of the medium. Each of the oscillators is separated with one another by a spacing l_s. The oscillators only vibrate along the z-direction. The isotropic continuous medium is described by a set of elastic parameters (μ, λ and ρ). The Rayleigh waves propagate at the surface in a non-reciprocal way that the transmission or reflection depends on directions of incidence at specific frequencies. Reproduced from Journal of the Mechanics and Physics of Solids 146, 104196 (2021), with the permission of Elsevier Publishing.

where $\widetilde{u} = u_0 + \delta u + \cdots$ and $\widetilde{w} = w_0 + \delta w + \cdots$. The perturbed potential functions can be written as

$$\widetilde{\Phi} = \widetilde{D}_1(\xi, z)\, e^{i(\widetilde{q}x - \widetilde{\omega}t)}, \tag{3.9}$$

$$\widetilde{\Psi} = \widetilde{D}_2(\xi, z)\, e^{i(\widetilde{q}x - \widetilde{\omega}t)}, \tag{3.10}$$

in which $\widetilde{q} = q_0 + \delta q + \cdots$, $\widetilde{\omega} = \omega_0 + \delta\omega + \cdots$, and $\widetilde{D}_i = D_i + \delta D_i + \cdots$, and δq, $\delta\omega$ and δD_i are the first-order correction terms to q_0, ω_0 and D_i, respectively. According to the Bloch theorem, the two potential functions are 2π-periodic functions of ξ. Therefore, we can decompose the leading-order amplitude of the potential function into $D_1(\xi, z) = \sum_{j\in\mathbb{Z}} D_1^j(z) e^{ij\xi}$, where j denotes the Fourier order and $\mathbb{Z}$ denotes the collection of integer numbers. By keeping the terms of leading-order correction and considering only the jth-order harmonic component, substituting Eq. (3.9) into the perturbed

Eqs. (3.3) and (3.4) leads to

$$\partial_z^2 D_1^j(z) + \left(\omega_j^2/c_L^2 - q_j^2\right) D_1^j(z) = 0, \tag{3.11}$$

$$\partial_z^2 D_2^j(z) + \left(\omega_j^2/c_T^2 - q_j^2\right) D_2^j(z) = 0, \tag{3.12}$$

where $\omega_j = \omega_0 + j\omega_m$ and $q_j = q_0 + jq_m$. On the other hand, the equation of motion of surface oscillators can be written as

$$m\partial_t^2 Z^j + K_m\left(Z^j - w_{z=0}^j\right) = 0, \tag{3.13}$$

where Z^j is the jth-order harmonic component of the mass displacement up to the leading-order correction. We assume a traveling wave solution reading $Z = \sum_{j\in\mathbb{Z}} Z_0^j e^{ij\xi} e^{i(\tilde{q}x - \tilde{\omega}t)}$ for the oscillator mass motion and keep only the leading-order terms. Following the supplementary material of [89] and the process detailed in Appendix A, we obtain the characteristic equation of leading-order correction which describes the Rayleigh wave dispersion in the presence of space-time modulated oscillators.

$$\left(\frac{m\omega_j^2}{K} - 1\right)\left[\left(2 - \frac{\omega_j^2}{q_j^2 c_T^2}\right)^2 - 4\sqrt{1 - \frac{\omega_j^2}{q_j^2 c_T^2}}\sqrt{1 - \frac{\omega_j^2}{q_j^2 c_L^2}}\right] = \frac{m}{A\rho}\frac{\omega_j^4}{q_j^3 c_T^4}\sqrt{1 - \frac{\omega_j^2}{q_j^2 c_L^2}}. \tag{3.14}$$

This equation is exactly the one obtained in [89], but with higher-order terms. For the Rayleigh wave propagating along $-x$ direction, the dispersion relation can be easily obtained by conducting similar derivation theretofore. Moreover, we can define an eigenmode $\boldsymbol{\varphi}^j(\omega_j, q_j)$ which describes the mode shape of Rayleigh waves in the presence of the spring-mass oscillators by matching the stress conditions as

$$\boldsymbol{\varphi}^j(\omega_j, q_j) = \begin{bmatrix} u^j \\ w^j \end{bmatrix} = \begin{bmatrix} iq_j(e^{-q_j p_j z} - 2\frac{s_j p_j}{r_j} e^{-q_j s_j z}) \\ -q_j p_j(e^{-q_j p_j z} - \frac{2}{r_j} e^{-q_j s_j z}) \end{bmatrix}, \tag{3.15}$$

where $r_j = 2 - \omega_j^2/c_T^2 q_j^2$, $p_j = \sqrt{1 - \omega_j^2/c_L^2 q_j^2}$, and $s_j = \sqrt{1 - \omega_j^2/c_T^2 q_j^2}$. The displacement of the oscillator mass Z_0^j accordingly reads

$$Z_0^j = \frac{\Omega^2 q_j p_j}{\omega_j^2 - \Omega^2}\left(1 - \frac{2}{r_j}\right), \tag{3.16}$$

where $\Omega = \sqrt{K/m}$ represents the resonant frequency of the unperturbed oscillators. The dispersion diagram is calculated in Fig. 3.2 from Eq. (3.14) for j equal to 0 and +1. In general, when the pump wave has its first N Fourier components non-zero, j can take integer values between $-N$ and N. The hatched area represents the bulk modes which mainly survive in the bulk region of the

semi-infinite medium and hence are of less interest in this work. For the fundamental harmonic $\boldsymbol{\varphi}^0(\omega_0, q_0)$ in absence of modulation, a large band gap generated by the local resonance of oscillators can be witnessed. The lower branch goes towards the resonance frequency Ω as q increases, while the upper branch approaches gradually the non-dispersive Rayleigh dispersion curve ($\omega = c_R q$) which is not shown here. With modulation turned on, the first-order harmonics $\boldsymbol{\varphi}^1(\omega_{-1}, q_{-1})$ and $\boldsymbol{\varphi}^1(\omega_1, q_1)$ appear with linear shifts of dispersion curves, with respect to the fundamental mode $\boldsymbol{\varphi}^0$. In Fig. 3.2, points of no-intersection correspond to uncoupled cases in which only mode $\boldsymbol{\varphi}^0$ exists, leading to the eigenmode

$$\boldsymbol{\varphi}(\xi) = V_0 \boldsymbol{\varphi}^0, \tag{3.17}$$

where V_0 is the linear amplitude of $\boldsymbol{\varphi}^0$. This means physically that the incident mode $\boldsymbol{\varphi}^0$ will not get scattered while propagating in the space-time modulated area. On the other hand, points of intersections $\boldsymbol{\varphi}^0 \cap \boldsymbol{\varphi}^{\pm 1}$ correspond to coupled cases where more than one eigenmodes exist. Accordingly, the eigenmode reads

$$\boldsymbol{\varphi}(\xi) = V_0 \boldsymbol{\varphi}^0 + V_{\pm 1} \boldsymbol{\varphi}^{\pm 1} e^{\pm i\xi}, \tag{3.18}$$

which is the sum of a pair of coupled modes with the amplitudes V_0 and $V_{\pm 1}$ respectively. Figure 3.2 graphically illustrates three pairs of coupled modes denoted as A, B and C. Taking pair A as an example, if one leg, say $\boldsymbol{\varphi}^0 \cap \boldsymbol{\varphi}^1$, is incident from left, the other leg, $\boldsymbol{\varphi}^0 \cap \boldsymbol{\varphi}^{-1}$, is scattered and also propagates along the $-x$-direction. On the other hand, $\boldsymbol{\varphi}^0 \cap \boldsymbol{\varphi}^1$ will not be scattered when incident from right. This indicates the non-reciprocal propagation of Rayleigh waves at the space-time modulated surface. In general, when the Rayleigh wave excited at any of the coupled modes from certain direction is scattered, it will not be scattered from the opposite direction. This is a direct consequence of the existence of space-time modulation which breaks the time-reversal symmetry. With the current parameters, following [121], pairs A and B correspond to veering pairs where the two interacting branches veer without the formation of directional bandgap (scattering and incidence in the same direction, and the group velocities of the two branches hold the identical sign), whereas pair C is a locking pair because the two interacting branches now lock around a directional bandgap (scattering and incidence in the opposite directions, and the group velocities of the interacting branches hold the opposite signs). It is worth noting that the non-reciprocity here only occurs in a narrow band of frequencies for given surface parameters. That being said, excitation far away from these non-reciprocal pairs on the dispersion curve will only yield fundamental harmonic

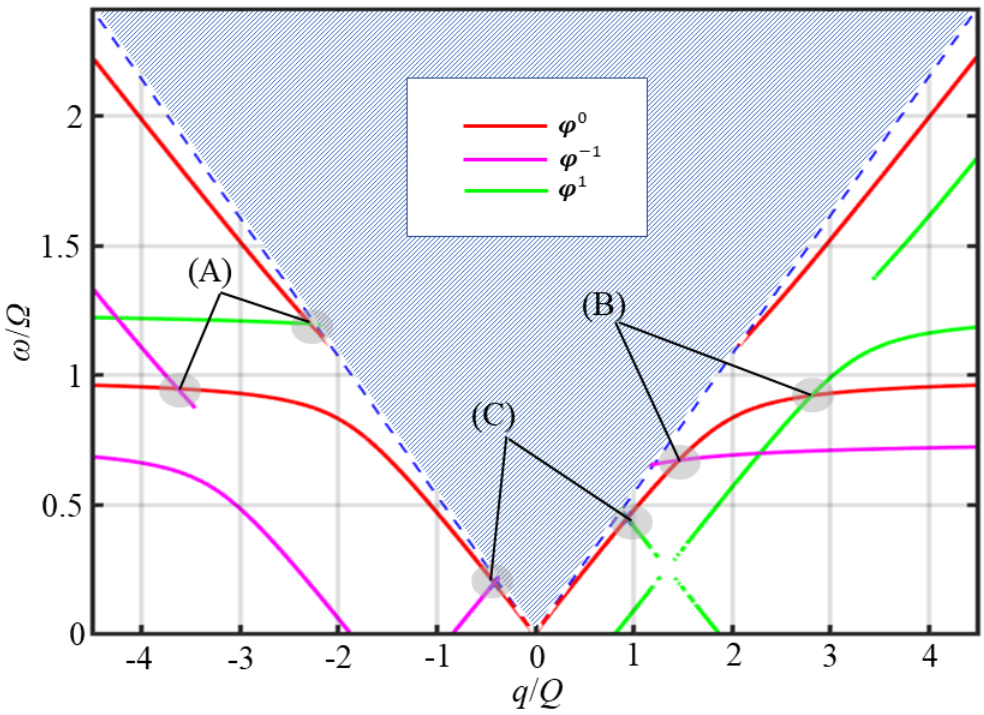

Figure 3.2: Coupling and non-reciprocity: A breaking of time-reversal symmetry produces three pairs of coupled modes (A), (B) and (C). Pairs (A) and (B) manifest as veering pairs, while pair (C) is the locking one. The pattern-hatched area represents the region of bulk modes, enclosed by a shear-wave cone (blue dashed). The constitutive parameters used here are set as $\rho = 2.2$ g/cm^3, $\lambda = 12.354$ GPa, $\mu = 28.826$ GPa, $K = 2400$ N/m, $m = 1.315 \times 10^{-15}$ kg, and $A = 1.0101 \times 10^{-12}$ m^2. ω is normalized to the resonance frequency of oscillators $\Omega = \sqrt{K/m}$ while q is normalized to $Q = 2 \times 10^5$ m^{-1}. The modulation parameters throughout the paper are selected as $\omega_m = \Omega/4$ and $q_m = 1.35Q$. Reproduced from Journal of the Mechanics and Physics of Solids 146, 104196 (2021), with the permission of Elsevier Publishing.

wave whose frequency and wave number remain on the fundamental dispersion curve. To achieve broadband non-reciprocity, one may consider the possible approach of utilizing active circuit control to modify the modulation parameters of the surface oscillators in real-time [120]. Careful observation reveals that the dispersion curves for $\boldsymbol{\varphi}^{-1}$ and $\boldsymbol{\varphi}^{1}$ are truncated, as shown in Fig. 3.2, because Eq. (3.14) can only capture the propagating details of Rayleigh waves. To further determine the coupling between coupled modes at the points of intersections, the perturbatuion method for displacement fields of the modulated system will be conducted [108–110].

Orthogonality condition of modulated Rayleigh wave propagation

To further determine coupling of coupled modes at the intersection points of the perturbed system involving both the continuous and discrete parts, we assume a set of perturbed plane waves along

x-direction in terms of displacement fields as

$$\begin{aligned}\widetilde{u}\left(x,z,\xi\right)&=\widetilde{U}(\xi,z)e^{i(\widetilde{q}_x x-\widetilde{\omega}t)},\\ \widetilde{w}\left(x,z,\xi\right)&=\widetilde{W}(\xi,z)e^{i(\widetilde{q}_x x-\widetilde{\omega}t)},\\ \widetilde{Z}\left(x,z,\xi\right)&=\widetilde{Z}(\xi)e^{i(\widetilde{q}_x x-\widetilde{\omega}t)},\end{aligned}\tag{3.19}$$

where $\widetilde{U}=u+\delta u$, $\widetilde{W}=w+\delta w$, $\widetilde{q}_x=q_0+\delta q$, $\widetilde{Z}=Z_0+\delta Z$ and $\widetilde{\omega}=\omega_0+\delta\omega$, up to first-order corrections. Substituting Eq. (3.19) into the governing Eqs. (3.7) and (3.8) and the perturbed Eq. (3.13) and keeping only the first-order correction terms yields a new set of governing equations for the forced wave propagation.

$$\begin{aligned}&\begin{bmatrix}\left(2\mu+\lambda\right)\left(iq_0+q_m\partial_\xi\right)^2+\mu\partial_z^2 & \left(\mu+\lambda\right)\left(iq_0+q_m\partial_\xi\right)\partial_z\\ \left(\mu+\lambda\right)\left(iq_0+q_m\partial_\xi\right)\partial_z & \left(2\mu+\lambda\right)\partial_z^2+\mu\left(iq_0+q_m\partial_\xi\right)^2\end{bmatrix}\delta\boldsymbol{\varphi}\\ &\qquad\qquad+\boldsymbol{F}=\rho(i\omega_0+\omega_m\partial_\xi)^2\delta\boldsymbol{\varphi},\end{aligned}\tag{3.20}$$

$$-K\left(\delta Z-\delta w_{z=0}\right)+G=m\left(i\omega_0+\omega_m\partial_\xi\right)^2\delta Z,\tag{3.21}$$

where $\delta\boldsymbol{\varphi}=\left(\delta u,\delta w\right)^T$. The above equations describe the first-order correction terms, i.e. δu, δw and δZ, propagating at the space-time modulated surface. The corresponding stress boundary conditions of first-order corrections at $z=0$ now become

$$\left[\mu\left(iq_0+q_m\partial_\xi\right)\delta w+\mu\partial_z\delta u\right]_{z=0}=H,\tag{3.22}$$

$$\left[\lambda\left(iq_0+q_m\partial_\xi\right)\delta u+\left(2\mu+\lambda\right)\partial_z\delta w\right]_{z=0}=-\frac{K}{A}\left(\delta Z-\delta w_{z=0}\right)+I.\tag{3.23}$$

Here, we obtain a set of modulation-induced effective body forces of the first-order correction, reading

$$\boldsymbol{F}=\begin{bmatrix}\alpha\\ \beta\end{bmatrix},\tag{3.24}$$

$$G=-\delta K_m(\xi)\left(Z-w_0\right)+m\left(2\omega_0\delta\omega-2i\delta\omega\omega_m\partial_\xi\right)Z,\tag{3.25}$$

$$H=-i\mu\delta q w_{z=0},\tag{3.26}$$

$$I=-\frac{\delta K(\xi)}{A}\left(Z-w_{z=0}\right)-i\lambda\delta q u_{z=0},\tag{3.27}$$

where

$$\alpha = \left[(2\mu+\lambda)\left(-2q_0\delta q + 2iq_m\delta q\partial_\xi\right) + \rho\left(2\omega_0\delta\omega - 2i\delta\omega\omega_m\partial_\xi\right)\right]u + i\left(\mu+\lambda\right)\delta q\partial_z w,$$
$$\beta = \left[\mu\left(-2q_0\delta q + 2iq_m\delta q\partial_\xi\right) + \rho\left(2\omega_0\delta\omega - 2i\delta\omega\omega_m\partial_\xi\right)\right]w + i\left(\mu+\lambda\right)\delta q\partial_z u.$$

Equations (3.24-3.27) are functions of δq, $\delta\omega$ and δK. Among them, Eq. (3.24) corresponds to the effective body force applied on the continuum, while Eq. (3.25) represents the effective body force applied on the discrete spring-mass oscillator section.

In deriving the orthogonality condition, the effective body force in the continuum is coupled with the one in the discrete section through the stress boundary conditions of first-order corrections. The orthogonality condition requires all the effective body forces to do zero virtual work for all the possible eigenmodes [108–110]. By following the detailed derivation in Appendix B, we reach eventually the orthogonality condition relating the continuous and discrete sections:

$$w^*_{z=0}\left(\frac{Q_0}{A}\left\langle G\right\rangle - \left\langle I\right\rangle\right) - u^*_{z=0}\left\langle H\right\rangle + \int_0^\infty \boldsymbol{\varphi}^*\cdot\left\langle \boldsymbol{F}\right\rangle dz = 0. \tag{3.28}$$

where $Q_j = 1 - m\omega_j^2/(m\omega_j^2 - K)$, $j\in\mathbb{Z}$. Equation (3.28) indicates the virtual work done by the effective body forces G, I, H and $\boldsymbol{F}$ is zero. In other words, the body forces have to be perpendicular to the eigenvector in a way to avoid increasing and unbounded oscillating amplitudes in the system [108–110]. Based on the derived orthogonality condition of the spring-mass-decorated system, we can further examine the couplings between the coupled modes.

Uncoupled mode

We first consider the case of a lonely uncoupled mode. Without loss of generality, the considered harmonic here is chosen to be the fundamental mode $\boldsymbol{\varphi}^0\left(q_0,\omega_0\right)$. Combining Eqs. (3.15-3.17) and (3.24-3.27) and taking average on the resulting equations basically yield a set of averaged effective body forces for $\boldsymbol{\varphi}^0$

$$\begin{aligned}
\left\langle \boldsymbol{F}\right\rangle^0 &= \begin{bmatrix} V_0\left[-2q_0\delta q\left(2\mu+\lambda\right) + 2\rho\omega_0\delta\omega\right]u^0 + i\left(\mu+\lambda\right)\delta q\partial_z V_0 w^0 \\ V_0\left[-2\mu q_0\delta q + 2\rho\omega_0\delta\omega\right]w^0 + i\left(\mu+\lambda\right)\delta q\partial_z V_0 u^0 \end{bmatrix}, \\
\left\langle G\right\rangle^0 &= 2m\omega_0\delta\omega V_0 Z^0, \\
\left\langle H\right\rangle^0 &= -i\mu\delta q V_0 w^0_{z=0}, \\
\left\langle I\right\rangle^0 &= -i\lambda\delta q V_0 u^0_{z=0}.
\end{aligned} \tag{3.29}$$

Here, the amplitude V_0 can be chosen arbitrarily by linearity. Substituting Eq. (3.29) into Eq. (3.28) results in

$$\mathcal{I}^0 + i\mu\delta q w^0_{z=0} u^{0*}_{z=0} + w^{0*}_{z=0}\left(\frac{2}{A} m\omega_0 \delta\omega Q_0 Z^0 + i\lambda\delta q u^0_{z=0}\right) = 0, \tag{3.30}$$

where the integration reads $\mathcal{I}^j = \frac{1}{V_j}\int_0^\infty \boldsymbol{\varphi}^{j*}\cdot\langle \boldsymbol{F}\rangle^j \, dz$, $j \in \mathbb{Z}$. Using the mode shapes in Eqs. (3.15) and (3.16) into Eq. (3.30) and performing rearrangements yields the group velocity of Rayleigh waves for uncoupled modes in presence of modulated spring-mass oscillators.

$$v_g^0 = \frac{\delta\omega}{\delta q} = -\frac{a_0}{b_0}, \tag{3.31}$$

where a_j and $b_j, j \in \mathbb{Z}$ are functions of ω_j, q_j, K and m, and read

$$\begin{aligned}
a_j &= 2(\mu+\lambda)q_j^2 p_j \frac{(s_j p_j - 1)(s_j - p_j)}{r_j(p_j + s_j)} - 2q_j^2(2\mu+\lambda)\left(\frac{1}{2p_j} - \frac{4s_j p_j}{r_j(p_j+s_j)} + \frac{2s_j p_j^2}{r_j^2}\right) \\
&\quad - 2\mu q_j^2 p_j^2\left(\frac{1}{2p_j} - \frac{4}{r_j(p_j+s_j)} + \frac{2}{r_j^2 s_j}\right) - \mu q_j^2 p_j\left(1-\frac{2}{r_j}\right)\left(1 - 2\frac{s_j p_j}{r_j}\right) \\
&\quad + \lambda q_j^2 p_j\left(1-\frac{2}{r_j}\right)\left(1-\frac{2s_j p_j}{r_j}\right) \\
b_j &= 2q_j\rho\omega_j\left(\frac{1}{2p_j} - \frac{4s_j p_j}{r_j(p_j+s_j)} + \frac{2s_j p_j^2}{r_j^2}\right) + 2q_j\ p_j^2\rho\omega_j\left(\frac{1}{2p_j} - \frac{4}{r_j(p_j+s_j)} + \frac{2}{r_j^2 s_j}\right) \\
&\quad - \frac{2m}{A}\omega_j q_j p_j\ \left(1-\frac{2}{r_j}\right) Q_j Z^j
\end{aligned}$$

Alternatively, the expression of the group velocity can also be derived from a variation of the dispersion relation in Eq. (3.14).

Coupled mode

Then, we investigate the coupling between two harmonics at mode $\boldsymbol{\varphi}^0 \cap \boldsymbol{\varphi}^1$, which corresponds to the simplest case. We will first discuss the veering pairs (pairs A and B in Fig. 3.2), since the coupled modes involved have the wave numbers of identical sign. In this way, the mode shape in the continuous medium takes the form given in Eq. (3.18) while that in the discrete section is changed accordingly as

$$Z^j = \frac{\Omega^2 q_j p_j}{\omega_j^2 - \Omega^2}\left(1 - \frac{2}{r_j}\right),\ j = \pm 1. \tag{3.32}$$

Substituting the mode shape given in Eq. (3.18) into the effective body forces given in Eqs. (3.24-3.27) results in a new set of effective body forces for the coupled modes.

$$
\begin{aligned}
\boldsymbol{F} &= \begin{bmatrix} \alpha \\ \beta \end{bmatrix}, \\
G &= -\delta K(\xi)(V_0 Z^0 + V_1 Z^1 e^{i\xi} - V_0 w^0_{z=0} - V_1 w^1_{z=0} e^{i\xi}), \\
&\quad + 2m\omega_0 \delta\omega V_0 Z^0 + 2m\omega_1 \delta\omega V_1 Z^1 e^{i\xi}, \\
H &= -i\mu\delta q(V_0 w^0_{z=0} + V_1 w^1_{z=0} e^{i\xi}), \\
I &= \frac{\delta K(\xi)}{A}(V_0 Z^0 + V_1 Z^1 e^{i\xi} - V_0 w^0_{z=0} - V_1 w^1_{z=0} e^{i\xi}), \\
&\quad - i\lambda\delta q(V_0 u^0_{z=0} + V_1 u^1_{z=0} e^{i\xi}),
\end{aligned}
\tag{3.33}
$$

where

$$
\begin{aligned}
\alpha = V_0[-2q_0\delta q\,(2\mu+\lambda) + 2\rho\omega_0\delta\omega]u^0 + V_1[-2q_1\delta q\,(2\mu+\lambda) \\
+ 2\rho\omega_1\delta\omega]u^1 e^{i\xi} + i\,(\mu+\lambda)\,\delta q\partial_z(V_0 w^0 + V_1 w^1 e^{i\xi}),
\end{aligned}
$$

$$
\begin{aligned}
\beta = V_0[-2\mu q_0\delta q + 2\rho\omega_0\delta\omega]w^0 + V_1[-2\mu q_1\delta q \\
+ 2\rho\omega_1\delta\omega]w^1 e^{i\xi} + i\,(\mu+\lambda)\,\delta q\partial_z(V_0 u^0 + V_1 u^1 e^{i\xi}).
\end{aligned}
$$

Repeating the procedures used in the uncoupled scenario for both the fundamental and first-order harmonics yields

$$
\begin{bmatrix} \mathcal{E}_{11} & \mathcal{E}_{12} \\ \mathcal{E}_{21} & \mathcal{E}_{22} \end{bmatrix} \begin{bmatrix} V_0 \\ V_1 \end{bmatrix} = \boldsymbol{\mathcal{E}} \begin{bmatrix} V_0 \\ V_1 \end{bmatrix} = 0, \tag{3.34}
$$

where

$$
\begin{aligned}
\mathcal{E}_{11} &= a_0\delta q + b_0\delta\omega \\
\mathcal{E}_{12} &= q_0 p_0 \frac{\delta K}{A}(1-\frac{2}{r_0})\left(Z^1 + q_1 p_1(1-\frac{2}{r_1})\right)(Q_0+1) \\
\mathcal{E}_{21} &= q_1 p_1 \frac{\delta K}{A}(1-\frac{2}{r_1})\left(Z^0 + q_0 p_0(1-\frac{2}{r_0})\right)(Q_1+1) \\
\mathcal{E}_{22} &= a_1\delta q + b_1\delta\omega
\end{aligned}
\tag{3.35}
$$

and $\left\langle \delta K e^{i\xi} \right\rangle = \left\langle \delta K e^{-i\xi} \right\rangle = \delta K$ (also see Appendix C for detailed derivation). Solving the eigenvalue problem $|\boldsymbol{\mathcal{E}}| = \mathbf{0}$ leads to first-order corrections to the dispersion curve around the coupled modes $\boldsymbol{\varphi}^0 \cap \boldsymbol{\varphi}^1$.

$$\delta\omega = \frac{-(a_1 b_0 + a_0 b_1)}{2 b_0 b_1}\delta q \pm \frac{1}{2 b_0 b_1}\sqrt{(a_1 b_0 - a_0 b_1)^2 (\delta q)^2 + 4 b_0 b_1 \mathcal{E}_{12}\mathcal{E}_{21}}. \tag{3.36}$$

By picking $\delta K = 0$ (unmodulated scenario), $\mathcal{E}_{12}$ and $\mathcal{E}_{21}$ in Eq. (3.35) vanish, and the above expression (3.36) gives the Rayleigh wave group velocities v_g^0 and v_g^1 for the uncoupled modes $\boldsymbol{\varphi}^0$ and $\boldsymbol{\varphi}^1$, respectively. Following Eq. (3.36), the veering zone width of frequency $2\delta\omega$ at the critical point ($\delta q = 0$) reads $2\delta\omega(\delta q = 0) = 2\sqrt{b_0 b_1 \mathcal{E}_{12}\mathcal{E}_{21}}/(b_0 b_1)$. We take the two veering pairs in Figs. 3.3(a) and 3.3(b) as an example. The oscillator spacing l_s is solely dependent of the area occupied by the individual oscillator, since we fixed the thickness of the semi-infinite medium. We first plot the intersection frequency and wave number of the fundamental and first-order harmonics in function of l_s to show that tuning l_s shifts the spectral location of the intersection of the two veering branches; see Figs. 3.4(a) and 3.4(c). As l_s increases, the intersection frequency increases as well as the magnitude of the intersection wave number. The veering zone widths $2\delta\omega$ at a certain l_s for both pairs are also plotted in Figs. 3.4(b) and 3.4(d) in functions of l_s and the modulation strength δK. As can be seen, at any l_s, $2\delta\omega$ increases monotonically with the increasing δK. This can be easily concluded from the fact that $\mathcal{E}_{12}$ and $\mathcal{E}_{21}$ are both proportional to δK based on Eq. (3.35), thereby leading $2\delta\omega$ to be proportional to δK as well. On the other side, $2\delta\omega$ is insensitive to the variation of l_s for both veering pairs, at least within the range considered. For the non-reciprocal locking pair (pair C in Fig. 3.2), the two legs are in opposite propagating directions, and hence perform opposite elliptical particle motion directions for the displacement fields. In this way, the expressions of mode shapes of the locking pair need to be accordingly corrected as

$$\begin{aligned}
\boldsymbol{\varphi}^0 &= \begin{bmatrix} u^0 \\ w^0 \end{bmatrix} = \begin{bmatrix} iq_0(e^{q_0 p_0 z} - 2\frac{s_0 p_0}{r_0}e^{q_0 s_0 z}) \\ q_0 p_0(e^{q_0 p_0 z} - \frac{2}{r_0}e^{q_0 s_0 z}) \end{bmatrix} \\
\boldsymbol{\varphi}^1 &= \begin{bmatrix} u^1 \\ w^1 \end{bmatrix} = \begin{bmatrix} iq_1(e^{-q_1 p_1 z} - 2\frac{s_1 p_1}{r_0}e^{-q_1 s_1 z}) \\ -q_1 p_1(e^{-q_1 p_1 z} - \frac{2}{r_1}e^{-q_1 s_1 z}) \end{bmatrix} \\
Z^j &= \frac{\Omega^2 q_j p_j}{\omega_j^2 - \Omega^2}\left(1 - \frac{2}{r_j}\right)
\end{aligned} \tag{3.37}$$

Substituting Eq. (3.37) into Eqs. (C.3-C.6) in Appendix C and simply repeating the same procedures of deriving the veering couplings leads to first-order corrections to the dispersion curve of the locking pair. To graphically illustrate the couplings, we plot the first-order corrections to the three pairs

and the dispersion curve of the space-time modulated system in Fig. 3.3, with the same parameters used in plotting Fig. 3.2 and a non-zero modulation strength $\delta K = 0.1K$. Figs. 3.3(a)-3.3(c) illustrate how the first corrections to the dispersion curve unveil the couplings at these three pairs. Taking the veering pair B shown in Fig. 3.3(b) as an example, when the lower-frequency point of intersection for mode $(0.668\Omega, 1.469Q)$ is incident, it will be converted into the other mode $(0.668\Omega + \omega_m, 1.469Q + q_m)$ at higher frequency within an interaction or conversion length which will be discussed later. Generally speaking, the excitation of one of the coupled legs in the space-time modulated medium leads to the creation of the other leg. The conversion, taking place at certain frequencies in certain directions, will not occur in the opposite propagation direction at the same frequency, which shows non-reciprocity due to the loss of time-reversal symmetry. On the other hand, the interacting branches of the pairs A and B veer since both coupled modes have the wave numbers of same signs. There is no band gap formed in the vicinity of them such that the incident waves in principle will not be reflected within the modulation area. Specifically, the upper branch refers to the optical branch where $Z(t)$ and $w_{z=0}(t)$ oscillate out-of-phase, while the lower branch is called acoustic branch where $Z(t)$ and $w_{z=0}(t)$ exhibit in-phase vibration. Pair B exhibits the one-way mode conversion between the acoustic mode and the optical one. By contrast, the two interacting branches of the locking pair C shown in Fig. 3.2(c) lock and involves two band gaps about the coupled modes. It indicates that any incidence close to one of the coupled modes will be totally reflected into the other one within certain interaction lengths. It is worth mentioning that since the proposed system here is weakly and slowly modulated, i.e. $\delta K \ll K$ and $|\omega_m/q_m| < c_R$, the locking pair is always stable, featuring horizonal directional bandgaps. In strongly modulated systems ($|\omega_m/q_m| > c_R$), it is likely for the system to be unstable to allow the existence of vertical bandgap where the frequency is purely imaginary [122, 123]. The previous work has already demonstrated the transition from stable to unstable bandgaps when the modulation speed or amplitude in the active system increases [110]. Recent experimental results also proved that the presence of intrinsic losses can quench the unstability, making the strongly modulated systems stable [124]. Lastly, we recover the dispersion curve of Rayleigh waves in the modulated medium in Fig. 3.3(d). The dashed curves correspond to the uncoupled dispersion curves of fundamental and first-order harmonics. The blue solid curve represents the fixed dispersion diagram up to the first-order correction. In this work, we only consider the first-order correction because it already yields the satisfactory prediction of dispersion curves of coupled modes. Higher-order correction terms may enhance the wave mode coupling shown in Fig. 3.3 to some degrees. However, their importance can almost be neglected compared with the first-order terms because of the weak modulation considered.

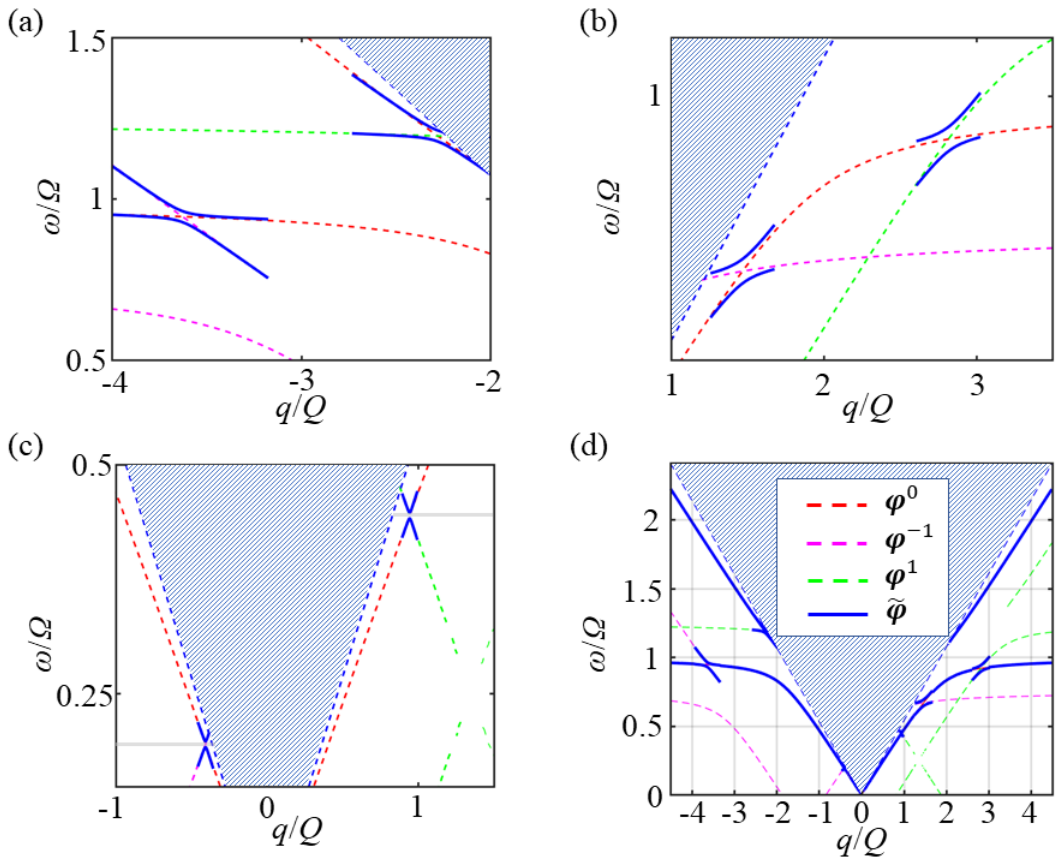

Figure 3.3: First-order corrections to the dispersion curve and the corrected dispersion relations up to the first-order correction: A non-zero modulation $\delta K = 0.1K$ enables the couplings between different harmonics. The first-order corrections to the pairs A, B and C in Fig. 3.2 are illustrated in (a), (b) and (c), respectively. The two shaded areas in (c) represent the two band gaps generated by the modulation. The corrected dispersion curve of the Rayleigh wave propagation in the space-time modulated semi-infinite medium is shown in (d), up to the first-order correction. Reproduced from Journal of the Mechanics and Physics of Solids 146, 104196 (2021), with the permission of Elsevier Publishing.

Transmission-type conversion

The Rayleigh wave propagating in the space-time modulated medium is converted from one harmonic to one another in the vicinity of the coupled pairs. To characterize their mode conversion properties, we need to discuss separately the veering pairs and locking one. This is simply because the former pairs hold the same signs in group velocity while the latter one is opposite. For the veering pairs, we start by defining the group velocities for the uncoupled harmonics as

$$v_g^0 = -\frac{a_0}{b_0}, \quad v_g^1 = -\frac{a_1}{b_1} \tag{3.38}$$

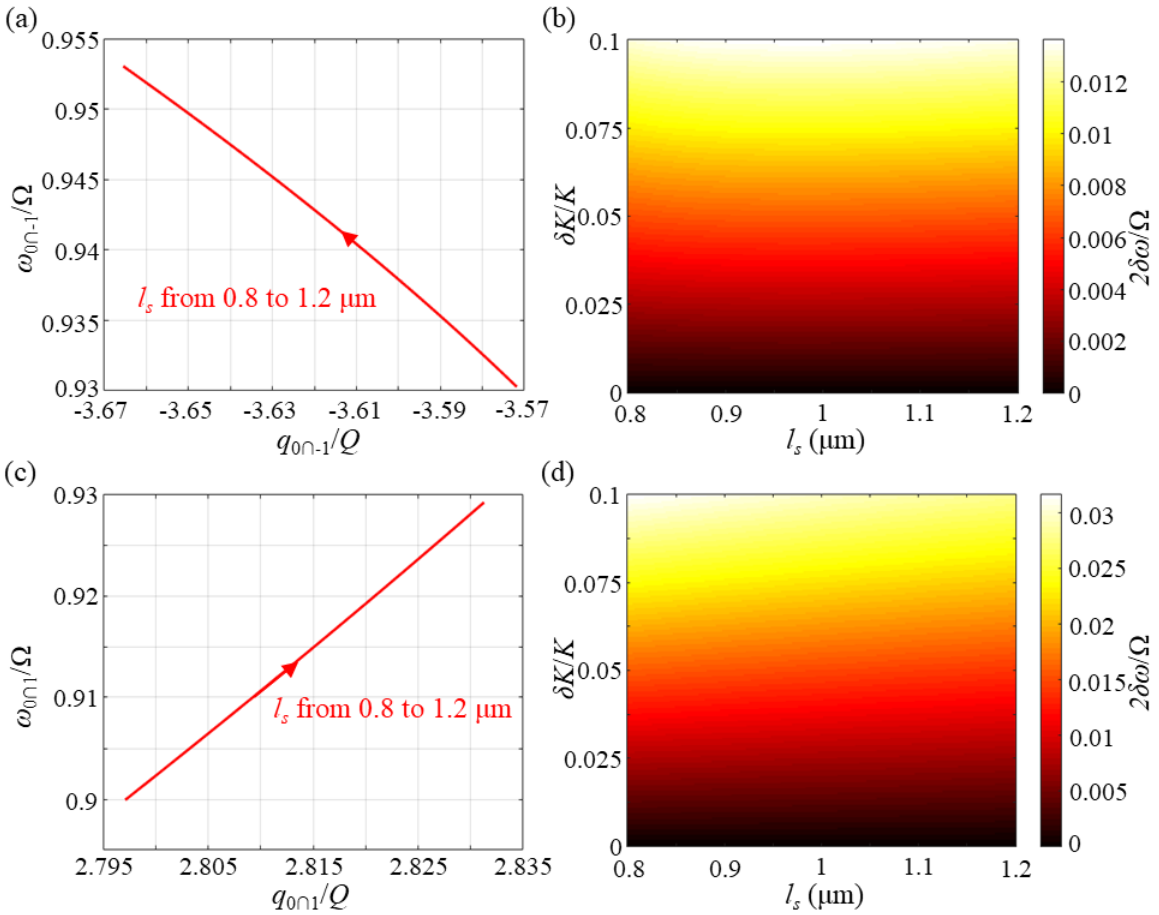

Figure 3.4: Parametric study on the influence oscillator spacing ls and modulation strength δK on the intersection frequency and wave number of the fundamental and the first-order harmonics and the veering zone width $2\delta\omega$. (a) and (b) correspond to the veering pair A, while (c) and (d) correspond to the veering pair B. The red arrows in (a) and (c) indicate the increasing direction of l_s. Reproduced from Journal of the Mechanics and Physics of Solids 146, 104196 (2021), with the permission of Elsevier Publishing.

Substituting Eq. (3.38) into Eq. (3.36) and utilizing the derivation process detailed in [110] and Appendix D, we can conclude that at the propagation length $d = \pi/(2\delta q_a)$ within the modulated area, where $\delta q_a = \sqrt{\left[\frac{\delta\omega}{2}\left(\frac{1}{v_g^0} - \frac{1}{v_g^1}\right)\right]^2 + \frac{\mathcal{E}_{12}\mathcal{E}_{21}}{b_0 b_1 v_g^0 v_g^1}}$, $\boldsymbol{\varphi}^0$ reaches its minimum while $\boldsymbol{\varphi}^1$ reaches the maximum. Typically, the total conversion from $\boldsymbol{\varphi}^0$ to $\boldsymbol{\varphi}^1$ can be expected when $C_b = 0$, namely, $\delta\omega = 0$. In this case, we have

$$\delta q_{\pm} = \pm\sqrt{\frac{\mathcal{E}_{12}\mathcal{E}_{21}}{b_0 b_1 v_g^0 v_g^1}}, \quad C_{\pm} = \pm\frac{b_0 v_g^0}{\mathcal{E}_{12}}\sqrt{\frac{\mathcal{E}_{12}\mathcal{E}_{21}}{b_0 b_1 v_g^0 v_g^1}} \tag{3.39}$$

For the eigenmode $\boldsymbol{\varphi}^0\,(0.668\Omega, 1.469Q)$ corresponding to the veering pair B propagating along the $+x$-direction, we have the normalized conversion length $Qd = 9.56$ and the inverted amplification

factor $\frac{1}{|C|} = 0.9726$. To quantitatively illustrate the dependence of Qd and $\frac{1}{|C|}$ on (ω_1, q_1) and the potential tunability of the one-way frequency conversion, we plot in Fig. 3.5 based on expressions (3.39) by tuning q_m and ω_m. For a given input mode (ω_0, q_0) marked with yellow pentagrams, the possible output modes are distributed along the dispersion curve of the uncoupled mode (red curves). As can be seen in Fig. 3.5(a), the closer the coupled mode (ω_1, q_1) is to the resonance frequency of the unmodulated oscillator, the shorter the normalized conversion length appears to be. On the other hand, inverted amplification factor decays as the coupled frequency ω_1 increases. Further, analytical calculations about various combinations of δK and K, shown in Figs. 3.5(c) and 3.5(d), indicate that an increase in δK leads to a decrease in the normalized conversion length Qd when K is fixed. This can be derived from Eqs. (3.35) and (3.39) as well. By contrary, when δK is fixed, an increase in K results in an increasing Qd. This behavior is more prominent at larger δK. On the other hand, the variation in δK barely affect the inverted amplification factor $\frac{1}{|C|}$, as can also be observed in Eqs. (3.35) and (3.39). However, an increasing K magnifies $\frac{1}{|C|}$.

Reflection-type conversion

For the locking pair C, the two wave numbers of the coupled modes are opposite in sign. In this case, reflection-type conversion takes place. Subsequently, expression (D.2) can be corrected to

$$\delta q_{\pm} = \frac{\delta\omega}{2}\left(\frac{1}{v_g^0} + \frac{1}{v_g^1}\right) \pm i\sqrt{\frac{\mathcal{E}_{12}\mathcal{E}_{21}}{b_0 b_1 v_g^0 v_g^1} - \left[\frac{\delta\omega}{2}\left(\frac{1}{v_g^0} - \frac{1}{v_g^1}\right)\right]^2} = \pm i\delta q_c + \delta q_b \tag{3.40}$$

As can be seen the first-order correction wave number are complex valued in the vicinity of ω_0, specifically for the range

$$|\delta\omega| \leq 2\left|\frac{1}{v_g^0} - \frac{1}{v_g^1}\right|^{-1}\sqrt{\frac{\mathcal{E}_{12}\mathcal{E}_{21}}{b_0 b_1 v_g^0 v_g^1}} \tag{3.41}$$

In this way, the solution for $\boldsymbol{\varphi}^0(\omega_0, q_0)$ incident from the right side is, for $x > 0$,

$$\boldsymbol{\varphi} = V_{0+}e^{-\delta q_c x}\left(\boldsymbol{\varphi}^0 e^{i(q_0 x - \omega_0 t)} + (C_a + C_b)\,\boldsymbol{\varphi}^1 e^{i(q_1 x - \omega_1 t)}\right)e^{i(\delta q_b x - \delta\omega t)} \tag{3.42}$$

The solution given in (3.42) indicates that at (ω_0, q_0) the right incidence $\boldsymbol{\varphi}^0$ penetrates into the space-time modulated medium exponentially decaying to vanish within a distance of order $1/|\delta q_c|$, and then is reflected into $\boldsymbol{\varphi}^1(\omega_1, q_1)$ propagating at q_1 opposite to q_0. This behavior is graphically illustrated as two band gaps at the locking pairs C, as shown in Fig. 3.3.

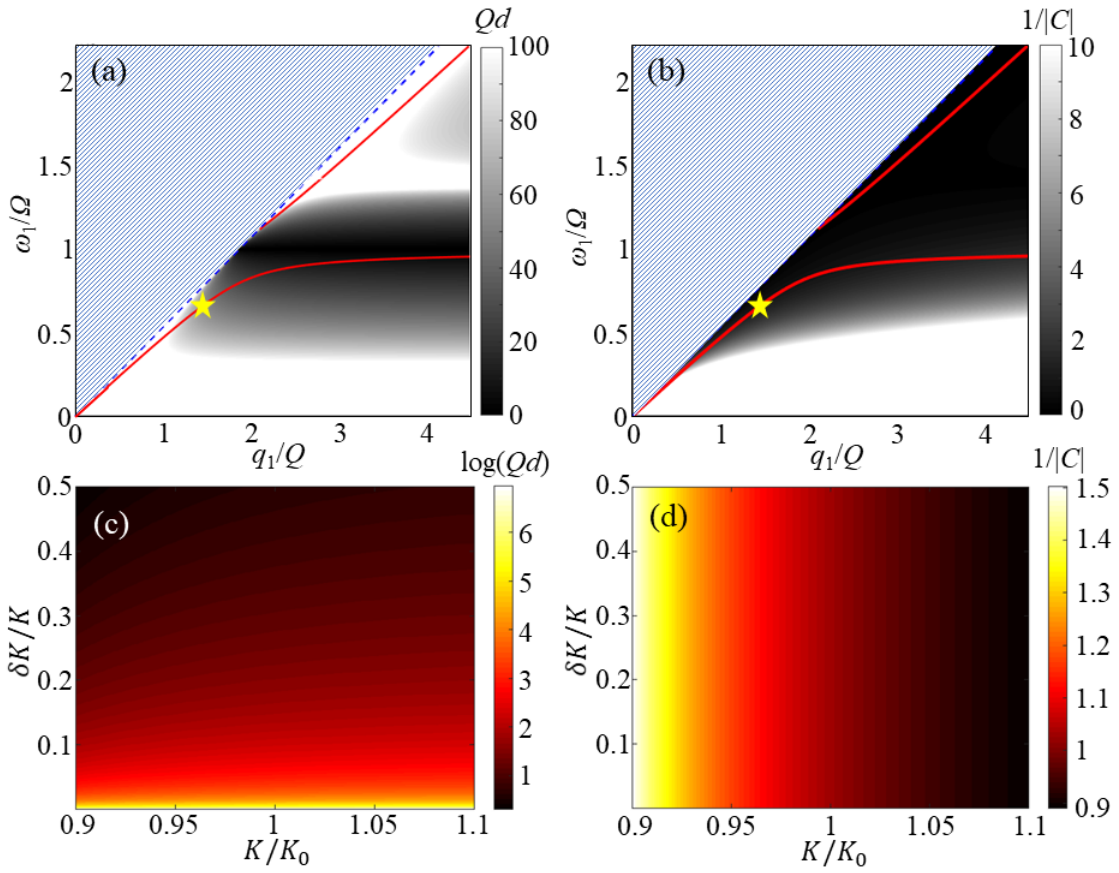

Figure 3.5: Dependence of the normalized conversion length Qd (a) and the inverted amplification factor $\frac{1}{|C|}$ (b) on (ω_1, q_1) for an incidence at the mode (ω_0, q_0), marked with yellow pentagrams. The pattern-hatched areas denote the bulk regions, and the red curves are the dispersion curves of the Rayleigh wave in the unmodulated system. (c) and (d) show dependence of log(Qd) and $\frac{1}{|C|}$, respectively, on the variations of K and δK. Here, $K_0 = 2.4 \times 10^3 N/m$. Reproduced from Journal of the Mechanics and Physics of Solids 146, 104196 (2021), with the permission of Elsevier Publishing.

3.3 Numerical discussions: nonreciprocal transmission and one-way mode conversion

Prediction of asymmetric dispersion curve

To validate the analytical modeling, a transient simulation is conducted using COMSOL Multiphysics to predict the dispersion curve in the modulated system. A 2-cycle broadband burst signal, centered at $\omega_c = \Omega$ and described as $A_0 \sin(\omega_c t)\,[1 - \cos(\omega_c t/2)]$ is used to generate Rayleigh waves propagating in different directions, as shown in Fig. 3.6(a). The low-reflecting boundaries are adopted in the ends of boundary to reduce reflection. On the surface, 600 oscillators are distributed uniformly with a spacing $l_s = \lambda_m/20$. Dispersion curve of Rayleigh wave propagation in the system with oscillators is

numerically secured, which is also validated by analytical solution (see Appendix E). After that, the space-time modulation is applied to 600 oscillators and numerical simulation is then conducted to obtain time-domain signals of the Rayleigh wave at different locations. The 2D Fourier transform in space and in time is adopted on the obtained signals to retrieve the dispersion curve with non-zero modulation for both directions. The results are shown in Fig. 3.6(b) and great agreement with the analytical prediction is illustrated in Fig. 3.3(d). In the figure, two non-reciprocal veering pairs A and B discussed in the analytical section can be directly visualized. However, the locking pair C at lower frequencies is hardly seen in Fig. 3.6(b) due to its extremely narrow band gap for the given modulation parameters. Nevertheless, the non-reciprocal scattering is numerically witnessed here in the vicinity of the two veering pairs on the recovered dispersion curves. Scattering of elsewhere on the dispersion curve of fundamental harmonic will be reciprocal. Aside from the couplings between the fundamental and first-order harmonics, we can also observe the couplings between other higher-order harmonics. In particular, one of them is highlighted in Fig. 3.6(b) by the green window (C), which reveals the coupled mode $\boldsymbol{\varphi}^1 \cap \boldsymbol{\varphi}^2$. This has not been discussed in detail in the analytical section since the strengths of the higher-order couplings are relatively weak compared to the ones of lower-order couplings, as can be seen in Fig. 3.6(b).

Non-reciprocal transmission

Numerical simulation is also conducted to confirm the non-reciprocal propagation of the Rayleigh wave, as shown in Fig. 3.7(a). We first test the non-reciprocity at the veering pair B $(0.668\Omega, 1.469Q)$, which corresponds to the case of the right-going Rayleigh wave by placing a modulation area comprising of 1000 unit cells between two free surfaces. The excitation used here is once again the tone burst signal, but with a much narrower linewidth (50 cycle) and a center frequency at 0.668Ω. The source, highlighted as the green point in Fig. 3.7, here consists of only a single point load which is embedded in the space-time modulation area. The excited Rayleigh wave propagates along two opposite directions; see Fig. 3.7(a). The time-domain signals, collected at the two highlighted points, are shown in Fig. 3.7(b) for both directions of Rayleigh wave propagation. For the right-going incidence, i.e. along the modulation direction, the time-domain response (red in Fig. 3.7(b)) is greatly distorted and delayed due to the coexistence of modes $\boldsymbol{\varphi}^0$, $\boldsymbol{\varphi}^1$ and even $\boldsymbol{\varphi}^2$ with difference group velocities. While for the left-going incidence (blue dashed in Fig. 3.7(b)), the time-domain signal resembles the excitation, indicating that the modulation barely functions for this direction. The corresponding frequency spectra are illustrated in Fig. 3.7(c) through Fourier transformation

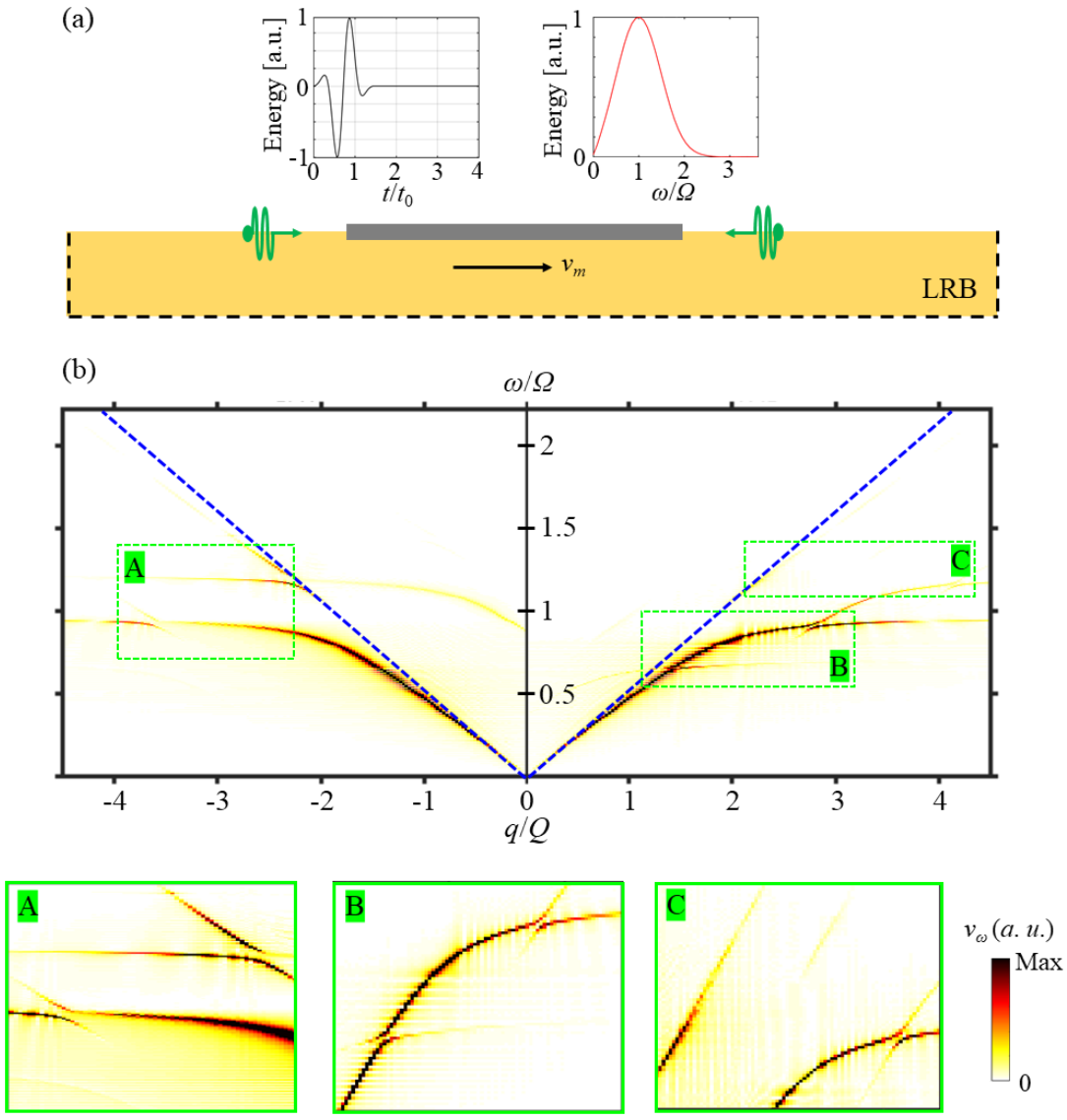

Figure 3.6: (a) Schematic illustration of the numerical model used to retrieve the dispersion curve. The top panel gives the time- and frequency-domain spectra of the excitation. The bottom panel shows the numerical model, with a space-time modulation (STM) area highlighted in gray and composed of 600 oscillators. The black dashed arrow indicates the modulation direction. Two sources carrying the above excitation are placed, as highlighted in green. The low-reflecting boundaries (LRBs) are applied to minimize the effects of the undesired reflected waves. (b) The recovered dispersion curve is numerically obtained through a 2D Fourier transform. The blue dashed lines correspond to the dispersion curve of shear bulk waves. In particular, the green windows highlight the two pairs (A) and (B) and the coupling between the first-order and second-order harmonics (C). The color maps of the insets are adjusted accordingly for better visualization of the details of dispersion relation. Reproduced from Journal of the Mechanics and Physics of Solids 146, 104196 (2021), with the permission of Elsevier Publishing.

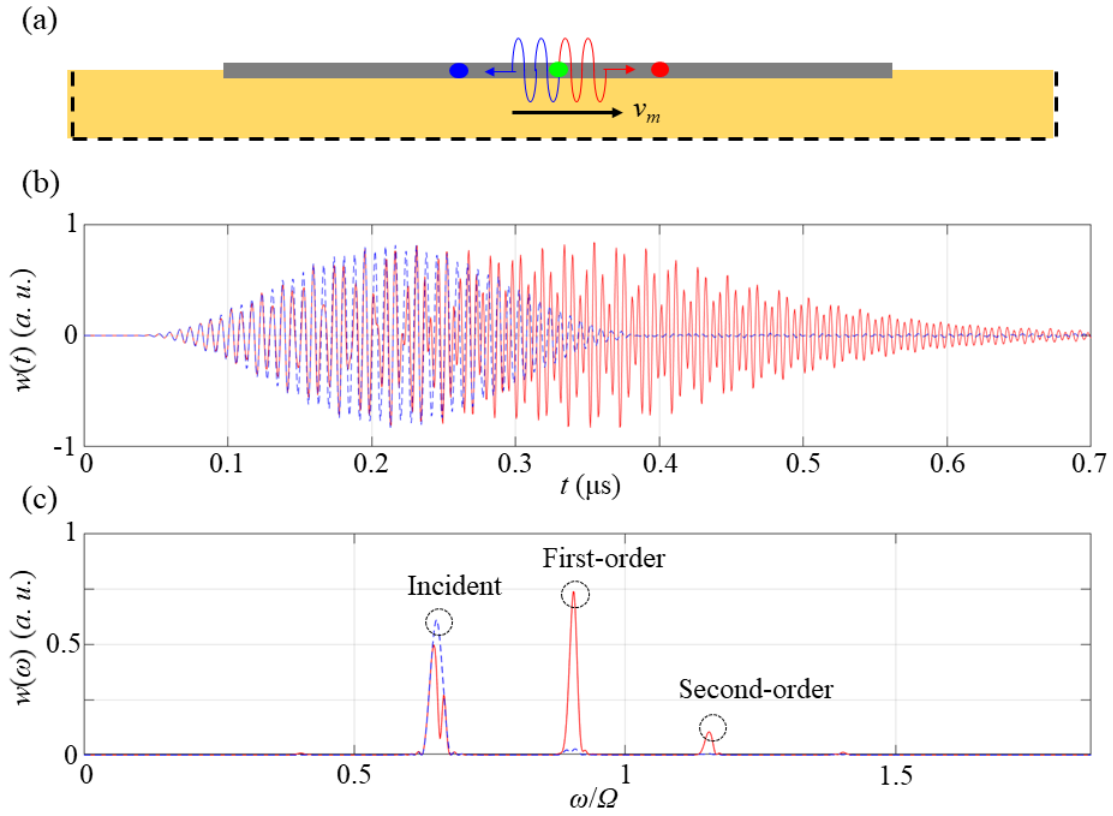

Figure 3.7: Schematic illustrations of the simulation models. Unlike the previous case of retrieving the dispersion diagram, there are in total 1000 spring-mass oscillators involved, and a point load, embedded in the center of the space-time modulation area, is assigned to serve as the source. Two points (red and blue) separating equally to the source are designated to collect the time-domain response. The arrow denotes the direction of modulation. In this way, the red point corresponds to the Rayleigh wave propagation along the direction of modulation while the blue one indicates the opposite scenario. (b) presents the time-domain signals collected at the two points indicating different directions of incidence. The corresponding frequency-domain spectra (c) are derived through Fourier transform. The nearly total conversion of pair B takes place at the spectral position highlighted by the circles. Reproduced from Journal of the Mechanics and Physics of Solids 146, 104196 (2021), with the permission of Elsevier Publishing.

of the time-domain data. Comparison between the illustrated results prove the non-reciprocity at the veering pair B. The right-going Rayleigh wave at $\boldsymbol{\varphi}^0(0.668\Omega, 1.469Q)$ nearly undergoes a total conversion into the first-order harmonic $\boldsymbol{\varphi}^1(0.668\Omega + \omega_m, 1.469Q + q_m)$ and even the second-order harmonic $\boldsymbol{\varphi}^1(0.668\Omega + 2\omega_m, 1.469Q + 2q_m)$, as has been denoted by the black circles in Fig. 3.7(c). On the contrary, the left-going Rayleigh wave at $\boldsymbol{\varphi}^0$ does not experience any conversion, demonstrating non-reciprocal propagation of the Rayleigh wave in the proposed system. Figures 3.8(a) and 3.8(b) show the harmonic frequency spectra against the oscillator positions for the two opposite propagation directions. The spectra were produced through Fourier transform upon the time-domain data of

displacement w collected at all the spring-mass oscillators. They reveal the harmonic conversion process while the Rayleigh waves propagate in the two opposite directions. In Fig. 3.8(a), since the propagation direction is indentical to the modulation speed v_m, the incidence excites both the first- and second-order harmonics (see Fig. 3.7). During the propagation within the modulated area, the intensity of the incident fundamental harmonic component reaches the local maximum when the first-order and second-order harmonic components reach their local minimums, and vice versa. While for the left-going wave, no such conversion occurs, and the intensity of the incident harmonic component remains unchanged when the wave propagates in the left direction [see Fig. 3.8(b)]. In Figs. 3.8(c) and 3.8(d), we plot the time-frequency-amplitude maps for the two receiver stations indicated as blue and red points in Fig. 3.7. Since there always exists a trade-off between the frequency and time resolutions, here we set the frequency resolution as 0.0233Ω, corresponding to a time resolution of 0.1243 μs. Three different colors are used to highlight the analytically predicted frequencies of the incident fundamental, excited first- and second-order harmonics. Figure 3.8(c) shows the results collected at the red point (identical position of the red point in Fig. 3.7) for the right-going wave. The incident harmonic is converted into the first-order and second-order harmonics soon after the incidence reaches the red point. The first-order and second-order harmonic components last longer in time at this receiver station than the incident harmonic one does since the group velocities of the first-order and second-order harmonics are smaller than that of the incident harmonic (see Figs. 3.3 and 3.6). In addition, along the modulation direction, the incident harmonic component appears to be more durable in terms of time than that of the opposite case [see comparison between Figs. 3.8(c) and 3.8(d)]. This is simply because around the veering pairs $(\omega_{0\cap1}, q_{0\cap1})$ corrected by equation (3.36), the dispersion curve gives smaller group velocities when compared to the uncoupled area $(\omega_{0\cap1}, -q_{0\cap1})$ (see Figs. 3.3 and 3.6). As for the left-going Rayleigh wave, nearly no conversion between the incident and the higher order harmonics can be visualized [see Fig. 3.8(d)]. Note that the results in Figs. 3.8(c) and 3.8(d) can clearly illustrate the non-reciprocal harmonic conversion, even though the time resolution is not considered high owing to the compromise we have made between the transient simulation efficiency and the simulation time span (currently 0.85 μs). To better the quality of the time-frequency-amplitude maps, one can increase the simulation time span while preserving the current simulation sampling frequency (currently 8 GHz).

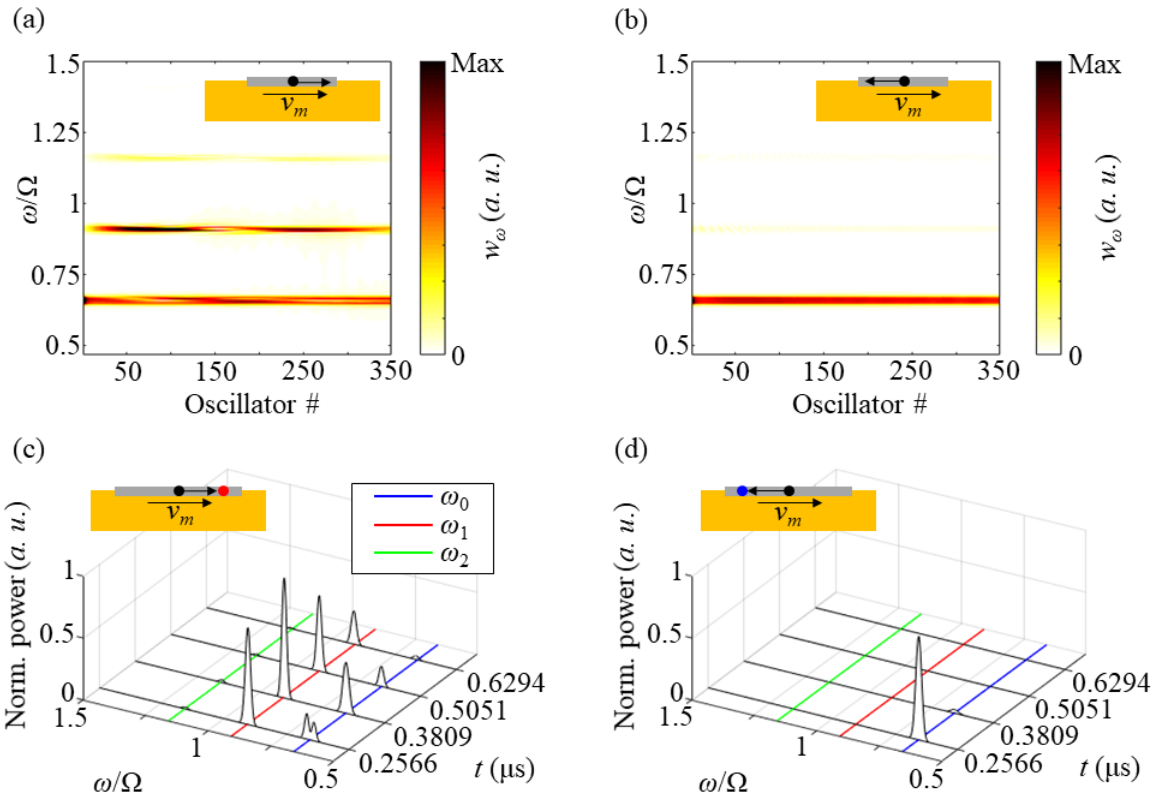

Figure 3.8: Illustration of the harmonic conversion process. (a) and (b) Evolution of the harmonic spectra of the Rayleigh waves propagating against the oscillator position along the two opposite directions. (c) and (d) Time-frequency-amplitude maps for the two receiver stations in Fig. 3.7. (c) corresponds to the right-going wave collected at the red point, while (d) corresponds to the left-going wave collected at the blue point. In (c) and (d), the blue, red and green lines represent the frequencies of the incident fundamental, excited first-order and second-order harmonics, respectively. The frequency resolution is taken as 0.0233Ω, which consequently leads to a time resolution of 0.1243 μs. Reproduced from Journal of the Mechanics and Physics of Solids 146, 104196 (2021), with the permission of Elsevier Publishing

One-way mode conversion

Mode conversion of Rayleigh waves can be realized in the proposed system. The spectral relocation of the energy of the veering pair B shown in Fig. 3.7(c) refers to an acoustic-acoustic conversion, as can be concluded from Figs. 3.3(b) and 3.3(d). It indicates that the incidence starts from in-phase oscillations between the displacement of oscillator mass Z and the vertical displacement of the surface w undergoes a transition between higher-order harmonics, and still remains in-phase. As can be seen in Fig. 3.9, at $t = 0.05$ μs, the system starts from in-phase oscillations between Z (blue dashed) and $2w$ (red solid). As the Rayleigh wave propagates along the modulation direction (right half of Fig. 3.9), it undergoes a mode conversion from φ^0, with longer wavelength, to φ^1, with shorter

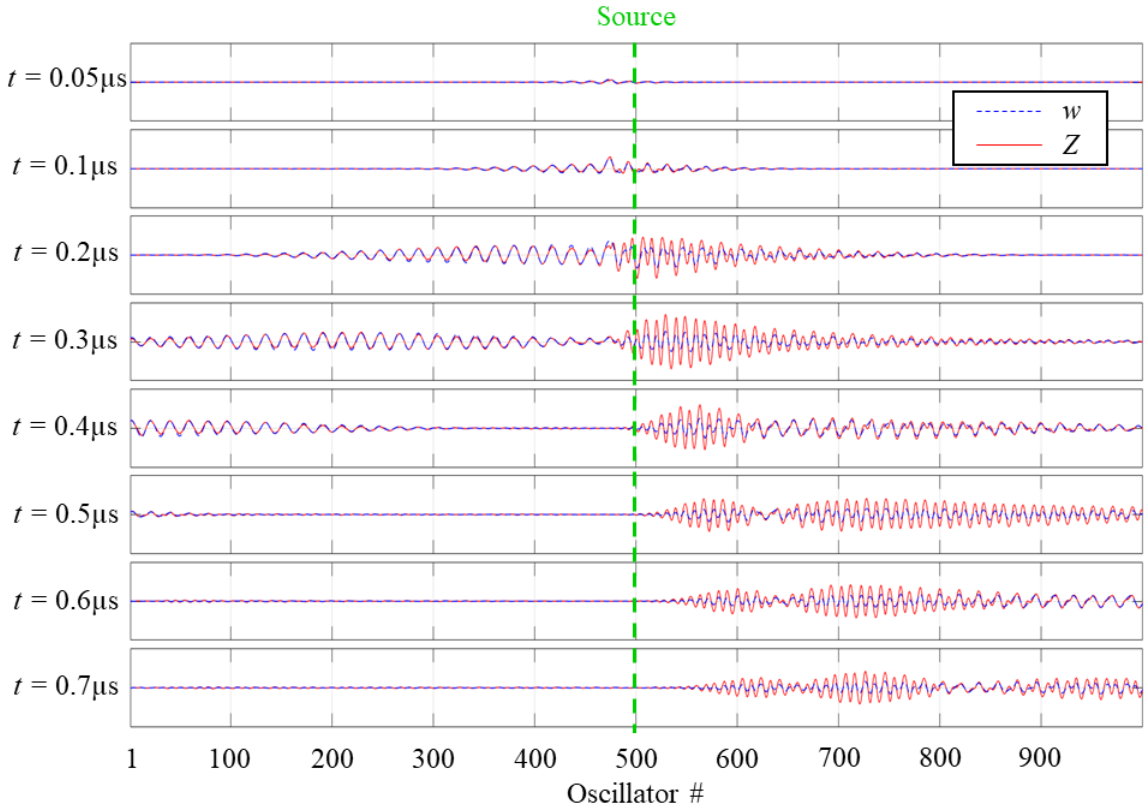

Figure 3.9: Mode conversion of pair B. The displacements of oscillator masses Z (red solid) and the displacement $2w$ (blue dashed) are plotted against the oscillator position at various time instants. For clear observation, the vertical displacement w has been magnified by 2. The green dashed line represents the position of the source. Reproduced from Journal of the Mechanics and Physics of Solids 146, 104196 (2021), with the permission of Elsevier Publishing.

wavelength. The oscillator mass displacements Z are obviously amplified after $t = 0.2$ μs due to the fact that the generated first-order harmonics $\boldsymbol{\varphi}^1$ locates quite close to the resonance frequency Ω; see Fig. 3.3. Moreover, $\boldsymbol{\varphi}^1$ propagates slower than $\boldsymbol{\varphi}^0$ does, since they differs in terms of group velocity; see Fig. 3.3. Compared to the mode conversion case, the trivial scenario with the direction of incidence opposite to the modulation direction exhibits neither mode conversion nor amplified displacement Z, as can be seen from the left half of Fig. 3.9. The oscillation between Z and w remains in-phase, once again indicating the acoustic branch. Interestingly, slow wave phenomenon for the incidence $\boldsymbol{\varphi}^0$ can also be observed as can be seen from the comparison between these two cases. The propagation speeds for two opposite directions are different. Most importantly, the mode conversion in the proposed system is not restricted to acoustic-acoustic and the conversion between acoustic and optical modes can be achieved by choosing appropriate modulation parameters (ω_m, λ_m). In Fig. 3.10, we send in a tone-burst signal centered at 1.18Ω at the green point, which

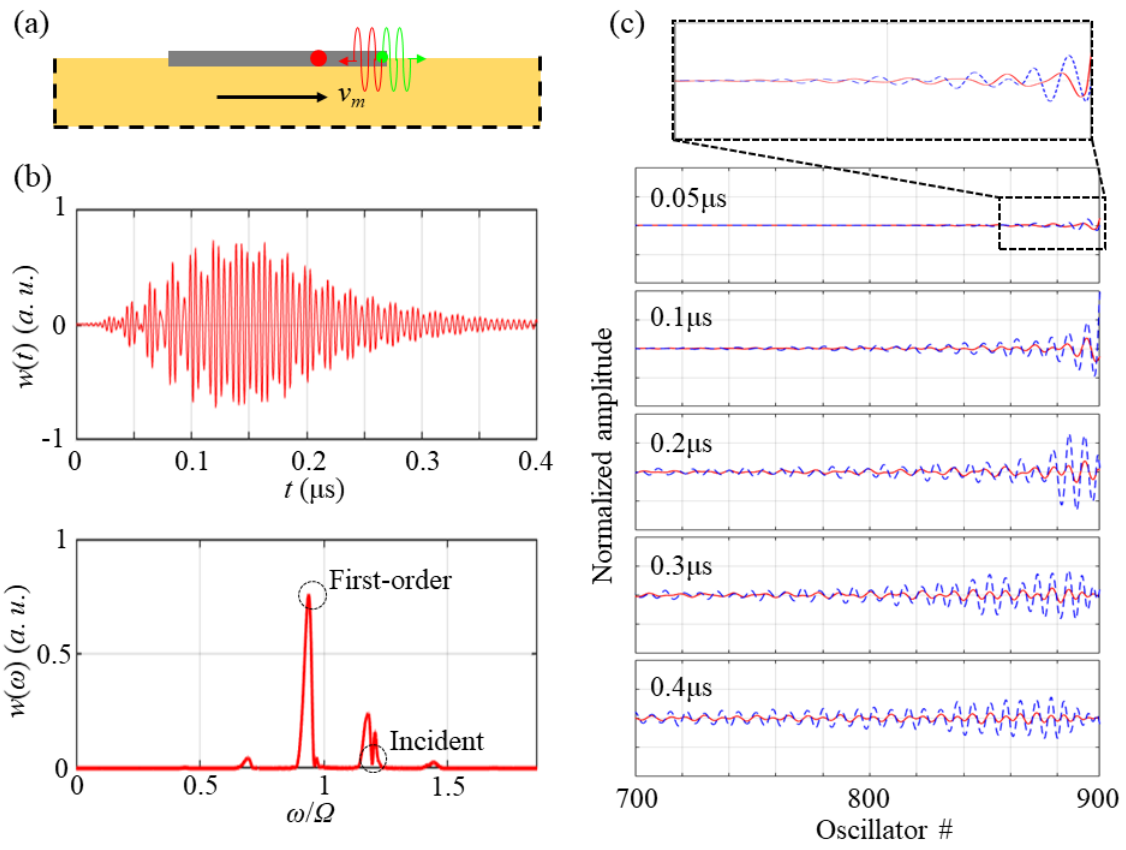

Figure 3.10: (a) The center frequency of the tone-burst is selected so as to match pair A. Other settings are identical to those in Fig. 3.7 except that only 900 oscillators are included and the source is still positioned inside the modulation area but close to the right end of the modulation area. (b) The time-domain and the corresponding frequency-domain spectrum are presented, showing the generation of higher-order harmonics. (c) Similar to Fig. 3.9, the time-domain signals for Z (blue dashed) and $2w$ (red solid) are shown in functions of oscillator position at different time instants. The inset provides a magnified view of the initial state of the combined spring-mass semi-infinite system. Reproduced from Journal of the Mechanics and Physics of Solids 146, 104196 (2021), with the permission of Elsevier Publishing,

corresponds to the selection of the veering pair A (Fig. 3.3(a)). Similarly to the case of pair B, nearly total conversion can be observed from $\boldsymbol{\varphi}^0$ at 1.17Ω to $\boldsymbol{\varphi}^1$ at $1.18\Omega - \omega_m$, as illustrated in Fig. 3.10(b). To reveal the optical-acoustic conversion of this pair, we then plot in Fig. 3.10(c) the transient signal against the oscillator position as we have already done for pair B in Fig. 3.9. Unlike pair B, the system operating at pair A initiates from out-of-phase oscillations of Z and w at the instant $t = 0.05\mu s$, corresponding to the optical mode; see the highlighted inset of Fig. 3.10(c) for an amplified view. While the Rayleigh wave propagates along the correct direction, namely, opposite to the modulation direction, it undergoes a conversion from the optical mode to the acoustic one and the relative phase difference between Z and w gradually vanishes, suggesting that the system

operates now at the acoustic mode. Also, at the output frequency $1.18\Omega - \omega_m$ close to the resonant frequency Ω, the strength of Z experiences a great amplification.

3.4 Summary

In summary, a strategy to realize the non-reciprocal propagation of Rayleigh waves and the associated one-way mode conversion is theoretically proposed, with the help of space-time modulated spring-mass oscillators distributed on the surface of the hosting medium. In the proposed system, the spring constant is modulated temporarily and spatially at the same time in a wave-like fashion. The resulting "pump wave" breaks the time-reversal symmetry, and hence gives birth to the non-reciprocal phenomena. The interactions between this "pump wave" and the travelling Rayleigh wave deliver a remarkable consequence that the group velocities in the vicinity of the interactions require to be corrected accordingly. Analytical and numerical approaches well recover the perturbed dispersion diagram in the presence of the space-time modulation. More importantly, three non-reciprocal pairs, enabling non-reciprocal propagation of Rayleigh waves, are revealed by solving the coupling of harmonics around the interaction points. One of them exhibits the one-way mode conversion between the acoustic and the optical modes. Further, tunability has been investigated as well to provide information and guidance for the potential experimental implementations in the future.

The content of this section is reproduced from *Journal of the Mechanics and Physics of Solids* **146**, 104196 (2021), with the permission of Elsevier Publishing.

Chapter 4

ENGINEERING NONRECIPROCAL WAVE DISPERSION IN A NONLOCAL MICROPOLAR METABEAM

4.1 Introduction

Metamaterials are capable of creating wave-bearing and/or topological devices to manipulate elastic and acoustic waves, such as topological wave propagation and mechanical interfacial waveguiding by using engineered microstructures [125–129]. However, as has been mentioned in the Introduction, passive metamaterials cannot fulfill many novel functions as practical devices because of their lack of tunability or adaptive properties. To overcome this limitation, active and/or programmable mechanical metamaterials composed of energy-generating microstructures with feedback control become a promising platform to create adaptive functional and topological materials [50, 130, 131]. Active metamaterials are also non-Hermitian systems which contain non-conservative forces that require an internal or external source of energy to be present.

In the area of active elastic metamaterials, the active spring with feedback control has been pursued to establish non-reciprocal interactions in a mechanical lattice that emulates the non-Hermitian Su–Schrieffer–Heeger (SSH) model [132]. To physically realize those active springs, a 1D robotic metamaterial including a combination of local sensing, computation, communication, and actuation was suggested to break reciprocity at the level of the local interactions between the building blocks themselves [133]. Zero-frequency edge states in the non-Hermitian topological phase and unidirectional wave amplification were demonstrated. In contrast to the ordinary topological band theory, non-Hermitian mechanical systems exhibit unique features such as band structure sensitive to boundary conditions. By introducing active springs coupled with other local deformations, non-Hermiticity of the active interaction enters the linear elasticity of a continuum solid through

odd elastic moduli, which are active moduli that violate Maxwell-Betti reciprocity [134]. The odd elastic moduli when combined with anisotropy can give rise to the non-Hermitian skin effect [135]. Nonetheless, the aforementioned active systems exhibit either of the following fundamental limitations: the active nonreciprocal effects either vanish from the linear response in the quasistatic limit or they require the presence of background sources of linear or angular momentum [131, 133, 136, 137]. To remove this obstacle, a freestanding active metabeam with piezoelectric elements and electronic feed-forward control was developed that gives rise to odd micropolar elasticity. In addition, inspired by those active metamaterials with local feedback interaction, 1D and 2D elastic lattices with nonlocal feedback interactions were explored to demonstrate a series of unconventional phenomena stemming from their non-Hermiticity [137]. However, little work has been successful in physically realizing active metamaterials with nonlocal feedback or feed-forward control in a continuum level.

This Chapter reports the design, construction, and experimental demonstration of a freestanding active metamaterial with nonlocal feed-forward control. The metamaterial is constructed with piezoelectric elements mounted on a beam and controlled by nonlocal electrical circuits. The nonlocal interaction is considered into an effective complex bending stiffness which is related to the wave propagation direction, transfer function and nonlocal order. The proposed nonlocal micropolar metabeam supports nonreciprocal flexural wave amplification and attenuation as well as localized bulk modes due to their non-Hermiticity. The resulting unidirectional amplification and attenuation of waves propagating through the metambeam is also shown. To gain intuition into the mechanics of the metabeam, analytical modeling including continuum and discrete representations are used. The nonlocal metabeam is also employed to engineer the anomalous wave dispersion such as tunable roton-like dispersion. Its reciprocity can be easily maintained or broken through electrically programmable transfer functions. The tunable nonlocal micropolar metabeam with programmable feed-forward control could provide a platform for the investigation of topological phases of non-Hermitian systems.

4.2 Nonlocal micropolar elasticity and elastodynamics

Design of the nonlocal micropolar metabeam

The proposed structure consists of an aluminum host beam and an array of piezoelectric patches (PZT-5A) on top and bottom of the host beam [see Fig. 4.1(a) and 4.1(b)]. The motion of the host micropolar beam can be characterized by two independent degrees of freedom: the flexural displacement $w(x)$ of the midplane and the other being the rotation angle $\phi(x)$ of the cross section

with respect to the vertical axis; see Fig. 4.1(c). Each PZT patch pair performs as a sensor-actuator feed-forward loop. The actuating patches apply elongation or contraction to the top surface of the host beam, depending on the voltage applied. Conversely, the sensing patches extract voltages from the elongation and contraction of the bottom surface. The nonlocal interaction is realized by connecting the $(n+a)$th sensor to the nth actuator through an electronic microcontroller with a transfer function H, where a is the nonlocal order and satisfies $a \geq 1$ for non-vanishing nonlocality [see Fig. 4.1(c)]. As a result, the nth actuator exerts an external bending moment which is proportional to the bending deformation $\partial_x \phi(x+\delta x)$ at the $(n+a)$th unit cell. We will demonstrate that the frequency bands of the metabeam are complex with non-Hermiticity due to the presence of energetic gain and loss along opposite propagation directions. Such behavior is also tunable due to the reprogrammability of H, which can be exploited to establish multiple frequency bands with interchanging non-reciprocal behavior.

Nonlocal micropolar elasticity

The equations of motion for a freestanding nonlocal micropolar beam, as shown in Fig. 4.1, are built based on conservation laws. Linear and angular momentum conservation indicate

$$\rho \ddot{w} = \partial_x \sigma_{zx}, \tag{4.1}$$

$$I \ddot{\phi} = \partial_x M + \sigma_{zx}, \tag{4.2}$$

where ρ and I are the mass density and cross-sectional moment of inertia, respectively, and σ_{zx} and M are the shear stress and bending moment, respectively. In particular, σ_{zx} and M at x are obtained through the general constitutive relations reading

$$\begin{bmatrix} \sigma_{zx}(x) \\ M(x) \end{bmatrix} = \underbrace{\begin{bmatrix} \mu(\omega) & C_b(\omega) \\ C_s(\omega) & B(\omega) \end{bmatrix} \begin{bmatrix} s(x) \\ b(x) \end{bmatrix}}_{\text{local}} + \underbrace{\begin{bmatrix} \mu^{(P)}(\omega) & C_b^{(P)}(\omega) \\ C_s^{(P)}(\omega) & B^{(P)}(\omega) \end{bmatrix} \begin{bmatrix} s(x+\delta x) \\ b(x+\delta x) \end{bmatrix}}_{\text{nonlocal}}, \tag{4.3}$$

where μ and B are the shear and bending moduli of the piezoelectric metabeam without active control. C_b and C_s are the off-diagonal micropolar moduli, the feedback "(P)" represents the moduli

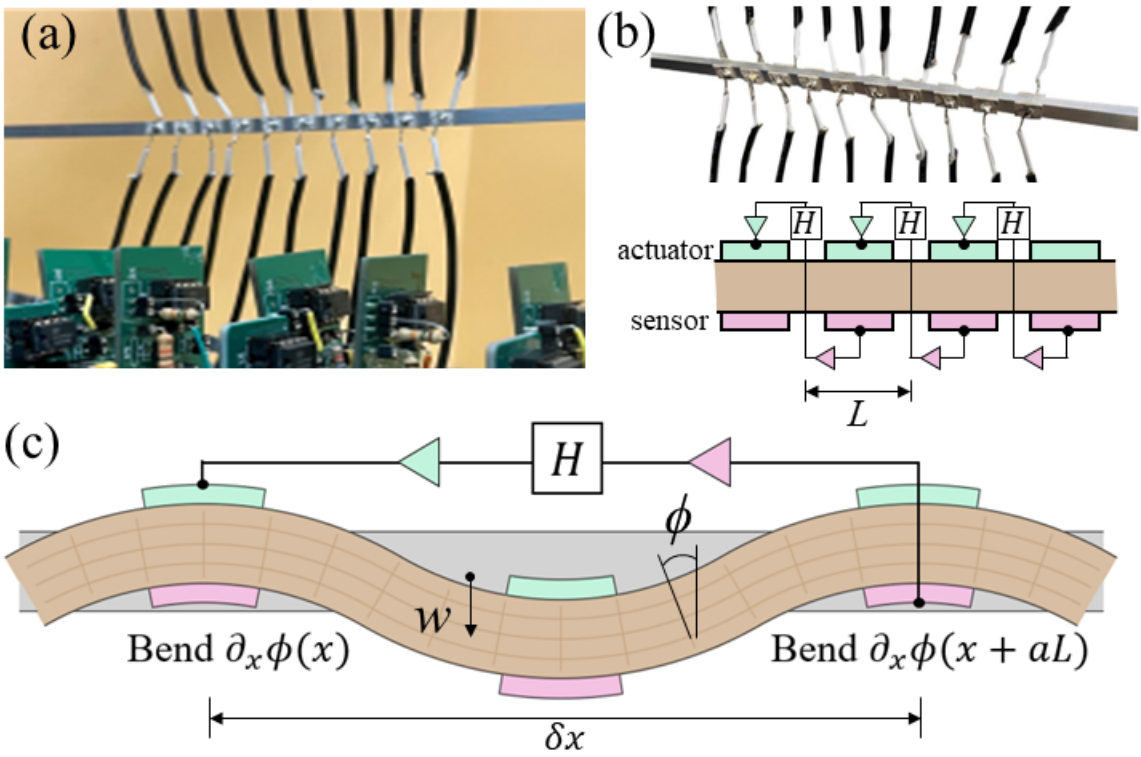

Figure 4.1: **Design and mechanics of a nonlocal micropolar metabeam**. (a) A photograph of the proposed nonlocal micropolar metabeam with a programmable electronic microcontroller system in the foreground. The host beam is 5 mm wide and 3 mm thick. It is made of aluminum (ρ_b=2700 kg/m^3, G_b=26 GPa, $E_b = 69$ GPa). All the piezoelectric patches mounted on the beam are PZT-AJ (ρ_p=7600 kg/m^3,$\epsilon_{33}^T = 1900\epsilon_0$, $d_{31} = -1.75 \times 10^{-10}$ C/N, $d_{33} = 4 \times 10^{-10}$ C/N, $d_{15} = 5.9 \times 10^{-10}$ C/N) with a thickness of 0.64 mm, a side length of 6.4 mm and a width of 4.9 mm. (b) An illustration of the full nonlocal metabeam, later used in the experiments, is shown in the top panel. The bottom panel shows the schematic of a segment of the metabeam. The top and bottom piezoelectric patches serve as actuators and sensors, respectively. They are connected beyond nonlocally by the transfer function H. The illustrated example here corresponds to a nearest-neighbor nonlocal configuration. The lattice constant is $L = 10$ mm. (c) Schematic illustration of the mechanics of the nonlocal micropolar metabeam. The motion of the metabeam can be described by two independent micropolar degrees of freedom: flexural displacement w and rotation angle ϕ. The $(n + a)$th sensor is connected to the nth actuator through H in a periodic way. This equivalently means the nonlocal bending at $x + \delta x$, where $\delta x = aL$, is modulated by H and then contributes to the local bending at x.

induced by $H(\omega)$, and the shear deformation $s(x)$ and the bending curvature $b(x)$ read, respectively,

$$s(x) = \partial_x w(x) - \phi(x) \tag{4.4}$$

$$b(x) = \partial_x \phi(x). \tag{4.5}$$

The local stress state possesses two components: the local contribution from the host beam with piezoelectric patches and the nonlocal contribution produced by $H(\omega)$. Due to the arrangement of sensor-actuator pairs, the nonlocal shear barely contributes to the local shear and bending at lower frequencies, nor does the nonlocal bending to the local one, implying $\mu^{(P)} = C_s^{(P)} = C_b^{(P)} \approx 0$. Under harmonic assumption (ω, k), Eq. (4.3) becomes

$$\begin{bmatrix} \sigma_{zx}(\omega) \\ M(\omega) \end{bmatrix} = \begin{bmatrix} \mu(\omega) & C_b(\omega) \\ C_s(\omega) & B_{\text{eff}}(\omega) \end{bmatrix} \begin{bmatrix} s(\omega) \\ b(\omega) \end{bmatrix} = \mathbf{C}(\omega) \begin{bmatrix} s(\omega) \\ b(\omega) \end{bmatrix}, \tag{4.6}$$

where $C_b, C_s \approx 0$ at lower frequencies, and $B_{\text{eff}} = B + B^{(P)} e^{ik\delta x}$ is the effective bending modulus. Thus far, we have used a homogeneous beam model to approximate the actual piezoelectric-based metabeam. This presentation works well only within the quasistatic limit, where $|k|$ is small.

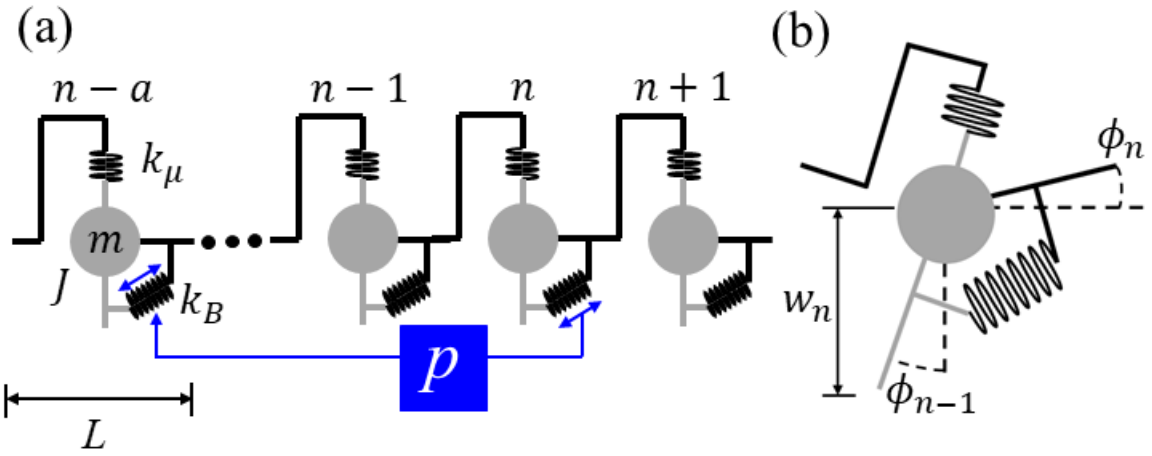

Figure 4.2: **Discrete spring-mass representation of the nonlocal micropolar metabeam.** (a) The discrete model consists of a central mass m with moment of inertial J, a Hookean spring k_μ, a torsional spring k_B, and the lattice spacing L. The feedback from nth to the $(n-a)$th unit cells is represented by p. (b) Schematic of the deformation of the nth lattice unit cell with w_n and ϕ_n denoting as its flexural displacement and rotation angle, respectively.

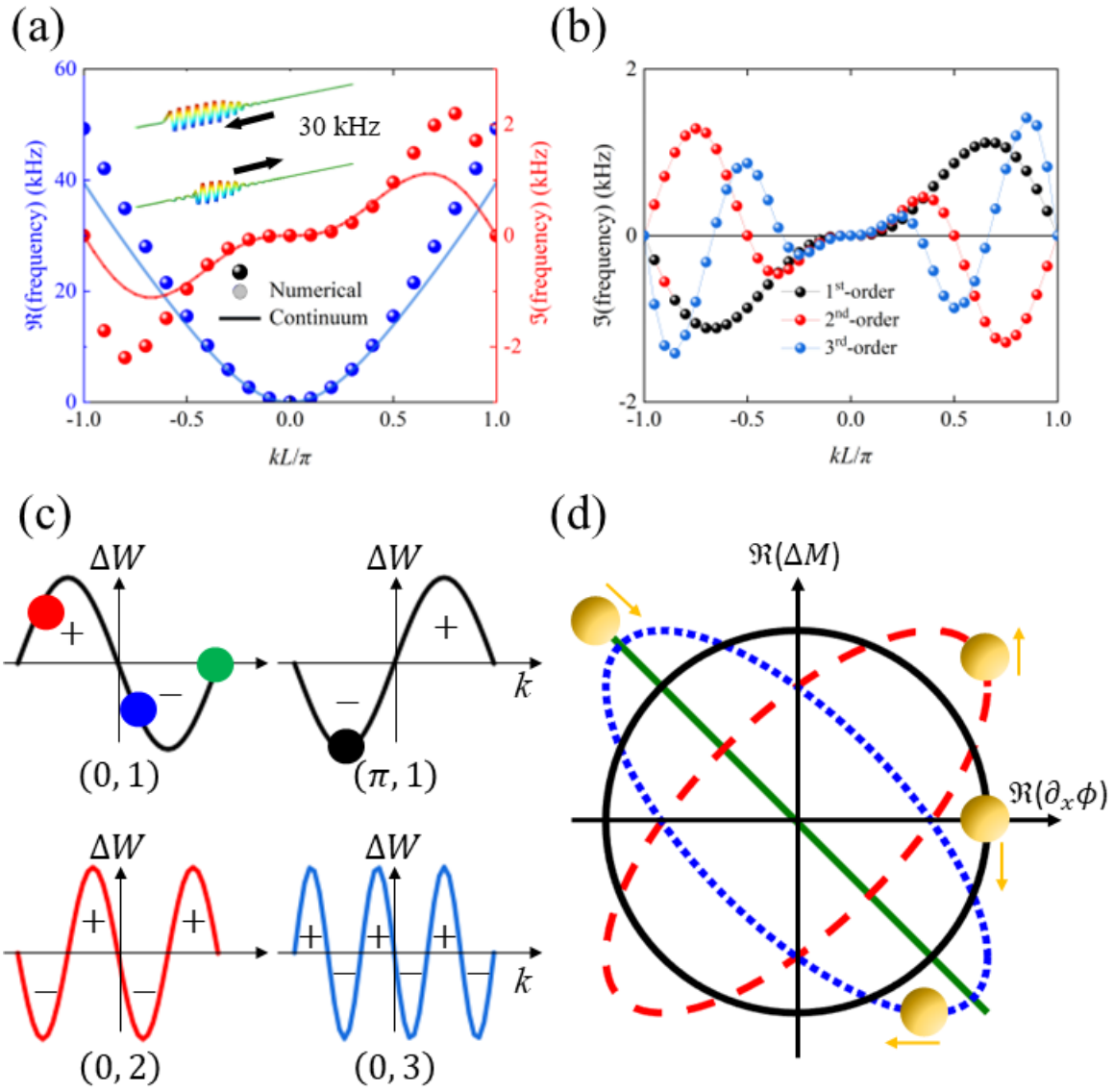

Figure 4.3: **Complex dispersion engineering for nonreciprocal amplification and attenuation**. (a) Complex dispersion for 1^{st}-order nonlocal configuration. The sold curves are analytical results from the continuum theory. The symbols represent the numerical results from a fully-coupled Finite-element software (COMSOL Multiphysics). The inset shows two representative scenarios featuring the nonreciprocity for the opposite propagation directions at 30 kHz. (b) Imaginary dispersion band for the 1^{st}-, 2^{nd}-, and 3^{rd}-order nonlocalities. (c) Work done by nonlocal bending, ΔW, with $|P|e^{i\Phi_P}$ and $\delta x = aL$. Four situations are shown with different (Φ_P, a). The signs "+" and "-" correspond to the positive and negative ΔW. In particular, four representative states are selected. (d) Trajectories of the selected four states in the $\Re(\Delta W) - \Re(\partial_x \Phi)$ space with $|b| = |P| = 1$. The particle direction indicates the evolution from one end of IRZ to the other.

Nonlocal micropolar elastodynamics

Considering $\mathbf{C}$ is frequency independent at the quasistatic limit, we revisit the linearized continuum equations given in Eqs. (4.1) and (4.2), where under the harmonic assumption of $e^{i(kx-\omega t)}$ and an

instant control ($\delta t = 0$), the strain-stress relations read

$$\begin{bmatrix} \sigma_{zx} \\ M \end{bmatrix} = \begin{bmatrix} \mu & 0 \\ 0 & B + P(\cos k\delta x + i \sin k\delta x) \end{bmatrix} \begin{bmatrix} s \\ b \end{bmatrix}. \tag{4.7}$$

Combining Eqs. (4.1), (4.2) and (4.7) we arrive eventually at

$$\omega^4 - [\frac{\mu}{I} + k^2(\frac{\mu}{\rho} + \frac{B_{\text{eff}}}{I})]\omega^2 + \frac{B_{\text{eff}}\mu}{I\rho}k^4 = 0. \tag{4.8}$$

At a specific wave number k, we can solve for the complex ω. For the nonlocal metabeam, we conduct numerical simulations for a unit cell using COMSOL Multiphysics to determine all the moduli of $\mathbf{C}$ which are found approximately frequency independent at small $|k|$ [138]. By selecting properly prescribed strain boundaries and measuring the reaction forces, we empirically find the system parameters $B_{eff} = 8.24 \times 10^4$ kgm^2/s^2 and $\mu = 5.612 \times 10^9$ kg/s^2. The feedback coefficient $P(\omega)$ is approximated to be $P(\omega) = \Gamma H(\omega)$ with $\Gamma = 7.5 \times 10^2$ kgm^2/s^2. The normalized effective mass density and moment of inertia are computed to be $\rho = 4.776 \times 10^3$ kg/m^3 and $I = 3.2 \times 10^{-3}$ kgm.

A discrete representation of the nonlocal micropolar metabeam

It is also intuitive to discretize the continuous nonlocal micropolar metabeam into a discrete model [138]. Here, we consider a 1D lattice whose unit cell consists of a rigid mass, a Hookean spring and a torsional spring; see Figs. 4.2(a) and 4.2(b). The vertical position and orientation of the nth rigid mass are represented by w_n and ϕ_n, respectively; also see Fig. 4.2(b). The Hookean spring connected to the nth mass causes a tension force

$$T_n = k_\mu(w_{n-1} - w_n + L\phi_{n-1}) \tag{4.9}$$

with $k_\mu = \mu/L$, while the torsional spring exerts a bending moment

$$\tau_n = k_B(\phi_{n-1} - \phi_n) \tag{4.10}$$

with $k_B = B/L$. Since the metabeam is modulated by a nonlocal feed-forward control loop, an additional bending moment τ_n^{act} is added on the $(n-a)$th unit cell, meaning that

$$\tau_n^{act} = p(\phi_{n-1} - \phi_n), \tag{4.11}$$

where $p = Pe^{ikaL}/L$. In this design, the considered uniform distribution of bending moment does not necessarily cause shear force. Therefore, considering the equilibrium conditions within each unit cell, we obtain

$$m\ddot{\omega}_n = T_n - T_{n-1}, \tag{4.12}$$

$$J\ddot{\phi}_n = \tau_n - \tau_{n+1} + \tau_n^{act} - \tau_{n+1}^{act} - LT_{n+1}, \tag{4.13}$$

where $m = \rho L$ and $J = IL$. Combining all expressions above leads to

$$m\ddot{\omega}_n = k_\mu(w_{n-1} - 2w_n + w_{n+1}) + Lk_\mu(\phi_{n-1} - \phi_n), \tag{4.14}$$

$$J\ddot{\phi}_n = (k_B + p)(\phi_{n-1} - 2\phi_n + \phi_{n+1}) + Lk_\mu(w_{n+1} - w_n) - L^2k_\mu\phi_n. \tag{4.15}$$

Note that the discrete model of the metabeam is nothing but a finite-difference version of Eqs. (4.1) and (4.2) and should work well within the quasistatic region where small $|k|$ is considered.

4.3 Nonreciprocity, non-Hermitian skin effect and roton-like dispersion

Nonreciprocity and energy cycles

We first examine the complex dispersion engineering of the nonlocal metabeam. Equation (4.8) admits four solutions with two of them being the evanescent modes and the other two the propagating ones. We plot analytically the lowest complex band structure in the irreducible zone (IRZ) for $a = 1$ (1^{st}-order nonlocality) and $P = 1.384 \times 10^4$ kgm^2/s^2 ($H = 20$) in Fig. 4.3(a) (see the solid curves). The real part of the band structure $\Re(\omega)$ is symmetric with respect to $k = 0$, while its imaginary component $\Im(\omega)$ is antisymmetric, meaning that the amplification and attenuation of the flexural wave propagation are nonreciprocal in the x direction: flexural waves propagating in $-x$ and $+x$ undergo amplification and attenuation, respectively. Numerical eigenfrequency analysis confirms this

theoretical prediction, in spite of some discrepancies at higher frequencies due to the fact that Eq. (4.8) works properly only for small $|k|$. In addition, the dispersion given by the discrete model Eqs. (4.14) and (4.15) is also in good agreement with both numerical and analytical results at small $|k|$. The nonlocal order plays an important role in controlling the number of nonreciprocal amplification and attenuation regimes. As shown in Fig. 4.3(b), 2^{nd}- and 3^{rd}-order nonlocalities, corresponding to the $a = 2$ and $a = 3$ scenarios, generate two and three nonreciprocal amplification/attenuation regimes along a certain propagation direction, respectively.

For better understanding the wave nonreciprocity, the energy cycles of the metabeam are also studied. Here, we assume $P = |P|e^{i\Phi_P}$. Then, the local strain and nonlocal bending can be qualitatively expressed, respectively, as

$$\partial_x \phi \propto e^{-i\omega t}, \tag{4.16}$$

$$\Delta M \propto |P| e^{i\Phi_P} e^{ik\delta x} e^{-i\omega t}. \tag{4.17}$$

Then, we obtain the work done by the nonlocal bending:

$$\Delta W = \Re\left\{ \int_0^T i\omega \begin{pmatrix} s \\ b \end{pmatrix}^{\dagger} \begin{pmatrix} 0 & 0 \\ 0 & B_{\text{eff}} - B \end{pmatrix} \begin{pmatrix} s \\ b \end{pmatrix} \mathrm{d}t \right\} = 2\pi |b|^2 |P| \sin(\Phi_P + k\delta x), \tag{4.18}$$

where $T = 2\pi/\omega$ denotes the period. With non-vanishing nonlocality, i.e. $\delta x = aL \neq 0$, $\Delta W > 0$ when $\Phi_P + k\delta x \in (0, \pi)$. This physically means that the nonlocal bending ΔM does positive work, corresponding to a process where electrical energy is converted into the mechanical one. During this process, the flexural propagation experiences amplification. By contrast, $\Delta W < 0$ holds when $\Phi_P + k\delta x \in (\pi, 2\pi)$, indicating that ΔM now delivers negative work and features the attenuation behavior of the flexural propagation since mechanical energy is now converted into the electrical one. In the top panel of Fig. 4.3(c), we schematically show the k-dependent ΔM for $\Phi_P = 0$ and π for a 1^{st}-order nonlocal beam, which corresponds to positive and negative P. When $\Phi_P = 0$, a negative k (left propagation) experiences positive work done by the nonlocal bending, indicating amplification. As for a positive k (right propagation), the flexural waves are attenuated. This gives exactly a physical interpretation of the nonreciprocity in the metabeam system. A sign flip of P will flip the direction of the nonreciprocity. Alternatively, the sign of ΔW can also be visually determined by the trajectories of the strain-stress curves within one period in a $\Re(\Delta W) - \Re(\partial_x \Phi)$ plot; see Fig. 4.3(d). Moreover, the bottom panel of Fig. 4.3(c) illustrate the distribution of ΔW for

higher-order nonlocalities with $\Phi_P = 0$ or positive P. sgn(ΔW) can well predict the nonreciprocal attenuation/amplification bands when compared to the results shown in Fig. 4.2(b). Note that a local control ($\delta x = aL = 0$) can also do nonzero work, namely $\Delta W \neq 0$. However, this ΔW causes neither amplification nor attenuation, but either a hardening or softening of metabeam for both directions.

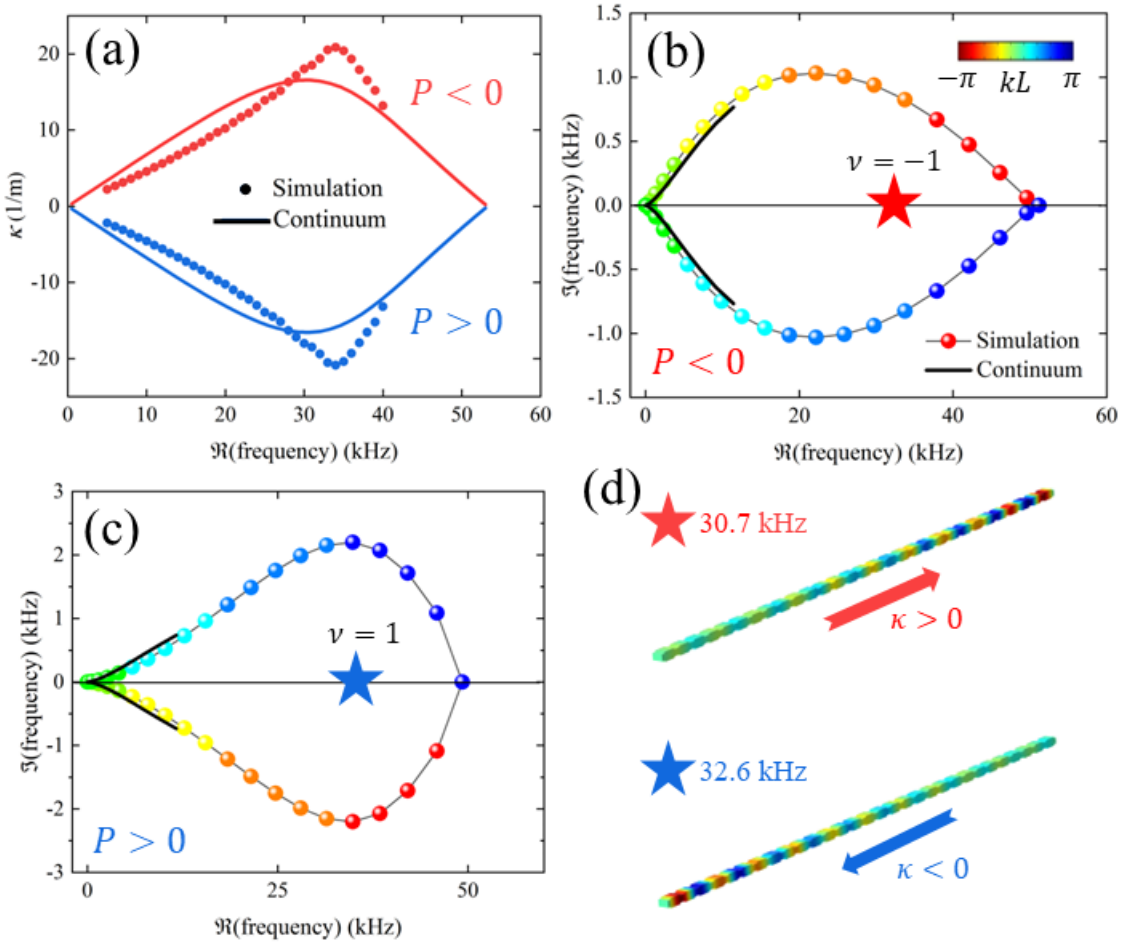

Figure 4.4: **Non-Hermitian skin effect.** (a) Calculation of the inverse decay length κ using FEM frequency-domain simulations (dotted) and analytical approach (solid) when $P > 0$ and $P < 0$. (b,c) The complex dispersion bands are displayed for $P < 0$ and $P > 0$. The winding number of each scenario ν is indicated. Comparison between the numerical simulations and continuum theory is shown. For both scenarios, two representative modes encircled by the two loops are selected. (d) The corresponding field distributions of the two selected modes feature the amplification and suppression of flexural waves.

Non-Hermitian skin effect

The nonreciprocal behavior can also be determined by inverse decay length κ, which can be analytically obtained by solving Eq. (4.8) for $k = q + i\kappa$ with purely real ω, where the positive q is the propagation constant. From Fig. 4.4(a), it can be found that $P > 0$ leads to a negative κ, corresponding to the attenuation behavior, whereas $P < 0$ results in a positive κ, corresponding to the amplification behavior. For comparison, we also obtain the numerical inverse decay length by conducting frequency-domain simulations using a finite metabeam including 60 unit cells. We emphasize that the flexural nonreciprocity of the metabeam can also be related to a non-Hermitian skin effect. For a complex frequency ω, the following topological index ν, the winding number of a dispersion band, can be defined as

$$\nu(\omega) = \frac{1}{2\pi i}\Sigma_\alpha \oint_{-\pi/L}^{\pi/L} \frac{\mathrm{d}}{\mathrm{d}k} \log[\omega_\alpha(k) - \omega]\mathrm{d}k, \tag{4.19}$$

in which $\omega_\alpha(k)$ denotes the frequency of the α band (in this work it is the lowest flexural band). From a geometrical standpoint, $\nu(\omega)$ counts the number of times the loops of a dispersion band over the IRZ encircles the selected frequency. Its sign is dependent of the handedness of the loops: $\nu(\omega) > 0$ if the rotation about the selected frequency is clockwise; $\nu(\omega) < 0$ otherwise. A non-zero $|\nu(\omega)|$ features the existence of localized bulk eigenmodes, while $\mathrm{sgn}(\nu(\omega))$ determines which side the eigenmodes are localized on. In Figs. 4.4(b) and 4.4(c), we plot the dispersion loops for $P < 0$ and $P > 0$, respectively. Comparison between the simulations and continuum theory is illustrated as well to show their good agreement for small $|k|$. In the two cases, one can find $\nu(\omega) = -1$ and $\nu(\omega) = 1$. Eigenmodes encircled by the $\nu(\omega) = -1$ loop are localized on the right boundary of the metabeam, whereas $\nu(\omega) = 1$ leads to localized eigenmodes on the left boundary; see also the confirmation given by Fig. 4.4(d) from numerical eigenfrequency analysis.

Band tilting

The transfer function H can also involve nonzero phase difference, i.e. $\arg(H) \neq 0$. When $\arg(H) = \pm\pi/2$, H becomes purely imaginary. From Eq. (4.7), it can be seen that the effective bending stiffness $\Re(B_{\mathrm{eff}})$ becomes direction dependent. In particular, its imaginary part vanishes only at $kL = \pi/2$. Similar to the nonlocal metabeam here, the reported odd-elasticity local platform with imaginary-valued control can also exhibit directional bending stiffness, but without amplification or attenuation across the entire IRZ, thus supporting free wave propagation. Figure 4.5(a) shows $\Re(\omega)$ is asymmetric when $H = 40i$ or equivalently $P = 5.1i \times 10^4$ kgm^2/s^2. This means that the left-

and right-going waves exhibit different group velocities, showing band tilting phenomenon. It is also seen that the numerical and analytical results match well at small $|k|$. To further examine the band tilting, we conduct harmonic simulations for incidence from both directions at 9.211 kHz, and the computed phase distributions of the flexural waves ($\arg(w) = 1i \times \log[w/|w|]$) are illustrated in Fig. 4.5(b). The band tilting effect is numerically observed from the wavelength difference.

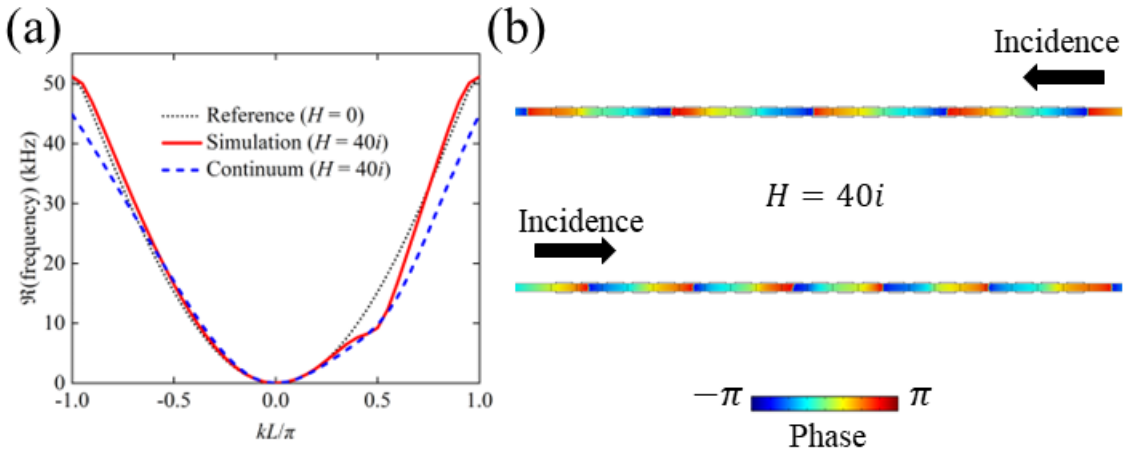

Figure 4.5: **Band tilt induced by nonlocality**. (a) The real spectrum for $H = 40i$ is shown accompanied by the comparison between the reference in absence of active loops (black dotted), eigenfrequency simulation (red solid) and the continuum theory by Eq. (4.7) (blue dashed). (b) Phase distributions of the right- and left-going flexural waves through the metabeam section at 9.211 kHz. The phase is defined as $\arg(w) = 1i \times \log[w/|w|]$. Only the phase changes within the host beam are illustrated.

Nonreciprocal roton-like dispersion

Roton dispersion relations initially found in correlated quantum systems at low temperatures were recently developed and investigated in mechanical and acoustic systems. One of the prominent features is multiple eigenmodes supported at a single frequency, featuring net negative energy flows which are analogous to the so-called "return flow". Up to now, there have been mainly two approaches to achieving the roton-like mechanical and acoustic bands: chiral [139] and nonlocal interactions [140, 141]. Here, we emphasize that with the nonlocal metabeam design, both reciprocal and nonreciprocal roton-like dispersion relations can be observed with the help of extra nonlocal degree of freedom.

Figure 4.6(a) schematically illustrates the functional unit capable of achieve both reciprocal and nonreciprocal roton-like behaviors. Instead of having a single nonlocal feed-forward loop, the design

now involves two loops (P_1 and P_2) with the opposite nonlocal orders, leading to

$$B_{\text{eff}} = B + P_1 e^{ik\delta x} + P_2 e^{-ik\delta x}. \tag{4.20}$$

The idea of using two loops is to accommodate a toggle function between roton-like reciprocity and nonreciprocity. In Figs. 4.6(b)-4.6(d), the formation of the reciprocal roton-like dispersion is first demonstrated in a 2^{nd}-order nonlocal configuration ($a = 2$), with $P_1 = P_2 = P$. Good agreement between numerical and analytical analyses validates the theoretical model in the continuum region. The roton-like dispersion appears when H exceeds about 20. Once it reaches roughly 23.8, the band touches $\omega = 0$ at a critical point at $kL = 0.5\pi$, because B_{eff} reaches zero; see Eq. (4.8). Within this range, only one roton minimum survives and three eigenmodes exist at a single frequency, with one of them exhibiting negative group velocity v_g. Continuing increasing H eventually induces a vertical bandgap within which flexural propagation at certain k is forbidden. This can also be interpreted as the emergence of negative effective bending stiffness across the certain range of k, similar to the conventional scenarios where single or double negative constitutive parameters take place in certain frequency ranges. Note that the numerically determined P is no longer in linear relation with H due to the double feed-forward controls and the value selection of H, vastly different from what we have seen in the previous sections. Overall, the roton-like behavior presented here shows similarity with those reported in three-dimensional (3D) mechanical metamaterials, since the nonlocal feedback control discussed here is equivalent to a reciprocal next-nearest-neighbor interaction. The fundamental difference lies in the realizations of nonlocal interactions: the design senses the nonlocal strain fields whereas the existing studies utilize passive reciprocal on-site interactions. Moreover, similar to those passive designs [140], increasing the nonlocal order will also increase the number of roton minimums.

What is more compelling is that the nonlocal metabeam is also capable of realizing nonreciprocal roton-like dispersion, or in other words, a roton-like behavior with unidirectional amplification/attenuation, which has not been reported yet. To achieve it, two unbalanced transfer functions $H_1 \neq H_2$ are required. As shown in Fig. 4.6(e), we plot the complex spectra for $H_1 = 26$ and $H_2 = 23$ using both numerical modeling and continuum theory given by Eq. (4.7). We confirm this novel behavior by examining the wave number dependent intensity difference between the two opposite directions at 2 kHz, as displayed by Fig. 4.6(f); also see the inset of Fig. 4.6(f), where a fast Fourier transform (FFT) is adopted on the spatial flexural displacements collected in an 81-unit-long metabeam for both directions. Specifically, the magnitude of the first positive-v_g mode is enhanced

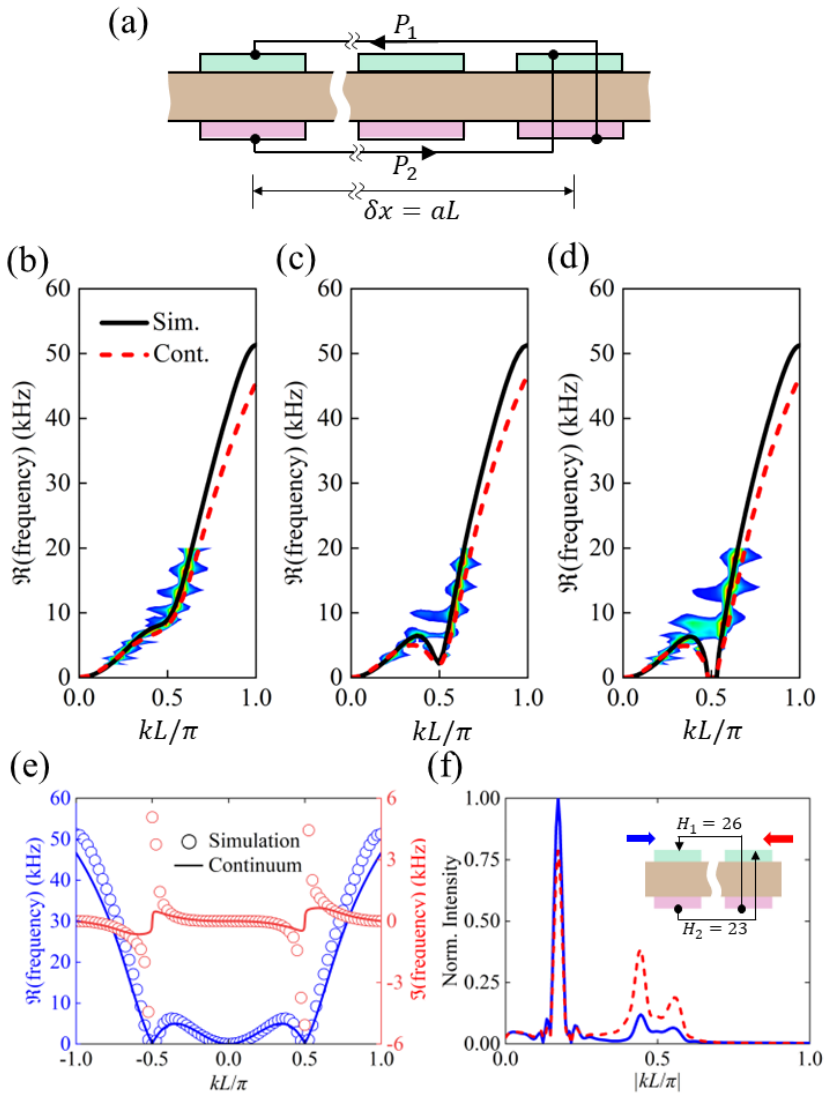

Figure 4.6: **Reciprocal and nonreciprocal roton-like dispersions**. (a) Schematic illustration of the nonlocal realization of the roton-like dispersion with a toggle between reciprocity and nonreciprocity. (b-d) Reciprocal roton-like dispersion relations enabled by $H_1 = H_2 = H$ or equivalently $P_1 = P_2 = P$. The change of the $\Re(\omega)$ band is shown when $H = 20$, $H = 23.5$, and $H = 24$, or numerically $P = 3.08 \times 10^4$ kgm^2/s^2, $P = 4.09 \times 10^4$ kgm^2/s^2 and $P = 4.2 \times 10^4$ kgm^2/s^2 under the continuum limit. The black and red curves represent the eigenfrequency simulation and continuum theory. The color fills are the FFT results. (e) Nonreciprocal roton-like dispersion relations enabled by $H_1 = 26$ and $H_2 = 23$ or equivalently $P_1 = 4.34 \times 10^4$ kgm^2/s^2 and $P_2 = 3.95 \times 10^4$ kgm^2/s^2 under the continuum limit. Comparison of the complex spectra between simulation and continuum theory is shown. (f) The normalized FFT-based intensity spectrum for the propagation of two opposite directions within the nonreciprocal roton-like configuration are shown at 2 kHz where the nonreciprocal roton-like behavior takes place.

in $+x$ due to the negative $\Im(\omega)$. On the contrary, the second positive-v_g mode and the negative-v_g one featuring "return flow" are amplified in $-x$. This observation clearly verifies the validity of the nonreciprocal roton-like mechanical behavior. Note that the switch between the reciprocal and

Parameters	Values
R1	1 MΩ
R2	1.5 kΩ
R3	6.8 kΩ
R6	1 kΩ
R7	22 kΩ
C1	1 nF
C2	4.7 nF
C3	0.47 nF

Table 4.1: Electrical components used in the nonlocal metabeam experiments.

nonreciprocal configurations can be done simply by adjusting the nonlocal feed-forward control loops, possessing potential tunability.

4.4 Experimental demonstration

To experimentally observe nonreciprocity, we fabricated a finite nonlocal metabeam consisting of 10 unit cells (a total length of $L_t = 100$ mm) and 9 active nonlocal feed-forward loops on a 6-foot-long aluminum host beam, as shown in Fig. 4.7(a). The transfer function, which is realized by the circuits in Fig. 4.7(b), reads

$$H(\omega) = \frac{H_0}{(i\omega/\omega_0)^2 + 2\eta(i\omega/\omega_0) + 1}, \tag{4.21}$$

where the cutoff frequency $\omega_0 = 2\pi \times 33.53$ kHz, the damping coefficient $\eta = 0.41$ and $H_0 = -22.5$. This transfer function corresponds to a feedback $P < 0$ for $H_0 < 0$. Based on the prediction given by Fig. 4.3(c), left and right flexural incidences will be amplified and attenuated. In the experiments, the probed vibration dynamics along the opposite directions confirms the nonreciprocity, as shown in Figs. 4.7(c) and 4.7(d). The magnitude of the left propagation at 20 kHz is amplified roughly by 232%, whereas that of the right propagation is suppressed by about 40%.

To examine the inverse decay length of the metabeam, we plot the comparison between experiments and numerical simulations using $\kappa = \pm \ln(v_{\text{norm}}^{\max})/L_t$ for left/right-propagated waves in Fig. 4.7(e), where $v_{\text{norm}}^{\max}$ is the maximum magnitude of the normalized velocity wave field. Good agreement can be found between the experiments and simulations. A value of $\kappa > 0$ implies amplification of the left-going waves with positive k. On the contrary, a value of $\kappa > 0$ implies attenuation of the right-going waves with negative k. A closer observation of the calculated κ reveals that the nonreciprocal amplification does not always take place within the entire spectrum. Above 23.5 kHz, both left- and right-going waves undergo suppression. This is owing to the choice of the low-pass filter which causes a band tilt of $\Re(\omega)$ by the nonzero $\Im(H(\omega))$. With a modest value of

H_0, the nonreciprocity will occur across the entire spectrum considered, although the amounts of amplification/attenuation would be inevitably diminished. Nevertheless, the nonreciprocity of the nonlocal metabeam is evidently validated by the experiments. Similar observations are also available with higher-order nonreciprocity. Specifically, more than one nonreciprocal amplification band regions will be found [137].

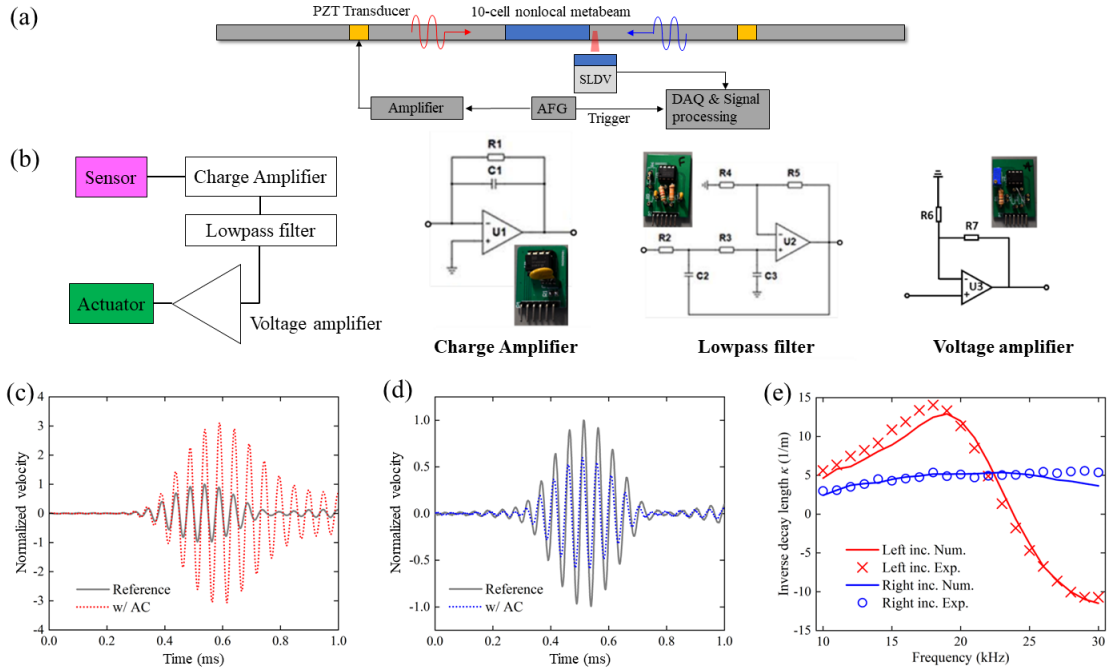

Figure 4.7: **Experimental demonstration of nonreciprocity**. (a) Schematic of the experimental setup including a 1^{st}-order nonlocal metabeam of 10 unit cells modulated by 9 active loops. The incidences from both sides are excited by two PZT-5A transducer connected to an amplifier and arbitrary function generator (AFG). The measurement and post-processing are implemented by a commercial laser vibrometer (PSV-400). The excitation is a 10-cycle tone burst signal centered at 20 kHz. (b) The schematic of the electrical control circuit system and the circuit diagrams of individual components. The experimental specifications are listed in TABLE 4.1. (c,d) Measured transient velocity wave signal at the output for both incident directions. Red and blue represent the left and right incidences, respectively, while the gray ones are reference signals when the active control is switched off. The results with active control are normalized the the maximum of the respective references. (e) Comparison of the inverse decay length κ between the experiments (symbols) and numerical transient analyses (solid).

4.5 Summary

The active metabeam enabled by nonlocal feed-forward control has been suggested in providing a physical realization of the nonlocal micropolar elastic media. Both the continuum and discrete models give accurate description of the complex band structure under the continuum limit. The

nonreciprocal flexural wave amplification and attenuation are numerically demonstrated and also experimentally validated. This peculiar wave propagation behavior can be attributed to the work done by the nonlocal bending, which is described as the exchange between mechanical energy and external electrical power. The non-Hermitian skin effect of the finite system is demonstrated and interpreted by the topology of the complex dispersion band. In addition, implementing a purely imaginary transfer function leads to the band tilting of the real spectrum. Last, by increasing the nonlocal degree of freedom, the roton-like mechanical dispersion with tunable options between reiciprocity and nonreciprocity is numerically verified. The nonlocal metabeam could serve as a power platform for engineering different topological wave dispersions and investigating various types of wave dynamics under the framework of non-Hermitian system.

Chapter 5

ODD MASS DENSITY

5.1 Introduction

The non-Hermitian elastic systems made of active components for energetic interactions with the environment has opened new perspectives for active material design. Significant efforts have been made in expanding conventional continuum mechanics to accommodate systems exhibiting odd elasticity with broken energy conservation laws, where the stiffness tensor is asymmetric [134, 135, 142]. As has been pointed out in Chapter 4, a material displaying odd elasticity must violate Maxwell-Betti reciprocity. This intriguing feature has been experimentally demonstrated by introducing piezoelectric elements and motors controlled by electrical circuits into host media [132, 133, 138]. These non-Hermitian systems with odd elasticity can also exhibit non-Hermitian skin effect in both 1D and 2D. Additionally, they were designed to perform basic robotic manipulations such as steering motion and forces [143]. However, all the odd metamaterials and related unconventional wave control are concentrated on odd elasticity and their related topological wave propagation.

In this Chapter, the non-Hermitian wave phenomena that arise from an active solid with odd mass density is examined. The mass density tensor of this solid appears to be asymmetric/odd. An elastic metamaterial with inner resonators is equipped with piezoelectric elements mounted on supporting beams and controlled by electrical circuits to break reciprocity between the local acceleration and active forces along the two perpendicular directions. This approach enables asymmetric coupling between longitudinal and transverse motions in continuum solids. The odd mass density simultaneously breaks parity and Maxwell-Betti reciprocity. The active solid can perform energy phase transition between energy-unbroken and energy-broken phases separated by exceptional points, in analogy to the non-Hermitian $\mathcal{PT}$ symmetric systems with balanced gain and loss introduced in Chapter 2. A 1D nonreciprocal wave coupling where only transverse waves can be coupled into longitudinal ones

but not vice versa is experimentally observed. Additionally, mechanical wave amplification and the related non-Hermitian skin effect are also numerically demonstrated in 2D active solids. This work paves an alternative way to realize a new class of active solids and provides design guidelines for odd density behaviors in active solids.

5.2 Conceptualization of odd mass density

Odd mass density tensors for active metamaterials

The 2D mechanical metamaterial with inner resonators periodically distributed in the matrix has been intensively investigated in the past decades for generating sub-wavelength bandgaps and their unconventional wave control abilities in elastic solids [144, 145], as shown in Fig. 5.1(a). To understand the working mechanism, effective mass density properties of the metamaterial can be formulated by considering a mass-in-mass unit. For the passive 2D metamaterial; see Fig. 5.1(b), the equations of motions of the inner and outer masses can be easily obtained as

$$F_i + (u_i - U_i)\, k_i = M\ddot{U}_i, \tag{5.1}$$

$$(U_i - u_i)\, k_i = m\ddot{u}_i, \tag{5.2}$$

where F_i is the external force applied on the outer mass M in $\boldsymbol{x}_i$, U_i and u_i are displacements of the outer and inner masses along the $\boldsymbol{x}_i$ direction, respectively. Substituting Eq. (5.2) into Eq. (5.1) subjected to harmonic forces, we readily obtain

$$F_i = -\hat{M}_{ij} a^2 \omega^2 U_j, \tag{5.3}$$

where

$$\hat{M}_{ij} = \begin{bmatrix} \hat{M}_{11}(\omega) & 0 \\ 0 & \hat{M}_{22}(\omega) \end{bmatrix} \tag{5.4}$$

is the effective mass density tensor of the metamaterial with $\hat{M}_{11}(\omega) = \frac{M}{a^2} + \frac{k_1 m}{a^2(k_1 - \omega^2 m)}$ and $\hat{M}_{22}(\omega) = \frac{M}{a^2} + \frac{k_2 m}{a^2(k_2 - \omega^2 m)}$, and $A = a^2$ is the unit area. As noticed, for passive designs, the effective mass density tensor, $\hat{M}_{ij}$, is always symmetric, i.e. $\hat{M}_{12} = \hat{M}_{21}$, and the components, $\hat{M}_{11}$ and $\hat{M}_{22}$, can be positive or negative values depending on the operation frequency ω. For the unit with

symmetric mass density tensor, the total work done by the external force is equal to the change of kinetic energy of the mass, which means that the mass itself neither injects nor dissipates kinetic energy. The passive metamaterial is then a classical Hermitian system.

Consider now an active unit by installing a stretch sensor to k_2 and a force actuator on top of k_1, as shown in Fig. 5.1(c). The sensed stretch $u_2 - U_2$ is fed to the actuator using an active bond k_a. The active force generated by the active bond and applied on the outer mass along the $\boldsymbol{x}_1$ direction can be written as $F_a = (u_2 - U_2)k_a$. Note that k_a is not necessary to be a real number. Instead, it can be a complex number leading to phase difference between the stretch and the force F_a for harmonic motions. As a matter of fact, the active bond builds a new relationship between the stretch and the perpendicular force, which is absent in passive units. In addition, the active bond is nonlocal, given that the stretch and the force are not at the same location. As a result, the active bond induces no feedback stretch in k_2 for infinitesimal deformations. The effect of the active bond is hence feed-forward. By adding the active bond into equations of motion given in Eqs. (5.1) and (5.2), the effective mass density tensor of the active unit can be obtained as

$$\hat{M}_{ij} = \begin{bmatrix} \hat{M}_{11}(\omega) & \hat{M}_{12}(\omega) \\ 0 & \hat{M}_{22}(\omega) \end{bmatrix}, \tag{5.5}$$

where the off-diagonal term

$$\hat{M}_{12} = -\frac{k_a \omega^2 m^2}{a^2(k_1 - \omega^2 m)(k_2 - \omega^2 m)} \tag{5.6}$$

characterizes the relationship between the acceleration and the external force perpendicular to the acceleration. It can be easily seen that $\hat{M}_{12}$ is linearly controlled by the active bond k_a and regulated by the two resonance modes along the two perpendicular directions, as both the sensing and actuation are resonance-dependent.

Anisotropy and energy cycle

Interestingly, the effective mass density tensor of the active unit is asymmetric, $\hat{M}_{12} \neq \hat{M}_{21}$. In the design, the acceleration along the $\boldsymbol{x}_1$ direction does not induce an external force along the $\boldsymbol{x}_2$ direction, because no sensors along the $\boldsymbol{x}_1$ direction and no actuators along the $\boldsymbol{x}_2$ direction are placed, and the feedback from the active bond is absent. Consequently, $\hat{M}_{21} = 0$. It is useful to split $\hat{M}_{ij}$ into two tensors: a symmetric (even) mass density tensor, $\hat{M}^e_{ij}$, and an antisymmetric (odd)

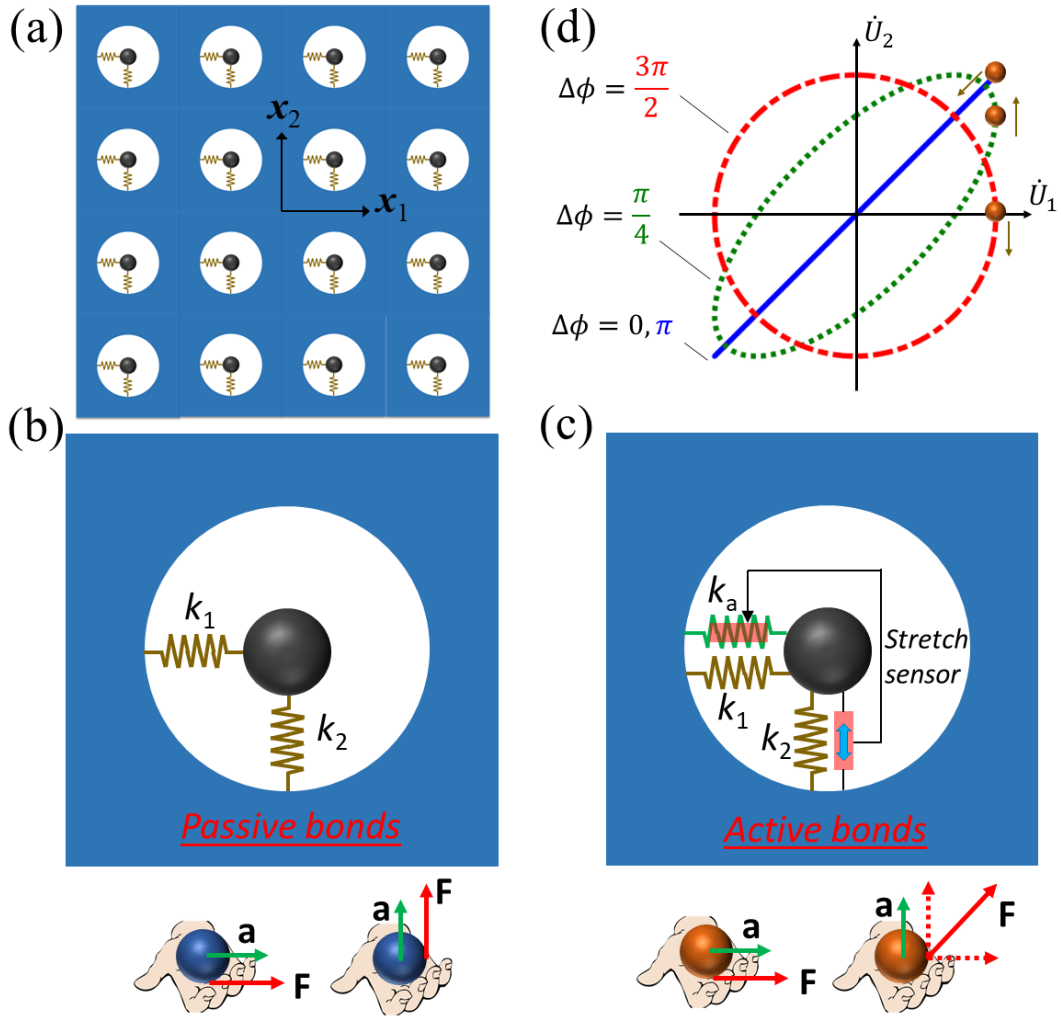

.

Figure 5.1: (a) 2D elastic metamaterial enabled by inner resonators with a lattice size a. (b) Passive unit cell that carries conventional mass supports symmetric force-acceleration relationship: the accelerations align always with the resulting forces. In the unit cell, the inner (black) and outer (blue frame) masses are denoted as m and M, respectively. The Hookean bonds have spring constants k_1 and k_2 in the $\boldsymbol{x}_1$ and $\boldsymbol{x}_2$ directions. (c) Active unit cell that carries odd mass comes with asymmetric force-acceleration relationship: orthogonal accelerations generates non-orthogonal forces, and the process is asymmetric. In addition to the Hookean k_1 and k_2, the unit cell conceptually consists of a stretch strain sensor which measures $u_2 - U_2$ in $\boldsymbol{x}_2$ and an active Hookean bond which generates an active force $F_a = (u_2 - U_2)k_a$ in $\boldsymbol{x}_1$. (d) Kinetic energy cycle of the odd mass with $\hat{M}_{12} \in \mathbb{R}$ and being positive. The particle indicates the velocity trajectory for each selected value of $\Delta\phi = \phi_1 - \phi_2$ from 0 to $2\pi/\omega$; see Eq. (5.8). Clockwise and counterclockwise trajectories of the particle encircle nonzero area on the map, indicate nonzero work done, and correspond to kinetic energy generated and lost, respectively.

mass density tensor, $\hat{M}^o_{ij}$,

$$\hat{M}_{ij} = \hat{M}^e_{ij} + \hat{M}^o_{ij} = \begin{bmatrix} \hat{M}_{11} & \hat{M}^e_{12} \\ \hat{M}^e_{21} & \hat{M}_{22} \end{bmatrix} + \begin{bmatrix} 0 & \hat{M}^o_{12} \\ -\hat{M}^o_{12} & 0 \end{bmatrix}, \tag{5.7}$$

where $\hat{M}^e_{12} = \hat{M}^o_{12} = \hat{M}_{12}/2$. The even part of the mass density tensor, $\hat{M}^e_{12}$, modulates anisotropy of the effective mass density tensor in the active metamaterial. This can be understood by finding principal effective mass densities of $\hat{M}^e_{ij}$ along principal directions through rotational coordinate transformations. Thus, $\hat{M}^e_{12}$ is a parameter contributing to mass anisotropy of the active metamaterial.

The odd part of the mass density tensor, $\hat{M}^o_{12}$, demands a force always perpendicular to the acceleration. This is a direct consequence of the active bond that, under some conditions, can inject or dissipate energy into or from the active metamaterial. To see this characteristics, we assume $\hat{M}^o_{12} \in \mathbb{R}$, $\dot{U}_1 = \bar{V}_1 \sin(\omega t + \phi_1)$, and $\dot{U}_2 = \bar{V}_2 \sin(\omega t + \phi_2)$. The work done by the external force in one cycle of oscillations reads

$$W_F = \int_0^{2\pi/\omega} \hat{M}^o_{ij} \ddot{U}_i \dot{U}_j \mathrm{d}t = -2\pi \hat{M}^o_{12} \bar{V}_1 \bar{V}_2 \sin(\phi_1 - \phi_2). \tag{5.8}$$

On the other hand, the induced kinetic energy due to $\hat{M}^o_{ij}$ is always zero. Balance of energy then requires $W_F + W_I = 0$, where W_I is the internal energy gain or loss caused by the active bond. In particular, when $\dot{U}_1$ and $\dot{U}_2$ are in-phase or out-of-phase, $W_F = W_I = 0$ and the active bond is in a silence mode without energy exchange. The effect of the active bond is only seen in the symmetric part of the mass, $\hat{M}^e_{ij}$. Other than these two specific cases, the active bond will do positive or negative work. When $W_F > 0$, the active bond will absorb energy from the active metamaterial. On the other hand, when $W_F < 0$, the active bond will pump energy into the active metamaterial. The total energy absorbed or pumped is proportional to $\hat{M}^o_{12} \bar{V}_1 \bar{V}_2$ and in a sine relationship with the phase difference $\Delta\phi = \phi_1 - \phi_2$ between $\dot{U}_1$ and $\dot{U}_2$ [Fig. 5.1(d)]. Note that the energy transfer can happen under specific conditions, such that phase transitions and exceptional points are foreseen. In this sense, the active metamaterial now becomes a classical Non-Hermitian system with energy loss and gain.

5.3 Physical realization and 1D nonreciprocal wave coupling

Physical realization

To realize odd mass density tensors, we propose a design of an active elastic metamaterial with inner resonators by cutting slots from a single-phase plate to form horizontal and vertical beams, which connect the central block and its outer surrounding matrix [see the blue region in Fig. 5.2(a)]. The central block functions as the inner mass, and the beams serve as the springs along the $\boldsymbol{x}_1$ and $\boldsymbol{x}_2$ directions. Two piezoelectric patches are bonded on the horizontal beams as stretch sensors, and the sensing signal is fed into a transfer function H that sends to two piezoelectric patches bonded on the vertical beams as actuators [Fig. 5.2(a)]. When the central block moves vertically, one sensing piezoelectric patch is under tension (or compression), and the other is under compression (or tension) [Fig. 5.2(b)]. The total sensing signal is then obtained from the two opposite charges Q_s from the sensing patches. The transfer function $H(\omega)$ processes the sensing voltage and sends output signals V_a to the two actuating patches, with $V_a = HQ_s/C_0$, where C_0 is the reference capacitance. The two actuating patches with opposite polarization bend the two vertical beams to produce horizontal forces applied on the central block and the surrounding material, $F_a \propto V_a$ [Fig. 5.2(c)]. However, when the central block moves horizontally, all the vertical beams are bent and horizontal beams remain straight, as horizontal beams are much stiffer in response to horizontal motions. As a result, the two sensing patches do not sense the motion and the electronic loop will not produce any output voltages. Therefore, the electromechanical control loop is entirely feed-forward: vertical motion induces horizontal forces, while horizontal motion does not induce vertical forces.

The design is validated first by performing numerical simulations to calculate the effective mass density tensor of the active metamaterial using COMSOL Multiphysics [Fig. 5.2(d)]. In the simulations, we prescribe an acceleration, $\bar{a}_i$, on the boundaries of the unit cell and calculate the total reactor forces, $\bar{F}_i$. The effective mass density tensor is attained based on Eq. (5.3); see also Appendix F. In the design, $H = 1$, $C_0 = 2$ nF, and the lengths of horizontal and vertical beams facing the central block are different, leading to different resonance frequencies of the horizontal and vertical modes. As shown in Fig. 5.2(d), the resonance behavior of $\hat{M}_{11}$ and $\hat{M}_{22}$ agrees well with that predicted by Eq. (5.4). Further, $\hat{M}_{12}$ is nonzero and displays a double resonance behavior and $\hat{M}_{21}$ indeed vanishes. Therefore, the effective mass density tensor is asymmetric. The detailed design parameters are provided in Fig. 5.3(a). The design can be employed in further experimental and numerical studies to exploit other profound properties of the odd mass density. Additionally, the

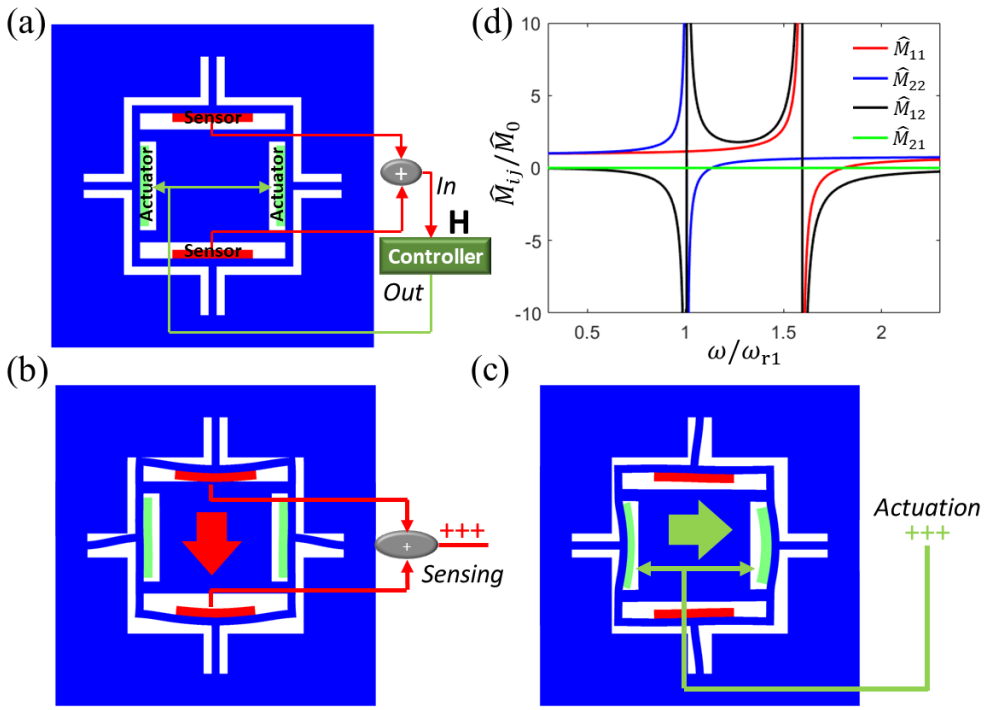

Figure 5.2: Active unit cell design for odd mass density. (a) The metamaterial unit cell, which exhibits odd mass, consists of a structured steel frame and four PZT patches (PZT-5A) with two of them being stretch sensors and the other being actuators. The asymmetric actuation is achieved by a programmable controller which connects the sensors and actuators and is characterized by a transfer function H. (b, c) The schematic illustration of deformation distribution reveals how the two orthogonal motions are coupled in an asymmetric way: The sensors sense the vertical deformation and feed the sensing voltage processed by the controller to the actuators for horizontal actuation. While the reverse is forbidden owing to the absence of a horizontal sensor. (d) Numerically obtained effective mass density tensor $\hat{M}_{ij}$, normalized with $\hat{M}_0 = \hat{M}_{11}(\omega = 0.3\omega_{r1})$. The frequency is normalized with the first resonance frequency $\omega_{r1} = 2\pi \times 10.81$ kHz. The evaluated mass densities are normalized with $\hat{M}_0 = \hat{M}_{11}(\omega/\omega_{r1} = 0.3)$

parametric study shown in Figs. 5.3(b) and 5.3(c) indicate that the magnitude and phase of the odd mass $\hat{M}_{12}$ linearly scale with those of the transfer function H, suggesting the linearity of the odd mass metamaterial.

Experiments

We fabricate a unit of the active metamaterial on a steel beam to test its wave transmission properties [Fig. 5.4(a)]. We also leverage it as a way to show the existence of asymmetric/odd mass density tensors. Details about the fabrication and circuit design as well as implementation are similar to those used in the realization of nonlocal metabeam (see Chapter 4) and can be found in Appendix G. In the study, we focus on two fundamental modes supported by the beam structures: longitudinal modes

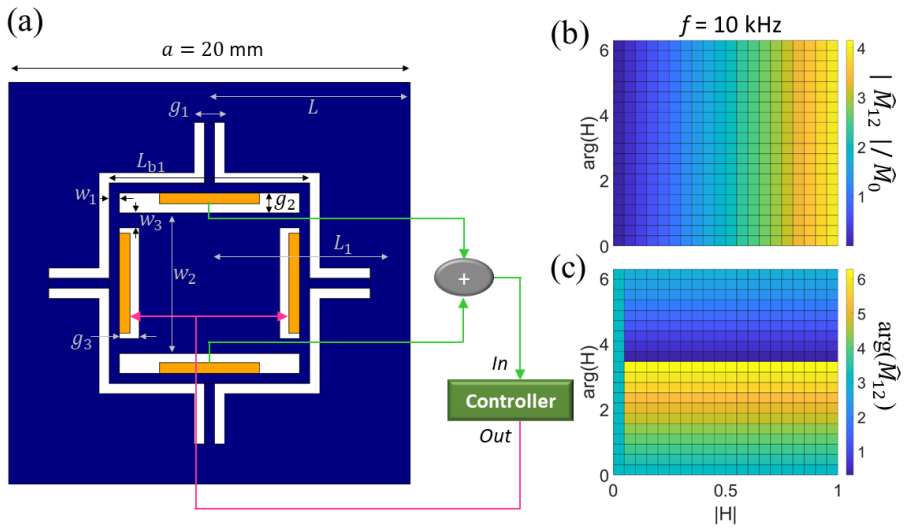

Figure 5.3: (a) Design of the unit cell for 1D nonreciprocal wave coupling. The dimensions are $L = a/2 = 10$ mm, $L_1 = 9$ mm, $L_{b1} = 10$ mm, $w_1 = 0.5$ mm, $w_2 = 7$ mm, $w_3 = 0.75$ mm, $g_1 = 1.5$ mm, and $g_2 = g_3 = 1$ mm. The four piezoelectric patches (PZT-5A, 5 mm $\times$ 0.55 mm $\times$0.55 mm) are highlighted in blue. (b) Dependence of the normalized magnitude $|\hat{M}_{12}|/\hat{M}_0$ on $\arg(H)$ and $|H|$, where ρ_0 denotes the static principal mass density. (c) Dependence of the phase $\arg(\hat{M}_{12})$ on $\arg(H)$ and $|H|$. The results are considered at 10 kHz.

dominated by the velocity component $\dot{u}$ and transverse modes dominated by the velocity component $\dot{v}$. When the beam is symmetric about the neutral axis, the two modes are decoupled. Introducing geometric asymmetry can make the two modes coupled, and the wave mode conversion has been observed in various passive designs [146, 147]. However, wave mode interactions demonstrated so far have always been reciprocal, namely, longitudinal modes can be converted into transverse modes either partially or totally; transverse modes can also be converted back into longitudinal modes in a similar manner.

The wave mode conversion embraced by the odd mass can no longer be reciprocal. To illustrate this behavior, sensing patches are aligned along the $\boldsymbol{x}_1$ direction and actuating patches along the $\boldsymbol{x}_2$ direction; see Fig. 5.4(a). Since only transverse motions can be sensed in this case, which in turn generates longitudinal forces thanks to the active bond, transverse waves induce longitudinal waves when passing through the active metamaterial. The wave signals of $\dot{v}$ and $\dot{u}$ shown in Figs. 5.4(b) and 5.4(c) demonstrate this behavior, where transmitted waves from the active metamaterial have both v and u components with the transverse incidence, and v remains the same regardless of the controller being switched on or off. The experimental results yield satisfactory agreement with numerical simulations, as can be seen from Fig. 5.5 where the transfer matrix method is used for analytically predicting the transmission behaviors; also see Appendix H. The corresponding experimentally

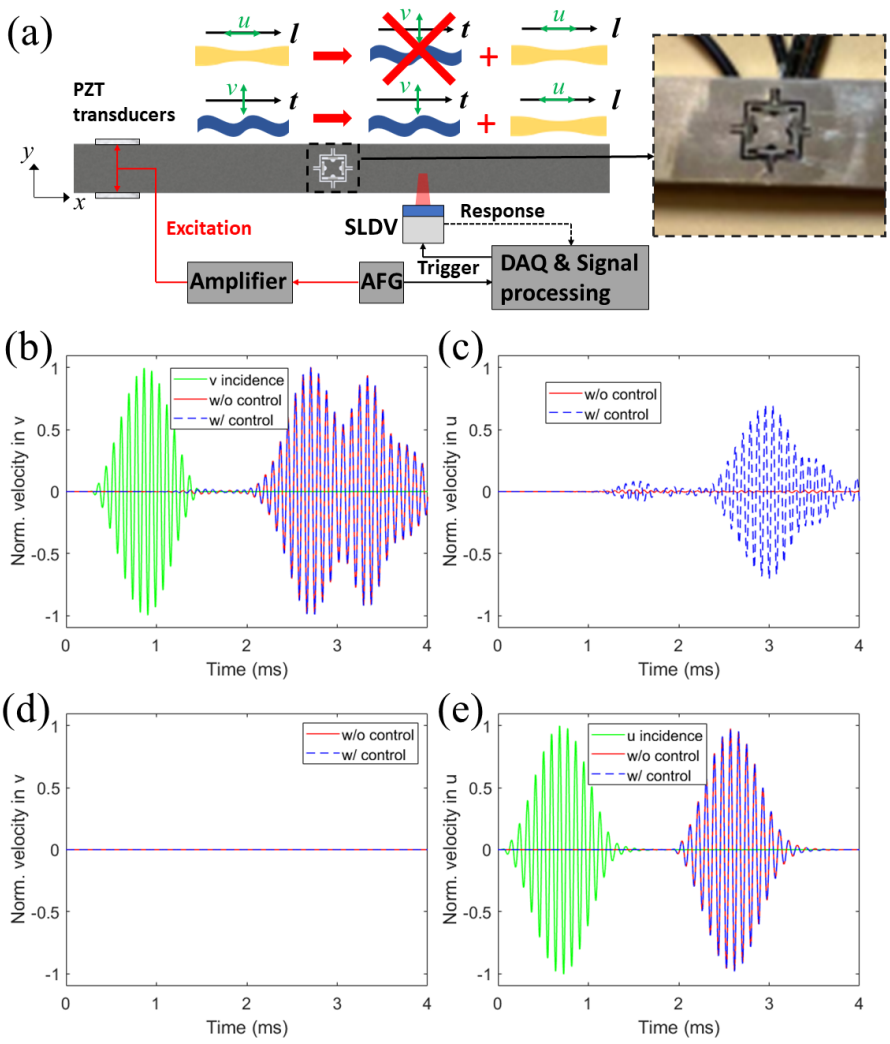

Figure 5.4: Experimental demonstration of 1D nonreciprocal wave coupling enabled by odd mass. (a) Schematic of the experimental test bed that includes an active metamaterial with odd mass on a steel host beam. Transverse (t) incidence generates both transverse (t) and longitudinal (l) transmission, whereas the reverse is forbidden. The green arrows define the wave polarization u and v. The inset displays a photo of the metamaterial functional unit. In the experiment, the incidence from the left is excited by two symmetrically placed PZT-5A patches connected to an voltage amplifier and arbitrary function generator (AFG). The measurement and post-processing are implemented by a commercial laser vibrometer system (PSV-400). (b,c) Measured normalized transient velocities (b) $\dot{v}$ and (c) $\dot{u}$ at the output under a transverse incidence when the active control is OFF (red solid) and ON (blue dashed). (d,e) Numerical normalized transient velocities (d) $\dot{v}$ and (e) $\dot{u}$ at the output under a longitudinal incidence when the active control is OFF (red solid) and ON (blue dashed). The excitation in both cases is a 15-cycle tone burst centered at 11.3 kHz. All measured data are normalized with the maximums of their own incidence (green).

measured transient field distributions are displayed in Fig. 5.6 as well for a better demonstration. On the other hand, no transverse wave components can be observed from a longitudinal incidence, as shown in Figs. 5.4(d), 5.4(e) and 5.5. Similarly, if one rotates the active metamaterial by 90°, longitudinal waves induce transverse waves, but not the reverse. Further, the transmitted and reflected signals measured from experiments can be employed to retrieve the effective mass tensors of the active metamaterial, where we can assume the unit embedded in the beam as a point scatterer.

5.4 2D unconventional wave manipulation enabled by odd mass density

Wave propagation in 2D elastic medium with odd mass density tensors

To further explore the nonstandard dynamics supported by odd mass density tensors, we study wave propagation in a 2D active metamaterial. Note that, in the subsequent examples, we consider the cases of $\hat{M}^o_{12} \in \mathbb{R}$. To facilitate the analysis, it is useful to rewrite the asymmetric mass density tensor along principal directions of the symmetric mass density tensor. The transformed mass density tensor reads (Appendix I)

$$\tilde{M}_{ij} = \begin{bmatrix} \tilde{M}_{11} & \tilde{M}_{12} \\ -\tilde{M}_{12} & \tilde{M}_{22} \end{bmatrix}, \tag{5.9}$$

where $\tilde{M}_{ij} = \hat{M}_{kl}\tilde{\beta}_{ki}\tilde{\beta}_{lj}$, and $\tilde{\beta}_{ki}$ is the rotation matrix from x_i to $\tilde{x}_i$ with $\tilde{x}_i$ being the principal axis of $\hat{M}^e_{ij}$. At continuum limit, equilibrium equations can be written in $\tilde{x}_i$ as

$$(\lambda + \mu)\,\tilde{u}_{j,ji} + \mu\tilde{u}_{i,jj} = -\omega^2\tilde{M}_{ij}\tilde{u}_j, \tag{5.10}$$

where $\tilde{u}_i$, λ, and μ denote the transformed displacement, first, and second Lamé's constants, respectively. We assume harmonic wave solutions $\tilde{u}_\alpha = \tilde{U}_\alpha e^{i(\tilde{q}_\beta \tilde{x}_\beta - \omega t)}$ for Eq. (5.10), where $\tilde{q}_\beta = q\tilde{r}_\beta$. q and $\tilde{r}_\beta$ are the wave number and direction cosine $\cos\tilde{\theta}_\beta$ where $\tilde{\theta}_\beta$ is the angle between the principal directional and $\boldsymbol{x}_\beta$. Dispersion relations indicated by Eq. (5.10) then read

$$q^2 = \omega^2 \frac{I_1 \pm \sqrt{I_1^2 - 4I_2\left(\tilde{M}_{11}\tilde{M}_{22} + \tilde{M}_{12}^2\right)}}{2I_2}, \tag{5.11}$$

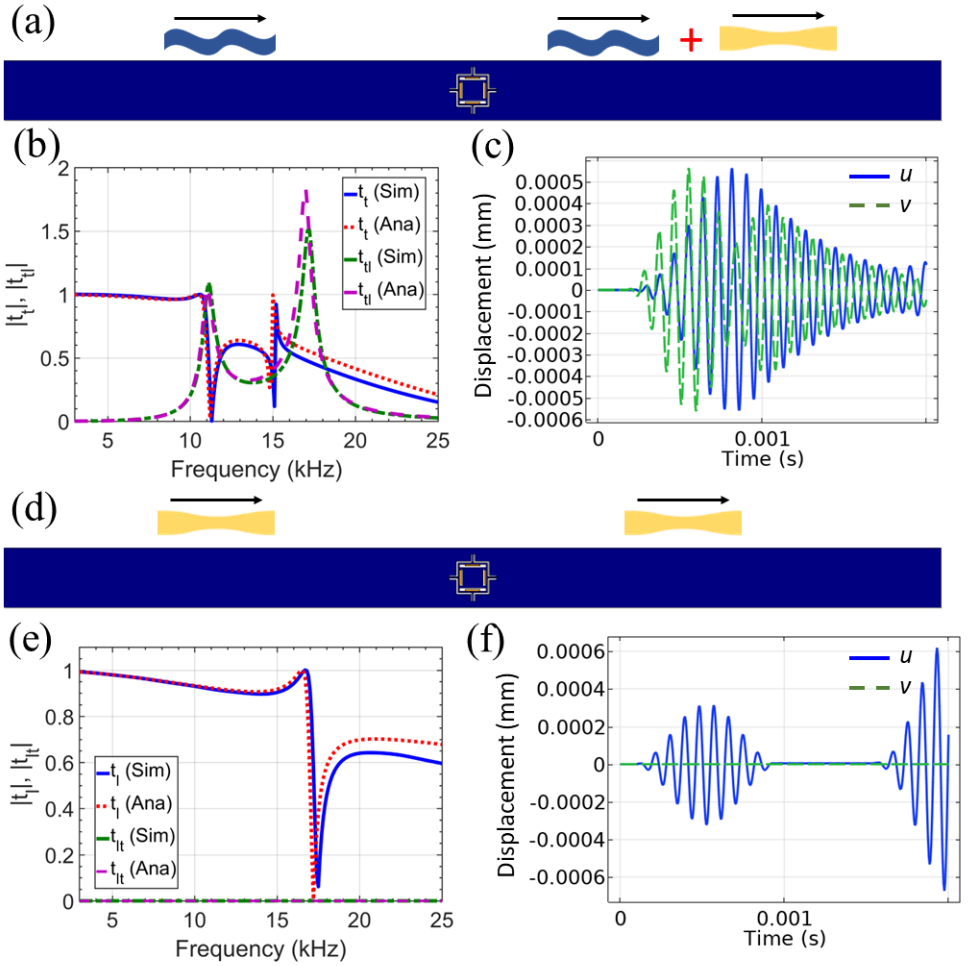

Figure 5.5: 1D nonreciprocal wave coupling. (a) Schematic of the transverse incidence. (b) Analytical and numerical comparison for both transmissions. (c) Transient analysis results for the output displacements u and v for longitudinal and transverse modes, respectively. (d) Schematic of the longitudinal incidence. (e) Analytical and numerical comparison for both transmissions. (f) Transient analysis results for the output displacements u and v for longitudinal and transverse modes, respectively.

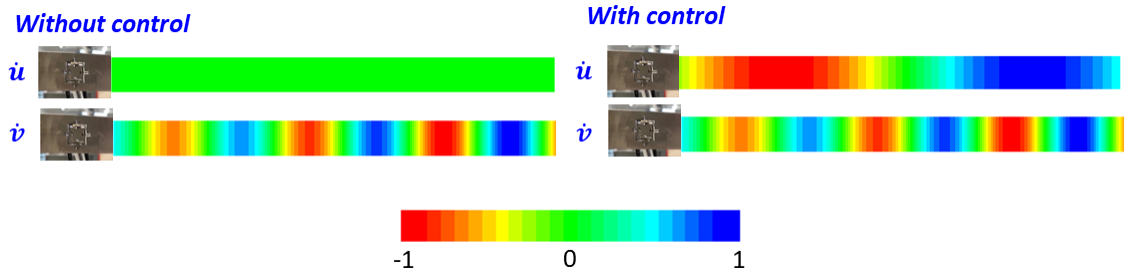

Figure 5.6: Experimentally measured normalized velocity field distributions for 1D nonreciprocal wave coupling. The output velocities $\dot{u}$ and $\dot{v}$ for longitudinal and transverse modes are displayed without and with the active control.

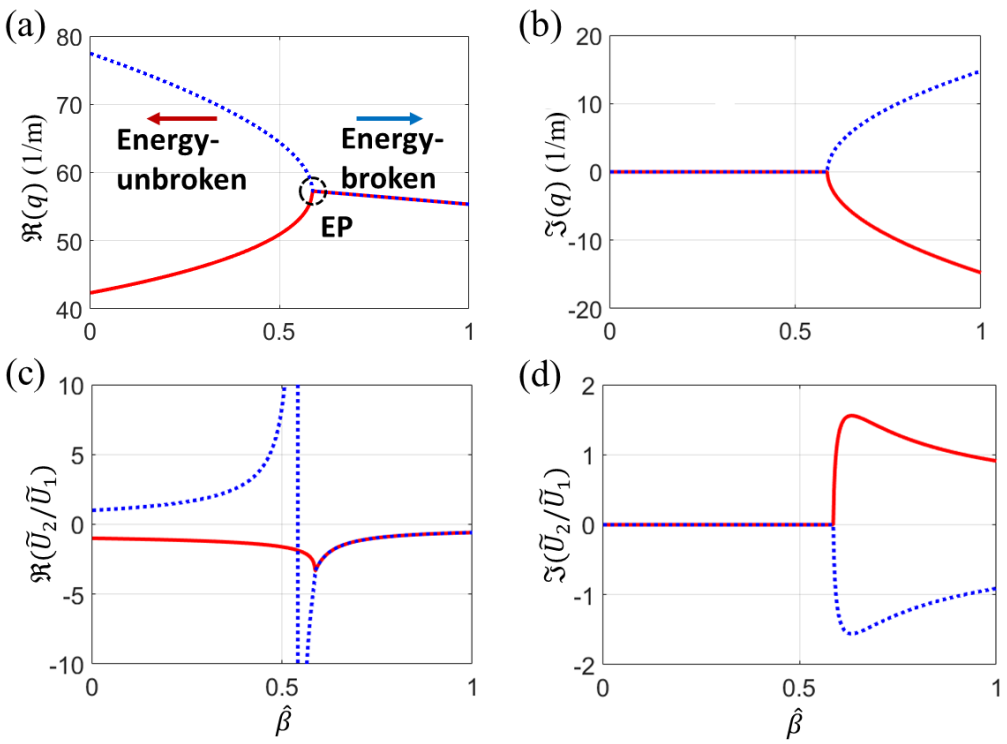

Figure 5.7: Energy phase transition at $\theta_1 = 0$ by tuning $\hat{\beta}$. (a) Real and (b) imaginary parts of wave numbers q in function of $\hat{\beta}$. The EP is indicated, together with the energy-unbroken and energy-broken phases. (c) Real and (d) imaginary parts of $\tilde{U}_2/\tilde{U}_1$ of eigenvectors in function of $\hat{\beta}$.

where $I_1 = D_{22}\tilde{M}_{11} + D_{11}\tilde{M}_{22}$, $I_2 = D_{11}D_{22} - D_{12}^2$, and $D_{11} = (\lambda + 2\mu)\, r_1^2 + \mu r_2^2$, $D_{22} = (\lambda + 2\mu)\, r_2^2 + \mu r_1^2$, $D_{12} = (\lambda + \mu)\, r_1 r_2$. $r_1 = \arccos\theta_1$ and $r_2 = \arccos\theta_2$ are the direction cosines with respect to $\tilde{\boldsymbol{x}}_1$ and $\tilde{\boldsymbol{x}}_2$ after the transformation. Clearly, given a real ω, there always exists two independent modes, characterized by the two solutions of q^2. Note that the odd mass density of the active metamaterial, $\hat{M}_{12}$, is involved in three terms in Eq. (5.11), $\tilde{M}_{11}$ and $\tilde{M}_{22}$ as well as $\tilde{M}_{12}$ to collectively control wave propagation along different directions.

The most striking characteristics of Eq. (5.11) is the emergence of the term $\tilde{M}_{12}^2$ related to q^2, and q^2 need not be always greater than zero. For example, when $I_1^2 < 4I_2\left(\tilde{M}_{11}\tilde{M}_{22} + \tilde{M}_{12}^2\right)$, q becomes a complex number, indicating energy gain or loss when waves travel along certain directions. The fact of q evolution from originally a real number to a complex number underpins a phase transition governed by the odd mass density. To see the phase transition in more details, we consider wave propagation along one of the principal directions, in which the effective mass density is smallest. For simplicity, we assume $\hat{M}_{11} = \hat{M}_{22}$, and $\tilde{x}_i$ is obtained by rotating x_i by $\pi/4$. Figures 5.7(a) and 5.7(b) show the real and imaginary parts of the two q with different odd mass densities. Figures 5.7(c) and 5.7(d) show the real and imaginary parts of the corresponding eigenvectors (polarization states of quasi-pressure

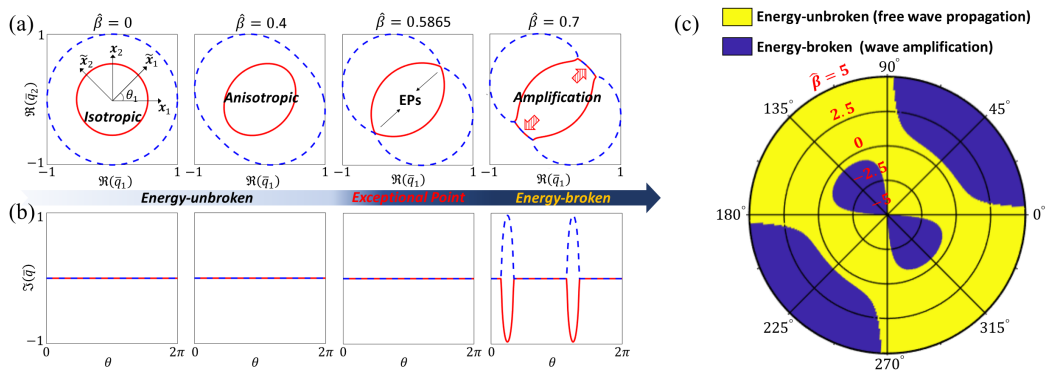

Figure 5.8: Energy phase transition. (a) Iso-frequency contours $\Re(\bar{q}_1)$ and $\Re(\bar{q}_2)$ for both propagating modes when the system operates in energy-unbroken phases (isotropic with $\hat{\beta} = 0$ and anisotropic with $\hat{\beta} = 0.4$), at exceptional point ($\hat{\beta} = 0.5865$), and in energy-broken phase ($\hat{\beta} = 0.7$). $\bar{q}$ is the wave number normalized with the maximum in each case. Principal directions $\tilde{\boldsymbol{x}}_1$ and $\tilde{\boldsymbol{x}}_2$ are illustrated by rotating $\boldsymbol{x}_1$ and $\boldsymbol{x}_2$ by $\tilde{\theta}_1$. Here, $\tilde{\theta}_1 = \pi/4$. (b) θ dependence of the imaginary components of wave numbers, $\Im(\bar{q}_1)$ and $\Im(\bar{q}_2)$, for both modes correspondingly in the four representative phases mentioned in (a). In both (a) and (b), we select $\lambda = 37.4$ GPa, $\mu = 27$ GPa, and $\hat{M}_{11} = \hat{M}_{22} = 16277$ kg/m^3. Here, the blue and red modes correspond to those given in Fig. 5.7. (c) The energy phase diagram in the space of θ in black (azimuthal) and $\hat{\beta}$ in red (radial). The yellow region is the energy-unbroken phase and supports free wave propagation. While the dark blue regions are energy-broken phase where wave amplification occurs.

and quasi-shear modes). In the figures, we define $\hat{\beta} = \hat{M}_{12}/\hat{M}_{11}$. For zero or small $\hat{\beta}$ leading to $I_1^2 > 4I_2\left(\tilde{M}_{11}\tilde{M}_{22} + \tilde{M}_{12}^2\right)$, there exists two different real q, and the corresponding eigenvectors are both real. $\hat{M}_{12}$ only induces anisotropy, which, however, is different from passive anisotropic mass densities, where eigenvectors of different modes are orthogonal. For the active metamaterials presented here, the presence of $\tilde{M}_{12}$ makes eigenvectors of different modes no longer orthogonal. Since the system in this phase region is energy conserved, we say this phase is an energy-unbroken phase. Further, by increasing $\hat{\beta}$ such that $I_1^2 = 4I_2\left(\tilde{M}_{11}\tilde{M}_{22} + \tilde{M}_{12}^2\right)$, the two q and their associated eigenvectors coalesce, forming an EP. Further increasing $\hat{\beta}$ to make $I_1^2 < 4I_2\left(\tilde{M}_{11}\tilde{M}_{22} + \tilde{M}_{12}^2\right)$, the two q appear in a complex conjugate pair, and wave propagation accompanied with energy gain (blue mode) and loss (red mode) can be anticipated in this phase region. Thus, we say this phase is an energy-broken phase. In addition to the complex q, the eigenvectors are also complex, coinciding with the work done condition designated by Eq. (5.8).

Next, we examine the phase transition along different directions. Figure 5.8(a) shows the iso-frequency curves for the real part of the wave numbers, $\Re(q)$, with different odd mass densities. Figure 5.8(b) shows the imaginary part of the wave numbers, $\Im(q)$, along different directions θ. Note that θ represents the direction angle with respect to $\boldsymbol{x}_1$ before transformation. In the figures, we select $\hat{\beta} = 0$, 0.4, 0.5865 and 0.7. When $\hat{\beta} = 0$, the active metamaterial is reduced to a passive one

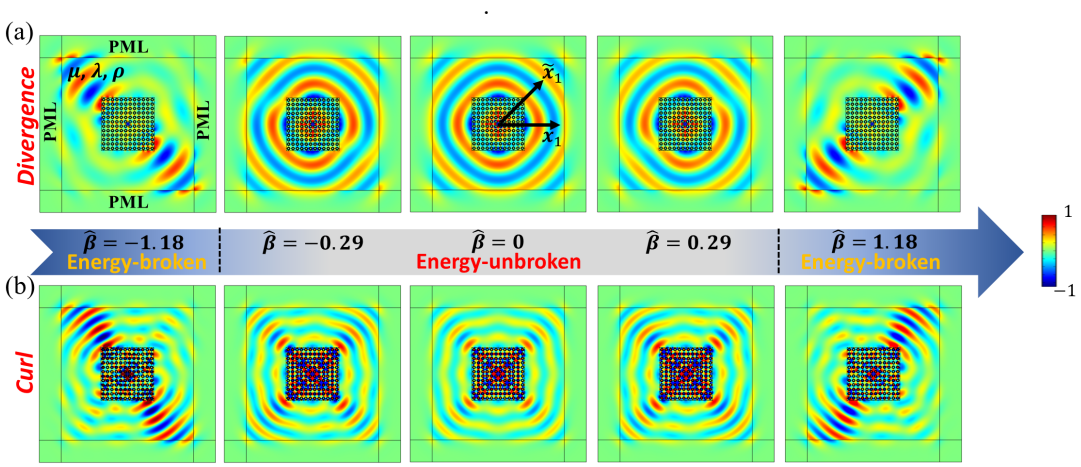

Figure 5.9: Demonstration of energy phase transition and directional wave amplification. (a) Numerically evaluated divergence fields of displacement at 16 kHz for various $\hat{\beta}$ under a pressure loading. (b) Numerically evaluated curl fields of displacement at 16 kHz for various $\hat{\beta}$ under a shear loading. In both figures, $\hat{\beta} = 0$ (energy-unbroken isotropic), $\hat{\beta} = \pm 0.29$ (energy-unbroken anisotropic), and $\hat{\beta} = \pm 1.18$ (energy-broken) are achieved with the transfer functions $H = 0$, $H = \pm 0.2$, and $H = \pm 1$, respectively. The 2D odd mass region, composed of 12×12 unit cell and possessing odd mass density, is embedded in a normal isotropic background ($\rho = 16277$ kg/m^3, $\mu = 27.4$ GPa, $\lambda = 37$ GPa) surrounded with perfect matched layers (PMLs). The point sources for the pressure and shear excitation are realized by setting normal and tangential boundary loads, respectively. The fields obtained from simulations are all normalized with their own maximums. The principal direction $\boldsymbol{x}_1$ is indicated.

with isotropic mass densities, where waves travel equally to different directions. In Fig. 5.8(a), blue dashed and red solid curves represent pressure and shear wave modes, respectively. When $\hat{\beta} = 0.4$, no gain and loss can be found along any directions, the active metamaterial is in the energy-unbroken phase. Due to anisotropy, waves propagate at different phase velocities along different directions. In particular, along the principal directions of $\pi/4$, quasi-pressure waves travel at the higher phase velocities, while quasi-shear waves travel at the lower phase velocities. Similar conclusions can be attained along the directions of $3\pi/4$, where the principal mass density along this principal direction is largest. When $\hat{\beta} = 0.5865$, two exceptional points are formed along the principal direction with the smallest principal mass density, namely the directions of $\pi/4$ and $5\pi/4$. Further increasing $\hat{\beta}$ to 0.7, the active metamaterial enters the energy-broken phase around these directions. As expected, $\Im(q)$ becomes nonzero, and waves are attenuated and amplified along those directions. In addition, four exceptional points are formed at the boundaries of those directions. Note also that, for all the cases, the wave behavior obeys mirror symmetry with respect to the principal axes of the even mass density tensor. This is the direct consequence of the q^2 term in Eq. (5.11). The conclusion that the exceptional points (wave attenuation and amplification) are first observed along the principal

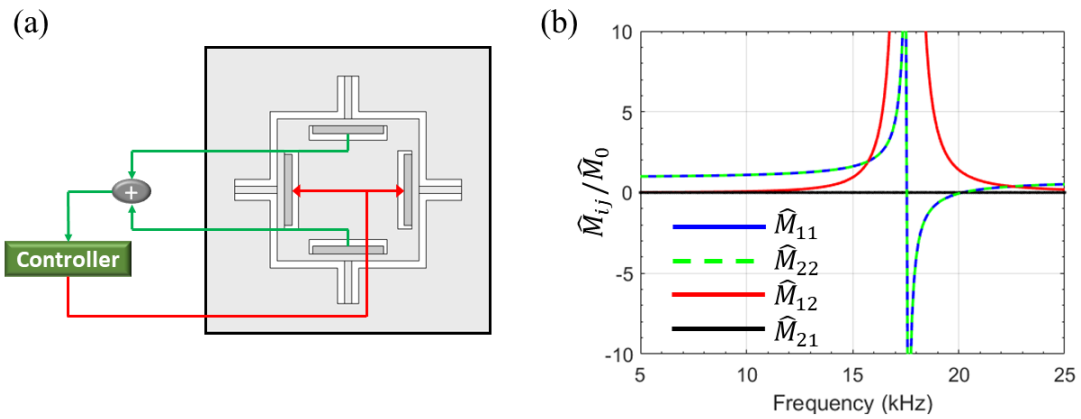

Figure 5.10: (a) Design of the unit cell for the investigation of the energy phase transition and 2D wave manipulation. (b) Numerically determined entries of the effective mass density tensor $\hat{M}_{ij}$.

direction with the smallest principal mass density still holds when $\hat{M}_{11} \neq \hat{M}_{22}$. The launch pattern of the exceptional points in the active solid provides a tool to tailor the wave amplification direction using $\hat{M}_{11}$ and $\hat{M}_{22}$ through designing passive metamaterial structures and a numerical demonstration will be given in the following.

To further examine the energy phase transition and directional wave amplification, harmonic wave propagation in a 2D active medium is conducted by applying cylindrical wave excitation via a point source in COMSOL Multiphysics, as shown in Fig. 5.9. For simplicity, the active unit is given in Fig. 5.10(a) and preserves C4 structure symmetry to ensure $\hat{M}_{11} = \hat{M}_{22}$. The effective odd mass density tensor shown in in Fig. 5.10(b) is determined using Eq. (5.3). To determine the effective stiffness tensor $\mathbf{C}$, the retrieval process requires specific boundary conditions [148–150]; see Appendix F. Here, the transfer function is selected as $H = 1$, and only one resonance is visible across the frequency range, simply due to that the C4 symmetry of the unit cell yields $\hat{M}_{11} = \hat{M}_{22}$. Also, $\hat{M}_{12}$ is nonzero everywhere and reaches maximum at the resonance, whereas $\hat{M}_{21}$ remains nearly vanishing across the considered range, achieving the odd mass density. Meanwhile, the metamaterial admits an orthotropic stiffness tensor and is governed by the Hooke's law stating $\sigma_{ij} = C_{ijkl}\epsilon_{kl}$ where ϵ_{kl} is the displacement gradient. The stiffness constants are found numerically to be $C_{1111} = C_{2222} = 88.13$ GPa, $C_{1122} = C_{2211} = 27.61$ GPa, $C_{1212} = C_{2121} = 26.67$ GPa, and $C_{1221} = C_{2112} = 26.32$ GPa in Voigt notation at 16 kHz using the mentioned homogenization method [148, 149]. Interestingly, the odd mass causes some minor stress asymmetry, possibly due to the existence of the asymmetric control [147, 151]. The couplings between the normal and shear components are five-order smaller and hence are ignored. To suppress reflected waves from the finite boundaries, the active solid is embedded in a homogenized medium with almost the same effective stiffness tensor attached to the perfectly

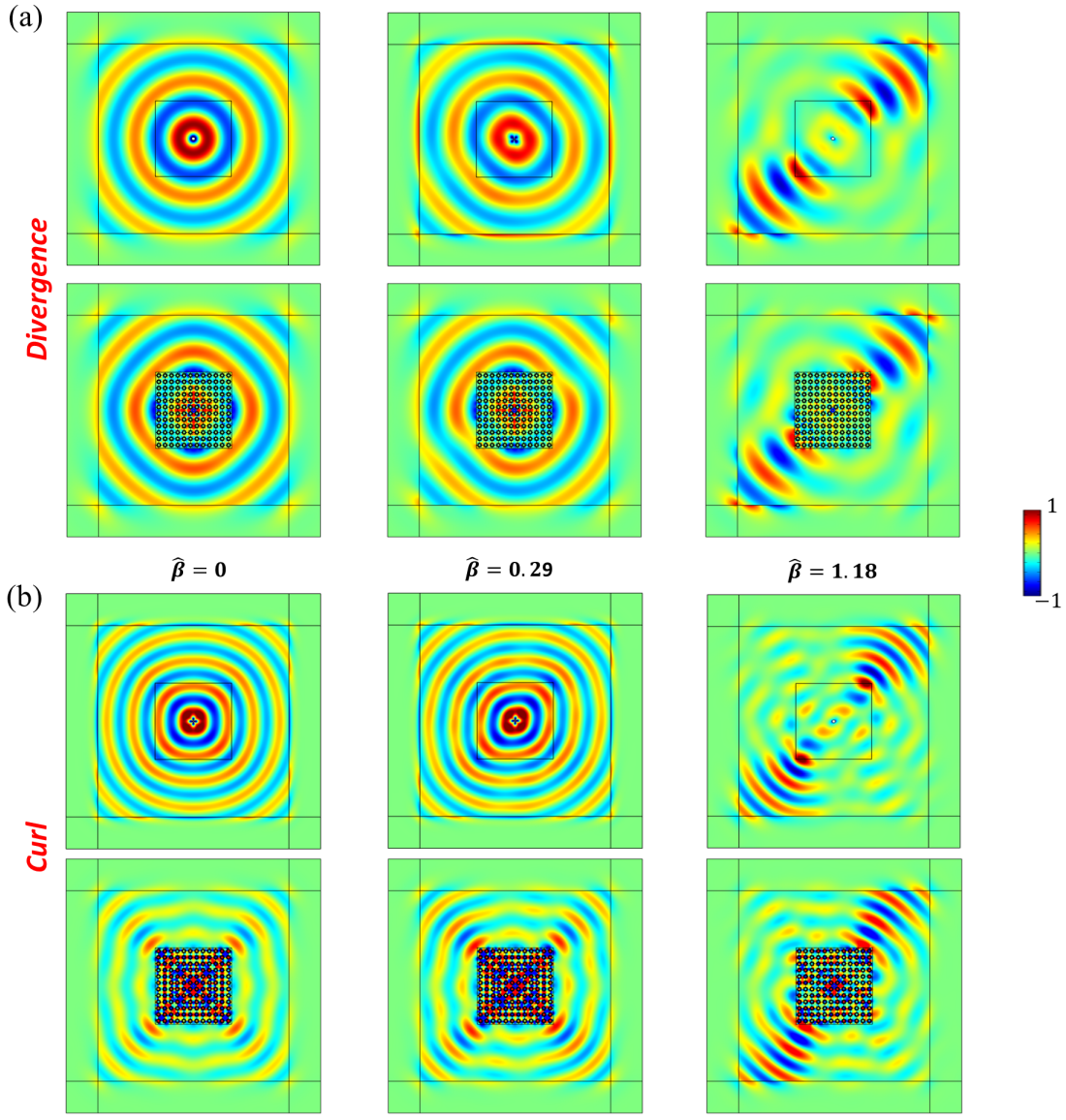

Figure 5.11: Comparison between actual structures and homogenized media. (a) Numerically evaluated divergence fields of displacement at 16 kHz for various $\hat{\beta}$ under a pressure loading. (b) Numerically evaluated curl fields of displacement at 16 kHz for various $\hat{\beta}$ under a shear loading. In both (a) and (b), the top panels show the field distributions of the homogenized media, whereas the bottom panels illustrate the corresponding actual structures. The field distributions are normalized with their own maximums.

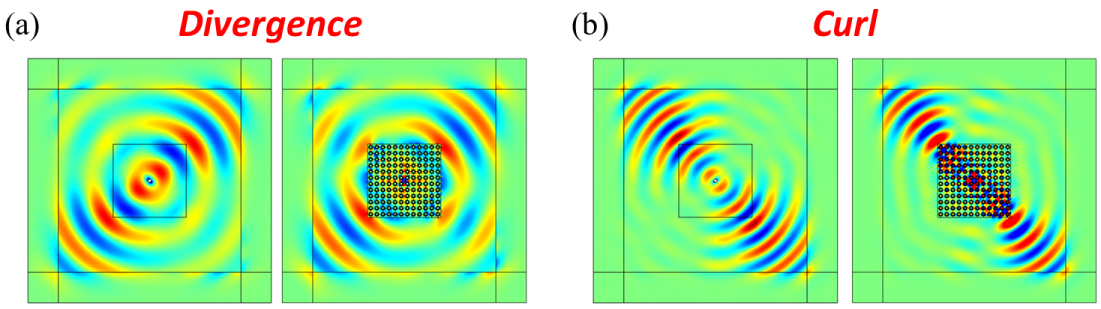

Figure 5.12: Comparison between actual structures and homogenized media for $H = i$ ($\hat{\beta} = 1.18i$). (a, b) Numerically evaluated (a) divergence and (b) curl fields of displacement at 16 kHz for $\hat{\beta} = 1.18i$ under a pressure and shear loading, respectively. The field distributions are normalized with their own maximums.

matched layers (PMLs). From Figs. 5.9(a) and 5.9(b) showing both the divergence and curl of the displacement fields, it can be concluded that the active solid can operate from the energy-unbroken phase to the energy broken phase through the exceptional points by increasing or decreasing $\hat{\beta}$ from $\hat{\beta} = 0$ (energy conservation). The wave propagation behavior becomes more anisotropic with the increase or decrease of the $\hat{\beta}$ in the energy-unbroken phase. It also indicates strong directional wave amplification when $\hat{\beta} = 1.18$ at which the system operates in the energy-unbroken phase. The directions of the wave amplification indeed coincide with the principal directions of the mass density tensors, which are $\theta_1 = \frac{\pi}{4}/\frac{3\pi}{4}$ and $\frac{5\pi}{4}/\frac{7\pi}{4}$ for $\hat{\beta} = 1.18/-1.18$. Note that minor unexpected scattering at the corners is found in the curl fields for the energy-unbroken phase; see Fig. 5.9(b). This is due to the unit cell size being comparable to the operating wavelength, thereby weakening the long-wavelength assumption to some extent. To validate the simulation and related wave phenomena, comparison of the wave field distributions obtained from both effective medium and real structures at all $\hat{\beta}$ is conducted and shown in Fig. 5.11, and very good agreement is observed.

It is also interesting to point out that the wave amplification along the principal directions still holds when the transfer function is an purely imaginary number, say $H = i$, equivalent to $\hat{\beta} = 1.18i$; see Fig. 5.12. In comparison with the cases of real $\hat{\beta}$, here the wave amplification direction for one of the two modes shifts to the other principal direction by $\pi/2$. It should also be mentioned that the active solid with purely imaginary $\hat{\beta}$ always operates in the energy-broken phase without energy phase transition behavior.

Anisotropic mass densities, namely $\hat{M}_{11} \neq \hat{M}_{22}$, provides another degree of freedom in tuning directions of the wave amplification in the active solid. Due to the anisotropy, the principal directions of the mass density differ from those of the isotropic mass density with different phase velocities.

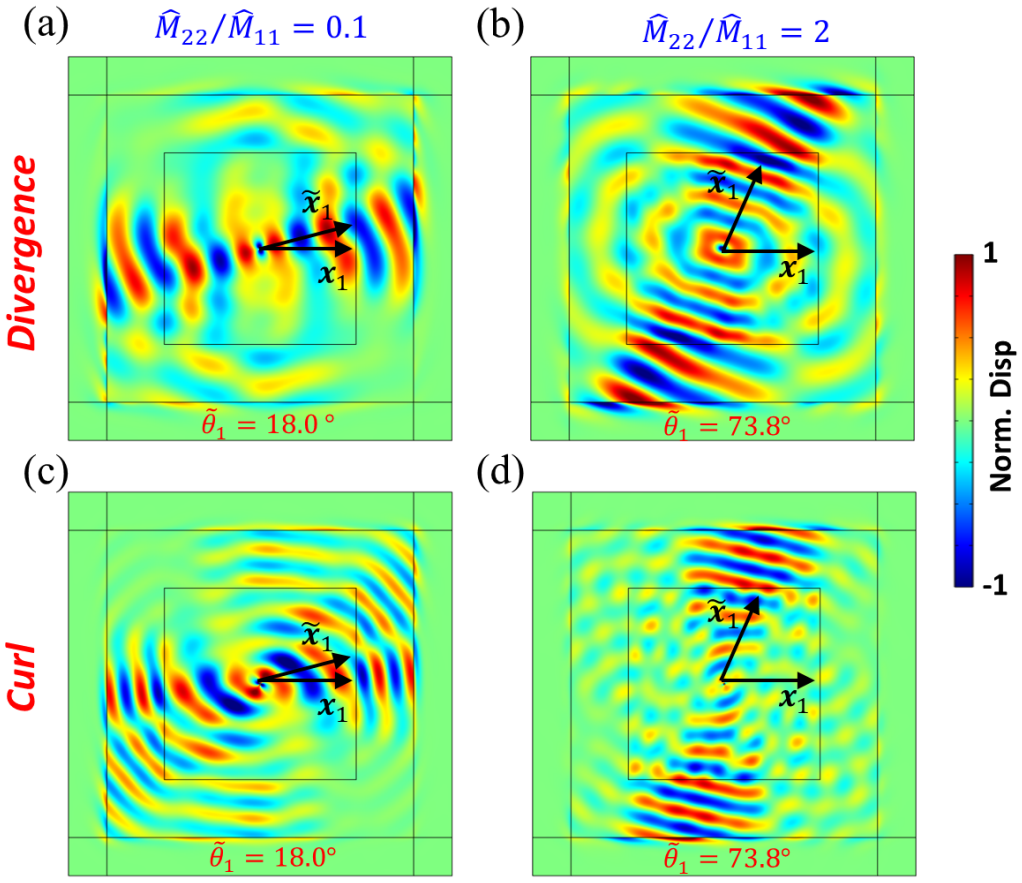

Figure 5.13: Wave manipulation with anisotropic odd mass density tensor. (a, b) Normalized divergence fields of displacement at (a) $\hat{M}_{22}/\hat{M}_{11} = 0.1$ and (b) $\hat{M}_{22}/\hat{M}_{11} = 2$. (c, d) Normalized curl fields of displacement at (c) $\hat{M}_{22}/\hat{M}_{11} = 0.1$ and (d) $\hat{M}_{22}/\hat{M}_{11} = 2$. $\hat{\beta} = 0.6144$ is assumed (energy-broken phase). The background media are the same as the previous. The stiffness property of the odd mass regions (500 mm $\times$500 mm) are consistent with that of the background in order to improve impedance matching. In both field plots, $\hat{M}_{11}$ is selected as 16277 kg/m^3. The field intensities are normalized with their own maximums at 16 kHz. On the bottom of each field plot, the theoretical principal direction $\tilde{\theta}_1$, defining $\boldsymbol{x}_1$ and predicting maximum amplification steering angle, is indicated in red.

In this way, the wave amplification directions can be adjusted accordingly. To illustrate this wave phenomena, the normalized divergence and curl fields of wave displacement are plotted in Figs. 5.13 for the effective active media with $\hat{M}_{22}/\hat{M}_{11} = 0.1$ and 2, and $\hat{\beta}$ fixed at 0.6144. The angle change of directional wave amplification for both pressure and shear waves confirms the functionality of the mass density anisotropy. The predicted angles of directional wave amplification are indeed mainly along the principal directions of the mass density from the analytical analysis (Appendix I. Some discrepancies are observed, which may attribute to the material impedance mismatch between the real active solid and its surrounding background.

In addition, the $\tilde{\theta}_1$ tunability of directional wave amplification due to the mass density anisotropy is systematically investigated when $\hat{M}_{22}/\hat{M}_{11}$ takes values between 0.1 and 2. A pressure point source is used for generating cylindrical waves. Similar to the above in Fig. 5.13, the stiffness constants of the odd-mass-density region here are identical to those of the background for good impedance matching. Examining the steering angles for pressure waves in Figs. 5.14(a)-5.14(f) reveals that the numerical results agree well with the theoretical prediction. Similarly, Examining the steering angles for shear waves in Figs. 5.14(g)-5.14(l) also reveals satisfactory agreement with the theoretical prediction. The undesired scatterings originate from the impedance mismatch at the interfaces, which can be hardly removed. Nevertheless, the steered pressure and shear beams enabled by the wave amplification of odd mass exhibit dominant intensities over the unwanted scatterings, proving the validity of the functionality of the mass density anisotropy.

5.5 Pseudo-Hermiticity and non-Hermitian skin effect

Pseudo-Hermiticity

As the active solid with odd mass density is a non-Hermitian system, it is also interesting to find how the non-Hermiticity would influence the nature of bulk modes. To start with, we emphasize that the system possesses a generalized $\mathcal{PT}$ symmetry stating $[\mathcal{K}, \hat{M}_{ij}^{-1} D] = 0$, where $\mathcal{K}$ is an antiunitary complex conjugation operator [135], by clarifying that the system with odd mass density is pseudo-Hermitian. Based upon Ref. [152], a 2×2 matrix $\mathbf{Q}$ with pseudo-Hermiticity can be written as

$$\mathbf{Q} = \epsilon\sigma_0 + (\gamma \mathbf{n}_1 + i\rho \sin\alpha \mathbf{n}_2 + i\rho \cos\alpha \mathbf{n}_3) \cdot \boldsymbol{\sigma}, \tag{5.12}$$

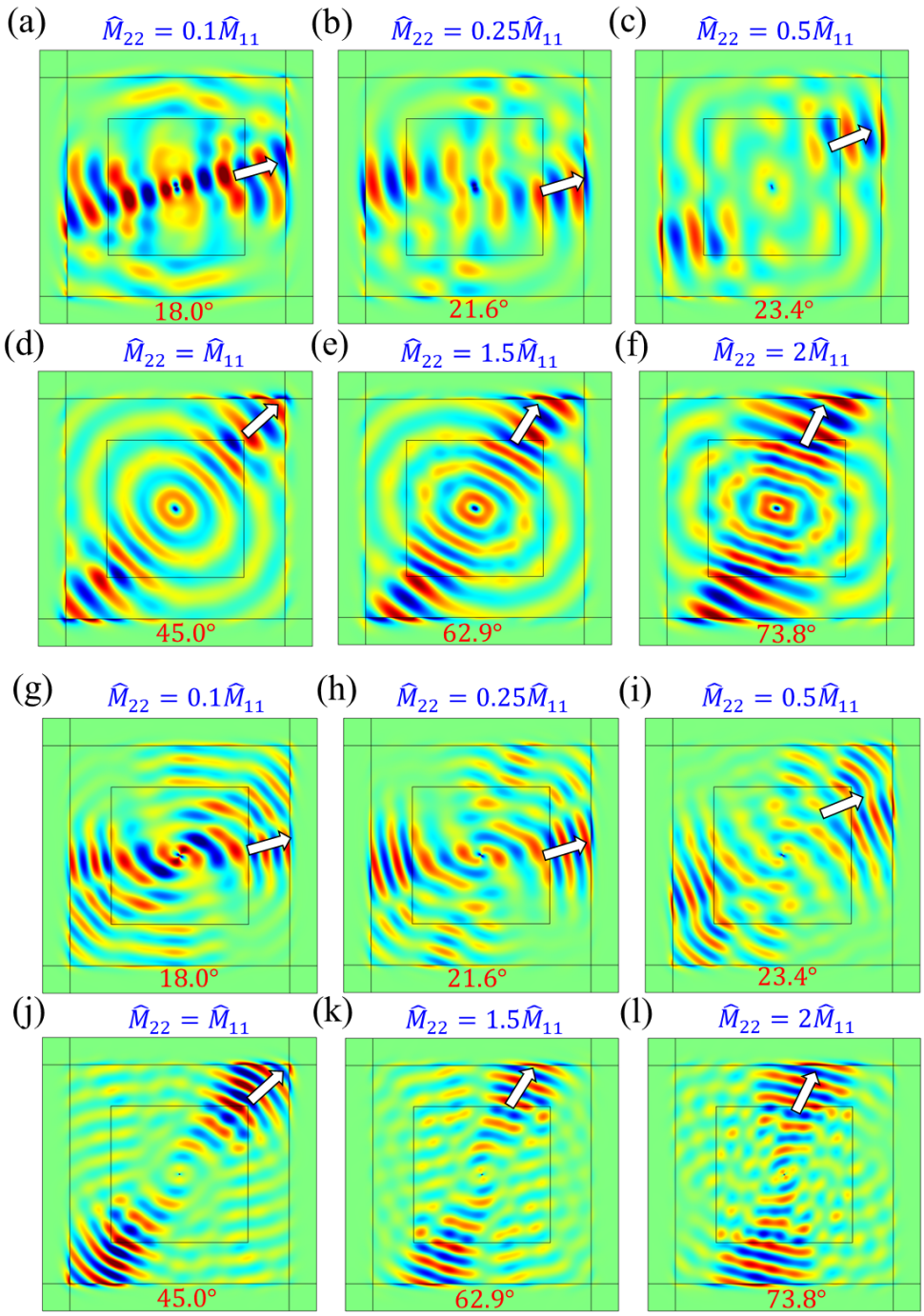

.

Figure 5.14: Pressure and shear wave beam steering with mass density anisotropy in the presence of odd mass density. Normalized (a-f) divergence and (g-l) curl fields of displacement when $\hat{M}_{22}/\hat{M}_{11}$ takes 0.1, 0.25, 0.5, 1, 1.5 and 2. The background media are the same as the previous. While the stiffness properties of the odd mass regions are consistent with that of the background for better impedance matching. In all field plots, $\hat{M}_{11}$ and $\hat{\beta}$ are fixed at 16277 kg/m^3 and 0.6144, respectively. All the field intensities are normalized with their respective maximums at 16 kHz. On the bottom of each field plot, the theoretical principal direction angle θ_1 for the maximum amplification rate is indicated in red.

where σ_0 is a 2×2 identity matrix, and $\boldsymbol{\sigma} = (\boldsymbol{\sigma}_x, \boldsymbol{\sigma}_y, \boldsymbol{\sigma}_z)^{\mathbf{T}}$ are Pauli matrices, with

$$\mathbf{n}_1 = (\sin\Theta\cos\Phi, \sin\Theta\sin\Phi, \cos\Theta), \tag{5.13}$$

$$\mathbf{n}_2 = (\cos\Theta\cos\Phi, \cos\Theta\sin\Phi, -\sin\Theta) \tag{5.14}$$

$$\mathbf{n}_3 = (-\sin\Phi, \cos\Phi, 0). \tag{5.15}$$

The pseudo-Hermitian matrix $\mathbf{Q}$ admits 6 real variables and is said to be $\mathbf{n}_1 \cdot \boldsymbol{\sigma}$-pseudo-Hermitian. Its eigenvalues read

$$\lambda_{1,2} = \epsilon \pm \sqrt{\gamma^2 - \rho^2}. \tag{5.16}$$

The spectrum of $\mathbf{Q}$ is real when $\gamma^2 - \rho^2 > 0$. Then, it is always accompanied with a positive definite operator η reading

$$\eta = p[\gamma\sigma_0 + (o\mathbf{n}_1 + \rho\cos\alpha\mathbf{n}_2 - \rho\sin\alpha\mathbf{n}_3) \cdot \boldsymbol{\sigma}], \tag{5.17}$$

and resulting in

$$\eta\mathbf{Q}\eta^{-1} = \mathbf{Q}^{\dagger}. \tag{5.18}$$

Above, p and o are arbitrary real constants satisfying the conditions $p\gamma > 0$ and $o^2 < \gamma^2 - \rho^2$. In this case, we have

$$\boldsymbol{D}\mathbf{u} = -\omega^2\hat{\boldsymbol{M}}\mathbf{u}. \tag{5.19}$$

The above is written as

$$\begin{bmatrix} (\lambda+2\mu)c^2 + \mu s^2 & (\lambda+\mu)cs \\ (\lambda+\mu)cs & (\lambda+2\mu)s^2 + \mu c^2 \end{bmatrix} \mathbf{u} = \frac{\omega^2}{q^2} \begin{bmatrix} \hat{M}_{11} & \hat{M}_{12} \\ 0 & \hat{M}_{22} \end{bmatrix} \mathbf{u}. \tag{5.20}$$

in which $c \equiv \cos\theta$ and $s \equiv \sin\theta$. Without loss of generality, we select $\hat{M}_{11} = \hat{M}_{22} = \hat{M}_c$ and $\hat{M}_{12} = \hat{\beta}\hat{M}_c$. By rearranging Eq. (5.20), we arrive at

$$\begin{bmatrix} A - B\beta & B - C\beta \\ B & C \end{bmatrix} \mathbf{u} = \frac{\hat{M}_c\omega^2}{q^2}\mathbf{u}, \tag{5.21}$$

where

$$A = (\lambda + 2\mu)c^2 + \mu s^2, \tag{5.22}$$

$$B = (\lambda + \mu)cs, \tag{5.23}$$

$$C = (\lambda + 2\mu)s^2 + \mu c^2. \tag{5.24}$$

Comparing Eq. (5.21) with Eq. (5.12), one can easily find the proposed system can be expressed by Eq. (5.12) with the substitutions

$$\epsilon = \frac{1}{2}(A + C - \hat{\beta}B), \tag{5.25}$$

$$\gamma = -\frac{1}{2}\hat{\beta}C, \tag{5.26}$$

$$\rho\cos\Theta = \frac{1}{2}(A - C - \hat{\beta}B), \tag{5.27}$$

$$\rho\sin\Theta = \frac{1}{2}(2B - \hat{\beta}C), \tag{5.28}$$

$$\Phi = \alpha = 0. \tag{5.29}$$

Therefore, the odd-mass system admits η_θ-pseudo-Hermiticity, where $\eta_\theta = \mathbf{n}_1(\Theta)\cdot\boldsymbol{\sigma}$. The condition $\gamma^2 - \rho^2 > 0$ for real spectrum of ω^2 can be recast as

$$\hat{\beta}^2B^2 - 2B^2(A + C)\hat{\beta} + 4B^2 + (A - C)^2 > 0. \tag{5.30}$$

Therefore, the $\mathcal{PT}$-unbroken regions, shown in Fig. 5.7, are determined by

$$\hat{\beta} > \frac{2(A + C)}{B} + \frac{2}{B^2}\sqrt{B^2AC - B^4}, \tag{5.31}$$

$$\hat{\beta} < \frac{2(A + C)}{B} - \frac{2}{B^2}\sqrt{B^2AC - B^4}. \tag{5.32}$$

By calculation, one can find that the $\mathcal{PT}$-unbroken and $\mathcal{PT}$-broken phase regions coincide with the energy-unbroken and energy-broken regions, respectively.

Non-Hermitian skin effect induced by odd mass density

we impose open boundary condition (OBC) and periodic boundary condition (PBC) along $\boldsymbol{x}_2$ direction in the finite active solid and assume $q_1 = 1$ rad/m in reciprocal space along the $\boldsymbol{x}_1$ direction. The spectra for $\hat{\beta} = 0.2$ and $\hat{\beta} = 0.9$ are plotted in Figs. 5.15(a) and 5.15(b), respectively. We find the

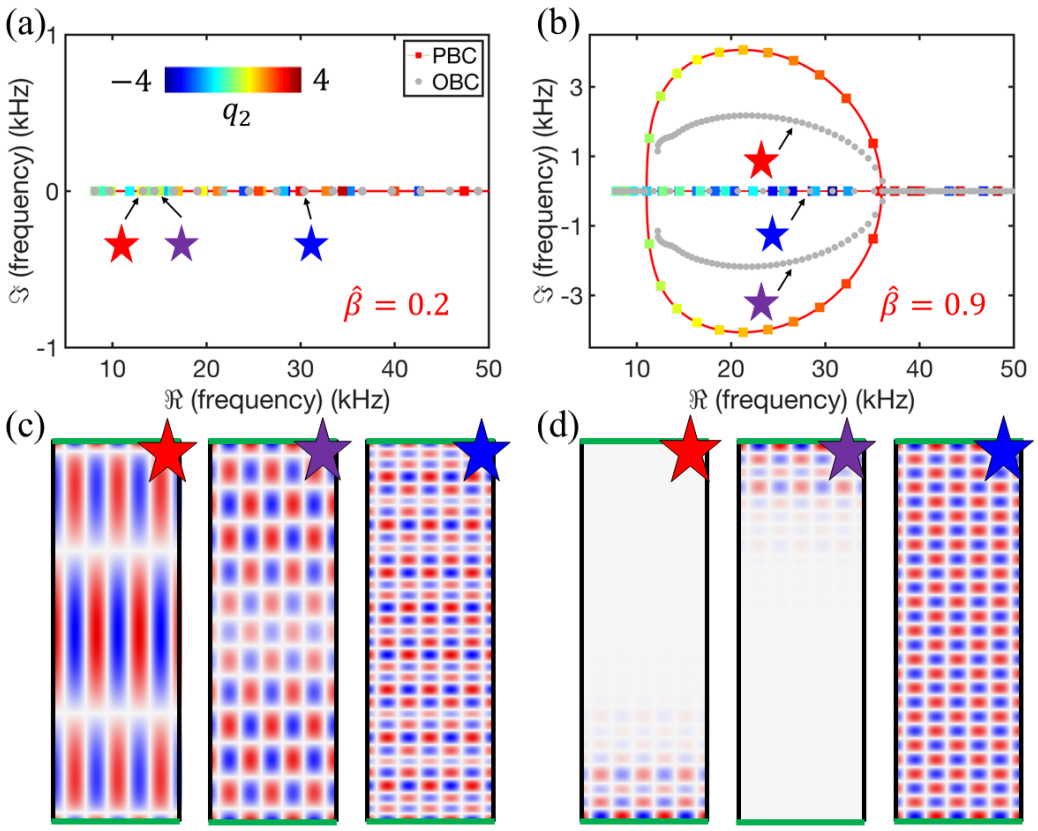

Figure 5.15: Non-Hermitian skin effect induced by odd density. (a, b) The complex spectrum when the system operates at $\hat{\beta} = 0.2$ and 0.9. The squares with the hue indicating the wave number q_2 and gray circular scatters are results from PBC and OBC, respectively. (c) Numerically computed OBC eigenmodes at $\hat{\beta} = 0.2$ for a finite ribbon. The corresponding eigenfrequencies are 12.94, 15.48 and 30.30 kHz from left to right. (d) Numerically computed eigenmodes at $\hat{\beta} = 0.9$. The corresponding eigenfrequencies are $27.71 + 0.324i$, $27.71 - 0.324i$ and 28.14 kHz from left to right. The top and bottom are set with open boundary conditions. Without loss of generality, the horizontal wave number is fixed at $q_1 = 1$ rad/m.

OBC and PBC spectra coincide in the energy-unbroken region with $\hat{\beta} = 0.2$, but are drastically distinct from the each other in the energy-broken region with $\hat{\beta} = 0.9$. To retrace this spectral discrepancy, the vertical wave number q_2 should be extended to the generalized Brillouin zone (GBZ), which is a loop on the complex plane; see the next subsection for the details about the derivation of the GBZ. Figs. 5.15(c) and 5.15(d) illustrate the eigenmodes under the OBC for $\hat{\beta} = 0.2$ and $\hat{\beta} = 0.9$, respectively. The active solids can only host bulk modes when the system is in the energy-unbroken phase [153, 154]. However, we notice that some eigenmodes localize on the open edges when the system is in energy-broken phase, which correspond to an elastic manifestation of the non-Hermitian skin effect [135, 152, 155]. The complex frequency means that the skin modes are amplified (attenuated) for positive (negative) $\Im$(frequency). This skin mode is different from the Rayleigh wave mode whose amplitude is invariant since the frequency is real in classic elasticity. In addition, the skin modes always appear in pairs with one localized on the top while the other on the bottom since the eigenfrequencies always exhibit complex conjugate in the energy-broken phase.

Reconstruction of correspondence between open boundary condition and periodic boundary condition spectra on generalized Brillouin zone

For the Hermitian system, the OBC spectrum for infinite system size $L \to \infty$ is continuous and it is the same as the PBC spectrum for the wave number with the periodicity over the Brillouin zone. However, in Fig. 5.15(b), we find discrepancies between the OBC and PBC spectra in the energy-broken phase region. Here we reconstruct the correspondence between the OBC and PBC spectra by extending to a generalization Brillouin zone (GBZ). First, we will derive the OBC spectrum equation of odd-mass-density system analytically. Then under the condition $L \to \infty$, we reduce the OBC spectrum equation to a simpler one that gives the GBZ. Substituting the wave number on the generalized Brillouin zone into the dispersion relation, we can obtain the PBC spectrum on the GBZ, which would be identical to the OBC spectrum with $L \to \infty$.

For a solid with odd mass density, the equations of motion are

$$\begin{aligned} \sigma_{11,1} + \sigma_{12,2} &= \hat{M}_{11}\ddot{u} + \hat{M}_{12}\ddot{v} \\ \sigma_{12,1} + \sigma_{22,2} &= \hat{M}_{22}\ddot{v}. \end{aligned} \quad . \tag{5.33}$$

Constitutive relation for plane strain problem is

$$\begin{bmatrix} \sigma_{11} \\ \sigma_{22} \\ \sigma_{12} \end{bmatrix} = \begin{bmatrix} \lambda+2\mu & \lambda & 0 \\ \lambda & \lambda+2\mu & 0 \\ 0 & 0 & \mu \end{bmatrix} \begin{bmatrix} \varepsilon_{11} \\ \varepsilon_{22} \\ \varepsilon_{12} \end{bmatrix} \tag{5.34}$$

Substituting Eq. (5.34) into Eq. (5.33), the equations of motion expressed by displacements are

$$\begin{bmatrix} (\lambda+2\mu)\partial_1^2+\mu\partial_2^2 & (\lambda+\mu)\partial_1\partial_2 \\ (\lambda+\mu)\partial_1\partial_2 & (\lambda+2\mu)\partial_2^2+\mu\partial_1^2 \end{bmatrix} \begin{bmatrix} u \\ v \end{bmatrix} = \begin{bmatrix} \hat{M}_{11} & \hat{M}_{12} \\ 0 & \hat{M}_{22} \end{bmatrix} \begin{bmatrix} \ddot{u} \\ \ddot{v} \end{bmatrix} \tag{5.35}$$

With the substitution of the standing wave solution $u = ue^{i(q_1x_1+q_2x_2-\omega t)}, v = ve^{i(q_1x_1+q_2x_2-\omega t)}$ into Eq. (5.35), we have

$$\begin{bmatrix} (\lambda+2\mu)q_1^2+\mu q_2^2 & (\lambda+\mu)q_1q_2 \\ (\lambda+\mu)q_1q_2 & (\lambda+2\mu)q_2^2+\mu q_1^2 \end{bmatrix} \begin{bmatrix} u \\ v \end{bmatrix} = \omega^2 \begin{bmatrix} \hat{M}_{11} & \hat{M}_{12} \\ 0 & \hat{M}_{22} \end{bmatrix} \begin{bmatrix} u \\ v \end{bmatrix} \tag{5.36}$$

The vanishing of determinant gives the polynomial equation

$$c_1q_2^4 + c_2q_2^3 + c_3q_2^2 + c_4q_2 + c_5 = 0 \tag{5.37}$$

where the coefficients can be obtained from the expansion of determinant. Equation (5.37) gives four roots $q_2^1, q_2^2, q_2^3, q_2^4$ with the arrangement of $\Im(q_2^1) \leq \Im(q_2^2) \leq \Im(q_2^3) \leq \Im(q_2^4)$. Accordingly, the four corresponding eigenvectors are

$$\begin{aligned} u_i &= -(\lambda+\mu)q_qq_2 + \omega^2\hat{M}_{12} \\ v_i &= (\lambda+2\mu)q_1^2 + \mu q_2^2 - \omega^2\hat{M}_{11}, \quad i = 1,2,3,4. \end{aligned} \tag{5.38}$$

The superposition of the eigenstates gives the general solution

$$\begin{bmatrix} u \\ v \end{bmatrix} = \sum_{i=1}^{4} C_i e^{iq_2^i x_2} \begin{bmatrix} u_i \\ v_i \end{bmatrix} \tag{5.39}$$

Here, we consider the system to be infinite along the $\boldsymbol{x}_1$ direction. While along the $\boldsymbol{x}_2$ direction, we

impose OBCs (stress free boundary conditions) which are

$$\begin{cases} \sigma_{22}|_{x_2=0} = 0 \\ \sigma_{11}|_{x_2=0} = 0, \end{cases} \qquad \begin{cases} \sigma_{21}|_{x_2=L} = 0 \\ \sigma_{12}|_{x_2=L} = 0. \end{cases} \tag{5.40}$$

With the substitution of the constitutive relation, they become

$$\begin{aligned} &[\lambda u_{,1} + (\lambda + 2\mu) v_{,2}]\,|_{x_2=0} = 0 \\ &(u_{,2} + v_{,1})\,|_{x_2=0} = 0 \end{aligned} \tag{5.41}$$

and

$$\begin{aligned} &[\lambda u_{,1} + (\lambda + 2\mu) v_{,2}]\,|_{x_2=L} = 0 \\ &(u_{,2} + v_{,1})\,|_{x_2=L} = 0 \end{aligned} \tag{5.42}$$

Substituting the general solution Eq. (5.39) into boundary conditions Eqs. (5.41) and (5.42), we have

$$\begin{bmatrix} A_1(0) & A_2(0) & A_3(0) & A_4(0) \\ B_1(0) & B_2(0) & B_3(0) & B_4(0) \\ e^{iq_2^1 L} A_1(L) & e^{iq_2^2 L} A_2(L) & e^{iq_2^3 L} A_3(L) & e^{iq_2^4 L} A_4(L) \\ e^{iq_2^1 L} B_1(L) & e^{iq_2^2 L} B_2(L) & e^{iq_2^3 L} B_3(L) & e^{iq_2^4 L} B_4(L) \end{bmatrix} \begin{bmatrix} C_1 \\ C_2 \\ C_3 \\ C_4 \end{bmatrix} = 0 \tag{5.43}$$

where $A_i = \lambda q_1 u_i(x_2) + (\lambda + 2\mu) q_2^i v_i(x_2), B_i = q_2^i u_i(x_2) + q_1 v_i(x_2)$. The vanishing of determinant gives the frequency spectrum for OBC

$$\begin{vmatrix} A_1(0) & A_2(0) & A_3(0) & A_4(0) \\ B_1(0) & B_2(0) & B_3(0) & B_4(0) \\ e^{iq_2^1 L} A_1(L) & e^{iq_2^2 L} A_2(L) & e^{iq_2^3 L} A_3(L) & e^{iq_2^4 L} A_4(L) \\ e^{iq_2^1 L} B_1(L) & e^{iq_2^2 L} B_2(L) & e^{iq_2^3 L} B_3(L) & e^{iq_2^4 L} B_4(L) \end{vmatrix} = 0; \tag{5.44}$$

also see the red dots in Fig. 5.16(a).

Then we turn to derive the GBZ by using the method for the lattice system [156]. The solution of Eq. (5.44) can be simplified for large L, which forms the corresponding continuum spectrum. Let

us rewrite Eq. (5.44) with a more general form for the determinant of a $2M$ dimensional matrix

$$\begin{vmatrix} f_1\left(q_2^1,\omega,\mathcal{S}\right) & \cdots & f_1\left(q_2^{2M},\omega,\mathcal{S}\right) \\ \vdots & \vdots & \vdots \\ f_M\left(q_2^1,\omega,\mathcal{S}\right) & \cdots & f_M\left(q_2^{2M},\omega,\mathcal{S}\right) \\ g_1\left(q_2^1,\omega,\mathcal{S}\right)e^{iq_2^1L} & \cdots & g_1\left(q_2^{2M},\omega,\mathcal{S}\right)e^{iq_2^{2M}L} \\ \vdots & \vdots & \vdots \\ g_M\left(q_2^1,\omega,\mathcal{S}\right)e^{iq_2^1L} & \cdots & g_M\left(q_2^{2M},\omega,\mathcal{S}\right)e^{iq_2^{2M}L} \end{vmatrix} = 0. \tag{5.45}$$

where $M = 2$ for the current problem, and $\mathcal{S}$ is the set of the system parameters $\lambda, \mu, \hat{M}_{ij}, L,$ and q_1. By expanding the determinant given in Eq. (5.45), we have

$$\sum_{P,Q} F\left(q_2^{i\in P}, q_2^{j\in Q}, \omega, \mathcal{S}\right) \prod_{l\in P} e^{iq_2^l L} = 0 \tag{5.46}$$

The sets P and Q are two disjoint subsets of the set $\{1,\cdots,2M\}$ such that the number of elements of each subset is M. In this way, the sum included in Eq. (5.44) is taken over all the sets P and Q.

We now consider asymptotic behavior of the solutions of Eq. (5.46) for large L. When not all of $\Im(q_y^1),\cdots,\Im(q_y^{2M})$ are 0, the only possible solution is $\Im(q_2^M) = \Im(q_2^{M+1})$. If $\Im(q_2^M) \neq \Im(q_2^{M+1})$, there is only one leading term proportional to $e^{iq_2^{M+1}L}\cdots e^{iq_2^{2M}L}$ in Eq. (5.46) in the limit of a large L. Thus it leads to

$$F\left(q_2^{i\in P'}, q_2^{j\in Q'}, \omega, \mathcal{S}\right) = 0 \tag{5.47}$$

with $P' = \{M+1,\cdots,2M\}$ and $Q' = \{1,\cdots,M\}$. This equation neither depends on L, nor allows continuum spectrum. On the other hand, when $\Im(q_2^M) = \Im(q_2^{M+1})$, there are two leading terms proportional to $e^{iq_2^M L}\cdots e^{iq_2^{2M}L}$ and to $e^{iq_2^{M+1}L}\cdots e^{iq_2^{2M}L}$, and Eq. (5.46) can be rewritten as

$$\frac{e^{iq_2^M L}}{e^{iq_2^{M+1}L}} = -\frac{F\left(q_2^{i\in P_0}, q_2^{j\in Q_0}, \omega, \mathcal{S}\right)}{F\left(q_2^{i\in P_1}, q_2^{j\in Q_1}, \omega, \mathcal{S}\right)} \tag{5.48}$$

with $P_0 = \{M+1,\cdots,2M\}, Q_0 = \{1,\cdots,M\}, P_1 = \{M, M+2,\cdots,2M\}$, and $Q_1 = \{1,\cdots,M-1, M+1\}$. In such a case, we can expect that the difference between $\Re(q_2^M)$ and $\Re(q_2^{M+1})$ can be changed almost continuously for a large L, producing continuum bands.

In the current case, $\Im(q_2^1) = \cdots = \Im(q_2^{2M}) = 0$ just corresponds to a Hermitian situation, and there is no leading term in Eq. (5.46). Therefore, we have to solve Eq. (18), completely. However, for Hermitian situations, $\Re(q_2^1),\cdots,\Re(q_2^{2M})$ can change continuously for a large L, and the frequency

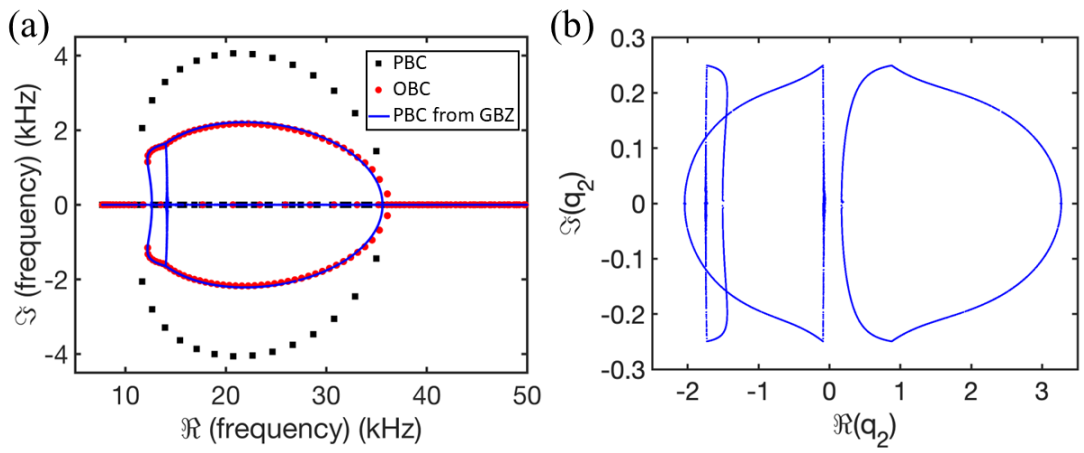

Figure 5.16: Frequency spectrum and GBZ. (a) The frequency spectrum for PBC, OBC are from Fig. 5.15(b). The PBC spectrum from GBZ is calculated based on Eqs. (5.49) and (5.37). (b) Generalized Brillouin zone is calculated based on Eqs. (5.49) and (5.37).

spectrum is actually the dispersion curve. Therefore, the frequency spectrum obtained in this case is included in

$$\Im(q_2^M) = \Im(q_2^{M+1}), \tag{5.49}$$

with the dispersion relation Eq. (5.37). Then, we can get the continuous frequency spectrum for both Hermitian and non-Hermitian cases.

By solving Eq. (5.49) with Eq. (5.37), we can get the GBZ which are curves in the complex plane; also see 5.16(b). The GBZ tells us which end the mode is localized at in this study. With the substitution of the complex wave numbers of the GBZ into the dispersion curve given by Eq. (5.37), we can get the PBC spectrum from GBZ; see blue solid line in 5.16(a). We find that the OBC spectrum is same as the PBC spectrum from the GBZ. This suggests the reconstruction of the correspondence between OBC and PBC spectra based upon the GBZ. Actually, solving Eqs. (5.49) and (5.37) not only gives the GBZ but also gives the frequency spectrum. Therefore, we need not substitute the complex wave numbers of the GBZ to the dispersion curve.

5.6 Summary

In conclusion, the active metamaterial presented here demonstrates odd mass density that are enabled by sensing, actuating and local computation. The minimal on-board electronics that power the interior local resonators enable its non-Hermitian wave functions including the directional wave amplification and the non-Hermitian skin effect. Odd mass density extends the range of possible couplings between

conventional forces and deformation along two perpendicular directions by including antisymmetry in their relationship. This design can be flexibly tuned through computer coding and scaled via microelectromechancial systems (MEMS). The mechanical approach relies on a feed-forward control loop, a generic concept that can exist in both metamaterial and biological contexts. Combining the principles illustrated here with odd moduli, nonlinearities, and strong dissipation suggests new approaches for the control of wave propagation in active solids and fluids.

Chapter 6

INDEPENDENT FLEXURAL WAVE FREQUENCY CONVERSION BY A LINEAR ACTIVE META-LAYER

6.1 Introduction

Wave frequency is one of the fundamental parameters governing wave propagation and its interaction with matters. Most physical laws on wave propagation and wave–matter interaction are frequency-dependent. Altering frequency can break the limits currently imposed by laws of physics for a given frequency condition, such as imaging resolution limits, wave energy transport, and wave propagation behavior. Manipulating flexural waves in platelike structures has been of considerable interest with widespread applications in nondestructive structural health monitoring, vibration suppression and control [20, 43, 157–162]. In linear time-invariant plate-type media, energy exchange among waves at different frequencies is prohibited since those waves are decoupled. On the other hand, flexural waves at different frequencies can exchange energy among themselves due to the coupling and mixing of different frequency components during the propagation in nonlinear or time-modulated plate media, where linearity or time invariance is broken [109, 113, 120, 136, 163, 164]. However, nonlinear and time-modulated wave conversion is in general amplitude-dependent and also takes place in a way that is impossible to be manipulated individually and independently, limiting its wave control applications [120, 136, 164, 165]. A linear mechanism-based wave conversion, which is independent of incident amplitude and provides generation of freely controlled harmonics, could offer far more freedom in wave manipulation and therefore is the major motivation of this study.

Rapid advances in control of the phase and amplitude of wave scattering from planar or linear arrays of scatterers have stimulated the development of optic, acoustic and elastic metasurfaces with subwavelength building blocks that use amplitude or phase-sensitive scattering to enable wavefront

control. To date, metasurfaces have mostly been designed for wave beam steering [166–170] and focusing [170–172], self-bending beam generation [170, 173], control of dynamic pulse [174, 175], as well as wave mode and polarization conversion [176–178]. To enhance their functionality and dynamic performance in scenarios where tunability and adaptivity are required, active metasurfaces have been recently suggested by incorporating an active medium into passive metasurface structure. For example, the active mechanical meta-layers have been developed by introducing piezoelectric sensors and actuators into host structures [49, 50]. Thus far, the active metasurfaces reported are mainly linear and time-invariant for dynamic control, and the interference wave phenomena are only observed at single frequency. To exploit the frequency mixing, optical time-varying metasurfaces have been proposed [179, 180]. In those designs, the refractive index is temporally modulated using a pump or carrier wave, efficiently enabling enriched wave functions compared with time-invariant designs, i.e. simultaneous control of spatial and temporal spectra of light [181, 182], and modulated frequency conversion [183]. However, to the best of my knowledge, there exists no strategies or designs of linear metasurfaces that could achieve independent and controllable frequency conversion in optics, acoustics, and mechanics.

In this Chapter, a linear active meta-layer in a structural beam for independent frequency conversion of flexural waves is reported, which is underpinned by a unique physical principal related to circuit time modulation of sensing signals. The active meta-layer is driven by a time-dependent transfer function through bonded piezoelectric actuators and sensors to perform independent parallel operations over waves at different frequencies. The design breaks energy conservation by pumping in electrical energy to cancel incidence and freely emit arbitrary transmitted waves as demanded (Fig. 6.1). Thus far, no existing experimental designs can break the fundamental limitation imposed by the physics laws of wave diffraction such as Snell's law and Rayleigh criterion to realize such linear and independent mode conversion of flexural waves in a very thin dimension. Additionally, phase- and frequency-gradient meta-layers for frequency-converted wave steering and dynamic beam steering are demonstrated, respectively. The physical realization of the meta-layer is the key to accomplish these novel wave functions.

6.2 Programmable time-modulated metabeam

The linear active meta-layer is constructed by bonding a large piezoelectric patch on one surface and two small piezoelectric patches on another surface of a host beam (see Fig. 6.1). The large piezoelectric patch serves as the sensor to sense the bending curvature at its position. The two small

piezoelectric patches are actuators that can generate bending moments to the beam. The sensor and actuators are connected by an electrical control loop. In the design, a charge amplifier is connected to the sensing patch, leading to the sensing voltage $V_s(t)$. Antisymmetric voltages are applied on the two patches (one is $V_a(t)$, the other is $-V_a(t)$), which collectively produce an effective shear load on the beam. As a result, the sensor cannot detect the actuation, making the control loop feedforward. A digital microcontroller is implemented into the electrical control loop to send out the signal $V_a(t)$ based on the input $V_s(t)$. Remarkably, the feed-forward control loop enables multiple independent parallel operations in the microcontroller, as each of the operations has no effect on the sensing signal, preventing interactions with other operations. To realize frequency conversion, the microcontroller is driven by two independent operations to generate the superimposed actuation signal as $V_a(t) = V_a^{(0)}(t) + \bar{V}_a(t)$, where $V_a^{(0)}(t)$ is used to cancel the incident wave in the transmitted field and $\bar{V}_a(t) = \sum_{n=1}^{N} V_a^{(n)}(t)$ is mainly for the wave conversion with multiple desired frequencies in the transmitted field.

6.3 Theoretical analysis

To find the relationship between $V_a^{(0)}(t)$ and $V_s(t)$, we first calculate the wave field generated by $V_a^{(0)}(t)$ using the Green's function as

$$\tilde{w}_a(x) = \mathrm{sgn}(x)(e^{-ik_1|x|} + e^{-k_2|x|})\kappa_a \tilde{V}_a \tag{6.1}$$

where $\tilde{w}_a(x)$ and $\tilde{V}_a$ denote the harmonic wave profile and the amplitudes of the actuation voltage, and κ_a, k_1, and k_2 are real constants representing the actuation coefficient, wave number, and attenuation constant, respectively. They read

$$k_1 = -i\sqrt{\frac{-\alpha - \sqrt{\alpha^2 - 4D_0\beta}}{2D_0}}, \tag{6.2}$$

$$k_2 = \sqrt{\frac{-\alpha + \sqrt{\alpha^2 - 4D_0\beta}}{2D_0}}, \tag{6.3}$$

$$\alpha = \frac{\rho_0\omega^2 D_0}{G_0} + J_0\omega^2, \tag{6.4}$$

$$\beta = \frac{(J_0\omega^2 - G_0)\rho_0\omega^2}{G_0}. \tag{6.5}$$

In the derivation, we assume the active meta-layer is located at $x = 0$, and the dimension of the meta-layer is much shorter than the wavelength such that the actuation of the meta-layer can be

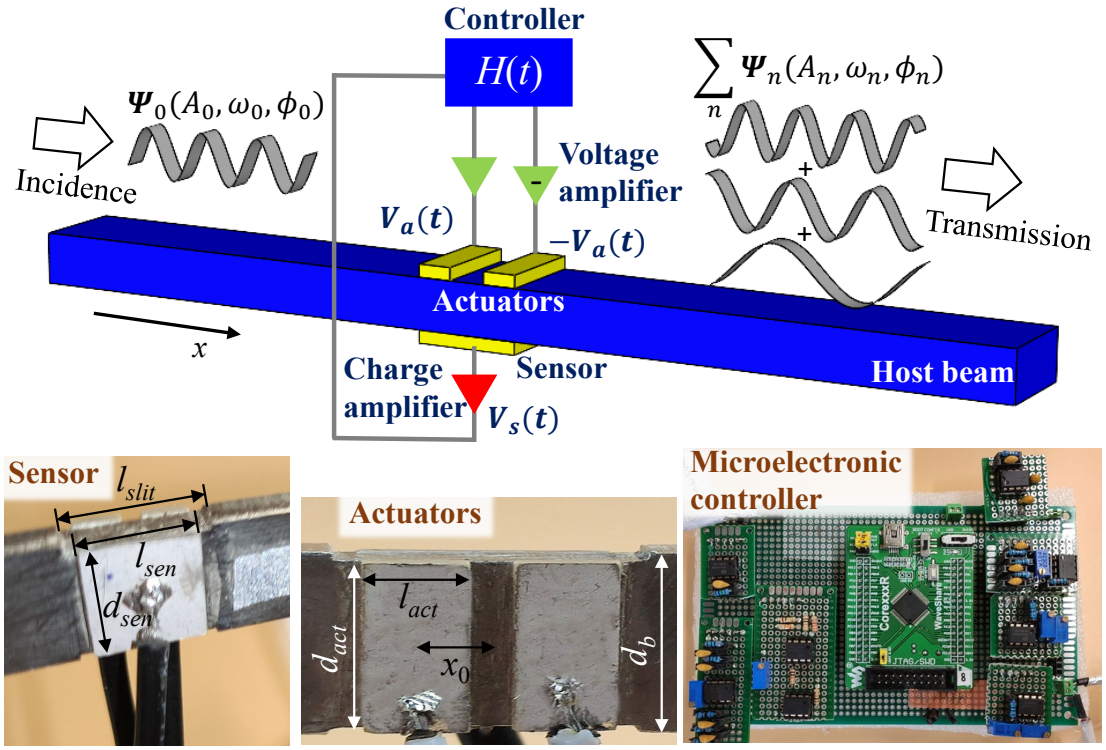

Figure 6.1: Schematic illustration of the programmable time-modulated metabeam for continuous dynamic control of flexural wave propagation. The meta cell converts the incident wave $\Psi_0(A_0, \omega_0, \phi_0)$ into an arbitrary combination of transmitted wave components $\Sigma_n \Psi_n(A_n, \omega_n, \phi_n)$, via a programmable feed-forward control system that exhibits time modulation and realizes antisymmetric actuation. The terms A_n, ω_n and ϕ_n denote the field magnitude, frequency and phase of the nth-order harmonic, respectively. The bottom layer shows the photos of the mechanical (actuators and sensor) and the microelectronic control circuit. The piezoelectric patches (PZT-5J, $l_{\text{sen}} = d_{\text{sen}} = d_{\text{act}}$=10 mm, $l_{\text{act}} = 4$ mm, $x_0 = 3$ mm.) are mounted to a 3-mm-thick steel beam of $d_b = 11$ mm via conductive epoxy. The thicknesses of the sensor and actuators are 0.5 mm and 1 mm, respectively. The slit used to diminish the interactions between adjacent meta cells has a length of $l_{\text{slit}} = 12$ mm. The microelectronic controller is responsible for generating the time-dependent transfer function. $V_s(t)$ and $V_a(t)$ are the respective electrical voltages from the charge amplifier and voltage amplifier. They follow the relationship $H(t) = V_a(t)/V_s(t)$. Reprinted figure with permission from Q. Wu, X. D. Zhang, P. Shivashankar, Y. Y. Chen, and G. L. Huang, Physical Review Letters, 128, 244301 (2022). Copyright (2022) by the American Physical Society.

treated as a point shear load. Considering an incident flexural wave $\tilde{w}_i(x) = \tilde{W}_i e^{-ik_1 x}$ with a complex amplitude $\tilde{W}_i$, the sensing signal can be obtained as $\tilde{V}_s = \tilde{W}_i/\kappa_s$, where κ_s is a real constant denoting the sensing coefficient. To achieve wave cancellation in the transmitted field, the traveling wave component of $\tilde{w}_a(x)$ should be out of phase with $\tilde{w}_i(x)$ for $x > 0$, leading to

$$\frac{\tilde{V}_a}{\tilde{V}_s} = -\frac{\kappa_s}{\kappa_a} \tag{6.6}$$

As a result, $V_a^{(0)}(t)$ is always proportional to $V_s(t)$. This simple relationship, however, produces complexity to the design of the electrical control system in experiments, as the control system usually requires filters for system stability, which, otherwise, induce the phase change between $V_a^{(0)}(t)$ and $V_s(t)$. In experiment, we employ an analog differentiator circuit together with a second-order filter in the microcontroller to approximate this linear relationship (see Supplementary Information for detailed circuit designs). In particular, the relationship between the output and input signals of the second-order filter in the microcontroller reads $\frac{\ddot{V}_{\text{out}}}{{\omega_0}^2} + \frac{\dot{V}_{\text{out}}}{2\mu\omega_0} + V_{\text{out}} = A_0 V_{\text{in}}$, where $\mu = 0.6$, $A_0 = \frac{\kappa_s}{2\mu\omega\kappa_a}$, and the cutoff frequency ω_0 is selected as the operation frequency.

Next, to construct $V_a^{(n)}(t)$ using $V_s(t)$ for active emission of waves at a different frequency, we consider harmonic incidence with a real time-domain sensing signal $V_s(t) = \frac{\tilde{W}_i}{\kappa_s}\cos(\omega t + \phi_0)$. With this assumption, $V_a^{(n)}(t)$ can be attained by mixing $V_s(t)$ with a carrier wave as

$$V_a^{(n)}(t) = A_n[V_s(t)\cos(\delta\omega_n t + \phi_n) - V_s(t - \frac{3\pi}{2\omega})\sin(\delta\omega_n t + \phi_n)] \tag{6.7}$$

where A_n controls the amplitude of the emitted wave, $\delta\omega_n$ is the change in frequency, and ϕ_n modulates the phase of the emitted wave. Note that the presence of $V_s(t - \frac{3\pi}{2\omega})$ requires the prior knowledge of the sensing signal. In experiments, instead of recording the sensing signal in the microcontroller, we calculate $\dot{V}_s(t)$ at the current time step, and let $V_s(t - \frac{3\pi}{2\omega}) = \frac{\dot{V}_s(t)}{\omega}$. Using Eq. (6.7), $\bar{V}_a(t)$ can be electronically computed in parallel with $V_a^{(0)}(t)$, and the total excitation voltage $V_a(t)$ is enabled for frequency conversion. Note that the active meta-layer for frequency conversion is designed at a single frequency, which should also be known before its operation. However, in practical applications, adaptive filters can be implemented into the microcontroller, which could circumvent the need of the prior knowledge of the operation frequency. In addition, the active meta-layer can work well for narrow-band signals, not just single-frequency incidences, evidenced by the results reported below.

To illustrate linearity of the active meta-layer, we perform numerical simulations with different

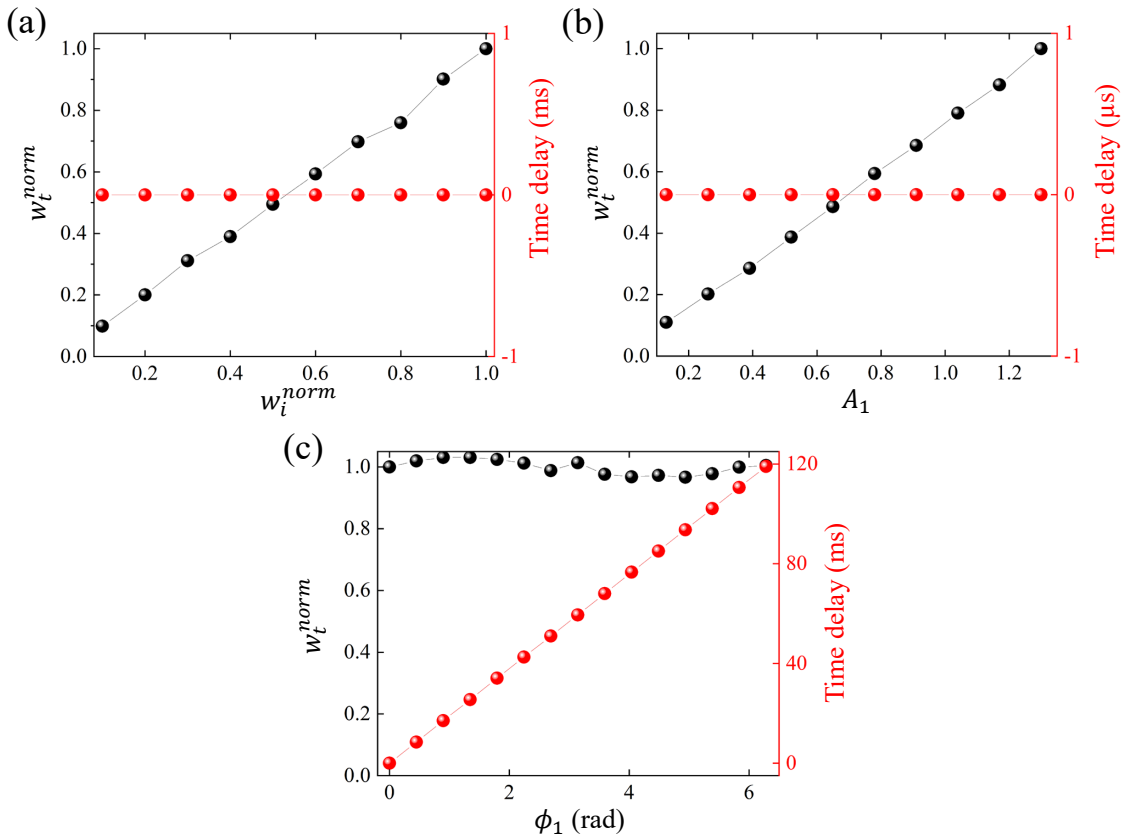

Figure 6.2: Linear independent control over frequency conversion from 10 to 8.5 kHz. Transmitted displacement ratio of wave packets w_t^{norm} and time delay are numerically demonstrated by sweeping (a) maximum incident displacement w_i^{norm} from 0.1 to 1, (b) amplitude A_1 given in Eq. (6.7) from 0.13 to 1.3, and (c) phase shift ϕ_1 from 0 to 2π. In each cases, the parameters that are not swept remain unchanged as used in Fig. 6.4. Reprinted figure with permission from Q. Wu, X. D. Zhang, P. Shivashankar, Y. Y. Chen, and G. L. Huang, Physical Review Letters, 128, 244301 (2022). Copyright (2022) by the American Physical Society.

incidences for the frequency conversion demonstrated in Fig. 6.4a. In the simulations, the normalized maximum displacement of the incident wave package, $w_i^{\text{norm}} = w_i^{\max}/\bar{w}_i^{\max}$, changes from 0.1 to 1, where $\bar{w}_i^{max}$ denotes the maximum displacement of the incident wave package with the central frequency being 10 kHz in Fig. 6.4(a). Figure 6.2(a) shows the normalized maximum displacement of the transmitted wave package, $w_t^{\text{norm}} = w_t^{\max}/\bar{w}_t^{\max}$, and the relative time delay compared with that in Fig. 6.2(a). Similarly, $\bar{w}_t^{\max}$ represents the maximum displacement of the transmitted wave package with the central frequency being 8.5 kHz in Fig. 6.2(a). It can be clearly seen that w_t^{norm} is proportional to w_i^{norm}, and the relative time delay remains zero for all w_i^{norm}, indicating linearity of the active meta-layer. Further, to show independency between different harmonics of the active meta-layer, we conduct another set of numerical simulations with different A_1 and ϕ_1 still for the frequency down conversion demonstrated in Fig. 6.4(a). As shown in Fig. 6.2(b) where $\phi_1 = 0$,

w_t^{norm} linearly increases with A_1, and the relative time delay still remains close to zero. While, in Fig. 6.2(c), A_1 keeps unchanged and ϕ_1 increases from 0 to 2π, giving rise to linear changes of the relative time delay. In all the simulations, wave cancellation has not been impaired to any extent, and no waves with other frequency components have been detected in the transmitted domain, successfully demonstrating the independent control over frequency-converted waves.

6.4 Experimental demonstration: arbitrary frequency conversion

To validate the design for frequency conversion, we fabricate the linear active meta-layer on a steel beam and construct the corresponding electrical control system for experimental testing We implement the metamaterial on a steel beam in the experiment. As shown in Fig. 6.3(a), the unit cell of the metamaterial consists of three piezoelectric patches and a feedforward-controlled circuit. The piezoelectric patches (STEMiNC PZT 5J: $10 \times 10 \times 0.5$ mm, $10 \times 4 \times 1$ mm) are mounted to the beam via conductive epoxy. The relatively large piezoelectric patch is referred as a sensor. The other two piezoelectric patches with identical parameters are used as actuators, which are bonded symmetrically to the sensor on the reverse side of the beam. The digital feedforward-controlled circuit is composed of a charge-amplifier, differential circuit, DC bias voltage circuit, microprocessor (STM32F405) with built-in analog-to-digital converter (ADC) and digital-to-analog converter (DAC), high-pass and low-pass circuit, voltage amplifier and inverting voltage amplifier. The values of all electrical components are listed in TABLE 6.1. The precise operational amplifiers, OPA445 from Texas Instruments, are chosen to make the circuit boards in the experiment. More specifically, a charge-amplifier is connected to the sensor to sense the voltage signals. These sensing voltage signals are digitalized by the ADC and then fed to the microprocessor after going through the DC bias voltage circuit. The second order transfer function used for wave cancellation reads

$$H_0(s) = \frac{1}{(s/\omega_0)^2 + 2\eta s\omega_0 + 1}. \tag{6.8}$$

The digital values are transferred into the analog voltage signals by the DAC. Finally, the output signals go through one voltage amplifier and one inverting voltage amplifier, and are applied on the two actuators, respectively, producing antisymmetric actuations.

In experiments, incident flexural waves are launched from the left of the active meta-layer using a piezoelectric actuator bonded on the host beam. We select 15-peak tone-burst signals with the

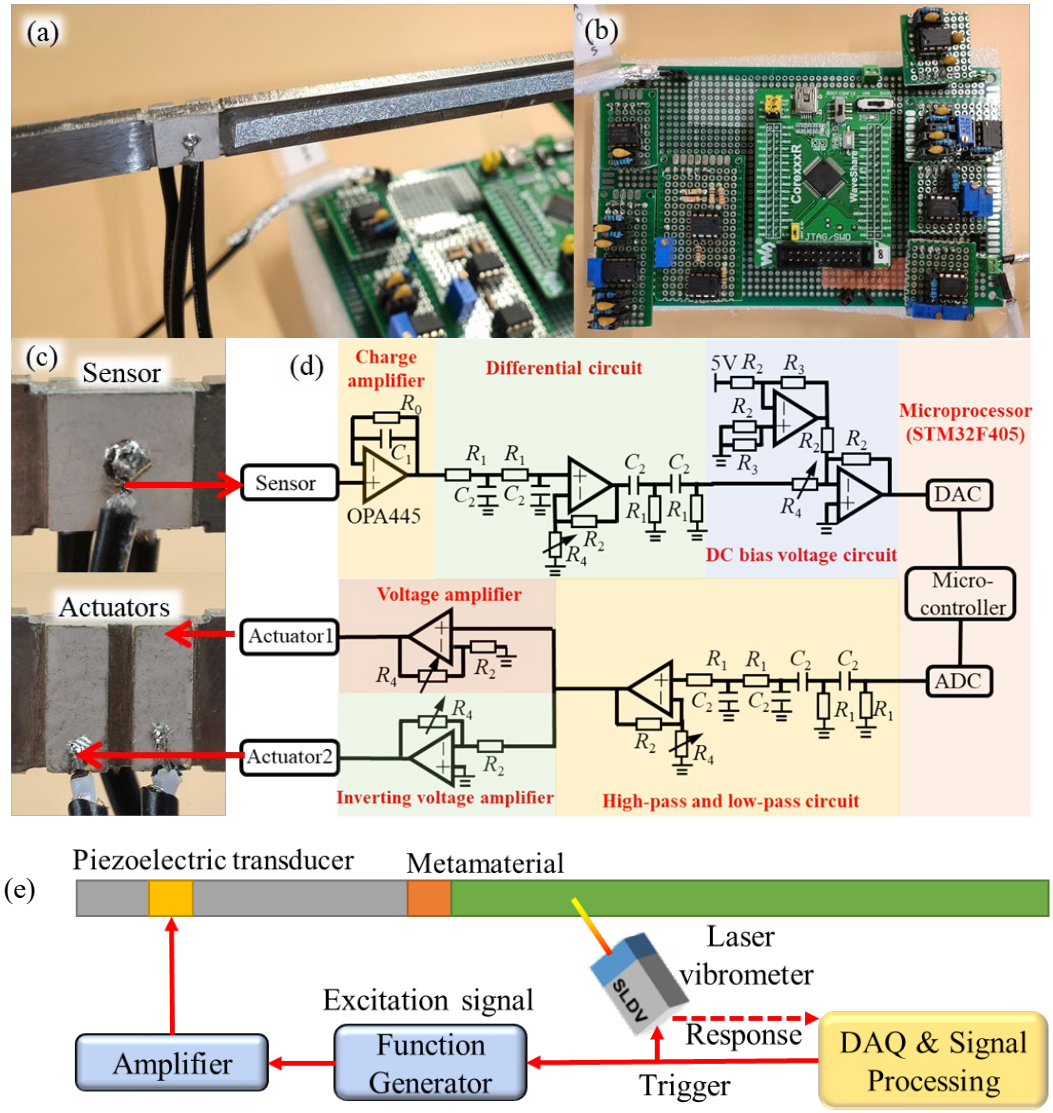

Figure 6.3: Experimental setup. (a) Photo of the time-modulated meta cell. (b) Photo of the circuit. (c) Photos of the sensor and actuators. (d) Illustration of the feed-forward control. (e) Illustration of the measurement process. In the experimental measurement, a piezoelectric patch is attached on the left side of the beam to generate incident flexural waves. 15-peak tone-burst signals, central frequencies are selected as 10 kHz, are generated by a signal generator (Tektronix AFG3022C) and amplified by a high voltage amplifier (Krohn-Hite), and then employed to the beam. Blu Tacks are attached to the both ends of the beam to absorb the reflected waves. The transverse velocity wave fields are measured on the surface of the beam by a scanning laser Doppler vibrometer (Polytec PSV-400). Reprinted figure with permission from Q. Wu, X. D. Zhang, P. Shivashankar, Y. Y. Chen, and G. L. Huang, Physical Review Letters, 128, 244301 (2022). Copyright (2022) by the American Physical Society.

Parameters	Values
C_1	10 pF
C_2	10 nF
R_0	100 MΩ
R_1	330 Ω
R_2	10 kΩ
R_3	3.3 kΩ
R_4	0∼100 kΩ

Table 6.1: Electrical components used in the experiments.

central frequency being 10 kHz as incident signals. The out-of-plane velocity field in the transmitted domain is measured using a scanning laser Doppler vibrometer. Figure 6.4 shows the transmitted wave signals in time and frequency domains measured from experiments (green solid curves). For comparison, corresponding time-dependent numerical simulations are performed using COMSOL Multiphysics (red dashed curves). In Fig. 6.4(a), frequency down conversion is realized by imposing $N = 1$, $\delta\omega_1 = -2\pi \times 1.5$ kHz, and $\phi_1 = 0$. The black dotted curve in the frequency domain represents the frequency components of the incident wave measured without the electrical control system. It can be clearly seen that the active meta-layer successfully converts the frequency from 10 to 8.5 kHz as desired, both experimentally and numerically. Importantly, no waves at other frequencies appear in the transmitted spectrum, in stark contrast with nonlinear and time-modulated materials. Similarly, the linear active meta-layer also supports frequency up conversion, i.e. from 10 to 11.5 kHz by enforcing $\delta\omega_1 = 2\pi \times 1.5$ kHz, as shown in Fig. 6.4(b). Note that small spectral discrepancies are visible between the experiments and simulations. This could result from the boundary reflection and signal minor distortion in the digital microcontroller, which are not properly considered in the numerical simulation and can result in wider band in the transmitted waves. In addition to the single-frequency conversion, the active meta-layer is capable to create frequency-comb signals. To demonstrate this, we let $V_a^{(0)}(t) = 0$, releasing the incident wave to the transmitted domain and impose $N = 2$ with $\delta\omega_1 = -2\pi \times 1.5$ kHz and $\delta\omega_2 = 2\pi \times 1.5$ kHz to actively emit waves with the other two frequency components. As shown in Fig. 6.4(c), the transmitted wave peaks at three frequencies, 8.5, 10, and 11.5 kHz, as demand. The quality factor of those peaks can be enhanced by impinging incident waves containing enough numbers of peaks in the tone-burst signals.

Dynamic control of flexural waves using time-modulated meta-layer

In addition to the demonstration of linear frequency conversion, we emphasize that the system is dynamically tunable by reprogramming the time-modulated transfer function. The wave cancellation

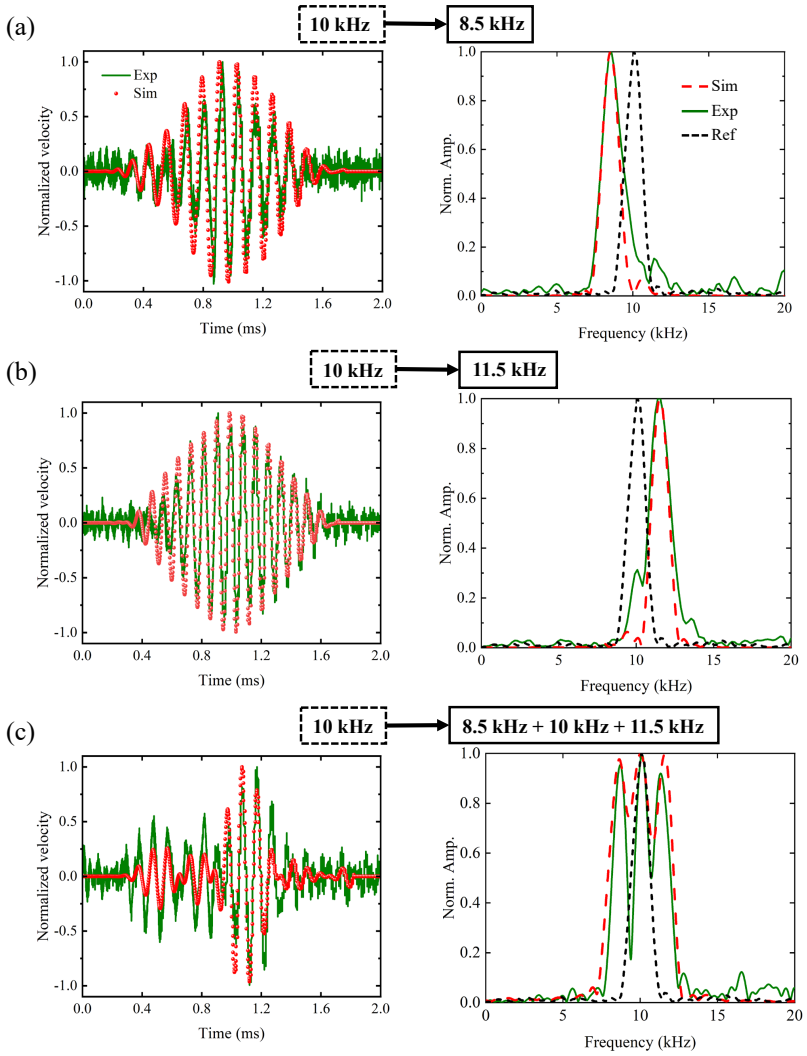

Figure 6.4: Demonstrations of the frequency shifting function in three typical scenarios: 10 kHz incidence is converted into (a) transmission of 8.5 kHz, (b) transmission of 11.5 kHz, and (c) transmission of $8.5 + 10 + 11.5$ kHz (frequency comb). The red and green curves represent the numerical and experimental results, respectively. The black dotted curves in the frequency spectra denote the incidence wave as the reference. Reprinted figure with permission from Q. Wu, X. D. Zhang, P. Shivashankar, Y. Y. Chen, and G. L. Huang, Physical Review Letters, 128, 244301 (2022). Copyright (2022) by the American Physical Society.

is realized experimentally. The measured time-domain signals and the corresponding converted frequency spectrum are presented in Fig. 6.5. It can be readily seen that the zero-order wave component is completely canceled at ω_0. The frequency components around ω_0 are heavily suppressed as well.

The frequency shifting function that simply shifts the incident frequency to one another can be obtained by adding another transfer function of generating higher-order waves in addition to the frequency cancelation. This has been explained theoretically by Eq. (6.7). As can be seen in Fig. 6.6,

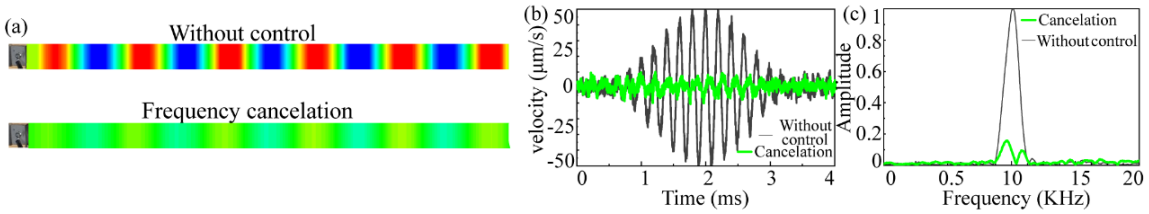

Figure 6.5: Frequency cancelation effect for the zero-order incidence ω_0. (a) Experimentally measured velocity fields. (b) Time-domain signals. (c) Frequency-domain signals. Reprinted figure with permission from Q. Wu, X. D. Zhang, P. Shivashankar, Y. Y. Chen, and G. L. Huang, Physical Review Letters, 128, 244301 (2022). Copyright (2022) by the American Physical Society.

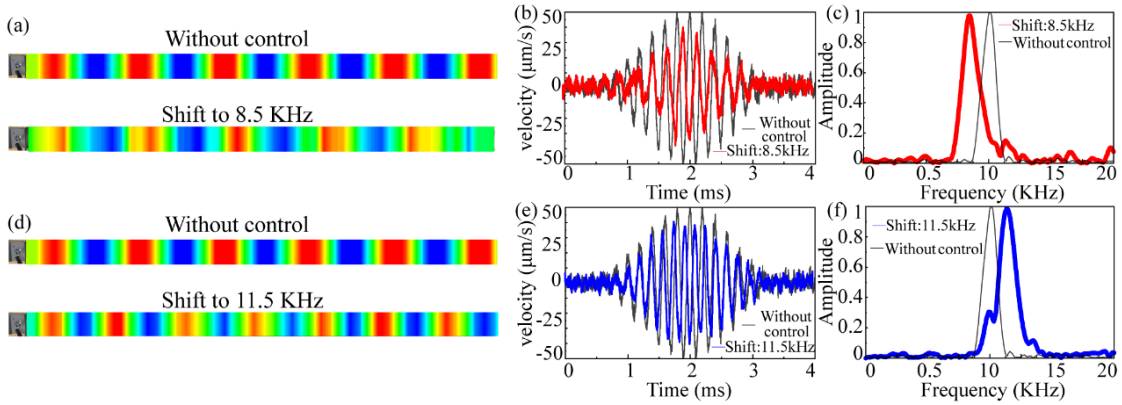

Figure 6.6: Frequency shifter. (a-c) Measured velocity fields, time-domain and frequency-domain signals for the frequency shifter that shifts 10 kHz to 8.5 kHz. (d-f) Measured velocity fields, time-domain and frequency-domain signals for the frequency shifter that shifts 10 kHz to 11.5 kHz. Reprinted figure with permission from Q. Wu, X. D. Zhang, P. Shivashankar, Y. Y. Chen, and G. L. Huang, Physical Review Letters, 128, 244301 (2022). Copyright (2022) by the American Physical Society.

the two first-order waves can be generated with the zero-order incidence getting canceled, achieving frequency shifting effect. We also provide the experimental measurement for arbitrary combination of different frequencies. In Figs. 6.7(a-d), the first-order waves along with the incident zero-order can be observed in the frequency spectra. In Figs. 6.7(e-f), we also show the combination of three wave components with two being the first-order and the other being the zero-order.

6.5 Programmable metasurfaces enabled by independent frequency conversion

Implementing an array of the linear active meta-layers to a plate enables spacial operations of the wavefront together with the frequency conversion. We first construct a phase-gradient meta-layer

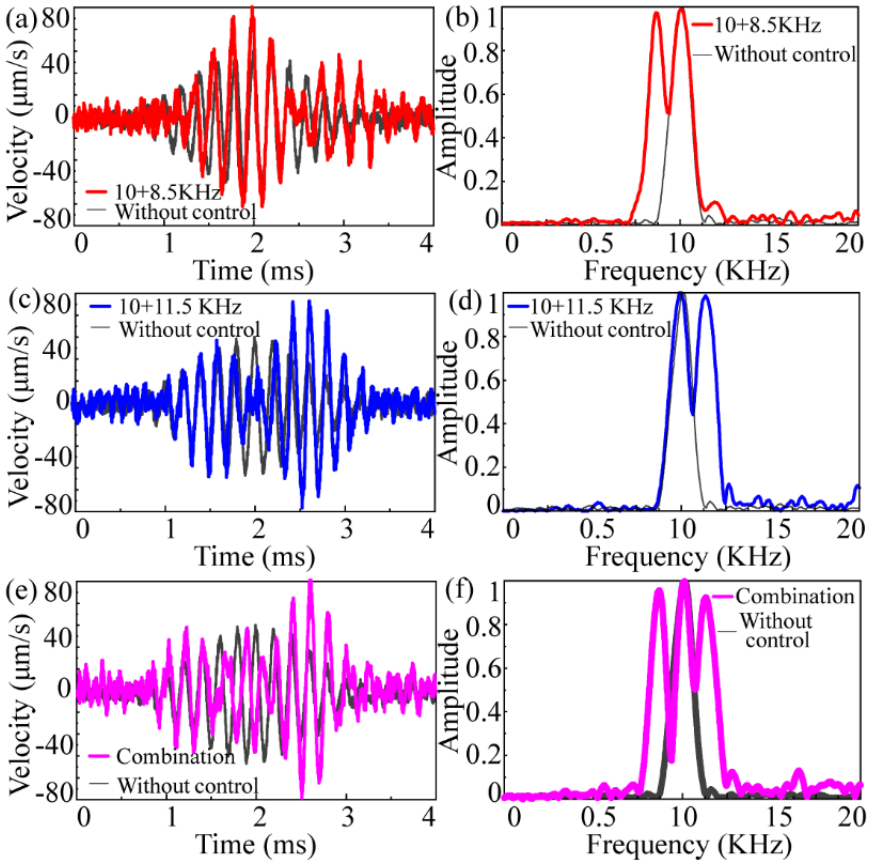

Figure 6.7: Frequency comb. (a-b) Measured time-domain and frequency-domain signals for the frequency comb 8.5 + 10 kHz. (c-d) Measured time-domain and frequency-domain signals for the frequency comb 10 + 11.5 kHz. (e-f) Measured time-domain and frequency-domain signals for the frequency comb 8.5 + 10 +11.5 kHz. Reprinted figure with permission from Q. Wu, X. D. Zhang, P. Shivashankar, Y. Y. Chen, and G. L. Huang, Physical Review Letters, 128, 244301 (2022). Copyright (2022) by the American Physical Society.

to steer the frequency-converted wave direction; see Fig. 6.10(a). In the simulations, we keep $\delta\omega_1$ and A_1 unchanged among each of the meta-layer units and ϕ_1 is arranged as a linear profile along the vertical direction. The phase difference between adjacent units is the key parameter of metasurface-related structures in achieving beam deflection with arbitrary angle of deflection. To demonstrate the phase difference generated by the prescribed phase of the transfer function ϕ_1, here we illustrate the simulation results. Figure 6.8 shows that with ϕ_1 changing from 0 to $13\pi/7$, the time delay is varied evenly, which straightforwardly illustrates the ability of the meta-layer to independently tune the phase of the transmitted higher-order waves. The numerical results shown in Fig. 6.2(c) are extracted directly from the simulations shown here in Fig. 6.9.

As shown in the upper panel of Fig. 6.10(b), the incident wave beam with the central frequency being 10 kHz is transformed to a beam with the central frequency becoming 11.5 kHz and, at the

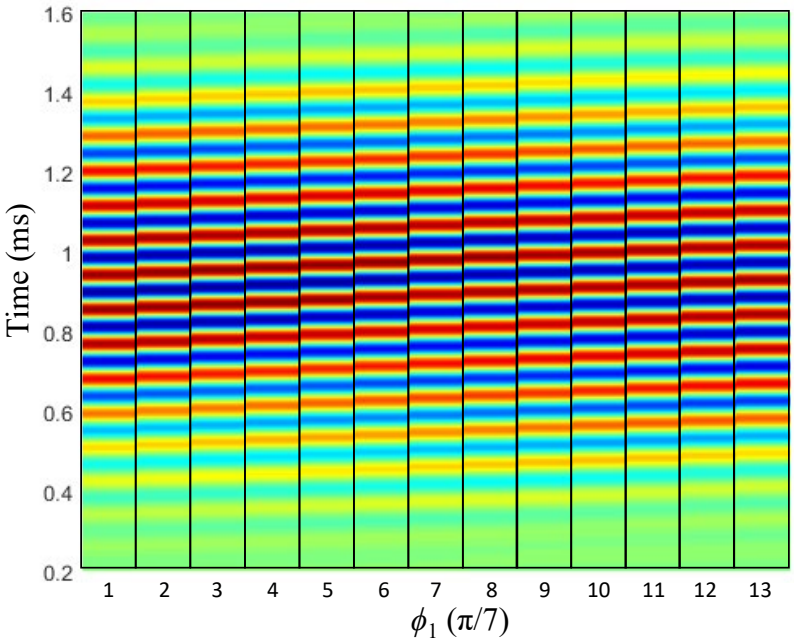

Figure 6.8: Time-domain signals at the output of the meta-layer for transmitted first-order wave component with various phases shift ϕ_1 at 10 kHz. Reprinted figure with permission from Q. Wu, X. D. Zhang, P. Shivashankar, Y. Y. Chen, and G. L. Huang, Physical Review Letters, 128, 244301 (2022). Copyright (2022) by the American Physical Society.

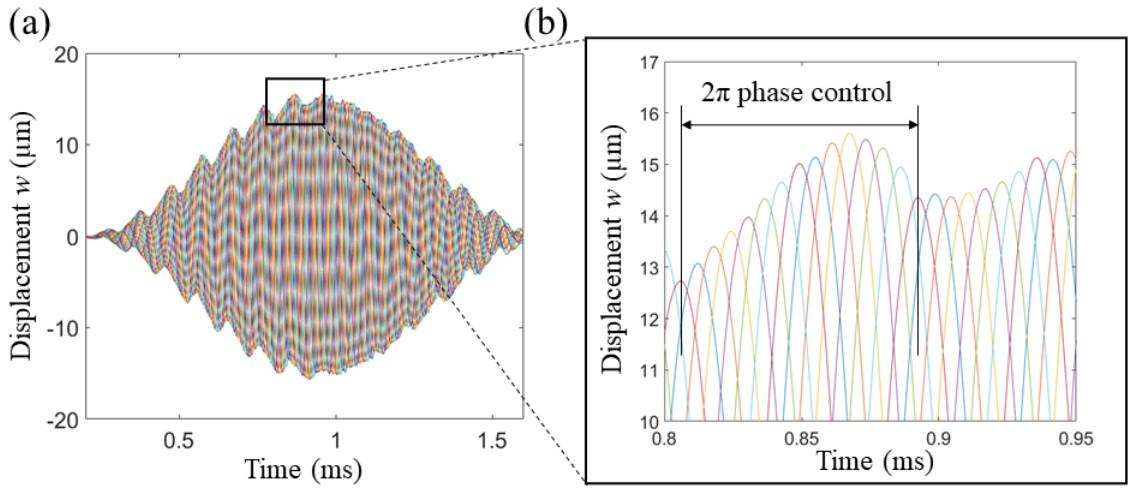

Figure 6.9: (a) Time-domain signals for transmitted first-order wave component at various phase shifts. (b) Magnified view of the time-domain signal in (a) for presenting the accurate 2π phase control. The excitation frequency is 10 kHz. Reprinted figure with permission from Q. Wu, X. D. Zhang, P. Shivashankar, Y. Y. Chen, and G. L. Huang, Physical Review Letters, 128, 244301 (2022). Copyright (2022) by the American Physical Society.

same time, steered to a direction of $\theta_1 = 19.2$ degrees, where $d\phi_1/dy = 0.13\pi$ rad/m. In addition, another frequency-converted wave steering with $\delta\omega_2 = -2\pi \times 1.5$ kHz and $d\phi_2/dy = -0.13\pi$ rad/m is performed. It is noticed that the incident wave beam is transformed into two beams with central

frequencies becoming 11.5 and 8.5 kHz, and steered to two directions of 19.2 and -22.4 degrees, respectively; see the lower panel in Fig. 6.10(b). Note that the mixing effect makes the two beams somewhat indistinguishable. This could be resolved by either considering a later time instant or enlarging the frequency difference of the output harmonics.

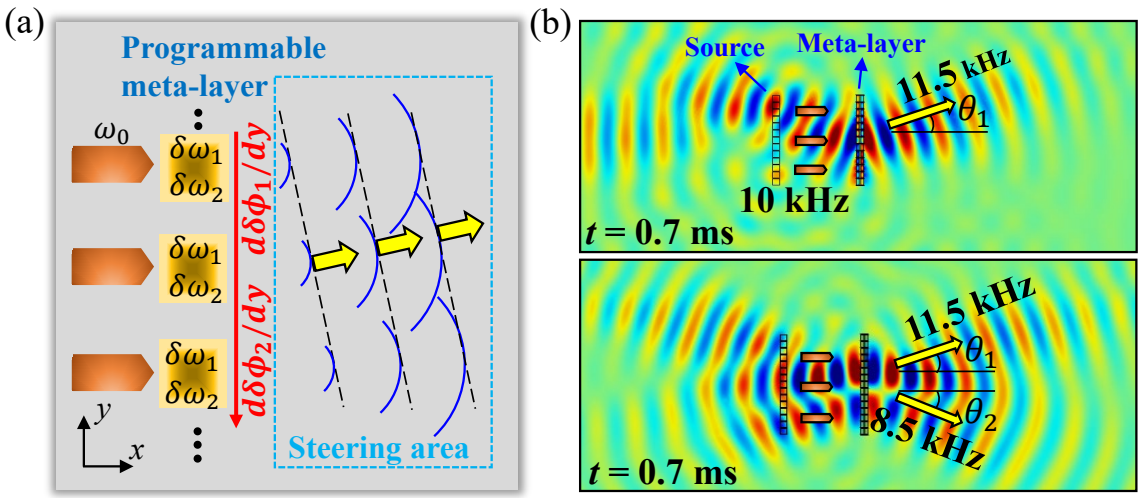

Figure 6.10: (a) Schematic of a phase-gradient programmable meta-layer that consists of 14 cells and features the flexural beam steering with frequency shifts. The red arrow indicates the phase gradient's direction. (b) Top panel shows flexural beam steering with the frequency shift $\delta\omega = 2\pi \times 1.5$ kHz and phase gradient $d\phi_1/dy = 0.13\pi$ rad/m, while the bottom shows the conversion into additional 8.5 kHz with a phase gradient $d\phi_2/dy = -0.13\pi$ rad/m, respectively. Both fields are obtained at 0.7 ms in the transient analysis. The inputs are set as 10 kHz, and the output wave directions are indicated by the yellow arrows. Reprinted figure with permission from Q. Wu, X. D. Zhang, P. Shivashankar, Y. Y. Chen, and G. L. Huang, Physical Review Letters, 128, 244301 (2022). Copyright (2022) by the American Physical Society.

Figure 6.11 shows the simulation model for the transient analysis. The plane wave excitation is achieved with an array of piezoelectric actuators. Since perfectly matched layers are disabled in time-domain simulations, here we use low-reflecting boundary conditions to define the edges of the host plate. The bottom panel of Fig. 6.11 clearly show the flexural wave distributions at 8 different time instants for the beam steering of generated first-order wave ($\omega_1 = 2\pi \times 8.5$ kHz). In particular, the field at $t = 0.7$ ms has been selected in the top panel of Fig. 6.10(b).

In addition, we illustrate a frequency-gradient meta-layer to realize dynamic wave steering, where the wave in the transmitted domain constantly changes its propagation direction in time; see Fig. 6.12(a) [182, 184]. To construct this meta-layer, we keep A_1 and ϕ_1 unchanged among each of the meta-layer units and organize a linear profile to $\delta\omega_1$ along the vertical direction. With this, flexural waves coming through each of the meta-layer units travel at different frequencies to collectively produce a flexural wave beam rotating in time thanks to the constructive wave interference (see

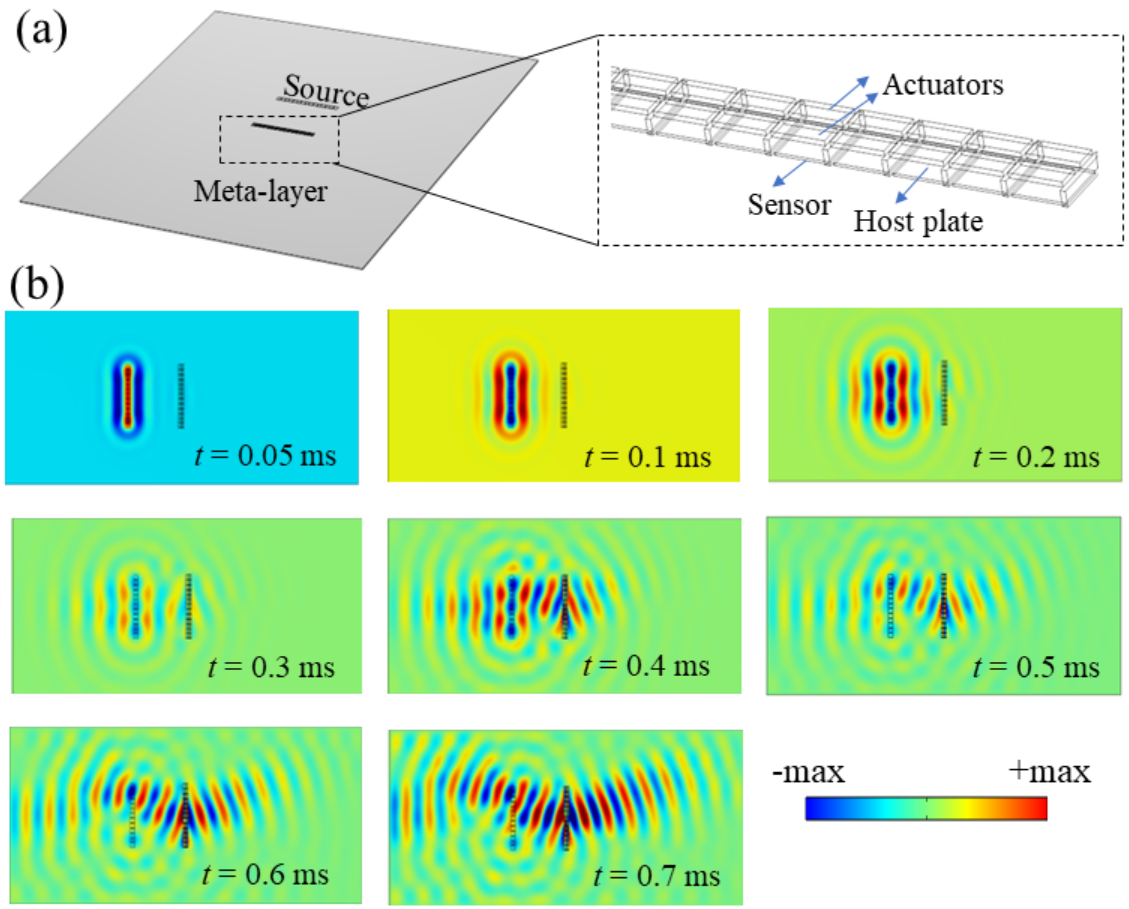

Figure 6.11: (a) Simulation model used in the frequency-shifted beam steering simulations. (b) Flexural field distributions at different time instants for the simulation shown in Fig. 4(b) of the main text. The color map of each figure is normalized to its own maximum. The excitation is 10 kHz. Reprinted figure with permission from Q. Wu, X. D. Zhang, P. Shivashankar, Y. Y. Chen, and G. L. Huang, Physical Review Letters, 128, 244301 (2022). Copyright (2022) by the American Physical Society.

Supplementary Information). Figures 6.12(b) and 6.12(c) show the simulated wave fields at different time steps with $d\delta\omega_1/dy = 2\pi \times 4.56$ and $2\pi \times 9.12$ kHz/m. Dynamic wave steering is clearly demonstrated, and a greater $d\delta\omega_1/dy$ induces faster angular speed of the wave beam.

To further characterize the wave manipulation by the dynamic beam steering, we first plot the dispersion diagram for flexural modes in a free plate in Fig. 6.13. In particular, we use the hue to distinguish the flexural modes from the others (longitudinal). Then, we proceed to present the analytical formulation of the flexural beam steering. The derivation is very similar to what has been presented in the optical counterpart [182, 184]. We assume all the meta units generate higher-order waves with the same amplitudes but different frequencies. Then the far-field spatio-temporal profile

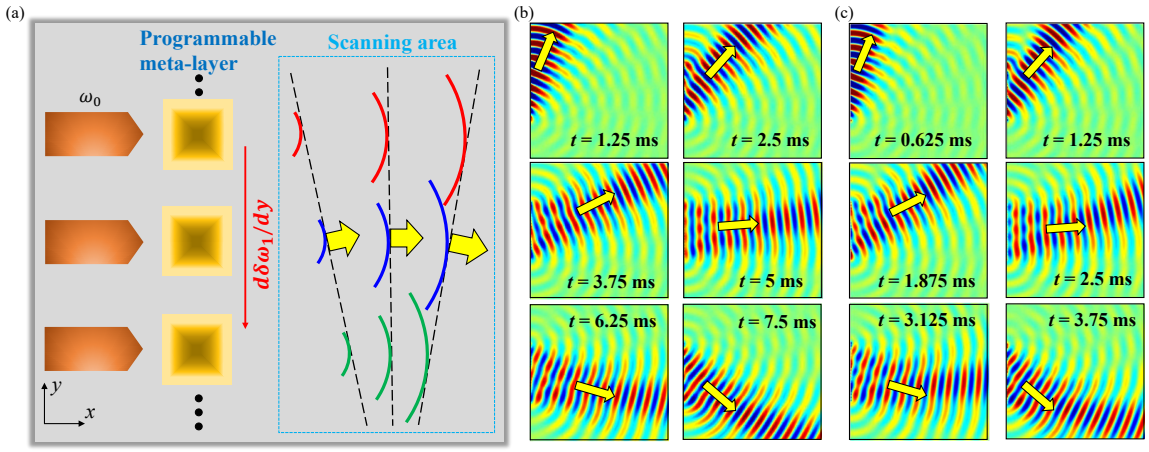

Figure 6.12: (a) Schematic of the frequency-gradient programmable meta-layer that contains 20 cells and provides dynamic control over the flexural beam steering as time progresses. The red arrow indicates the frequency gradient's direction. (b,c) Dynamic beam steering over time at the frequency gradients (b) $d\delta\omega_1/dy = 2\pi \times 4.56$ and (c) $2\pi \times 9.12$ kHz/m for 20 meta-layer units included. The inputs are set as 10 kHz, and the output wave directions are indicated by the yellow arrows at each time instant. Reprinted figure with permission from Q. Wu, X. D. Zhang, P. Shivashankar, Y. Y. Chen, and G. L. Huang, Physical Review Letters, 128, 244301 (2022). Copyright (2022) by the American Physical Society.

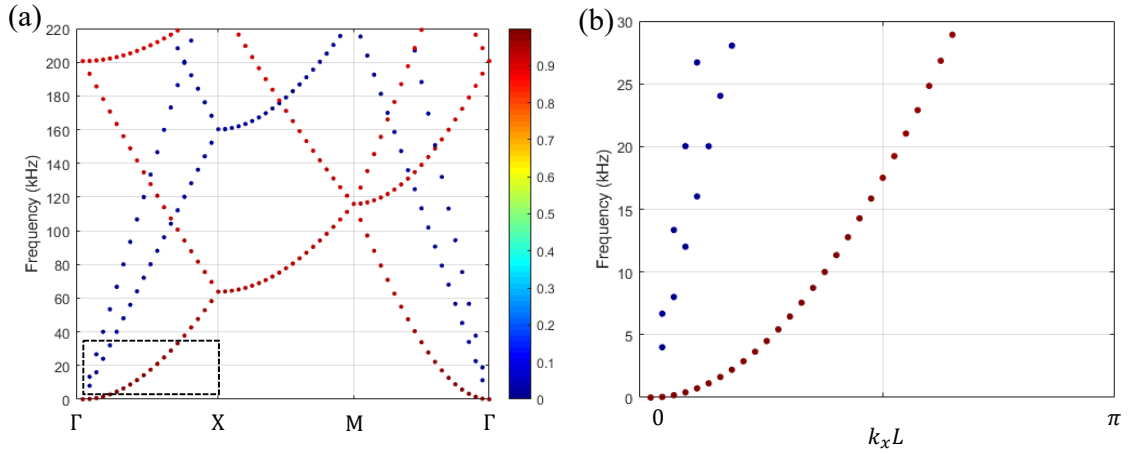

Figure 6.13: (a) Dispersion diagram for flexural wave mode in a free plate. The hue is defined as $\iiint_V \frac{|u_z|^2}{|u_x|^2+|u_y|^2+|u_z|^2} dV$ to distinguish the flexural modes from others. In the figure, the red color means flexural modes, whereas the blue means in-plane modes. (b) The magnified view of (a) at low frequencies. Reprinted figure with permission from Q. Wu, X. D. Zhang, P. Shivashankar, Y. Y. Chen, and G. L. Huang, Physical Review Letters, 128, 244301 (2022). Copyright (2022) by the American Physical Society.

takes the following form:

$$W(\boldsymbol{r}, t) = \sum_{n=-N}^{N} a_0 G(\boldsymbol{r} - \boldsymbol{r}_n) e^{i(k_n|\boldsymbol{r}-\boldsymbol{r}_n|-\omega_n t)}, \tag{6.9}$$

where a_0 denotes the transmitted wave magnitude, $\boldsymbol{r}_n = (0, nd)^T$ represents the position of the nth meta unit, $G(\boldsymbol{r} - \boldsymbol{r}_n)$ is a slowly varying-envelope describing the angular divergence of the radiation pattern, and $e^{ik_n|\boldsymbol{r}-\boldsymbol{r}_n|}$ is a fast-varying phase term. In the far-field region, $r \gg nd$, meaning that $G(\boldsymbol{r} - \boldsymbol{r}_n) \approx G(\boldsymbol{r})$ and $|\boldsymbol{r} - \boldsymbol{r}_n| \approx r + nd$. Assuming $\delta\omega \ll \omega_0$ and $\delta k \ll k_0$, we have, up to the first-order,

$$W(\boldsymbol{r}, t) \approx a_0 G(\boldsymbol{r}) e^{i(k_0 r - \omega_0 t)} \sum_{n=-N}^{N} e^{in(\delta k r + k_0 d \sin\theta - \delta\omega t)}, \tag{6.10}$$

where θ is the transverse angle in the cylindrical coordinate system. The above expression can be further modified into

$$W(\boldsymbol{r}, t) \approx 2a_0 G(\boldsymbol{r}) e^{i(k_0 r - \omega_0 t)} \sum_{n=0}^{N} \cos[n(\delta k r + k_0 d \sin\theta - \delta\omega t)]. \tag{6.11}$$

Since the steering beam is the result of constructive interference of the output wave components, the maximum intensity is always achieved when

$$\frac{r}{v} + \frac{k_0 d}{\delta\omega} \sin\theta - t = 0. \tag{6.12}$$

in which v denotes the group velocity. This means that the angular speed of the beam steering, $\frac{\sin\theta}{t - r/v}$, linearly scales with $\delta\omega/d$ at a certain r when we replace $t - r/v$ with another time term t'. Therefore, with the meta-layer unit spacing d fixed, the larger the frequency shift $\delta\omega$ is, the faster the beam is dynamically steered, which agrees with the numerical observations illustrated in Fig. 6.12 and leads to the same conclusion in the reported optical case [182, 184]. Since we have chosen $\delta\omega = 0.01\omega_0$ and $0.02\omega_0$ in the cases in the main text, the conditions $\delta\omega \ll \omega_0$ and $\delta k \ll k_0$ hold well, and the group velocity v within the considered spectral region barely changes ($\delta\omega$ and δk linearly scale); see Fig. 6.13. In addition, for dynamic beam steering in the demonstrations, we apply continuous sine waves. Wave dispersion can be ignored. Dispersion usually will not produce large impact on wave interference patterns, which are dominant by the phases of waves. While dispersion does influence how fast this wave package moves in space. After all, the flexural wave dispersion does not necessarily influence the dynamic beam steering here. The angular scanning speed is proportional to $\delta\omega/d$ for the choices of $\delta\omega$.

6.6 Summary

In summary, we introduce a linear active meta-layer for independent frequency conversion of flexural waves in elastic beam and plate. The active meta-layer is constructed in a beam by mounting piezoelectric elements connected with an electrical controller. The design embraces a feed-forward control loop that can naturally perform time-modulated independent parallel operations. We demonstrate the frequency conversion experimentally and numerically and prove independent wave frequency manipulation ability and its linearity. By implementing the linear active meta-layers in a plate, we also show wave beam steering of frequency-converted waves and dynamic beam steering using phase-gradient and frequency-gradient arrangements. Different from existing designs, the linear active meta-layer paves a way for fully control time-domain signals and wave energy of flexural waves. Furthermore, thanks to its simplicity, this active design can be easily extended to 2D and 3D active metamaterials for even more complicated wave manipulation and control.

Chapter 7

CONCLUSIONS

The dissertation introduces some conceptual metamaterial prototypes utilizing programmable piezoelectric shunts to break certain symmetry in order to observe asymmetry and nonreciprocity in elastic waves. By integrating analytical, numerical and experimental approaches, it has been demonstrated that the involved asymmetry and nonreciprocity are induced by the predefined interplay between the electrical and mechanical components of the active systems. First, by mapping the concept of non-Hermitian $\mathcal{PT}$ symmetry from optics onto elastics, the $\mathcal{PT}$ symmetry conditions for flexural waves have been theoretically and numerically examined in a 1D Euler-Bernoulli beam. Similar to the optical counterpart, this condition requires the bending stiffness and/or mass density to be symmetric in real part but antisymmetric in imaginary part. Shunted piezoelectric patches modulated with balanced positive and negative resistance can ensure this condition and cause the unidirectional reflectionlessness taking place at the exceptional points of the scattering matrix, where both eigenvalues and eigenvectors coalesce. The exceptional point separates the $\mathcal{PT}$-broken and $\mathcal{PT}$-unbroken phases for flexural wave propagation. The former breaks the conventional energy conservation law, while the latter does not. In the deeply subwavelength regime, the piezoelectric shunts with space-time modulation can be treated as a 1D metamaterial consisting of space-time modulated oscillator. With this in mind, the nonreciprocity of Rayleigh wave propagation has been investigated on the space-time modulated surface of a semi-infinite medium. The space-time modulation effectively breaks the time-reversal symmetry, and there exists nonreciprocal veering and locking pairs on the dispersion diagram. As a consequence, Rayleigh waves propagating along opposite directions around the nonreciprocal pairs undergo different conversion conditions. In other words, the wave and frequency conversion only takes place along one direction, exhibiting nonreciprocity of Rayleigh waves. It has also been pointed out that with a periodic, nonlocal connection of piezoelectric materials, modulated by certain transfer functions, similar nonreciprocity can take place for flexural

waves in a Timoshenko beam. Such a system shows both theoretically and experimentally that flexural waves experience either amplification or attenuation along one direction. Along the opposite direction, the situation is reversed. This is due to the parity symmetry broken by the nonlocal nonreciprocal interactions. The unidirectional amplification/attenuation can be well explained by the energy cycle of the additional bending stiffness induced by the nonlocal interactions. Additionally, the 1D non-Hermitian skin effect exists featuring a group of localized bulk modes on the open edges of a finite lattice. The nonreciprocity induced by nonlocal nonreciprocal interactions originates from the complex bending stiffness in the diagonal of the stiffness tensor. Later, another active solid, involving odd/asymmetric mass density tensor and featuring asymmetric off-diagonal terms, has been proposed to realize the nonreciprocity for in-plane motions. It has been shown for the first time that the odd mass density setup can achieve nonreciprocal wave coupling between the transverse and longitudinal in 1D. In 2D, it admits an energy phase transition which leads to directional wave amplification and attenuation. This behavior can be explained by the kinetic energy cycle of the odd mass. One of the main highlights of the odd mass density system is that the amplification behavior is tunable through tuning the electronic transfer function. the other highlight is the emergence of a group of bulk eigenmodes localized at the open edges of a 2D odd mass density solid. These bulk eigenmodes are the elastic manifestation of 2D non-Hermtian skin effect. The last part of the dissertation have proposed a linear active meta-layer powered by time-modulated transfer functions in a structural beam. It can convert a flexural incidence into flexural transmission of any frequencies, phases and amplitudes on demand. The system is linear, being irrelevant with incident amplitude, simply because of the time modulation of the sensing signal. The independent conversion among different frequencies is due to the parallel operation of each target frequency components by the time-dependent transfer function. More importantly, thanks to its comprehensive wave control capability, this meta-layer can serve as the building blocks of two novel active metasurfaces, conducting frequency-converted beam steering and dynamic beam steering for flexural waves in 2D.

The research of active elastic metamaterials has revolutionized the way of developing next-generation wave manipulation devices. It involves the knowledge in multiple seemingly independent areas such as mechanical, electrical engineering and control science. The interactions of the disciplines allow the active system to perform reconfigurable, adaptable and multifunctional tasks. As has been mentioned in the Introduction section, some conventional wave control strategies have been significantly influenced. For instance, much broader wave mitigation bandgaps and even multiple bandgaps coexisting can be pursued in a fairly simple structural platform with the help of active elastic metamaterials. This dissertation, benefiting from the advances in active elastic metamaterials,

propose some prototypes for demonstrating unconventional ways of manipulating elastic waves. These prototypes are scalable, and their principles could be properly mapped onto the micro/nano-scale scene. With the development of advanced manufacturing techniques in soft and flexible materials, active elastic metamaterials will impact upon the development of future multifunctional wave devices.

Appendix A

DERIVATION OF CHARACTERISTIC EQUATION OF RAYLEIGH WAVE TO THE LEADING ORDER

Due to the similarity between equations (3.11) and (3.12), we mainly focus on the derivation related to equation (3.11). By solving equation (3.11) for $D_1^j(z)$ and considering Rayleigh waves decaying toward $+z$-direction, the leading-order terms of the jth-order harmonic component of expression (3.9) reads

$$\Phi^j = A_1 e^{-q_j p_j z} e^{ij\xi} e^{i(\widetilde{q}x - \widetilde{\omega}t)}, \tag{A.1}$$

with $p_j = \sqrt{1 - \omega_j^2 / c_L^2 q_j^2}$. Similarly, one can obtain the leading-order shear potential function as

$$\Psi^j = B_1 e^{-q_j s_j z} e^{ij\xi} e^{i(\widetilde{q}x - \widetilde{\omega}t)} \tag{A.2}$$

with $s_j = \sqrt{1 - \omega_j^2 / c_T^2 q_j^2}$. In above equations, A_1 and B_1 are arbitrary wave amplitudes. Therefore, the leading-order terms of displacements u and w of the jth-order harmonic can be obtained as

$$u^j = \partial_x \Phi^j + \partial_z \Psi^j = q_j (i A_1 e^{-q_j p_j z} - s_j B_1 e^{-q_j s_j z}) e^{ij\xi} e^{i(\widetilde{q}x - \widetilde{\omega}t)} \tag{A.3}$$

$$w^j = \partial_z \Phi^j - \partial_x \Psi^j = -q_j (p_j A_1 e^{-q_j p_j z} + i B_1 e^{-q_j s_j z}) e^{ij\xi} e^{i(\widetilde{q}x - \widetilde{\omega}t)} \tag{A.4}$$

and the leading-order terms of the two stress components can be written as

$$\sigma_{zz}^j = \mu \, q_j^2 (r_j A_1 e^{-q_j p_j z} + 2 i s_j B_1 e^{-q_j s_j z}) \, e^{ij\xi} e^{i(\widetilde{q}x - \widetilde{\omega}t)} \tag{A.5}$$

$$\sigma_{xz}^j = \mu \, q_j^2 (-2 i p_j A_1 e^{-q_j p_j z} + r_j B_1 e^{-q_j s_j z}) \, e^{ij\xi} e^{i(\widetilde{q}x - \widetilde{\omega}t)}, \tag{A.6}$$

where μ is the shear modulus and $r_j = 2 - \omega_j^2/c_T^2 q_j^2$. On the other hand, the equation of motion of surface oscillators is written as

$$m\partial_t^2 Z^j + K_m \left(Z^j - w_{z=0}^j \right) = 0, \tag{A.7}$$

where Z^j is the jth-order harmonic component of the mass displacement up to the leading-order correction. Assuming a traveling wave solution reading $Z = \sum_{j\in\mathbb{Z}} Z_0^j e^{ij\xi} e^{i(\widetilde{q}x - \widetilde{\omega}t)}$ for the oscillator mass motion and keeping only the leading-order terms, equation (A.7) becomes then

$$Z^j = \frac{\Omega^2 w_{z=0}^j}{\Omega^2 - \omega_j^2}, \tag{A.8}$$

where $\Omega = \sqrt{K/m}$ represents the resonant frequency of the unperturbed oscillators. The exerted stress by the oscillators on the surface reads

$$\sigma_{zz}^{osc} = \frac{K_2(Z_0^j - w_0^j)}{A} = \frac{K\omega_j^2 w_{z=0}^j}{A\left(\Omega^2 - \omega_j^2\right)} \tag{A.9}$$

with A denoting the occupied area of each oscillator. Applying the boundary conditions $\sigma_{zz,z=0}^j = -\sigma_{zz}^{osc}$ and $\sigma_{xz,z=0}^j = 0$ and eliminating the two arbitrary wave amplitudes, we obtain the characteristic equation of leading-order correction which describes the Rayleigh wave dispersion in the presence of space-time modulated oscillators (see equation (3.14) in the main text).

Appendix B

DERIVATION OF ORTHOGONALITY CONDITION

Following the effective body forces given in the main text and considering the fact that the first-order correction terms are all periodic with respect to ξ, we take average on the forced governing equations to eliminate the propagating effect along the x-direction as

$$\begin{bmatrix} -q_0^2\left(2\mu+\lambda\right)+\mu\partial_z^2 & iq_0\left(\mu+\lambda\right)\partial_z \\ iq_0\left(\mu+\lambda\right)\partial_z & \left(2\mu+\lambda\right)\partial_z^2-q_0^2\mu \end{bmatrix}\delta\boldsymbol{\varphi}+\boldsymbol{F}=-\omega_0^2\rho\delta\boldsymbol{\varphi} \tag{B.1}$$

$$-K\left(\langle\delta Z\rangle-\langle\delta w_{z=0}\rangle\right)+\langle G\rangle=-\omega_0^2 m\langle\delta Z\rangle \tag{B.2}$$

$$\left(iq_0\mu\langle\delta w\rangle+\mu\partial_z\langle\delta u\rangle\right)_{z=0}=\langle H\rangle \tag{B.3}$$

$$\left[iq_0\lambda\langle\delta u\rangle+\left(2\mu+\lambda\right)\partial_z\langle\delta w\rangle\right]_{z=0}=-K/A\left(\langle\delta Z\rangle-\langle\delta w_{z=0}\rangle\right)+\langle I\rangle\,, \tag{B.4}$$

where the averaging operator takes the form of $\langle\rangle\equiv 1/2\pi\int_0^{2\pi}$. By projecting the governing equation (B.1) onto the complex conjugate mode shape $\boldsymbol{\varphi}^*$ and integrating over the semi-infinite space along the $+z$-direction, we have

$$\begin{aligned} &-iq_0\lambda\left(u^{ast}\langle\delta w\rangle\right)_{z=0}-\left[u^*\left(iq_0\mu\langle\delta w\rangle+\mu\partial_z\langle\delta u\rangle\right)\right]_{z=0}+\mu\left(\partial_z u^*\langle\delta u\rangle\right)_{z=0}\\ &-\left[u^*\left(iq_0\lambda\langle\delta u\rangle+\left(2\mu+\lambda\right)\partial_z\langle\delta w\rangle\right)\right]_{z=0}-iq_0\mu\left(w^*\langle\delta u\rangle\right)_{z=0}\\ &+\left(2\mu+\lambda\right)\left(\partial_z w^*\langle\delta w\rangle\right)_{z=0}+\int_0^\infty\boldsymbol{\varphi}^*\cdot\langle\boldsymbol{F}\rangle\,dz=0 \end{aligned} \tag{B.5}$$

The presence of the space-time modulation in this work makes the whole system a forced and non-Hermitian (non self-adjoint) system, which could be readily seen from equation (B.5) having been left multiplied by the complex conjugate eigenvector $\boldsymbol{\varphi}^*$ and right multiplied by $\delta\boldsymbol{\varphi}$ (being left multiplied by $\boldsymbol{\varphi}$ will simply lead to complex eigenvalues rather than the current negative, real ones). Following the notation in [185], this further implies the bi-orthogonality relation $\int_0^\infty\boldsymbol{\varphi}^*\boldsymbol{B}\delta\boldsymbol{\varphi}dz=0$,

where the operator $\boldsymbol{B}$ is an identity matrix in this work. In addition, the continuous part of the forced system has non-zero modulation-induced effective body force $\boldsymbol{F}$. As has been mentioned in the main text, in order for this system to remain stable, the body force needs to do deliver zero work within the entire semi-infinite medium, i.e. $\int_0^\infty \boldsymbol{\varphi}^* \cdot \langle \boldsymbol{F} \rangle \, dz = 0$ must hold, which returns equation (B.5) and corresponds to a continuous version of the discrete orthogonality condition presented in our recent paper [110]. Based on the governing equation (B.2) and boundary conditions (B.3) and (B.4), and considering the complex conjugates of the leading-order stress boundary conditions and the governing equation of motion of oscillators, we further simplify equation (B.5) into

$$\frac{m\omega_0^2}{A}\left(w^*_{z=0}\langle \delta Z\rangle - Z^*\langle \delta w_{z=0}\rangle\right) + w^*_{z=0}\left(\frac{\langle G\rangle}{A} - \langle I\rangle\right) - u^*_{z=0}\langle H\rangle + \int_0^\infty \boldsymbol{\varphi}^* \cdot \langle \boldsymbol{F}\rangle \, dz = 0 \quad \text{(B.6)}$$

Combining equations (3.13), (B.2) and (B.6), we reach eventually the orthogonality condition (3.28) in the main text.

$$w^*_{z=0}\left(\frac{Q_0}{A}\langle G\rangle - \langle I\rangle\right) - u^*_{z=0}\langle H\rangle + \int_0^\infty \boldsymbol{\varphi}^* \cdot \langle \boldsymbol{F}\rangle \, dz = 0. \quad \text{(B.7)}$$

Appendix C

DERIVATION OF THE FIRST-ORDER CORRECTION ON THE DISPERSION CURVES OF COUPLED MODES

Similar to the uncoupled scenario, we take average on the complete effective body forces for the coupled scenario in equation (3.33). In this case, the first-order harmonic $\boldsymbol{\varphi}^1$ is eliminated. The averaged effective body forces are the same as equation (3.29), except for the averaged body forces $\langle G\rangle^0$ and $\langle I\rangle^0$ taking different forms

$$\langle G\rangle^0 = -V_1 \left\langle \delta K e^{i\xi} \right\rangle \left(Z^1 - w^1_{z=0}\right) + 2m\omega_0 \delta\omega V_0 Z^0 \tag{C.1}$$

$$\langle I\rangle^0 = V_1 \frac{\left\langle \delta K\left(\xi\right) e^{i\xi} \right\rangle}{A} \left(Z^1 - w^1_{z=0}\right) - i\lambda\delta q V_0 u^0_{z=0}. \tag{C.2}$$

Multiplying the effective body forces (3.33) by $e^{-i\xi}$ and operating average simply gets rid of the fundamental harmonic $\boldsymbol{\varphi}^0$ and return the effective body forces of the first-order harmonic $\boldsymbol{\varphi}^1$.

$$\langle \boldsymbol{F}\rangle^1 = \begin{bmatrix} V_1\left[-2q_1\delta q\left(2\mu+\lambda\right) + 2\rho\omega_1\delta\omega\right]u^1 + i\left(\mu+\lambda\right)\delta q\partial_z V_1 w^1 \\ V_1\left[-2\mu q_1\delta q + 2\rho\omega_1\delta\omega\right]w^1 + i\left(\mu+\lambda\right)\delta q\partial_z V_1 u^1 \end{bmatrix} \tag{C.3}$$

$$\langle G\rangle^1 = -V_0 \left\langle \delta K e^{-i\xi} \right\rangle \left(Z^0 - w^0_{z=0}\right) + 2m\omega_1 \delta\omega V_1 Z^1 \tag{C.4}$$

$$\langle H\rangle^1 = -i\mu\delta q V_1 w^1_{z=0} \tag{C.5}$$

$$\langle I\rangle^1 = V_0 \frac{\left\langle \delta K\left(\xi\right) e^{-i\xi} \right\rangle}{A} \left(Z^0 - w^0_{z=0}\right) - i\lambda\delta q V_1 u^1_{z=0} \tag{C.6}$$

As can be seen from the expressions (C.1), (C.2), (C.4) and (C.6), the non-zero space-time modulation $\delta K\left(\xi\right)$ comes into play and gives rise to the interaction between modes $\boldsymbol{\varphi}^1$ and $\boldsymbol{\varphi}^0$. Substituting equations (3.29), (C.1), (C.2) and (C.3-C.6) into the orthogonality condition (3.28) yields equation

(3.34) in the main text.

$$\begin{bmatrix} \mathcal{E}_{11} & \mathcal{E}_{12} \\ \mathcal{E}_{21} & \mathcal{E}_{22} \end{bmatrix} \begin{bmatrix} V_0 \\ V_1 \end{bmatrix} = \boldsymbol{\mathcal{E}} \begin{bmatrix} V_0 \\ V_1 \end{bmatrix} = 0, \tag{C.7}$$

where

$$\begin{aligned} \mathcal{E}_{11} &= a_0\delta q + b_0\delta\omega \\ \mathcal{E}_{12} &= q_0 p_0 \frac{\delta K}{A}(1-\frac{2}{r_0})\left(Z^1 + q_1 p_1(1-\frac{2}{r_1})\right)(Q_0+1) \\ \mathcal{E}_{21} &= q_1 p_1 \frac{\delta K}{A}(1-\frac{2}{r_1})\left(Z^0 + q_0 p_0(1-\frac{2}{r_0})\right)(Q_1+1) \\ \mathcal{E}_{22} &= a_1\delta q + b_1\delta\omega \end{aligned} \tag{C.8}$$

and $\left\langle \delta K e^{i\xi} \right\rangle = \left\langle \delta K e^{-i\xi} \right\rangle = \delta K$.

Appendix D

DETAILS OF DERIVING THE CONVERSION PARAMETERS OF VEERING PAIRS

In this appendix, the derivation highly resembles that introduced in [110]. For the veering pairs discussed in the main text, we repeat the group velocities for the uncoupled harmonics:

$$v_g^0 = -\frac{a_0}{b_0}, \quad v_g^1 = -\frac{a_1}{b_1} \tag{D.1}$$

Substituting expression (D.1) into equation (3.36) and rearranging the resulting equation yields

$$\delta q_\pm = \frac{\delta\omega}{2}\left(\frac{1}{v_g^0}+\frac{1}{v_g^1}\right) \pm \sqrt{\left[\frac{\delta\omega}{2}\left(\frac{1}{v_g^0}-\frac{1}{v_g^1}\right)\right]^2 + \frac{\mathcal{E}_{12}\mathcal{E}_{21}}{b_0 b_1 v_g^0 v_g^1}} = \pm\delta q_a + \delta q_b. \tag{D.2}$$

By assuming a conversion coefficient $C = \frac{V_1}{V_0}$, we have

$$C_\pm = \left(\delta q_\pm - \frac{\delta\omega}{v_g^0}\right)\frac{b_0 v_g^0}{\mathcal{E}_{12}} = \left(\left(\frac{1}{v_g^1}-\frac{1}{v_g^0}\right)\delta\omega \pm \left(\delta q_+ - \delta q_-\right)\right)\frac{b_0 v_g^0}{2\mathcal{E}_{12}} = \pm C_a + C_b. \tag{D.3}$$

When the excitation frequency $\omega_0 + \delta\omega$ is close to the intersection frequency of the coupled mode ω_0, based on equations (D.2) and (D.3), the wave solution is a superposition of the two possible wave components

$$\begin{aligned}
\boldsymbol{\varphi}(x,t) &= \left(V_0\boldsymbol{\varphi}^0 e^{i(q_0 x-\omega_0 t)} + V_1\boldsymbol{\varphi}^1 e^{i(q_1 x-\omega_1 t)}\right)e^{i(\delta q x-\delta\omega t)} \\
&= \left[V_{0+}e^{i\delta q_a x}\left(\boldsymbol{\varphi}^0 e^{i(q_0 x-\omega_0 t)} + (C_a+C_b)\,\boldsymbol{\varphi}^1 e^{i(q_1 x-\omega_1 t)}\right)\right]e^{i(\delta q_b x-\delta\omega t)} \\
&+ \left[V_{0-}e^{-i\delta q_a x}\left(\boldsymbol{\varphi}^0 e^{i(q_0 x-\omega_0 t)} - (C_a-C_b)\,\boldsymbol{\varphi}^1 e^{i(q_1 x-\omega_1 t)}\right)\right]e^{i(\delta q_b x-\delta\omega t)}.
\end{aligned} \tag{D.4}$$

Without loss of generality, let us assume $x = 0$ is where the Rayleigh wave enters the modulated area. In order for $\boldsymbol{\varphi}^0$ to be the only existing one at $x = 0$, we take $V_{0\pm} = (C_a \mp C_b) V_0$. In this way, the previous solution (D.4) becomes

$$\begin{aligned}\boldsymbol{\varphi}(x,t) = 2V_0[&C_a \cos(\delta q_a x)\boldsymbol{\varphi}^0 e^{i(q_0 x - \omega_0 t)} - iC_b \sin(\delta q_a x)\boldsymbol{\varphi}^0 e^{i(q_0 x - \omega_0 t)} \\ &+ i\left(C_a^2 - C_b^2\right)\sin(\delta q_a x)\boldsymbol{\varphi}^1 e^{i(q_1 x - \omega_1 t)}]e^{i(\delta q_b x - \delta\omega t)}\end{aligned} \tag{D.5}$$

As x increases, the amplitude of $\boldsymbol{\varphi}^0$ decreases due to the fact that $|C_a| \geq |C_b|$ as long as the space-time modulation is turned on. Meanwhile, the amplitude of $\boldsymbol{\varphi}^1$ starts to increase. At $x = d = \pi/(2\delta q_a)$, $\boldsymbol{\varphi}^0$ reaches its minimum while $\boldsymbol{\varphi}^1$ reaches the maximum. Typically, the total conversion from $\boldsymbol{\varphi}^0$ to $\boldsymbol{\varphi}^1$ can be expected when $C_b = 0$, namely, $\delta\omega = 0$. In this case, we have the following expressions in the main text.

$$\delta q_\pm = \pm\sqrt{\frac{\mathcal{E}_{12}\mathcal{E}_{21}}{b_0 b_1 v_g^0 v_g^1}}, \quad C_\pm = \pm\frac{b_0 v_g^0}{\mathcal{E}_{12}}\sqrt{\frac{\mathcal{E}_{12}\mathcal{E}_{21}}{b_0 b_1 v_g^0 v_g^1}}. \tag{D.6}$$

Appendix E

NUMERICAL VALIDATION OF THE UNMODULATED MODEL

To verify the theoretical part, we conduct numerical simulations using a commercial software COMSOL Multiphysics. In the theoretical section, we assume a continuous span of spring-mass oscillators whose spring constants are space-time modulated in a wave-like fashion. However, in real cases the distribution of oscillators cannot be continuous. In order to effectively model the continuous section, we construct discrete spring-mass oscillators separated by spacing l_s, as shown in Fig. 3.1, with the help of lumped mechanical system module, as shown in Fig. E.1(a). At first, we start with unmodulated spring-mass oscillators to validate the simulation model. The parameters used here are identical to those used in the theoretical section (Fig. 3.1). As shown in Fig. E.1(a), the numerically modeled supercell is shown with its top surface decorated by five non-modulated spring-mass oscillators ($\delta K = 0$). The spacing is chosen as $l_s = \lambda_m/20$. Since the chosen spacing is much smaller than the operating wavelength, according to the long wavelength assumption, the discrete oscillators can be equivalently treated as a continuous spring-mass layer at the surface. The low-reflecting boundary (LRB) condition is applied on the bottom boundary of the supercell for diminishing the undesired reflection of bulk waves from the bottom. The supercell is bounded horizontally by two vertical Floquet periodic boundaries highlighted in blue. In this way, the supercell well represents a horizontally infinite system. Discrete points are distributed on the top surface, corresponding to the spring-mass oscillators. The displacements w at the bottom ends of springs are extracted at the points on the top surface. By contrast, the forces F exerted by the oscillators on the top surface is calculated at the bottom ends of springs and then is applied on the discrete points. The modal analysis gives the calculated bulk band structure shown in the left panel of Fig. E.1(b). The analytical and numerical obtained upper and lower branches are in good agreement. The existence

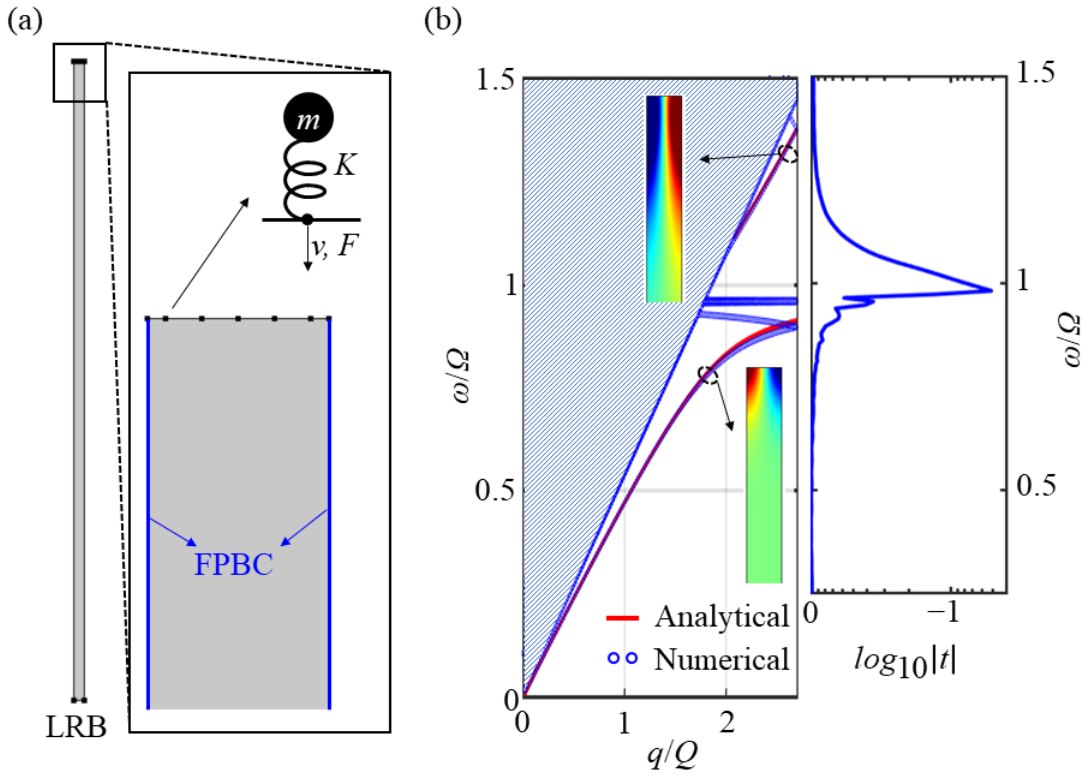

Figure E.1: (a) Schematic illustration of the supercell which represents a horizontally infinite semi-infinite medium decorated by non-modulated ($\delta K = 0$) spring-mass oscillators on the top surface. The discrete points represent the spring-mass oscillators. The top surface is set free while the bottom one is set with low-reflecting boundary condition (LRB). The two highlighted in blue are Floquet periodic boundary conditions. The z-directional displacement and the exerted force by the oscillators are recorded and extracted at the contact point. (b) The bulk band structure obtained from the modal analysis of the supercell is shown in the left panel. The numerical and analytical results agree well, except for the zone-folding curves. The mode shapes of the two highlighted branches are also extracted. The corresponding transmission coefficient, shows band gap for the Rayleigh wave around the resonance frequency, which exhibits great agreement with the supercell analysis. Reproduced from Journal of the Mechanics and Physics of Solids 146, 104196 (2021), with the permission of Elsevier Publishing.

of additional numerically obtained bands, which do not appear in the analytical section, is due to the zone folding since the supercell corresponds to a reducible lattice cell. The mode shapes for the upper (optical) and lower (acoustic) branches are also shown in the insets. They are out-of-phase due to the fact that the band gap is generated by the local resonance. To further verify the model, we construct an array of 600 non-modulated oscillators. Frequency-domain simulation produces the transmission coefficient which is shown in the right panel of Fig. E.1(b). A band gap for the Rayleigh wave can be visualized, which agrees well with the modal analysis results. This further proves the validity of our simulation models.

Appendix F

HOMOGENIZATION OF METAMATERIAL UNIT CELL WITH ODD MASS DENSITY

Effective properties of the odd mass metamaterial are obtained at the homogenization limit. The frequency-dependent effective mass density tensor is numerically obtained using COMSOL Multiphysics solid mechanics module by imposing a prescribed displacement $\mathbf{u}_P$ at the boundaries such that

$$\mathbf{F}^R = -\omega^2 V \begin{pmatrix} \hat{M}_{11} & \hat{M}_{12} \\ \hat{M}_{21} & \hat{M}_{22} \end{pmatrix} \mathbf{u}_P, \tag{F.1}$$

where $\mathbf{F}^R$, ω and V denote the boundary reaction forces, operating frequency and unit cell volume, respectively [148]. For instance, with the application of $\mathbf{u}_P = (1,0)^{\mathrm{T}}$ at the boundaries, integrating the reaction forces $\mathbf{F}_x^R$ and $\mathbf{F}_y^R$ allows to determine the entries $\hat{M}_{11}$ and $\hat{M}_{21}$ using Eq. F.1.

The retrieval of elasticity tensor $\mathbf{C}$ for the odd mass metamaterial requires specific boundary conditions [149, 150]. In the retrieval, at all the boundaries we apply a global strain field $\boldsymbol{u}_{pre} = \mathbf{E}\boldsymbol{r}e^{i\omega t}$, where $\boldsymbol{r}$ denotes the position vector of each discrete meshing point on the boundaries and

$$\mathbf{E} = \begin{pmatrix} \mathrm{E}_{11}^0 & \mathrm{E}_{12}^0 \\ \mathrm{E}_{21}^0 & \mathrm{E}_{22}^0 \end{pmatrix}. \tag{F.2}$$

Accordingly, the prescribed strain fields are given, respectively, by

$$\mathbf{E}_1 = \begin{pmatrix} 1 & 0 \\ 0 & 0 \end{pmatrix} \boldsymbol{r}, \tag{F.3}$$

$$\mathbf{E}_2 = \begin{pmatrix} 0 & 1 \\ 0 & 0 \end{pmatrix} \boldsymbol{r}, \tag{F.4}$$

$$\mathbf{E}_3 = \begin{pmatrix} 0 & 0 \\ 1 & 0 \end{pmatrix} \boldsymbol{r}, \tag{F.5}$$

$$\mathbf{E}_4 = \begin{pmatrix} 0 & 0 \\ 0 & 1 \end{pmatrix} \boldsymbol{r}. \tag{F.6}$$

The resulting stress is evaluated by the integration of the corresponding reaction forces at all the boundaries of the unit cell. The 16 entries of $\mathbf{C}$ are determined by establishing 16 equations from the selection of the prescribed global strain and evaluated stress.

Appendix G

SAMPLE FABRICATION AND EXPERIMENTAL PROCEDURE FOR ODD-MASS-DENSITY METAMATERIAL

Sample fabrication

The odd-mass metamaterial beam in experiments is constructed by mounting four piezoelectric patches (PZT-5A, 5 mm $\times$ 0.55 mm $\times$0.55 mm) via conductive epoxy onto a laser-cut stainless steel host beam. The two actuating piezoelectric patches are oppositely polarized such that the two vertical beams are bent producing forces applied on the central block and the surrounding material.

Experimental procedures

In experiments, an odd mass metamaterial unit cells is connected with external control circuits, see the schematics in Fig. 5.4 and Figs. G.1 and G.2 for more details about the experimental setup. Two piezoelectric transducers are attached on the top and bottom sides of host beam to generate transverse incidence. The transfer function used reads $\mathrm{H}(\omega) = H_0/(\omega^2/\omega_0^2 + 2\xi\omega/\omega_0 + 1)$, where $H_0 = 2 \times 10^8$, $\xi = 0.5$ and $\omega_0 = 2\pi \times 15$ kHz. We employ 15-cycle tone-burst signals with a central frequency of 11.3 kHz. We generate and amplify incident wave signals via an arbitrary waveform generator (Tektronix AFG3022C) and a high voltage amplifier (Krohn-Hite), respectively. In-plane velocity wave fields for u and v are measured on the surface of the right side of the metamaterial by a scanning laser Doppler vibrometer (Polytec PSV-400). To suppress reflected waves at the boundaries of the host beam, we clamp the edge and bond two layers of clay on the host beam with sufficient lengths. This way, waves can propagate through the metamaterial with approximated infinite boundary conditions in the background. The time-domain signals shown in Fig. 5.4 are

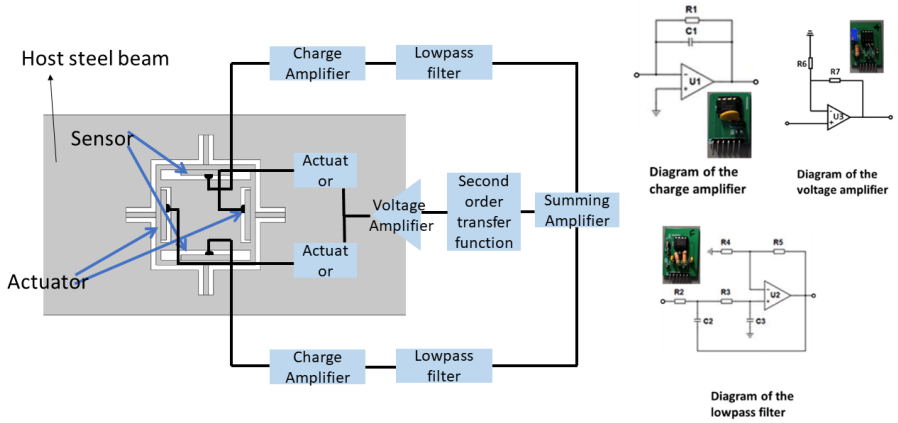

Figure G.1: Circuit diagram of the unit cell for the nonreciprocal wave coupling. The resulting transfer function reads $\mathrm{H}(\omega) = H_0/(\omega^2/\omega_0^2 + 2\xi\omega/\omega_0 + 1)$, where $H_0 = 2 \times 10^8$, $\xi = 0.5$ and $\omega_0 = 2\pi \times 15$ kHz.

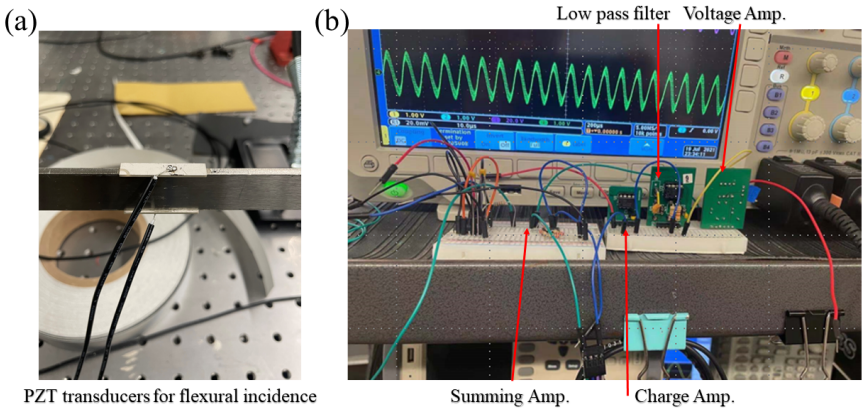

Figure G.2: (a) The photo of the PZT transducer which consists of two PZT-5A patches placed in parallel. This arrangement allows to generate transverse incidence. (b) The photo of the electrical control circuits, including low pass filter, voltage amplifier, summing amplifier and charge amplifier.

collected 120 mm away from the right boundary of the odd-mass metamaterial.

Appendix H

TRANSFER MATRIX METHOD FOR 1D NONRECIPROCAL WAVE COUPLING

Here, we utilize the transfer matrix method to analytically derive the transmission for the one-dimensional nonreciprocal wave coupling phenomenon. The unit cell design is shown in Fig. 5.3(a). The wave numbers read

$$q_l = \sqrt{\rho_b \omega^2 / E_b}, \tag{H.1}$$

$$q_b = (\rho_b A \omega^2 / D)^{1/4}, \tag{H.2}$$

$$q_{lm} = \sqrt{\rho_b \omega^2 / E_m}, \tag{H.3}$$

$$q_{bm} = (\rho_b A_0 \omega^2 / D_{b0})^{1/4}, \tag{H.4}$$

$$q_{lm1} = \sqrt{\rho_{b1} \omega^2 / E_{m1}}. \tag{H.5}$$

where

$$D_{b2} = 2D_{b0}, \tag{H.6}$$

$$K_b = E_b A, \tag{H.7}$$

$$K_m = E_m A_0, \tag{H.8}$$

$$K_1 = E_{m1} A. \tag{H.9}$$

At $x = -L$ and $x_1 = -L_1$,

$$\mathbf{M0}_n = \begin{bmatrix} 1 & 1 & 0 & 0 & 0 & 0 \\ iq_l K_b & -iq_l K_b & 0 & 0 & 0 & 0 \\ 0 & 0 & 1 & 1 & 1 & 1 \\ 0 & 0 & iq_b & -iq_b & q_b & -q_b \\ 0 & 0 & -q_b^2 D & -q_b^2 D & q_b^2 D & q_b^2 D \\ 0 & 0 & -iq_b^3 D & iq_b^3 D & q_b^3 D & -q_b^3 D \end{bmatrix} \begin{bmatrix} e^{-iq_l L_1} \\ e^{iq_l L_1} \\ e^{-iq_b L} \\ e^{iq_b L} \\ e^{-q_b L} \\ e^{q_b L} \end{bmatrix} \tag{H.10}$$

$$\mathbf{M}_{1n} = \begin{bmatrix} 1 & 1 & 0 & 0 & 0 & 0 \\ iq_{lm1} K_1 & -iq_{lm1} K_1 & 0 & 0 & 0 & 0 \\ 0 & 0 & 1 & 1 & 1 & 1 \\ 0 & 0 & iq_{bm} & -iq_{bm} & q_{bm} & -q_{bm} \\ 0 & 0 & -q_{bm}^2 D_{b2} & -q_{bm}^2 D_{b2} & q_{bm}^2 D_{b2} & q_{bm}^2 D_{b2} \\ 0 & 0 & -iq_{bm}^3 D_{b2} & iq_{bm}^3 D_{b2} & q_{bm}^3 D_{b2} & -q_{bm}^3 D_{b2} \end{bmatrix} \begin{bmatrix} e^{-iq_{lm1} L_1} \\ e^{iq_{lm1} L_1} \\ e^{-iq_{bm} L} \\ e^{iq_{bm} L} \\ e^{-q_{bm} L} \\ e^{q_{bm} L} \end{bmatrix} \tag{H.11}$$

$$\mathbf{N}_{1n} = \begin{bmatrix} 0 & 0 & 0 & 0 & 0 & 0 \\ 0 & 0 & 0 & 0 & 0 & 0 \\ 0 & 0 & 0 & 0 & 0 & 0 \\ 0 & 0 & 0 & 0 & 0 & 0 \\ 0 & 0 & 0 & 0 & iK_m dq_{lm} e^{-iq_{lm} L} & -iK_m dq_{lm} e^{iq_{lm} L} \\ 0 & 0 & 0 & 0 & -K_m dq_{lm}^2 e^{-iq_{lm} L} & -K_m dq_{lm}^2 e^{iq_{lm} L} \end{bmatrix} \tag{H.12}$$

At $x = L$ and $x_1 = L_1$,

$$\mathbf{M0}_p = \begin{bmatrix} 1 & 1 & 0 & 0 & 0 & 0 \\ iq_l K_b & -iq_l K_b & 0 & 0 & 0 & 0 \\ 0 & 0 & 1 & 1 & 1 & 1 \\ 0 & 0 & iq_b & -iq_b & q_b & -q_b \\ 0 & 0 & -q_b^2 D & -q_b^2 D & q_b^2 D & q_b^2 D \\ 0 & 0 & -iq_b^3 D & iq_b^3 D & q_b^3 D & -q_b^3 D \end{bmatrix} \begin{bmatrix} e^{iq_l L_1} \\ e^{-iq_l L_1} \\ e^{iq_b L} \\ e^{-iq_b L} \\ e^{q_b L} \\ e^{-q_b L} \end{bmatrix} \tag{H.13}$$

$$\mathbf{M}_{1p} = \begin{bmatrix} 1 & 1 & 0 & 0 & 0 & 0 \\ iq_{lm1}K_1 & -iq_{lm1}K_1 & 0 & 0 & 0 & 0 \\ 0 & 0 & 1 & 1 & 1 & 1 \\ 0 & 0 & iq_{bm} & -iq_{bm} & q_{bm} & -q_{bm} \\ 0 & 0 & -q_{bm}^2 D_{b2} & -q_{bm}^2 D_{b2} & q_{bm}^2 D_{b2} & q_{bm}^2 D_{b2} \\ 0 & 0 & -iq_{bm}^3 D_{b2} & iq_{bm}^3 D_{b2} & q_{bm}^3 D_{b2} & -q_{bm}^3 D_{b2} \end{bmatrix} \begin{bmatrix} e^{iq_{lm1}L_1} \\ e^{-iq_{lm1}L_1} \\ e^{iq_{bm}L} \\ e^{-iq_{bm}L} \\ e^{q_{bm}L} \\ e^{-q_{bm}L} \end{bmatrix} \tag{H.14}$$

$$\mathbf{N}_{1p} = \begin{bmatrix} 0 & 0 & 0 & 0 & 0 & 0 \\ 0 & 0 & 0 & 0 & 0 & 0 \\ 0 & 0 & 0 & 0 & 0 & 0 \\ 0 & 0 & 0 & 0 & 0 & 0 \\ 0 & 0 & 0 & 0 & iK_m dq_{lm} e^{iq_{lm}L} & -iK_m dq_{lm} e^{-iq_{lm}L} \\ 0 & 0 & 0 & 0 & -K_m dq_{lm}^2 e^{iq_{lm}L} & -K_m dq_{lm}^2 e^{-iq_{lm}L} \end{bmatrix} \tag{H.15}$$

At $x = 0$,

$$\mathbf{M}_{10} = \begin{bmatrix} 1 & 1 & 0 & 0 & 0 & 0 \\ iq_{lm1}K_1 & -iq_{lm1}K_1 & 0 & 0 & 0 & 0 \\ 0 & 0 & 1 & 1 & 1 & 1 \\ 0 & 0 & iq_{bm} & -iq_{bm} & q_{bm} & -q_{bm} \\ 0 & 0 & -q_{bm}^2 D_{b2} & -q_{bm}^2 D_{b2} & q_{bm}^2 D_{b2} & q_{bm}^2 D_{b2} \\ 0 & 0 & -iq_{bm}^3 D_{b2} & iq_{bm}^3 D_{b2} & q_{bm}^3 D_{b2} & -q_{bm}^3 D_{b2} \end{bmatrix} \tag{H.16}$$

$$\mathbf{N}_{10} = \begin{bmatrix} 0 & 0 & 0 & 0 & 0 & 0 \\ 0 & 0 & 0 & 0 & 0 & 0 \\ 0 & 0 & 0 & 0 & 0 & 0 \\ 0 & 0 & 0 & 0 & 0 & 0 \\ 0 & 0 & 0 & 0 & 0 & 0 \\ 0 & 0 & 0 & 0 & -K_m dq_{lm}^2 & -K_m dq_{lm}^2 \end{bmatrix} \tag{H.17}$$

$$\mathbf{T}_1 = \begin{bmatrix} 1 & 1 & -1 & -1 \\ iq_{lm}K_m d^2 & -iq_{lm}K_m d^2 & -iq_{lm}K_m d^2 & iq_{lm}K_m d^2 \\ e^{-iq_{lm}L} & e^{iq_{lm}L} & 0 & 0 \\ 0 & 0 & e^{iq_{lm}L} & e^{-iq_{lm}L} \end{bmatrix} \tag{H.18}$$

$$\mathbf{T}_2 = \begin{bmatrix} 0 & 0 & 0 & 0 \\ e^{-iq_{bm}L}\omega^2 m_I/L & e^{iq_{bm}L}\omega^2 m_I/L & e^{-q_{bm}L}\omega^2 m_I/L & e^{q_{bm}L}\omega^2 m_I/L \\ -iq_{bm}e^{-iq_{bm}L} & iq_{bm}e^{iq_{bm}L} & -q_{bm}e^{-q_{bm}L} & q_{bm}e^{q_{bm}L} \\ 0 & 0 & 0 & 0 \end{bmatrix}$$
$$\begin{bmatrix} 0 & 0 & 0 & 0 \\ -e^{iq_{bm}L}\omega^2 m_I/L & -e^{-iq_{bm}L}\omega^2 m_I/L & -e^{q_{bm}L}\omega^2 m_I/L & -e^{-q_{bm}L}\omega^2 m_I/L \\ 0 & 0 & 0 & 0 \\ -iq_{bm}e^{iq_{bm}L} & iq_{bm}e^{-iq_{bm}L} & -q_{bm}e^{q_{bm}L} & q_{bm}e^{-q_{bm}L} \end{bmatrix} \tag{H.19}$$

$$\mathbf{Tn} = \mathbf{T}_1^{-1}\mathbf{T}_2. \tag{H.20}$$

$$\mathbf{Tn}_{f11}(5:6, 3:6) = \mathbf{Tn}(1:2, 1:4), \tag{H.21}$$

$$\mathbf{Tn}_{f12}(5:6, 3:6) = \mathbf{Tn}(1:2, 5:8), \tag{H.22}$$

$$\mathbf{Tn}_{f21}(5:6, 3:6) = \mathbf{Tn}(3:4, 1:4), \tag{H.23}$$

$$\mathbf{Tn}_{f22}(5:6, 3:6) = \mathbf{Tn}(3:4, 5:8). \tag{H.24}$$

The rest entries of $\mathbf{Tn}$ are zeros.

$$\mathbf{F} = \begin{bmatrix} 0 & 0 & 0 & 0 & 0 & 0 \\ \omega^2\hat{M}_{11} & \omega^2\hat{M}_{11} & \omega^2\hat{M}_{12} & \omega^2\hat{M}_{12} & \omega^2\hat{M}_{12} & \omega^2\hat{M}_{12} \\ 0 & 0 & 0 & 0 & 0 & 0 \\ 0 & 0 & 0 & 0 & 0 & 0 \\ 0 & 0 & 0 & 0 & 0 & 0 \\ -\omega^2\hat{M}_{21} & -\omega^2\hat{M}_{21} & -\omega^2\hat{M}_{22} & -\omega^2\hat{M}_{22} & -\omega^2\hat{M}_{22} & -\omega^2\hat{M}_{22} \end{bmatrix} \tag{H.25}$$

$$\mathbf{M1}_n = \mathbf{M}_{1n} + 2\mathbf{N}_{1n}\mathbf{Tn}_{f11}, \tag{H.26}$$

$$\mathbf{M1}_p = \mathbf{M}_{1p} + 2\mathbf{N}_{1p}\mathbf{Tn}_{f22}, \tag{H.27}$$

$$\mathbf{M1}_{0n1} = \mathbf{M}_{10} + 2\mathbf{N}_{10}\mathbf{Tn}_{f11} - 2\mathbf{N}_{10}\mathbf{Tn}_{f21} - \mathbf{F}, \tag{H.28}$$

$$\mathbf{M1}_{0n2} = \mathbf{M}_{10} + 2\mathbf{N}_{10}\mathbf{Tn}_{f11} - 2\mathbf{N}_{10}\mathbf{Tn}_{f12} \tag{H.29}$$

The total transfer matrix reads

$$\mathbf{T} = \mathbf{M0}_n^{-1}(\mathbf{M1}_n\mathbf{M1}_{0n1}^{-1}\mathbf{M1}_{0n2} + 2\mathbf{N}_{1n}\mathbf{Tn}_{f12})(\mathbf{M1}_p + 2\mathbf{N}_{1p}\mathbf{Tn}_{f21}\mathbf{M1}_{0n1}^{-1}\mathbf{M1}_{0n2})^{-1}\mathbf{M0}_p \tag{H.30}$$

Appendix I

PRINCIPAL DIRECTION OF ODD MASS DENSITY TENSOR

Based upon Eq. 5.7, we can seperate the odd mass density tensor into even and odd parts. The principal mass density and directions can be found by solving eigenvalue problem for the even part

$$\hat{M}^e_{ij} = \begin{bmatrix} \hat{M}_{11} & \hat{M}^e_{12} \\ \hat{M}^e_{21} & \hat{M}_{22}. \end{bmatrix} \tag{I.1}$$

The eigenvalues read

$$\lambda_{1,2} \equiv \tilde{M}_{11,22} = \frac{\hat{M}_{11} + \hat{M}_{22} \pm \sqrt{(\hat{M}_{11} - \hat{M}_{22})^2 + 4\hat{M}^e_{12}\hat{M}^e_{21}}}{2}, \tag{I.2}$$

with $\hat{M}^e_{12} = \hat{M}^e_{21} = \hat{M}_{12}/2$. The corresponding eigenvectors can be written as a transformation matrix $\tilde{\beta}$ reading

$$\tilde{\beta} = \begin{bmatrix} \cos\tilde{\theta}_1 & -\sin\tilde{\theta}_1 \\ \sin\tilde{\theta}_1 & \cos\tilde{\theta}_1 \end{bmatrix}. \tag{I.3}$$

where the principal orientation of the smallest mass density takes $\tan(2\tilde{\theta}_1) = 2\hat{M}^e_{12}/(\hat{M}_{22} - \hat{M}_{11})$, since

$$(\hat{M}_{22} - \hat{M}_{11})\cos\tilde{\theta}_1 \sin\tilde{\theta}_1 = \hat{M}^e_{12}(\cos^2\tilde{\theta}_1 - \sin^2\tilde{\theta}_1). \tag{I.4}$$

must hold. While the odd part $\hat{M}^o_{ij}$ given in Eq. 5.7 is invariant under the transformation, namely

$$\hat{M}^o_{kl}\tilde{\beta}_{ki}\tilde{\beta}_{lj} = \hat{M}^o_{ij} = \begin{bmatrix} 0 & \hat{M}^o_{12} \\ -\hat{M}^o_{12} & 0 \end{bmatrix}. \tag{I.5}$$

with $\hat{M}^o_{12} = \hat{M}_{12}/2$. In this sense, the transformed mass density tensor reads

$$\tilde{M}_{ij} = \hat{M}_{kl}\tilde{\beta}_{ki}\tilde{\beta}_{lj} = \hat{M}^e_{kl}\tilde{\beta}_{ki}\tilde{\beta}_{lj} + \hat{M}^o_{ij} = \begin{bmatrix} \tilde{M}_{11} & \hat{M}^o_{12} \\ -\hat{M}^o_{12} & \tilde{M}_{22} \end{bmatrix}, \tag{I.6}$$

which represents Eq. 5.9.

BIBLIOGRAPHY

[1] E. Yablonovitch, "Inhibited spontaneous emission in solid-state physics and electronics," *Physical review letters*, vol. 58, no. 20, p. 2059, 1987.

[2] S. John, "Strong localization of photons in certain disordered dielectric superlattices," *Physical review letters*, vol. 58, no. 23, p. 2486, 1987.

[3] M. Sigalas and E. N. Economou, "Band structure of elastic waves in two dimensional systems," *Solid state communications*, vol. 86, no. 3, pp. 141–143, 1993.

[4] M. S. Kushwaha, P. Halevi, L. Dobrzynski, and B. Djafari-Rouhani, "Acoustic band structure of periodic elastic composites," *Physical review letters*, vol. 71, no. 13, p. 2022, 1993.

[5] E. Yablonovitch and T. Gmitter, "Photonic band structure: The face-centered-cubic case," *Physical Review Letters*, vol. 63, no. 18, p. 1950, 1989.

[6] R. Martínez-Sala, J. Sancho, J. V. Sánchez, V. Gómez, J. Llinares, and F. Meseguer, "Sound attenuation by sculpture," *nature*, vol. 378, no. 6554, pp. 241–241, 1995.

[7] Z. Liu, X. Zhang, Y. Mao, Y. Zhu, Z. Yang, C. T. Chan, and P. Sheng, "Locally resonant sonic materials," *science*, vol. 289, no. 5485, pp. 1734–1736, 2000.

[8] H. Huang and C. Sun, "Wave attenuation mechanism in an acoustic metamaterial with negative effective mass density," *New Journal of Physics*, vol. 11, no. 1, p. 013003, 2009.

[9] S. Yao, X. Zhou, and G. Hu, "Experimental study on negative effective mass in a 1d mass–spring system," *New Journal of Physics*, vol. 10, no. 4, p. 043020, 2008.

[10] A. Baz, "The structure of an active acoustic metamaterial with tunable effective density," *New Journal of Physics*, vol. 11, no. 12, p. 123010, 2009.

[11] Z. Yang, J. Mei, M. Yang, N. Chan, and P. Sheng, "Membrane-type acoustic metamaterial with negative dynamic mass," *Physical review letters*, vol. 101, no. 20, p. 204301, 2008.

[12] M. Yang, G. Ma, Z. Yang, and P. Sheng, "Coupled membranes with doubly negative mass density and bulk modulus," *Physical review letters*, vol. 110, no. 13, p. 134301, 2013.

[13] Y. Ding, Z. Liu, C. Qiu, and J. Shi, "Metamaterial with simultaneously negative bulk modulus and mass density," *Physical review letters*, vol. 99, no. 9, p. 093904, 2007.

[14] G. Ma, M. Yang, S. Xiao, Z. Yang, and P. Sheng, "Acoustic metasurface with hybrid resonances," *Nature materials*, vol. 13, no. 9, pp. 873–878, 2014.

[15] H. Nguyen, Q. Wu, J. Chen, Y. Yu, H. Chen, S. Tracy, and G. Huang, "A broadband acoustic panel based on double-layer membrane-type metamaterials," *Applied Physics Letters*, vol. 118, no. 18, p. 184101, 2021.

[16] G. Ma and P. Sheng, "Acoustic metamaterials: From local resonances to broad horizons," *Science advances*, vol. 2, no. 2, p. e1501595, 2016.

[17] H. Chen and C. T. Chan, "Acoustic cloaking in three dimensions using acoustic metamaterials," *Applied physics letters*, vol. 91, no. 18, p. 183518, 2007.

[18] X. Xu, C. Wang, W. Shou, Z. Du, Y. Chen, B. Li, W. Matusik, N. Hussein, and G. Huang, "Physical realization of elastic cloaking with a polar material," *Physical review letters*, vol. 124, no. 11, p. 114301, 2020.

[19] Y. Chen, M. V. Barnhart, J. Chen, G. Hu, C. Sun, and G. Huang, "Dissipative elastic metamaterials for broadband wave mitigation at subwavelength scale," *Composite Structures*, vol. 136, pp. 358–371, 2016.

[20] R. Zhu, X. Liu, G. Hu, C. Sun, and G. Huang, "A chiral elastic metamaterial beam for broadband vibration suppression," *Journal of Sound and Vibration*, vol. 333, no. 10, pp. 2759–2773, 2014.

[21] Y. Chen, R. Zhu, M. V. Barnhart, and G. Huang, "Enhanced flexural wave sensing by adaptive gradient-index metamaterials," *Scientific reports*, vol. 6, no. 1, pp. 1–11, 2016.

[22] X. Yan, R. Zhu, G. Huang, and F.-G. Yuan, "Focusing guided waves using surface bonded elastic metamaterials," *Applied Physics Letters*, vol. 103, no. 12, p. 121901, 2013.

[23] H. Lee, J. H. Oh, H. M. Seung, S. H. Cho, and Y. Y. Kim, "Extreme stiffness hyperbolic elastic metamaterial for total transmission subwavelength imaging," *Scientific reports*, vol. 6, no. 1, pp. 1–12, 2016.

[24] R. Zhu, X. Liu, G. Huang, H.-H. Huang, and C. Sun, "Microstructural design and experimental validation of elastic metamaterial plates with anisotropic mass density," *Physical Review B*, vol. 86, no. 14, p. 144307, 2012.

[25] R. Zhu, Y. Chen, Y. Wang, G. Hu, and G. Huang, "A single-phase elastic hyperbolic metamaterial with anisotropic mass density," *The Journal of the Acoustical Society of America*, vol. 139, no. 6, pp. 3303–3310, 2016.

[26] R. Zhu, X. Liu, G. Hu, C. Sun, and G. Huang, "Negative refraction of elastic waves at the deep-subwavelength scale in a single-phase metamaterial," *Nature communications*, vol. 5, no. 1, pp. 1–8, 2014.

[27] X.-N. Liu, G.-K. Hu, G.-L. Huang, and C.-T. Sun, "An elastic metamaterial with simultaneously negative mass density and bulk modulus," *Applied physics letters*, vol. 98, no. 25, p. 251907, 2011.

[28] C. Yang, M. Boorugu, A. Dopp, J. Ren, R. Martin, D. Han, W. Choi, and H. Lee, "4d printing reconfigurable, deployable and mechanically tunable metamaterials," *Materials Horizons*, vol. 6, no. 6, pp. 1244–1250, 2019.

[29] N. Yang, C.-W. Chen, J. Yang, and J. L. Silverberg, "Emergent reconfigurable mechanical metamaterial tessellations with an exponentially large number of discrete configurations," *Materials & Design*, vol. 196, p. 109143, 2020.

[30] R. L. Forward, "Electronic damping of vibrations in optical structures," *Applied optics*, vol. 18, no. 5, pp. 690–697, 1979.

[31] N. W. Hagood and A. Von Flotow, "Damping of structural vibrations with piezoelectric materials and passive electrical networks," *Journal of sound and vibration*, vol. 146, no. 2, pp. 243–268, 1991.

[32] M. Neubauer, R. Oleskiewicz, K. Popp, and T. Krzyzynski, "Optimization of damping and absorbing performance of shunted piezo elements utilizing negative capacitance," *Journal of sound and vibration*, vol. 298, no. 1-2, pp. 84–107, 2006.

[33] B. S. Beck, K. A. Cunefare, M. Ruzzene, and M. Collet, "Experimental analysis of a cantilever beam with a shunted piezoelectric periodic array," *Journal of Intelligent Material Systems and Structures*, vol. 22, no. 11, pp. 1177–1187, 2011.

[34] C. H. Park and A. Baz, "Vibration control of beams with negative capacitive shunting of interdigital electrode piezoceramics," *Journal of Vibration and Control*, vol. 11, no. 3, pp. 331–346, 2005.

[35] S. Behrens, A. Fleming, and S. Moheimani, "A broadband controller for shunt piezoelectric damping of structural vibration," *Smart materials and structures*, vol. 12, no. 1, p. 18, 2003.

[36] A. E. Bergamini, M. Zündel, E. A. Flores Parra, T. Delpero, M. Ruzzene, and P. Ermanni, "Hybrid dispersive media with controllable wave propagation: A new take on smart materials," *Journal of Applied Physics*, vol. 118, no. 15, p. 154310, 2015.

[37] A. Bergamini, T. Delpero, L. D. Simoni, L. D. Lillo, M. Ruzzene, and P. Ermanni, "Phononic crystal with adaptive connectivity," *Advanced Materials*, vol. 26, no. 9, pp. 1343–1347, 2014.

[38] F. dell'Isola, C. Maurini, and M. Porfiri, "Passive damping of beam vibrations through distributed electric networks and piezoelectric transducers: prototype design and experimental validation," *Smart materials and Structures*, vol. 13, no. 2, p. 299, 2004.

[39] L. Airoldi and M. Ruzzene, "Design of tunable acoustic metamaterials through periodic arrays of resonant shunted piezos," *New Journal of Physics*, vol. 13, no. 11, p. 113010, 2011.

[40] M. Collet, M. Ouisse, and M. N. Ichchou, "Structural energy flow optimization through adaptive shunted piezoelectric metacomposites," *Journal of Intelligent Material Systems and Structures*, vol. 23, no. 15, pp. 1661–1677, 2012.

[41] S.-B. Chen, J.-H. Wen, D.-L. Yu, G. Wang, and X.-S. Wen, "Band gap control of phononic beam with negative capacitance piezoelectric shunt," *Chinese Physics B*, vol. 20, no. 1, p. 014301, 2011.

[42] G. Wang, J. Wang, S. Chen, and J. Wen, "Vibration attenuations induced by periodic arrays of piezoelectric patches connected by enhanced resonant shunting circuits," *Smart materials and structures*, vol. 20, no. 12, p. 125019, 2011.

[43] Y. Chen, G. Huang, and C. Sun, "Band gap control in an active elastic metamaterial with negative capacitance piezoelectric shunting," *Journal of Vibration and Acoustics*, vol. 136, no. 6, 2014.

[44] Y. Chen, G. Hu, and G. Huang, "A hybrid elastic metamaterial with negative mass density and tunable bending stiffness," *Journal of the Mechanics and Physics of Solids*, vol. 105, pp. 179–198, 2017.

[45] X. Li, Y. Chen, G. Hu, and G. Huang, "A self-adaptive metamaterial beam with digitally controlled resonators for subwavelength broadband flexural wave attenuation," *Smart Materials and Structures*, vol. 27, no. 4, p. 045015, 2018.

[46] G. Wang and S. Chen, "Large low-frequency vibration attenuation induced by arrays of piezoelectric patches shunted with amplifier–resonator feedback circuits," *Smart Materials and Structures*, vol. 25, no. 1, p. 015004, 2015.

[47] Y. Chen, G. Hu, and G. Huang, "An adaptive metamaterial beam with hybrid shunting circuits for extremely broadband control of flexural waves," *Smart Materials and Structures*, vol. 25, no. 10, p. 105036, 2016.

[48] S. Li, J. Xu, and J. Tang, "Tunable modulation of refracted lamb wave front facilitated by adaptive elastic metasurfaces," *Applied Physics Letters*, vol. 112, no. 2, p. 021903, 2018.

[49] Y. Chen, X. Li, G. Hu, M. R. Haberman, and G. Huang, "An active mechanical willis meta-layer with asymmetric polarizabilities," *Nature communications*, vol. 11, no. 1, pp. 1–8, 2020.

[50] Y. Chen, X. Li, H. Nassar, G. Hu, and G. Huang, "A programmable metasurface for real time control of broadband elastic rays," *Smart Materials and Structures*, vol. 27, no. 11, p. 115011, 2018.

[51] X. Li, Y. Chen, X. Zhang, and G. Huang, "Shaping elastic wave mode conversion with a piezoelectric-based programmable meta-boundary," *Extreme Mechanics Letters*, vol. 39, p. 100837, 2020.

[52] X. Li, Y. Chen, R. Zhu, and G. Huang, "An active meta-layer for optimal flexural wave absorption and cloaking," *Mechanical Systems and Signal Processing*, vol. 149, p. 107324, 2021.

[53] C. M. Bender and S. Boettcher, "Real spectra in non-hermitian hamiltonians having p t symmetry," *Physical Review Letters*, vol. 80, no. 24, p. 5243, 1998.

[54] C. M. Bender, "Making sense of non-hermitian hamiltonians," *Reports on Progress in Physics*, vol. 70, no. 6, p. 947, 2007.

[55] C. E. Rüter, K. G. Makris, R. El-Ganainy, D. N. Christodoulides, M. Segev, and D. Kip, "Observation of parity–time symmetry in optics," *Nature physics*, vol. 6, no. 3, pp. 192–195, 2010.

[56] A. Guo, G. Salamo, D. Duchesne, R. Morandotti, M. Volatier-Ravat, V. Aimez, G. Siviloglou, and D. Christodoulides, "Observation of p t-symmetry breaking in complex optical potentials," *Physical review letters*, vol. 103, no. 9, p. 093902, 2009.

[57] Y. Aurégan and V. Pagneux, "P t-symmetric scattering in flow duct acoustics," *Physical review letters*, vol. 118, no. 17, p. 174301, 2017.

[58] K. G. Makris, R. El-Ganainy, D. Christodoulides, and Z. H. Musslimani, "Beam dynamics in p t symmetric optical lattices," *Physical Review Letters*, vol. 100, no. 10, p. 103904, 2008.

[59] Z. Lin, H. Ramezani, T. Eichelkraut, T. Kottos, H. Cao, and D. N. Christodoulides, "Unidirectional invisibility induced by p t-symmetric periodic structures," *Physical Review Letters*, vol. 106, no. 21, p. 213901, 2011.

[60] S. V. Dmitriev, A. A. Sukhorukov, and Y. S. Kivshar, "Binary parity-time-symmetric nonlinear lattices with balanced gain and loss," *Optics letters*, vol. 35, no. 17, pp. 2976–2978, 2010.

[61] B. Peng, Ş. Özdemir, S. Rotter, H. Yilmaz, M. Liertzer, F. Monifi, C. Bender, F. Nori, and L. Yang, "Loss-induced suppression and revival of lasing," *Science*, vol. 346, no. 6207, pp. 328–332, 2014.

[62] R. El-Ganainy, K. Makris, D. Christodoulides, and Z. H. Musslimani, "Theory of coupled optical pt-symmetric structures," *Optics letters*, vol. 32, no. 17, pp. 2632–2634, 2007.

[63] L. Feng, Y.-L. Xu, W. S. Fegadolli, M.-H. Lu, J. E. Oliveira, V. R. Almeida, Y.-F. Chen, and A. Scherer, "Experimental demonstration of a unidirectional reflectionless parity-time metamaterial at optical frequencies," *Nature materials*, vol. 12, no. 2, pp. 108–113, 2013.

[64] X. Zhu, H. Ramezani, C. Shi, J. Zhu, and X. Zhang, "P t-symmetric acoustics," *Physical Review X*, vol. 4, no. 3, p. 031042, 2014.

[65] K. Ding, G. Ma, M. Xiao, Z. Zhang, and C. T. Chan, "Emergence, coalescence, and topological properties of multiple exceptional points and their experimental realization," *Physical Review X*, vol. 6, no. 2, p. 021007, 2016.

[66] C. Shi, M. Dubois, Y. Chen, L. Cheng, H. Ramezani, Y. Wang, and X. Zhang, "Accessing the exceptional points of parity-time symmetric acoustics," *Nature communications*, vol. 7, no. 1, pp. 1–5, 2016.

[67] L. Feng, Z. J. Wong, R.-M. Ma, Y. Wang, and X. Zhang, "Single-mode laser by parity-time symmetry breaking," *Science*, vol. 346, no. 6212, pp. 972–975, 2014.

[68] T. Liu, X. Zhu, F. Chen, S. Liang, and J. Zhu, "Unidirectional wave vector manipulation in two-dimensional space with an all passive acoustic parity-time-symmetric metamaterials crystal," *Physical review letters*, vol. 120, no. 12, p. 124502, 2018.

[69] J. Christensen, M. Willatzen, V. Velasco, and M.-H. Lu, "Parity-time synthetic phononic media," *Physical review letters*, vol. 116, no. 20, p. 207601, 2016.

[70] R. Fleury, D. L. Sounas, and A. Alu, "Negative refraction and planar focusing based on parity-time symmetric metasurfaces," *Physical review letters*, vol. 113, no. 2, p. 023903, 2014.

[71] J. Luo, J. Li, and Y. Lai, "Electromagnetic impurity-immunity induced by parity-time symmetry," *Physical Review X*, vol. 8, no. 3, p. 031035, 2018.

[72] X. Zhu, L. Feng, P. Zhang, X. Yin, and X. Zhang, "One-way invisible cloak using parity-time symmetric transformation optics," *Optics letters*, vol. 38, no. 15, pp. 2821–2824, 2013.

[73] Y. Chong, L. Ge, and A. D. Stone, "P t-symmetry breaking and laser-absorber modes in optical scattering systems," *Physical Review Letters*, vol. 106, no. 9, p. 093902, 2011.

[74] S. Longhi, "Pt-symmetric laser absorber," *Physical Review A*, vol. 82, no. 3, p. 031801, 2010.

[75] Z. J. Wong, Y.-L. Xu, J. Kim, K. O'Brien, Y. Wang, L. Feng, and X. Zhang, "Lasing and anti-lasing in a single cavity," *Nature photonics*, vol. 10, no. 12, pp. 796–801, 2016.

[76] J. Wiersig, "Sensors operating at exceptional points: general theory," *Physical review A*, vol. 93, no. 3, p. 033809, 2016.

[77] R. Fleury, D. Sounas, and A. Alu, "An invisible acoustic sensor based on parity-time symmetry," *Nature communications*, vol. 6, no. 1, pp. 1–7, 2015.

[78] M. Sakhdari, M. Farhat, and P.-Y. Chen, "Pt-symmetric metasurfaces: wave manipulation and sensing using singular points," *New Journal of Physics*, vol. 19, no. 6, p. 065002, 2017.

[79] P.-Y. Chen, M. Sakhdari, M. Hajizadegan, Q. Cui, M. M.-C. Cheng, R. El-Ganainy, and A. Alù, "Generalized parity–time symmetry condition for enhanced sensor telemetry," *Nature Electronics*, vol. 1, no. 5, pp. 297–304, 2018.

[80] S. Assawaworrarit, X. Yu, and S. Fan, "Robust wireless power transfer using a nonlinear parity–time-symmetric circuit," *Nature*, vol. 546, no. 7658, pp. 387–390, 2017.

[81] L. Ge, Y. Chong, and A. D. Stone, "Conservation relations and anisotropic transmission resonances in one-dimensional pt-symmetric photonic heterostructures," *Physical Review A*, vol. 85, no. 2, p. 023802, 2012.

[82] D. R. Smith and N. Kroll, "Negative refractive index in left-handed materials," *Physical review letters*, vol. 85, no. 14, p. 2933, 2000.

[83] D. R. Smith, W. J. Padilla, D. Vier, S. C. Nemat-Nasser, and S. Schultz, "Composite medium with simultaneously negative permeability and permittivity," *Physical review letters*, vol. 84, no. 18, p. 4184, 2000.

[84] Z. Hou and B. Assouar, "Tunable elastic parity-time symmetric structure based on the shunted piezoelectric materials," *Journal of Applied Physics*, vol. 123, no. 8, p. 085101, 2018.

[85] O. Thorp, M. Ruzzene, and A. Baz, "Attenuation and localization of wave propagation in rods with periodic shunted piezoelectric patches," *Smart Materials and Structures*, vol. 10, no. 5, p. 979, 2001.

[86] R. Zhu, Y. Chen, M. V. Barnhart, G. Hu, C. Sun, and G. Huang, "Experimental study of an adaptive elastic metamaterial controlled by electric circuits," *Applied Physics Letters*, vol. 108, no. 1, p. 011905, 2016.

[87] B. Ash, S. Worsfold, P. Vukusic, and G. Nash, "A highly attenuating and frequency tailorable annular hole phononic crystal for surface acoustic waves," *Nature communications*, vol. 8, no. 1, pp. 1–7, 2017.

[88] S. Benchabane, R. Salut, O. Gaiffe, V. Soumann, M. Addouche, V. Laude, and A. Khelif, "Surface-wave coupling to single phononic subwavelength resonators," *Physical Review Applied*, vol. 8, no. 3, p. 034016, 2017.

[89] N. Boechler, J. Eliason, A. Kumar, A. Maznev, K. Nelson, and N. Fang, "Interaction of a contact resonance of microspheres with surface acoustic waves," *Physical review letters*, vol. 111, no. 3, p. 036103, 2013.

[90] A. Khelif, Y. Achaoui, S. Benchabane, V. Laude, and B. Aoubiza, "Locally resonant surface acoustic wave band gaps in a two-dimensional phononic crystal of pillars on a surface," *Physical Review B*, vol. 81, no. 21, p. 214303, 2010.

[91] T.-T. Wu, Z.-G. Huang, and S. Lin, "Surface and bulk acoustic waves in two-dimensional phononic crystal consisting of materials with general anisotropy," *Physical review B*, vol. 69, no. 9, p. 094301, 2004.

[92] D. Colquitt, A. Colombi, R. Craster, P. Roux, and S. Guenneau, "Seismic metasurfaces: Sub-wavelength resonators and rayleigh wave interaction," *Journal of the Mechanics and Physics of Solids*, vol. 99, pp. 379–393, 2017.

[93] R. Zhu, X. Liu, G. Hu, F. Yuan, and G. Huang, "Microstructural designs of plate-type elastic metamaterial and their potential applications: a review," *International Journal of Smart and Nano Materials*, vol. 6, no. 1, pp. 14–40, 2015.

[94] M. Badreddine Assouar and M. Oudich, "Dispersion curves of surface acoustic waves in a two-dimensional phononic crystal," *Applied Physics Letters*, vol. 99, no. 12, p. 123505, 2011.

[95] T.-T. Wu, Z.-G. Huang, T.-C. Tsai, and T.-C. Wu, "Evidence of complete band gap and resonances in a plate with periodic stubbed surface," *Applied Physics Letters*, vol. 93, no. 11, p. 111902, 2008.

[96] G.-Y. Li, G. Xu, Y. Zheng, and Y. Cao, "Non-leaky modes and bandgaps of surface acoustic waves in wrinkled stiff-film/compliant-substrate bilayers," *Journal of the Mechanics and Physics of Solids*, vol. 112, pp. 239–252, 2018.

[97] B. Liu, X. Chen, H. Cai, M. M. Ali, X. Tian, L. Tao, Y. Yang, and T. Ren, "Surface acoustic wave devices for sensor applications," *Journal of semiconductors*, vol. 37, no. 2, p. 021001, 2016.

[98] J. Devkota, P. R. Ohodnicki, and D. W. Greve, "Saw sensors for chemical vapors and gases," *Sensors*, vol. 17, no. 4, p. 801, 2017.

[99] V. Polewczyk, K. Dumesnil, D. Lacour, M. Moutaouekkil, H. Mjahed, N. Tiercelin, S. P. Watelot, H. Mishra, Y. Dusch, S. Hage-Ali *et al.*, "Unipolar and bipolar high-magnetic-field sensors based on surface acoustic wave resonators," *Physical Review Applied*, vol. 8, no. 2, p. 024001, 2017.

[100] M. Kadota, S. Ito, Y. Ito, T. Hada, and K. Okaguchi, "Magnetic sensor based on surface acoustic wave resonators," *Japanese journal of applied physics*, vol. 50, no. 7S, p. 07HD07, 2011.

[101] T. Aubert, O. Elmazria, B. Assouar, L. Bouvot, and M. Oudich, "Surface acoustic wave devices based on aln/sapphire structure for high temperature applications," *Applied Physics Letters*, vol. 96, no. 20, p. 203503, 2010.

[102] P. Delsing, A. N. Cleland, M. J. Schuetz, J. Knörzer, G. Giedke, J. I. Cirac, K. Srinivasan, M. Wu, K. C. Balram, C. Bäuerle *et al.*, "The 2019 surface acoustic waves roadmap," *Journal of Physics D: Applied Physics*, vol. 52, no. 35, p. 353001, 2019.

[103] C. C. Ruppel, "Acoustic wave filter technology–a review," *IEEE transactions on ultrasonics, ferroelectrics, and frequency control*, vol. 64, no. 9, pp. 1390–1400, 2017.

[104] M. Kadota, T. Nakao, N. Taniguchi, E. Takata, M. Mimura, K. Nishiyama, T. Hada, and T. Komura, "Surface acoustic wave duplexer for us personal communication services with good temperature characteristics," *Japanese journal of applied physics*, vol. 44, no. 6S, p. 4527, 2005.

[105] A. Colombi, P. Roux, S. Guenneau, P. Gueguen, and R. V. Craster, "Forests as a natural seismic metamaterial: Rayleigh wave bandgaps induced by local resonances," *Scientific reports*, vol. 6, no. 1, pp. 1–7, 2016.

[106] J. Artru, T. Farges, and P. Lognonné, "Acoustic waves generated from seismic surface waves: propagation properties determined from doppler sounding observations and normal-mode modelling," *Geophysical Journal International*, vol. 158, no. 3, pp. 1067–1077, 2004.

[107] K. A. Lurie, "Effective properties of smart elastic laminates and the screening phenomenon," *International Journal of Solids and Structures*, vol. 34, no. 13, pp. 1633–1643, 1997.

[108] H. Nassar, H. Chen, A. Norris, and G. Huang, "Non-reciprocal flexural wave propagation in a modulated metabeam," *Extreme Mechanics Letters*, vol. 15, pp. 97–102, 2017.

[109] ——, "Non-reciprocal flexural wave propagation in a modulated metabeam," *Extreme Mechanics Letters*, vol. 15, pp. 97–102, 2017.

[110] H. Nassar, X. Xu, A. Norris, and G. Huang, "Modulated phononic crystals: Non-reciprocal wave propagation and willis materials," *Journal of the Mechanics and Physics of Solids*, vol. 101, pp. 10–29, 2017.

[111] S. P. Wallen and M. R. Haberman, "Nonreciprocal wave phenomena in spring-mass chains with effective stiffness modulation induced by geometric nonlinearity," *Physical Review E*, vol. 99, no. 1, p. 013001, 2019.

[112] K. Yi, M. Collet, and S. Karkar, "Frequency conversion induced by time-space modulated media," *Physical review B*, vol. 96, no. 10, p. 104110, 2017.

[113] H. Nassar, B. Yousefzadeh, R. Fleury, M. Ruzzene, A. Alù, C. Daraio, A. N. Norris, G. Huang, and M. R. Haberman, "Nonreciprocity in acoustic and elastic materials," *Nature Reviews Materials*, vol. 5, no. 9, pp. 667–685, 2020.

[114] Z. Yu and S. Fan, "Complete optical isolation created by indirect interband photonic transitions," *Nature photonics*, vol. 3, no. 2, pp. 91–94, 2009.

[115] M. B. Zanjani, A. R. Davoyan, A. M. Mahmoud, N. Engheta, and J. R. Lukes, "One-way phonon isolation in acoustic waveguides," *Applied Physics Letters*, vol. 104, no. 8, p. 081905, 2014.

[116] R. Fleury, D. L. Sounas, C. F. Sieck, M. R. Haberman, and A. Alù, "Sound isolation and giant linear nonreciprocity in a compact acoustic circulator," *Science*, vol. 343, no. 6170, pp. 516–519, 2014.

[117] G. Trainiti and M. Ruzzene, "Non-reciprocal elastic wave propagation in spatiotemporal periodic structures," *New Journal of Physics*, vol. 18, no. 8, p. 083047, 2016.

[118] N. Swinteck, S. Matsuo, K. Runge, J. O. Vasseur, P. Lucas, and P. A. Deymier, "Bulk elastic waves with unidirectional backscattering-immune topological states in a time-dependent superlattice," *Journal of Applied Physics*, vol. 118, no. 6, p. 063103, 2015.

[119] F. Casadei, T. Delpero, A. Bergamini, P. Ermanni, and M. Ruzzene, "Piezoelectric resonator arrays for tunable acoustic waveguides and metamaterials," *Journal of Applied Physics*, vol. 112, no. 6, p. 064902, 2012.

[120] Y. Chen, X. Li, H. Nassar, A. N. Norris, C. Daraio, and G. Huang, "Nonreciprocal wave propagation in a continuum-based metamaterial with space-time modulated resonators," *Physical Review Applied*, vol. 11, no. 6, p. 064052, 2019.

[121] B. R. Mace and E. Manconi, "Wave motion and dispersion phenomena: Veering, locking and strong coupling effects," *The Journal of the Acoustical Society of America*, vol. 131, no. 2, pp. 1015–1028, 2012.

[122] E. Cassedy and A. Oliner, "Dispersion relations in time-space periodic media: Part i—stable interactions," *Proceedings of the IEEE*, vol. 51, no. 10, pp. 1342–1359, 1963.

[123] E. S. Cassedy, "Dispersion relations in time-space periodic media part ii—unstable interactions," *Proceedings of the IEEE*, vol. 55, no. 7, pp. 1154–1168, 1967.

[124] Y. Wang, B. Yousefzadeh, H. Chen, H. Nassar, G. Huang, and C. Daraio, "Observation of nonreciprocal wave propagation in a dynamic phononic lattice," *Physical review letters*, vol. 121, no. 19, p. 194301, 2018.

[125] S.-Y. Yu, C. He, Z. Wang, F.-K. Liu, X.-C. Sun, Z. Li, H.-Z. Lu, M.-H. Lu, X.-P. Liu, and Y.-F. Chen, "Elastic pseudospin transport for integratable topological phononic circuits," *Nature communications*, vol. 9, no. 1, pp. 1–8, 2018.

[126] S. H. Mousavi, A. B. Khanikaev, and Z. Wang, "Topologically protected elastic waves in phononic metamaterials," *Nature communications*, vol. 6, no. 1, pp. 1–7, 2015.

[127] H. Chen, H. Nassar, and G. Huang, "A study of topological effects in 1d and 2d mechanical lattices," *Journal of the Mechanics and Physics of Solids*, vol. 117, pp. 22–36, 2018.

[128] Q. Wu, H. Chen, X. Li, and G. Huang, "In-plane second-order topologically protected states in elastic kagome lattices," *Physical Review Applied*, vol. 14, no. 1, p. 014084, 2020.

[129] S. D. Huber, "Topological mechanics," *Nature Physics*, vol. 12, no. 7, pp. 621–623, 2016.

[130] Y.-Z. Wang, F.-M. Li, and Y.-S. Wang, "Active feedback control of elastic wave metamaterials," *Journal of Intelligent Material Systems and Structures*, vol. 28, no. 15, pp. 2110–2116, 2017.

[131] L. Sirota, R. Ilan, Y. Shokef, and Y. Lahini, "Non-newtonian topological mechanical metamaterials using feedback control," *Physical Review Letters*, vol. 125, no. 25, p. 256802, 2020.

[132] A. Ghatak, M. Brandenbourger, J. Van Wezel, and C. Coulais, "Observation of non-hermitian topology and its bulk–edge correspondence in an active mechanical metamaterial," *Proceedings of the National Academy of Sciences*, vol. 117, no. 47, pp. 29 561–29 568, 2020.

[133] M. Brandenbourger, X. Locsin, E. Lerner, and C. Coulais, "Non-reciprocal robotic metamaterials," *Nature communications*, vol. 10, no. 1, pp. 1–8, 2019.

[134] C. Scheibner, A. Souslov, D. Banerjee, P. Surówka, W. Irvine, and V. Vitelli, "Odd elasticity," *Nature Physics*, vol. 16, no. 4, pp. 475–480, 2020.

[135] C. Scheibner, W. T. Irvine, and V. Vitelli, "Non-hermitian band topology and skin modes in active elastic media," *Physical Review Letters*, vol. 125, no. 11, p. 118001, 2020.

[136] G. Trainiti, Y. Xia, J. Marconi, G. Cazzulani, A. Erturk, and M. Ruzzene, "Time-periodic stiffness modulation in elastic metamaterials for selective wave filtering: Theory and experiment," *Physical review letters*, vol. 122, no. 12, p. 124301, 2019.

[137] M. I. Rosa and M. Ruzzene, "Dynamics and topology of non-hermitian elastic lattices with non-local feedback control interactions," *New Journal of Physics*, vol. 22, no. 5, p. 053004, 2020.

[138] Y. Chen, X. Li, C. Scheibner, V. Vitelli, and G. Huang, "Realization of active metamaterials with odd micropolar elasticity," *Nature communications*, vol. 12, no. 1, pp. 1–12, 2021.

[139] J. Kishine, A. Ovchinnikov, and A. Tereshchenko, "Chirality-induced phonon dispersion in a noncentrosymmetric micropolar crystal," *Physical Review Letters*, vol. 125, no. 24, p. 245302, 2020.

[140] Y. Chen, M. Kadic, and M. Wegener, "Roton-like acoustical dispersion relations in 3d metamaterials," *Nature communications*, vol. 12, no. 1, pp. 1–8, 2021.

[141] J. A. Iglesias Martínez, M. F. Groß, Y. Chen, T. Frenzel, V. Laude, M. Kadic, and M. Wegener, "Experimental observation of roton-like dispersion relations in metamaterials," *Science advances*, vol. 7, no. 49, p. eabm2189, 2021.

[142] S. Shankar, A. Souslov, M. J. Bowick, M. C. Marchetti, and V. Vitelli, "Topological active matter," *Nature Reviews Physics*, pp. 1–19, 2022.

[143] M. Brandenbourger, c. Scheibner, J. Veenstra, V. Vitelli, and C. Coulais, "Limit cycles turn active matter into robots," *arXiv*, vol. 2108.08837, p. https://doi.org/10.48550/arXiv.2108.08837, 2022.

[144] X. Zhou and G. Hu, "Analytic model of elastic metamaterials with local resonances," *Physical Review B*, vol. 79, no. 19, p. 195109, 2009.

[145] X. Zhou, X. Liu, and G. Hu, "Elastic metamaterials with local resonances: an overview," *Theoretical and Applied Mechanics Letters*, vol. 2, no. 4, p. 041001, 2012.

[146] J. M. Kweun, H. J. Lee, J. H. Oh, H. M. Seung, and Y. Y. Kim, "Transmodal fabry-pérot resonance: theory and realization with elastic metamaterials," *Physical review letters*, vol. 118, no. 20, p. 205901, 2017.

[147] Q. Wu and G. Huang, "Omnidirectional wave polarization manipulation in isotropic polar solids," *International Journal of Solids and Structures*, vol. 241, p. 111481, 2022.

[148] X. Liu, G. Hu, C. Sun, and G. Huang, "Wave propagation characterization and design of two-dimensional elastic chiral metacomposite," *Journal of Sound and Vibration*, vol. 330, no. 11, pp. 2536–2553, 2011.

[149] Y. Wu, Y. Lai, and Z.-Q. Zhang, "Effective medium theory for elastic metamaterials in two dimensions," *Physical Review B*, vol. 76, no. 20, p. 205313, 2007.

[150] Y. Lai, Y. Wu, P. Sheng, and Z.-Q. Zhang, "Hybrid elastic solids," *Nature materials*, vol. 10, no. 8, pp. 620–624, 2011.

[151] H. Nassar, Y. Chen, and G. Huang, "Isotropic polar solids for conformal transformation elasticity and cloaking," *Journal of the Mechanics and Physics of Solids*, vol. 129, pp. 229–243, 2019.

[152] Y. Ashida, Z. Gong, and M. Ueda, "Non-hermitian physics," *Advances in Physics*, vol. 69, no. 3, pp. 249–435, 2020.

[153] F. K. Kunst and V. Dwivedi, "Non-hermitian systems and topology: A transfer-matrix perspective," *Physical Review B*, vol. 99, no. 24, p. 245116, 2019.

[154] E. J. Bergholtz, J. C. Budich, and F. K. Kunst, "Exceptional topology of non-hermitian systems," *Reviews of Modern Physics*, vol. 93, no. 1, p. 015005, 2021.

[155] S. Yao and Z. Wang, "Edge states and topological invariants of non-hermitian systems," *Physical review letters*, vol. 121, no. 8, p. 086803, 2018.

[156] K. Yokomizo and S. Murakami, "Non-bloch band theory of non-hermitian systems," *Physical review letters*, vol. 123, no. 6, p. 066404, 2019.

[157] C. H. Wang, J. T. Rose, and F.-K. Chang, "A synthetic time-reversal imaging method for structural health monitoring," *Smart materials and structures*, vol. 13, no. 2, p. 415, 2004.

[158] C. R. Farrar and K. Worden, "An introduction to structural health monitoring," *Philosophical Transactions of the Royal Society A: Mathematical, Physical and Engineering Sciences*, vol. 365, no. 1851, pp. 303–315, 2007.

[159] H. Peng and P. F. Pai, "Acoustic metamaterial plates for elastic wave absorption and structural vibration suppression," *International Journal of Mechanical Sciences*, vol. 89, pp. 350–361, 2014.

[160] G. Hu, L. Tang, A. Banerjee, and R. Das, "Metastructure with piezoelectric element for simultaneous vibration suppression and energy harvesting," *Journal of Vibration and Acoustics*, vol. 139, no. 1, 2017.

[161] H. Peng, P. F. Pai, and H. Deng, "Acoustic multi-stopband metamaterial plates design for broadband elastic wave absorption and vibration suppression," *International Journal of Mechanical Sciences*, vol. 103, pp. 104–114, 2015.

[162] M. D. Rao, "Recent applications of viscoelastic damping for noise control in automobiles and commercial airplanes," *Journal of Sound and Vibration*, vol. 262, no. 3, pp. 457–474, 2003.

[163] M. F. Müller, J.-Y. Kim, J. Qu, and L. J. Jacobs, "Characteristics of second harmonic generation of lamb waves in nonlinear elastic plates," *The Journal of the Acoustical Society of America*, vol. 127, no. 4, pp. 2141–2152, 2010.

[164] J. Marconi, E. Riva, M. Di Ronco, G. Cazzulani, F. Braghin, and M. Ruzzene, "Experimental observation of nonreciprocal band gaps in a space-time-modulated beam using a shunted piezoelectric array," *Physical Review Applied*, vol. 13, no. 3, p. 031001, 2020.

[165] X. Xu, Q. Wu, H. Chen, H. Nassar, Y. Chen, A. Norris, M. R. Haberman, and G. Huang, "Physical observation of a robust acoustic pumping in waveguides with dynamic boundary," *Physical review letters*, vol. 125, no. 25, p. 253901, 2020.

[166] M. Zheng, C. I. Park, X. Liu, R. Zhu, G. Hu, and Y. Y. Kim, "Non-resonant metasurface for broadband elastic wave mode splitting," *Applied Physics Letters*, vol. 116, no. 17, p. 171903, 2020.

[167] H. Lee, J. K. Lee, H. M. Seung, and Y. Y. Kim, "Mass-stiffness substructuring of an elastic metasurface for full transmission beam steering," *Journal of the Mechanics and Physics of Solids*, vol. 112, pp. 577–593, 2018.

[168] B. Assouar, B. Liang, Y. Wu, Y. Li, J.-C. Cheng, and Y. Jing, "Acoustic metasurfaces," *Nature Reviews Materials*, vol. 3, no. 12, pp. 460–472, 2018.

[169] L. Cao, Z. Yang, Y. Xu, S.-W. Fan, Y. Zhu, Z. Chen, B. Vincent, and B. Assouar, "Disordered elastic metasurfaces," *Physical Review Applied*, vol. 13, no. 1, p. 014054, 2020.

[170] H. Zhu and F. Semperlotti, "Anomalous refraction of acoustic guided waves in solids with geometrically tapered metasurfaces," *Physical review letters*, vol. 117, no. 3, p. 034302, 2016.

[171] Y. Jin, W. Wang, A. Khelif, and B. Djafari-Rouhani, "Elastic metasurfaces for deep and robust subwavelength focusing and imaging," *Physical Review Applied*, vol. 15, no. 2, p. 024005, 2021.

[172] J. Rong, W. Ye, S. Zhang, and Y. Liu, "Frequency-coded passive multifunctional elastic metasurfaces," *Advanced Functional Materials*, vol. 30, no. 50, p. 2005285, 2020.

[173] S. Tol, Y. Xia, M. Ruzzene, and A. Erturk, "Self-bending elastic waves and obstacle circumventing in wireless power transfer," *Applied Physics Letters*, vol. 110, no. 16, p. 163505, 2017.

[174] M. Dubois, E. Bossy, S. Enoch, S. Guenneau, G. Lerosey, and P. Sebbah, "Time-driven superoscillations with negative refraction," *Physical review letters*, vol. 114, no. 1, p. 013902, 2015.

[175] K. Tang, C. Xu, S. Guenneau, and P. Sebbah, "Pulse dynamics of flexural waves in transformed plates," *Advanced Functional Materials*, vol. 31, no. 15, p. 2009266, 2021.

[176] M. S. Kim, W. R. Lee, Y. Y. Kim, and J. H. Oh, "Transmodal elastic metasurface for broad angle total mode conversion," *Applied Physics Letters*, vol. 112, no. 24, p. 241905, 2018.

[177] X. Su, Z. Lu, and A. N. Norris, "Elastic metasurfaces for splitting sv-and p-waves in elastic solids," *Journal of Applied Physics*, vol. 123, no. 9, p. 091701, 2018.

[178] A. Colombi, V. Ageeva, R. J. Smith, A. Clare, R. Patel, M. Clark, D. Colquitt, P. Roux, S. Guenneau, and R. V. Craster, "Enhanced sensing and conversion of ultrasonic rayleigh waves by elastic metasurfaces," *Scientific Reports*, vol. 7, no. 1, pp. 1–9, 2017.

[179] A. Shaltout, A. Kildishev, and V. Shalaev, "Time-varying metasurfaces and lorentz non-reciprocity," *Optical Materials Express*, vol. 5, no. 11, pp. 2459–2467, 2015.

[180] L. Zhang, X. Q. Chen, R. W. Shao, J. Y. Dai, Q. Cheng, G. Castaldi, V. Galdi, and T. J. Cui, "Breaking reciprocity with space-time-coding digital metasurfaces," *Advanced Materials*, vol. 31, no. 41, p. 1904069, 2019.

[181] N. Chamanara, Y. Vahabzadeh, and C. Caloz, "Simultaneous control of the spatial and temporal spectra of light with space-time varying metasurfaces," *IEEE Transactions on Antennas and Propagation*, vol. 67, no. 4, pp. 2430–2441, 2019.

[182] A. M. Shaltout, V. M. Shalaev, and M. L. Brongersma, "Spatiotemporal light control with active metasurfaces," *Science*, vol. 364, no. 6441, 2019.

[183] D. Ramaccia, D. L. Sounas, A. Alù, A. Toscano, and F. Bilotti, "Phase-induced frequency conversion and doppler effect with time-modulated metasurfaces," *IEEE Transactions on Antennas and Propagation*, vol. 68, no. 3, pp. 1607–1617, 2019.

[184] A. M. Shaltout, K. G. Lagoudakis, J. van de Groep, S. J. Kim, J. Vučković, V. M. Shalaev, and M. L. Brongersma, "Spatiotemporal light control with frequency-gradient metasurfaces," *Science*, vol. 365, no. 6451, pp. 374–377, 2019.

[185] A. A. Mokhtari, Y. Lu, and A. Srivastava, "On the properties of phononic eigenvalue problems," *Journal of the Mechanics and Physics of Solids*, vol. 131, pp. 167–179, 2019.

VITA

Qian Wu was born in 1991, and obtained his Master degree in Condensed Matter Physics from Tongji University, Shanghai, China. He started his Ph.D. study in the Department of Mechanical and Aerospace Engineering at the University of Missouri-Rolla since August 2016, and then transferred to the Department of Mechanical and Aerospace Engineering at the University of Missouri-Columbia in August 2017 to continue his Ph.D. study.